UNIVERSITY
OF TASMANIA

Slamming of Large High-Speed Catamarans in Irregular Seas

by

Benjamin J. French

B.Eng. (Hons) University of Tasmania (2008)

Submitted in the fulfilment of the requirements for the Degree of

Doctor of Philosophy

at the

University of Tasmania

September 2012

Declaration of Originality and Authority of Access

This thesis contains no material which has been accepted for a degree or diploma by the University or any other institution, except by way of background information and duly acknowledged in the thesis, and to the best of the my knowledge and belief no material previously published or written by another person except where due acknowledgement is made in the text of the thesis, nor does the thesis contain any material that infringes copyright.

This thesis may be made available for loan and limited copying and communication in accordance with the Copyright Act 1968, subject to the confidentiality agreement signed by the University of Tasmania, Australian Maritime College, Incat Tasmania Pty Ltd and Revolution Design Pty Ltd.

Benjamin French

Abstract

Current design methods are limited in their ability to predict long term loading statistics relating to wave loads and fatigue from prolonged cyclic loading. These methods either neglect slam loads entirely or they are included as post-processed or simplified two-dimensional methods. The work presented in this thesis introduces a combined theoretical-empirical approach to determining long term load trends in realistic sea conditions during the initial stages of the design spiral. This method builds on a previously developed non-linear time-domain seakeeping strip theory method, for high-speed multi-hull vessels, using scale model testing in irregular seas as a basis for an empirical slam module.

Towing tank experiments, using an extensively instrumented 2.5m hydroelastic scale model wave-piercing catamaran representative of the 112m class Incat design, were used to develop a database of slam events in a range of realistic (but idealised) irregular sea conditions. A total of 2,103 slam events were identified over 22 test conditions during the scale model experiments. Large slams generally occurred in the conditions where motions were largest; however significant scatter was present with extreme events observed to be up to four times the median for most conditions.

Occurrence rates were found to be a function of encountered wave frequency and significant wave height. If the encountered wave frequency coincides with the motion resonance, slam rates increased. Increasing the significant wave height also increased slam occurrences. A wave height dependent slam threshold was identified by extrapolating occurrence rate trends with decreasing significant wave heights. Pressure measurements also revealed that the cross-deck structure was exposed to large local pressures at each measurement station, suggesting that ship designers should ensure the structure can withstand large local loads along the entire length of the bow.

The non-linear time-domain seakeeping program was extended to simulate motions and loads in irregular seas and a method for constructing idealised wave spectra was developed as an input to the seakeeping code. The extended code was verified by conducting a series of program tests and then validated by comparing computational ship motions with results from the scale model experiments in the absence of slamming.

A new module for predicting slam loads, based on a statistical analysis of scale model tests was then developed and integrated into the extended time-domain seakeeping method, allowing for the slam events to be determined on-line in the time-domain. Slams are identified by defining a location dependant immersion threshold criterion based on the geometry of the hull form combined with a stochastically determined variation originating from experimental observations.

In the event of a slam, the maximum load and slam duration are determined by empirical methods stemming from regression analyses on experimental data. Vessel forward speed and relative vertical velocity at the centre bow truncation are used to predict the maximum slam load. Slams loads are ramped up and down over a number of time steps. Forward speed and immersion at the centre bow truncation are key explanatory variables in the duration calculation. The slam load is then applied over a number of time steps according to its duration at the location where it was first triggered.

A case study is finally undertaken demonstrating the application of this method. A high-speed ferry service route was selected and real wave data used to determine expected wave environments. The computer simulation was run for a range of sea conditions and slam events are identified. Slam event statistics are then extrapolated to produce expectations for long term (20+ years) loading expectations showing how this method could be a valuable tool when considering the long term loading implications of a vessel for a particular route.

For Nan.

Acknowledgements

There are a number of people I would like to thank for their help over these past three-and-a-half-years. Without them this project would not have been as fun as it was.

My primary supervisor, Associate Professor Giles Thomas at the Australian Maritime College, he has read more drafts of this thesis than anyone would care to in a lifetime and has expertly guided me through many potential PhD pitfalls. Without his help I would still be lost in Chapter 4 or 5.

My other co-supervisors: Professor Michael Davis and Doctor Damien Holloway from the University of Tasmania, although being somewhat geographically isolated from the Maritime College, they provided useful guidance during our customary fortnightly phone, and later, Skype meetings. I had the pleasure of being taught by Mike and Damien during my undergraduate degree, and it was them who inspired me to follow a career in academia.

My colleagues, friends and tutors: Doctor Shinsuke Matsubara and Luciano Mason, both for their help with programming, outspoken and innovative ideas and good advice in all respects of life. Although they were not explicitly involved in my work, they always listened to my problems and suggested original solutions.

The postgraduates from the 'basement days'. I particularly miss the Friday afternoon discussions.

The AMC towing tank and support staff, I won't mention names for fear of missing someone out. I am eternally grateful for the support they provided during the model tests: without them, there would be no project.

The Australian Research Council and Incat Tasmania: for giving me the opportunity to contribute to this project.

My family: mother, father, Mathew, Hayden, for being around when I needed them.

And finally I would like to thank my lovely fiancée You Jia; you paint my world the most beautiful colours.

Contents

List of Figures

List of Tables

Nomenclature

Abbreviations

AMC	Australian Maritime College
BEAMSEA	Extension of BESTSEA, capable of determining global wave loads
BEM	Boundary Element Method
BESTSEA	**B**oundary **E**lement **S**trip Theory **T**ime Domain **SEA**keeping
CB	Centre Bow
CBT	Centre Bow Truncation
cdf	Cumulative Distribution Function
CFD	Computational Fluid Dynamics
cRIO	Compact Reconfigurable Input Output
DAQ	Data Acquisition
DFT	Discrete Fourier Transform
DNV	Det Norske Veritas
FEM	Finite Element Method
FPGA	Field Programmable Gate Array
HSM	Hydroelastic Segmanted Model
HSS	High-speed Sea Service
ITTC	International Towing Tank Conference
IQR	Interquartile Range
JONSWAP	**Jo**int **N**orth **S**ea **Wa**ve **P**roject
LCG	Longitudinal Centre of Gravity
LVDT	Linear Displacement Voltage Transducer
MARINTEK	Norwegian Marine Technology Research Institute
NI	National Instruments
OLS	Ordinary Least Squares
ONR	Office of Naval Research
pdf	Probability Density Function
RANSE	Reynolds-Averaged Navier-Stokes Equations
RAO	Response Amplitude Operator
SPH	Smoothed Particle Hydrodynamics
UTAS	University of Tasmania
VBM	Vertical Bending Moment

Notation

Greek Symbols

Δ	Mass displacement	kg
ε	Independent and identically distributed random number	
ζ	Wave amplitude	m
$\zeta(x, y, z, t)$	Free surface	m
η	Wave elevation	m
λ	Expected frequency	per unit of time
ξ_3	Heave displacement	m
ξ_5	Pitch angle	rad
ρ	Density	kg/m^3
ρ	Spearman's rank correlation coefficient	
Φ	Total linear velocity potential	m^2/s
ϕ	Disturbance potential	m^2/s
ϕ_1, ϕ_2	Normal distributions	
ϕ_d	Diffraction velocity potential	m^2/s
ϕ_i	Incident velocity potential	m^2/s
ϕ_r	Radiation velocity potential	m^2/s
ω_0	Wave angular frequency	rad/s
ω_e	Encountered wave frequency	rad/s
ω_e^*	Dimensionless encountered wave frequency	

Roman Symbols

A_1	Area under arch at CBT	m^2
A_2	Area of rectangle equivalent to A_1 with width b and height h_f	m^2
a_i, c_i	Regression coefficients	
b	Distance from centre line of vessel to centre line of demihull	m
c	Source location (complex)	m
c	Wave celerity	m/s
C_c	Centre bow force correction factor	
c_i	Individual elastic link calibration factor	Nm/V
$\bar{E}$	Average wave energy over one wavelength	J/m^2
e	Experimental residual	
F_3	Heave force	N
F_5	Pitch moment	Nm
F_a	Force on aft CB transverse beam	N

f_c	Cut-off frequency	Hz
f_e	Encountered wave frequency	Hz
F_f	Force on forward CB transverse beam	N
F_s	Slam load on centre bow	N
F_{slam}	Slam load factor	
F_X	Cumulative distribution function for the random variable X	
g	Gravitational constant	m/s^2
h	Water depth	m
$H_{1/3}$	Significant wave height	m
h_a	Maximum arch height at the CBT	m
h_f	Two-dimensional filling height	m
H_w	Wave height	m
I	Centre bow immersion at slam instant	m
I_5	Pitch moment of inertia	kgm^2
I_μ	Average immersion required for slam event	m
I_{CBT}	Immersion of CBT	m
$I_s(x)$	Threshold immersion required for slam event at location x	m
k	Wave number	rad/m
L	Vessel length	m
l_1	Distance from CB pin joint to elastic link	m
l_2	Distance between CB elastic links	m
$L_{measured}$	Experimentally measured slam load	N
L_p	Predicted slam load	N
L_{slam}	Total slam load	N
Loc	Slam location	m
M	Mass	kg
M	pdf of slam duration	
M_i	Moment at link i	Nm
N	Number of observations	
$\mathbf{n}$	Unit vector normal to the surface of a floating body	
n	Cut-off frequency as a multiple of f_e ($n = \frac{f_c}{f_e}$)	
P	Probability	
p	Pressure	N/m^2

p	Mixing factor	
P_E	Probability of exceedance	
Q_1	Lower quartile	
Q_2	Median	
Q_3	Upper quartile	
$Q(t)$	Source strength	m^2/s
r	Pearson's product-moment correlation coefficient	
$R(i)$	Slam weight at time i	
S	Wave energy spectral ordinate	$m^2/(rad/s)$
s, σ	Standard deviation	
S_α	Wave slope spectrum	$rad^2/(rad/s)$
S_ζ	Wave elevation spectrum	$m^2/(rad/s)$
$S_{x_{30}}$	Heave motion spectrum	$m^2/(rad/s)$
$S_{x_{50}}$	Pitch motion spectrum	$rad^2/(rad/s)$
S_i	Strain gauge signal i	V
T	Return period	$years$
t	Time	s
T_0	Modal period	s
$\bar{T}_p$	Mean period of peaks for chosen motion	s
T_H	Minimum run time	$minutes$
U	Vessel speed	m/s
V, V_{rel}	CBT relative vertical velocity at slam instant	m/s
V_{max}	CBT maximum relative vertical velocity prior to slam event	m/s
v_x, v_y, v_z	Velocity of water particles	m/s
w_2	Distance between forward and aft CB transverse beams	m
x, y, z	Cartesian coordinates	m
X	Predictor variable	
x_0, y_0, z_0	Cartesian coordinates - fixed in space	m
x_{30}	Heave displacement	m
x_{50}	Pitch angle	rad
x_{50max}	Maximum pitch angle prior to slam event	rad
x_i	The i^{th} observation of X	
Y	Criterion variable	
y_i	The i^{th} observation of Y	
z	Field position (complex)	m

Chapter 1

Introduction

Large lightweight high-speed aluminium catamarans are a key part of fast passenger/vehicle sea transport. More recently the military realised their potential for fast vehicle and troop transport so that their capabilities are now being pushed to the limit in global military exercises. Australia has been a leader in the catamaran ferry industry, with International Catamarans (Incat) Tasmania developing the first high-speed wave-piercing catamarans in the late 1970s. These early designs were capable of carrying passengers only. In 1990 Incat developed a larger wave-piercing model capable of transporting vehicles as well as passengers. Since then, high-speed catamaran ferries have become progressively larger and faster due to operators' increasing demand on passenger and vehicle capacity at reduced transit times. This is particularly evident in the military since their vessels need to be robust as they will be expected to operate consistently in extreme weather conditions into which regular commercial ferry operators would not venture. The Royal Australian Navy and the United States military have used Incat wave-piercer catamarans in a variety of roles.

Apart from Incat Tasmania, notable high-speed catamaran ferry producers include the Australian ship building company Austal, who have recently constructed a 127m trimaran capable of reaching speeds of 40 knots. Swedish company, Stena Line, developed the High-speed Sea Service classes HSS 900 (now retired) and HSS 1500 in the mid 1990's. At just over 125m long with the capacity to carry more than 1500 people and 375 vehicles, the HSS 1500 class (of which there are three vessels) is currently the longest high speed catamaran ferry class in existence, see Figure 1.1. Following experimentation with Incat and Austal designed aluminium ferries, the Office of Naval Research (ONR) commissioned the construction of the X-craft: Sea Fighter (FSF-1), a high-speed aluminium catamaran capable of speeds up to 50 knots, for use as a technology demonstrator [28].

Austal and Stena Line catamaran ferries and the American X-craft are all traditional in appearance, that is, they consist of two slender demihulls joined by a flat wetdeck cross structure. Incat catamarans on the other hand are unique, as they contain a distinctive centre bow located between the demihulls. This centre bow, shown in Figure 1.2, is designed to prevent

Figure 1.1: HSS 1500: Stena Explorer showing the flat wetdeck between the demihulls.

Figure 1.2: Hull 066, showing the distinctive Incat centre bow. Note the deployed ride control T-foil, attached at the centre bow truncation.

deck diving in following sea and reduce motions at other heading angles. In large wave conditions catamarans can not only be prone to deck diving in following seas, but also experience wetdeck slamming in head and bow quartering seas. A slam event is defined as a sudden localised impulsive structural load applied to a body when it enters a fluid with a small relative angle between the body surface and the fluid surface. In the case of a catamaran this commonly occurs when the cross deck structure impacts the water. Slamming can cause the hull to vibrate at its natural frequency; this vibration is known as whipping, which is felt as a shudder throughout the ship [51].

Severe wetdeck slamming has been known to cause structural damage and the consequential whipping has a negative effect on the fatigue life of the vessel [63, 67]. HSS Stena Discovery and Incat Hull 50 are two examples of vessels which have experienced damage resulting from extreme slamming.

1.1 Problem Definition and Aims

A problem encountered by many ship designers and operators is how to select a vessel design for a particular sea route. Scale model testing and numerical simulations are useful tools for understanding the motion characteristics of hull forms in various sea conditions. However long term statistics, relating to wave loads and fatigue from prolonged cyclic loading, are not accounted for in these methods. Numerical seakeeping codes often neglect slamming in their formulations or they include post-processed or two-dimensional methods. The ability to predict slam occurrence rates and severity by a time-domain numerical simulation would make an extremely valuable structural design tool. By taking a statistical approach it would be possible to simulate the entire service life of the vessel. Long-term statistics of the vessel loading could then be investigated to gain insight into long-term wave loading, slam occurrence rates, slam loads and also the fatigue life of the vessel for a given environment (service route for example) and operating conditions. The goal of this project is therefore to develop a stochastic slam load prediction model using a non-linear time-domain seakeeping program and experimental data from scale model testing in irregular seas as a basis.

1.2 Scope of Work

This project is a continuation of a long standing research collaboration between Incat Tasmania and the University of Tasmania (UTAS). A high speed ship motion code based on a time-domain strip theory, BESTSEA[1], was developed by Holloway and Davis [34, 36] and extensively validated for regular waves by investigating the motions of a number of conventional and novel hull forms [15]. The project originally focused on passenger comfort and structural vibrations but soon expanded into wave load investigations, and BESTSEA was rechristened BEAMSEA

[1] **B**oundary **E**lement **S**trip Theory **T**ime Domain **SEA**keeping.

when the capability to predict wave loads was added. A natural progression of this university-industry collaboration is to further expand the current models to enable the prediction of ship motions and loads in irregular seas. The theory is further expanded in this work with the development and implementation of an empirical slam module.

The time-domain seakeeping method has been extended to simulate motions and loads in an irregular seaway. A method for creating standard sea spectra was developed as a pre-processing unit for the irregular version of the seakeeping code. This irregular version of the seakeeping code was then verified by conducting extensive program tests and validated by comparing computational results with results from scale model experiments in irregular seas in the absence of slamming.

Scale model experiments were used to collect a database of slam events based on the performance of an Incat hull form over a range of realistic (but idealised) irregular sea conditions. Analysis of this database identified important slamming characteristics that aid the development of a statistical slam prediction model.

The seakeeping code was then further extended to include the implementation of a slam module which identifies the occurrence of a slam event within the simulation and then calculates the slam severity, duration and location based on parameters identified from scale model testing. This tool will be valuable for predicting slamming rates, wave loads including slamming and investigating the fatigue life of the vessel.

1.3 Arrangement of Thesis

This thesis is arranged into eight chapters detailing the main aspects of the project. The second chapter provides an overview of ship motion and load prediction methods, as well as attempts to incorporate slam events into such simulations. Slam investigations using hydroelastic segmented scale models are also reviewed. Section 2.4 then outlines the reasoning and methodology behind the approach taken in this project.

Chapter 3 introduces the 2.5m segmented catamaran model and describes the experimental procedure followed (including the technical instrumentation and calibration systems used). Three sets of tests were conducted in the Australian Maritime College towing tank. Test Set 1 investigated the motions of the catamaran in relatively mild irregular sea conditions, whilst Test Set 2 set gathered slam data in large sea states for the investigation into the characteristics of slam events and development of the empirical slam module. Test Set 3 focused on measuring the irregular wave spectra produced in the towing tank.

The time-domain seakeeping methodology is formally introduced in Chapter 4 and the random wave extension of the theory is presented. Once integrated into the computer program, it is verified by investigating its behaviour under certain tests. The code is then validated by comparing the time-domain simulations with a set of scale model tests described in Chapter 3.

Chapter 5 focuses on an in-depth analysis of the characteristics and kinematics of slam

events. A database of more than 2,000 slams was gathered during the analysis of Test Set 2. These slams are grouped by different parameters and their distributions investigated. This analysis forms the basis of the statistical slamming model presented in Chapter 6.

An application of the extended time-domain motions and loads (including slamming) method is demonstrated in Chapter 7. An actual high-speed ferry service route across the Tsugaru Strait, located between Honshū, the main island of Japan, and Hokkaidō, the northern island, is selected as the setting for this small case study. Wave data, collected by the Japanese and supplied to Revolution Design, is used to define the operating environment for the catamaran. A series of simulations are then conducted and long term statistics commonly used in the prediction of extreme floods and earthquakes are applied here to predict 'n-year' slam events for the purposes of design loads.

The project is then summarised, with conclusions and recommendations for future developments in Chapter 8.

Chapter 2

Background and Proposed Methodology

2.1 Introduction

A long-term load prediction tool must successfully combine several elements: vessel motions, global wave loads and impulsive slam loads. This chapter provides a general review of state-of-the-art theoretical ship motion and global loads prediction methods, followed by a discussion on slam load prediction methods, ranging from two-dimensional wedge entry methods to smoothed particle hydrodynamics, concentrating on the integration of these models into seakeeping codes. Applications of three-dimensional physical slam modelling, particularly the use of hydroelastic segmented models, are then reviewed in Section 2.3.

Finally, from these reviews a research methodology is developed, integrating these aspects into a practical tool for the prediction of long-term loading statistics of a high-speed catamaran.

2.2 Motion Prediction Methods

For a successful design it is imperative to know its seakeeping performance in the early stages of the engineering design process. Therefore some form of modelling (be it physical, analytical, or both) must be performed to determine, with confidence, an estimate of the ship's motions and loads in a realistic seaway. In the case of evolutionary design, hull performance knowledge may be gained from past measurements of a similar design, with little additional modelling required. However, if the design is novel no such data may exist and extensive modelling is necessary.

The analytical prediction of ship motions and loads is a complex problem. Traditionally, ship design rules have required simplified analyses based on scientific approaches and past experience. With the increasing development in computer resources since the 1960s, the seakeeping performance of a proposed ship hullform can be predicted early in the design process by using a variety of analytical and numerical methods including finite element methods (FEM), strip

theories and two-dimensional or three-dimensional panel methods (boundary element methods (BEM)) [50].

Ship motion theories were originally developed in the late 1950s with Korvin-Kroukovsky and Jacobs [42] being an example of an early strip theory. A breakthrough strip theory was proposed by Salvesen, Tuck and Faltinsen [60] in 1970, building on the work by Korvin-Kroukovsky and Jacobs. The Salvesen, Tuck and Faltinsen theory is formulated in the frequency domain and is best suited for low Froude numbers.

Strip theories assume that the body is rigid, motions are small, ship-hull sections are wall-sided, planing effects are ignored and the body has no effect on the waves (Froude-Krylov hypothesis). These assumptions allow the body to be divided into a number of two-dimensional 'strips' and the full three-dimensional problem can then be solved as a series of two-dimensional problems [51]. By also neglecting viscosity and assuming irrotational flow, potential flow theory can be applied.

Determining the two-dimensional added mass and damping coefficients (A_{jk}, B_{jk}), and excitation forces and moments (F_j) for each ship section is the most difficult and computationally intensive part in ship motion theory [60]. There are several numerical methods that can be used to estimate these coefficients.

Conformal mapping is one such technique, which involves transforming the two-dimensional hull section into a two-dimensional unit circle oscillating in an undisturbed free surface. The circle is allowed three modes of motion: sway, heave and roll. The velocity potential of this system can be determined, and then the sectional added mass, damping and excitation can be found by integrating the pressures given by the Bernoulli equation [56].

Another common method is the panel, or boundary element methods (BEM). These methods, originally developed in the late 1950s have been traditionally applied in the aerodynamics field to determine flow around arbitrary shaped bodies [32]. The BEM involves distributing sources around the body and numerically calculating the potential of the system and thus the velocities, pressures and the required coefficients without the need for a mapping technique. The application of panel methods to hydrodynamic problems is complicated by the presence of an infinite free surface which is not usually present in aerodynamic scenarios [34]. The free surface problem, along with other panelling issues has delayed their successful development in seakeeping codes.

One solution to the infinite free surface problem is to treat it like any other boundary and distribute sources on it. The simple source method[1] involves panelling and distributing simple sources and dipoles over the mean (or instantaneous, depending on the method) wetted body surface of the vessel and mean (or instantaneous) free water surface. Higher order solutions can be sought from a simple source method if desired. Since the free surface requires panelling to define it, it obviously cannot extend to infinity, therefore the far field needs to be truncated at some point, and a boundary condition allowing outgoing generated waves enforced. Past

[1] Also known as the Rankine source method, or Dawson method, named after a pioneer in this field [17].

experience, or a trial and error approach, is generally used to determine the required free surface extension to ensure minimal interference from unideal boundary conditions in the far field. Other issues such as modelling the intersection of the free surface and wetted body surface are still present.

An alternative approach to the simple source method involves selecting a suitable Green function to model the free surface and far field conditions. The advantage of using a Green function is it automatically satisfies the free surface and far field boundary conditions without the need of panelling. Therefore only the wetted surface of the vessel requires panelling. This also has the added advantage of reducing the number of sources required for a solution. The main disadvantage of the Green function method is that the function is usually first order, which means the free surface is linearised. Another drawback is computation costs for a Green function solution may be more intensive than a simple source method. Whilst the Green function solution method requires fewer sources than the simple source method, Green functions often contain special mathematical functions (convolution integrals, Bessel functions and error functions) which must be solved in an iterative manner, adding computational time and potential instability to the solution [34].

Green functions can be evaluated in either the time or frequency domain. Traditional methods operated in the frequency domain as this is less computationally intensive, however current trends suggest time domain methods are becoming more popular [2]. Zero-speed time-domain solutions generally require more computational time as they need to be time marched to evaluate the convolution integrals [41]. However, at forward speeds time-domain methods become more efficient. Time-domain methods lend themselves to easy adaptation to more general cases such as non-constant forward speed and manoeuvring [41].

Some seakeeping methods adopt a hybrid approach by combining panel methods and Green functions; the far field is solved using a transient Green function, while the inner field is solved by distributing Rankine sources over the hull, near field free surface and the near/far field interface. This approach is valuable because Rankine sources are found to be more robust in the near field and on the ship hull for modern ships with non-wall sided hullforms, resulting in improved numerical stability [72].

Three-dimensional codes are becoming popular for calculating dynamic loads and responses of vessels in waves. Currently, fully three-dimensional methods offer little improvement over two-dimensional or $2\frac{1}{2}$D methods [79], however if nonlinear effects are thought to be prominent, a three-dimensional analysis should be considered. Strip theories are still used for engineering purposes since two-dimensional and $2\frac{1}{2}$D theories are found to be more robust and computationally economic than a complete three-dimensional potential flow analysis [2]. However further experimental work is still needed to fully validate both of these theoretical approaches [59].

Panel methods are still employed in three-dimensional applications [9, 50]. Currently, due to computational requirements, full computational fluid dynamics (CFD) solutions are not commonly available for global ship motion and loads simulations. Field equation solvers for

CFD, such as FLUENT have been applied in seakeeping applications, but only for local problems [2], such as determining slamming loads.

Strip theories generally perform well up to moderate Froude numbers, however at higher speeds (at Froude numbers greater than 0.5), the traditional methods begin to lack accuracy. This is due to simplified free surface conditions with forward speed; unsteady waves induced by the ship are made to propagate in directions perpendicular to the longitudinal axis of the ship. Also the effect of local steady flow around the ship is assumed insignificant. Faltinsen and Zhao [25] published a paper in 1991 outlining an extension to the traditional 1970 theory [60] for high-speed applications which can be described as a $2\frac{1}{2}$D method, since the three-dimensional free surface condition is maintained but the ship's hull is still treated as two-dimensional strips.

A high Froude number time-domain strip theory utilising the Green function method, developed by Holloway [36] especially for high-speed catamarans is used in this project as a basis of ship motion prediction. This method is formulated in the time domain with a fixed reference frame. Therefore the strips are fixed in space and perpendicular to the direction of vessel motion. The solution starts for each strip when the bow enters the strip, and finished when the stern leaves the strip. Since this method is closely related to the presented project, a more complete introduction of this method is found in Chapter 4.

Many different approaches to the ship motion prediction problem have been introduced thus far, however little has been included about their validity under different circumstances. Davis and Holloway [13] conducted a survey on a number of published comparisons of computed (by strip theories) and experimentally measured motion results (with scale models). Figure 2.1 shows the survey results for heave motion and similarly Figure 2.2 shows pitch results. Froude number is displayed on the x-axis and the y-axis contains the ratio between computed and experimental results for a particular wave frequency close to the peak motion response of the vessel. Data is grouped according to the applied motion prediction method: three-dimensional periodic Green function (for example Ye and Hsiung [78]) conventional strip theory (such as that developed by Salvesen et al. [60]), time periodic three-dimensional Rankine source (such as the methods developed by Kring et al. [43] and Nakos and Sclavounos [55]), high speed slender ship strip theory (see Faltinsen and Zhao [25]), and time domain methods (such as the method developed by Holloway [36] and described in detail in Section 4.2).

Both figures show considerable variation in the results from different methods. Note that this survey was conducted on published data, therefore some inaccuracies from interpreting the published figures are present although this is considered minor in comparison to the magnitude of the peak motions. Also neglected in this survey is the complexity of the hull shape being tested and other environmental factors potentially limiting (or enhancing) a given method's ability to accurately predict motions.

It can be seen from Figure 2.1 that computational methods generally over predict heave motions for all Froude numbers (resulting in a computational/experimental ratio greater than unity). This adds weight to significance of the neglected frictional effects common in potential

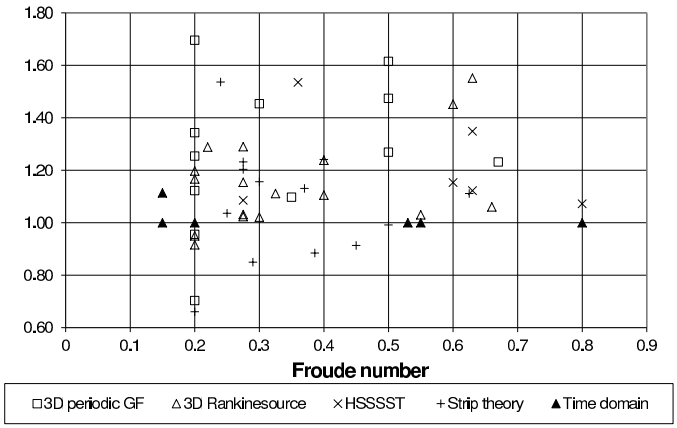

Figure 2.1: Ratio of computed/measured heave against Froude number. Data grouped by method. From Davis and Holloway [13].

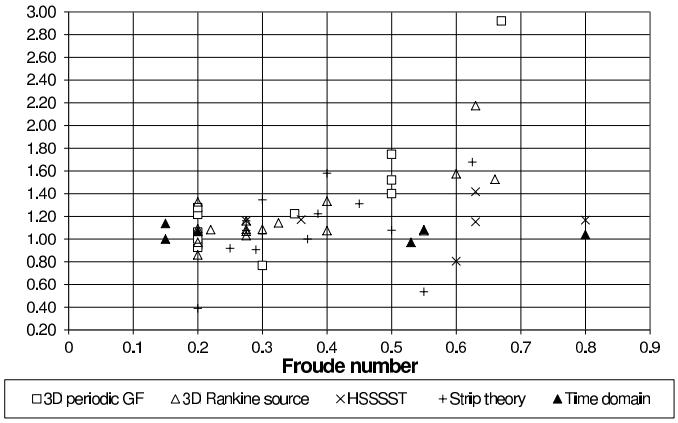

Figure 2.2: Ratio of computed/measured pitch against Froude number. Data grouped by method. From Davis and Holloway [13].

flow theories and it is also noted that other damping effects may contribute as the experiments have been conducted at model scale. In Figure 2.2, the computed/experimental ratio tends to increase with increasing Froude number. This has been partly attributed to high effective Froude number for sections near the bow and separated flow at the transom [13].

Time-domain (or $2\frac{1}{2}D$) methods are seen to give good results for high Froude numbers, and indeed at extreme Froude numbers there is little choice. Therefore in this project a time domain method was chosen as the tool for numerically predicting motions of the high-speed catamaran in irregular wave conditions, up to Froude numbers of 0.6.

2.2.1 Motion Prediction Including Slamming Considerations

Slamming is a very complicated process, which is often simplified by taking a similar approach to strip theory. The complex three-dimensional problem is simplified by using two-dimensional 'strips' and all assumptions associated with strip theory (i.e. the slender body assumption) apply. It is important to remember that two-dimensional methods are approximations and

three-dimensional flow effects are still present in reality [80].

Time-domain formulations have an advantage over frequency-domain methods in that they can account for slam loadings as solutions are time stepped, therefore the position and velocities of the vessel are known in time. The following discussion highlights several methods that have been developed to predict slamming pressures and loads (although not all of the methods shown here have been incorporated into time-domain seakeeping codes).

There are three common approaches to model slamming in seakeeping prediction methods: momentum theory, computational fluid dynamics and empirical methods.

The first approach is based on the pioneering wedge entry work by von Karman in 1929 [69] and Wagner in 1932 [70]. Von Karman developed a theory to predict the impact of seaplane floats when landing on water by performing a two dimensional momentum balance. When a seaplane float contacts the water, momentum from the float is transferred to an apparent mass of water. If a plate with length much greater than its width is accelerated in a fluid, the apparent increase in mass of the plate can be found to be equal to a cylinder of water with diameter equal to the width of the plate (see Figure 2.3). If the plate is wedge shaped (a typical shape for a seaplane float), the cylinder of apparent mass will consist of water and air. The effect of the apparent added mass of air can be neglected as the density of air is much less than that of water [69].

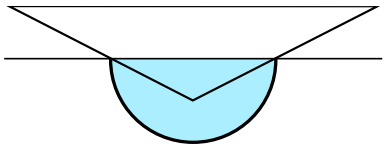

Figure 2.3: Vee shaped wedge and apparent mass (shaded) von Karman theory, adapted from Bisplinghoff and Doherty [7]

Wagner extended the von Karman wedge entry theory by taking into account the piled up water surface to determine the wetted breadth of a wedge penetrating water [3]. See Figure 2.4 for a diagram showing piled up water on a penetrating wedge; this effectively increases the width of the wetted plate. Blisplinghoff and Doherty [7] compared the theory of Wagner and von Karmon with those of Wagner-Sydow, Mayo, Kreps, and an expanding prism theory (which are all based on the Wagner and von Karmon methods) with two-dimensional drop test experiments. They found that the methods proposed by Mayo, Wagner-Sydow and the expanding prism theory compared the best with experimental results, although all theories showed acceptable trends. Brown, Wraith and Joubert [8] used a modified von Karman method for curved hulls to show local impact loads from slamming on yachts exceed design loads specified by the ABS.

Whelan et al. [76] further extended the theory of Wagner to model the acceleration of a symmetrical two-dimensional body entering calm water. This method was originally developed to model water entry of catamaran geometries containing a centre bow, however it is suitable for monohull applications as well. The theory consists of two phases; the initial phase considers

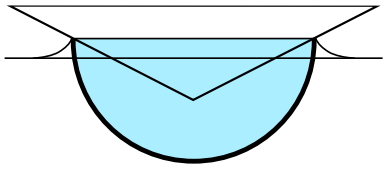

Figure 2.4: Wagner extension of the von Karman theory showing piled up water, adapted from Bisplinghoff and Doherty [7]

the general wedge entry problem of Wagner, while the second phase of the analysis accounts for arch closure events. During the initial centre bow entry, added mass is calculated using the regular Wagner method (taking piled up water into account), however once the arch closure event occurs, the effective added mass is changed to a large semi-circle of with diameter equal to the beam of the entire section, as shown in Figure 2.5. This method was able to reproduce trends identified with two-dimensional drop testing, however when extrapolated to full scale, the resulting slamming loads were found to be 2 to 3 times larger than full scale sea trials [16]. This is attributed to the limiting two-dimensional constraint; complete three-dimensional modelling is required to effectively account for the complex three-dimensional fluid interactions.

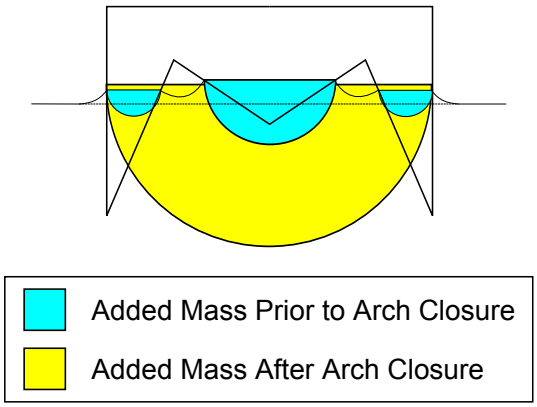

Figure 2.5: Modified Wagner method for catamaran sections with centre bows, adapted from Whelan et al. [76]

The slamming studies discussed thus far have assumed totally rigid two-dimensional bodies. Kvålsvold and Faltinsen [44] presented work on the hydroelastic modelling of slamming on catamaran wetdecks. The wetdeck is treated as a two-dimensional beam with supports at the transverse stiffeners. This method was compared with full-scale measurements of slamming on the Ulstein test vessel catamaran [23]. They found the theory best approximates hydroelastic impact theory when the dead rise angle of the wetdeck is low.

Zhao, Faltinsen and Aarsnes [80], developed a fully nonlinear boundary element method to determine pressure distributions and slamming loads on arbitrary two-dimensional shapes. Flow separation was considered and a three-dimensional correction is also applied. This approach was found to compare well with a Wagner-based method when flow separation does not occur, and it also compared well with experimental results when flow separation is present.

Computational fluid dynamics (CFD) is another approach that is becoming more popular with the ever increasing computational power of modern computers. In this method, the Navier-Stokes equations (or commonly the Reynolds-Averaged Navier-Stokes Equations (RANSE)) are solved in a finite element (2D) or finite volume (3D) domain to determine the pressure on wetdecks and bow forms of ships.

Arai et al. [3, 4, 5] modelled water entry problems using two-dimensional CFD. Results from Arai et al. [3] were compared to the classical momentum theory of Wagner. Arai's method takes into account gravity and spray effects, which were neglected in the earlier Wagner method, resulting in a lower pressure peak when compared with Wagner's method.

More recently, Hudson et al. [37] has applied CFD to wedge impacts when modelling high-speed rigid inflatable boats. Time histories of pressure distributions have been accurately predicted allowing for the calculation of forces on the wedge. These forces can then be applied to the equations of motion in a strip theory model, bypassing the need of potential flow to calculate pressures and forces common in conventional strip theory methods.

Nonlinear and three-dimensional effects such as two-phase flow of water and air may be better represented in a three-dimensional RANSE model. Currently, due to the computing time required to solve a 3D RANSE problem, it is not feasible to model ship motions in a fully 3D CFD domain. One solution to this problem is to model ship motions with a panel method, and slamming with a RANSE solver. This is the method used by El Moctar et al. [22]. They first used a linear frequency-domain Green function panel code to determine the appropriate design wave and COMET, a RANSE solver, to calculate ship motions and slamming loads.

Smoothed particle hydrodynamics (SPH) was applied by Veen and Gourlay [68] in catamaran slamming studies. With further development, SPH methods can potentially supersede of traditional mesh-based CFD methods for ship slamming problems. A complete three-dimensional SPH ship slam solution may involve millions of particles in order to sufficiently model the deformation of the fluid and require extensive memory and CPU time to be currently feasible [52].

Lin et al. [49] presented a seakeeping method capable of predicting motions and slamming loads. A hybrid panel/Green function method forms the basis of motions prediction while the semi-empirical wedge entry slamming model developed by Ge et al. [30] is incorporated into the motion prediction method, allowing slamming pressures to be added to the vessel.

Slam loading is often predicted numerically off-line and subsequently input into the seakeeping code. An example of this approach is the preliminary development of the slam module presented in Chapter 6 (see Section 6.1.1 for more detail). This is a common approach, but it is undesirable as slam loads are thought to have some, if modest, impact on subsequent vessel motions. Another example of a post-processed slam module is given by Weems et al. [72]. Two models are available in this module, a simple two-dimensional empirical model used for global impact forces and a two-dimensional nonlinear Wagner based method. The outputs from this module are the vertical and horizontal forces as well as local impact pressure on the hull

surface. Whipping calculations can then take place by using a non-uniform-section dynamic beam method. This is essentially a one dimensional finite element model where the ship girder is modelled as a beam of either a uniform or variable mass [72].

When determining local pressures, three-dimensional methods have been found to give more reliable results than the two-dimensional strip theory methods, however due to complexities of complete three-dimensional analyses, two-dimensional methods are commonly used for design purposes. Lindemark et al. [50] presented a paper describing the reasoning behind DNV's (Det Norske Veritas) design procedures, with the focus on fatigue analysis in gas carriers. DNV prefers the use of a three-dimensional panel method for ship motion predictions, with a pre-processor two-dimensional finite element program to calculate slamming pressures, results of which are input into the panel code.

This panel method was used to determine wave loads during the design of a 112m Incat wave-piercing catamaran [11]. First the seakeeping code was run in linear mode to determine the design waves, then in nonlinear mode with slamming incorporated. It was found that maximum bending moments were much lower than expected when compared with DNV rule guidance, suggesting problems with scaling two-dimensional slam predictions to three-dimensional models [11], similar to the problems identified by Davis et al. [16] after their two-dimensional drop tests . Two-dimensional numerical methods were found to satisfactorily model two-dimensional drop tests, however neither two-dimensional methods could be extended to three dimensions accurately. Therefore a three-dimensional slam investigation is required for the current investigation.

2.3 Hydroelastic Segmented Model Testing

An alternative method to numerical techniques for predicting the motions and loads experienced by high-speed crafts is to use physical model experiments. These can be in the form of the two-dimensional drop tests outlined above, or in scale model seakeeping experiments. A typical application of scale model testing (with rigid models) is the validation of seakeeping codes (an application of this can be found in Chapter 4). The discussion here concentrates on modelling wave loads, particularly slamming, and the subsequent structural response at model scale.

In order to accurately simulate the full scale slamming and whipping response, the model needs to be hydroelastic, allowing simultaneous interaction between the fluid flow and the structural response [6]. There are two main approaches when designing a hydroelastic model: the model may be continuous [71], or segmented [57]. Segmented models may contain a continuous rigid girder with the segments attached to the girder via load cells or other force/moment transducers. Dessi et al. [18] used a six segment model with a continuous backbone beam of varying cross-section. The beam was shaped to give the desired vertical bending behaviour. The segments were attached to the backbone beam with load cells measuring the vertical force, strain gauges mounted on the backbone beam measured bending moments. Another approach

is to use a segmented rigid backbone beam, joined together by elastic links at the hull segments [31]. In the case of wetdeck slamming on catamarans, the wetdeck may be segmented in the same manner as a monohull [29].

Using a segmented model to analyse a ship's structural response is challenging as it introduces further complexity to the experimentation. Ideally, the motions and loads of the model should match the hydroelastic behaviour of the full scale vessel, however experimental and technological limitations often prevent such a perfect correlation [20]. The number of segments required is defined by what mode of response is desired. For global bending moments, one cut (two segments) will suffice, however, as Okland et al. [57] identified, the location of the cut and mass distribution is critical to obtain a realistic response. Therefore finite element (FE) analysis is usually performed to locate the position of the cut. A model with three or four segments may be required to model wet-deck slamming as high modes may have a considerable influence on the resulting vessel response.

A 2.5m hydroelastic segmented catamaran model (full details of which can be found in Section 3.4) was used by Davis et al. [14] to measure bending moments and centre bow slam loads during towing tank tests in regular waves. The model was also used to investigate slams in irregular seas [64, 65]. Slams were found to be varied in severity, with the largest slam load equivalent to 70% of the full scale vessel displacement, however the majority of identified slams were of much lower severity. These irregular sea investigations were useful for identifying key slamming characteristics for different conditions.

2.4 Research Methodology

The primary aim of this project is to develop an integrated method for predicting ship motions and loads including slams in irregular seas for high-speed catamarans. By taking account of the numerical motions and loads prediction issues discussed in Section 2.2 and slam modelling techniques in Section 2.2.1, several key aspects present themselves:

1. A motions prediction method, valid for high Froude numbers, is required.

2. Numerical slam modelling is most suited for the time domain.

3. Limitation of two-dimensional slam models.

4. On-line slam mechanism is advantageous over off-line models.

The time-domain strip theory developed by Holloway [34] and optimised for high-speed multi-hull vessels is an ideal platform for motion and global loads prediction, however the method requires extension (and thus validation) in order to model ship motions in irregular seas. Validation of computational seakeeping methods typically rely on scale model tests, and the extended time-domain irregular sea method is no exception. Scale model tests are used to

validate the motions prediction tool by gathering ship motion data in irregular sea conditions mild enough not to induce slamming.

Currently, only two-dimensional analytical slamming methods have been integrated on-line into motions and loads prediction methods, with varied success. Two-dimensional slam load investigations were previously conducted by this project team, in the form of drop testing and an analytical Wagner-based wedge entry method modified for catamaran geometries [75], with the conclusion that the two-dimensional constraint severely restricts the ability to accurately predict slamming loads. Therefore for this work a three-dimensional approach was desired.

Scale model experimentation has been undertaken with the use of a hydroelastic segmented model of a typical Incat hull form, designed especially for the purpose of measuring global and slamming loads and the whipping response. Motions and loads of this model have been thoroughly investigated in regular waves [12, 45, 53], however as yet, research into slam loads in irregular seas is still in its infancy. Two sets of irregular sea tests have been conducted previously with the goal of characterising slam events (and the results published, [64, 65]), but both of these test sets had relatively narrow experimental scopes. The experimental test matrix, developed in Chapter 3, is substantially more ambitious than previous irregular sea investigations.

Scale model tests were chosen as the best means through which to investigate high-speed catamaran slamming and form the basis of a stochastic slam model. Scale model testing in a towing tank has an advantage over two-dimensional methods, such as drop testing since it overcomes the two-dimensional limitation by being three-dimensional, scale effects being the greatest restraint (scaling issues are inherent for all scale model experimentation, drop tests included). Because of the statistical foundation of the empirical slam module, a large number of experimentally measured slams are required to gain a reasonable representation the slam population.

Therefore a complete test matrix representative of realistic operating conditions for the full scale vessel is developed and motions, loads and wave data is collected for these conditions. The load data, in particular centre bow slam events, pressure and wave elevation measurements form the basis of the slam module. Distributions of the gathered data is then closely examined and interpreted as this is the first real opportunity to investigate extreme slam events. Key slamming parameters are identified and a statistical regression analysis on these parameters forms the basis of the empirical slam module. This module is then integrated in the time-domain strip theory, resulting in a hybrid deterministic/stochastic ship motions and loads prediction tool.

Figure 2.6 shows a flow chart outlining this project's research methodology. The foundation of this work is scale model experiments. The blue coloured rounded rectangles represent scale model experimentation or results from such analyses (scale model experimentation is presented in Chapter 3, motions in Chapter 4 and slams in Chapter 5). The red rounded rectangles represent the deterministic elements of the seakeeping model (Chapter 4) while the yellow

shows the development of the stochastic slam module (Chapter 6).

The integrated motions and slam prediction method is able to identify slams in the simulation, and the slam loads, durations and location are applied to the vessel on-line in the time domain.

From this simulation, and taking a statistical approach, it will be possible to investigate long term loading statistics of a vessel over her entire service life. This will be done by considering the expected operating conditions and completing a series of simulations representing the proportion of time spent under those conditions.

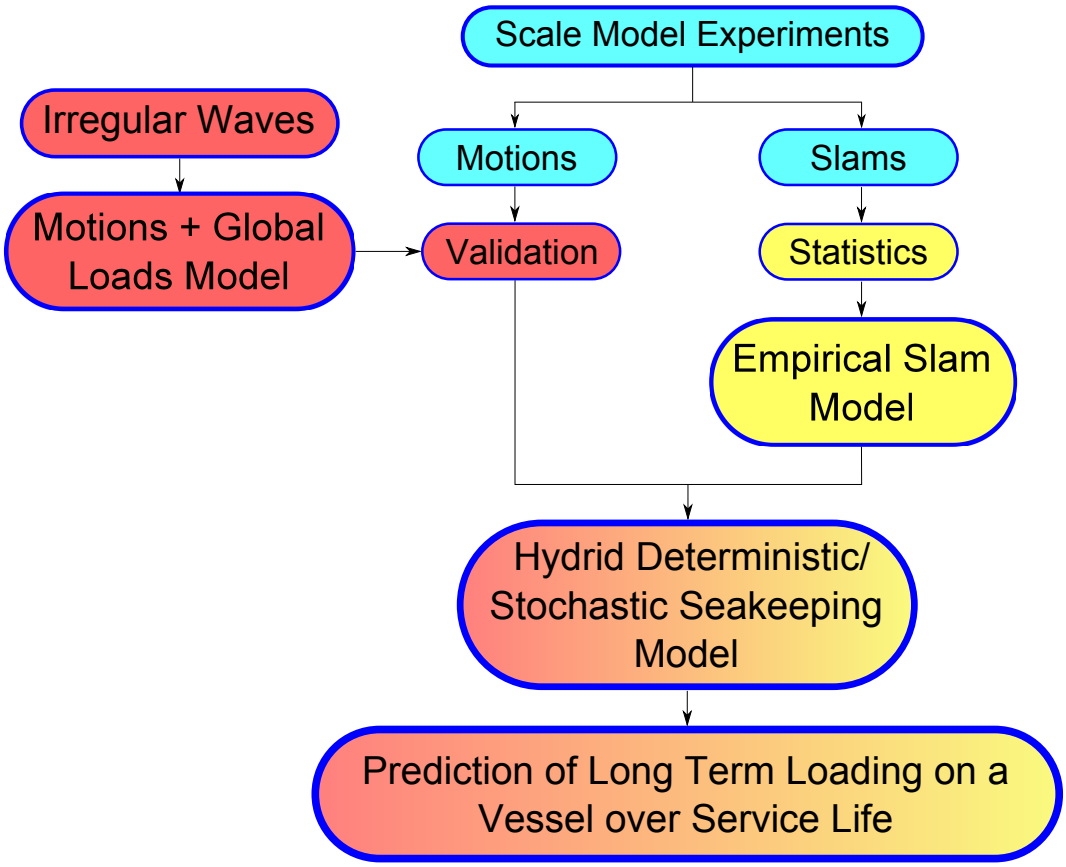

Figure 2.6: Research methodology highlighting important phases of this project.

Chapter 3

Experimentation

3.1 Introduction

The discussion in Chapter 2 emphasised not only the value of scale model experiments in the validation of numerical seakeeping codes but also the testing of hydroelastic segmented models (HSM) in global and local load investigations. The approach developed in Section 2.4 relies on extensive testing of hydroelastic models to compile a database of slam events and their characteristics as a basis for an empirical slam module.

This chapter introduces the facilities at the Australian Maritime College (AMC) and the test objectives as well as the testing procedure followed. Results of the experiments form the basis of the slam module presented in Chapter 6. Kinematic analysis of the measured slams is presented in Chapter 5 and motions and wave spectra measurements are presented in Chapter 4 when validating the time domain seakeeping code.

Figure 3.1: Towing Tank, Australian Maritime College, Launceston, Tasmania. Part of the carriage structure can be seen in the foreground.

Scale model testing of a 2.5m hydroelastic catamaran was undertaken during April and May 2010 at the AMC towing tank facility with the objective of measuring global ship motions and slam loads on the centre bow. Strains at the demihull segment links and centre bow surface pressure records during slamming were also recorded. The wave spectra produced by the towing tank wave maker was measured in a separate investigation during late May 2010. These wave spectra measurements were valuable for comparing the simulated spectra in the time domain code with those produced by the wave maker in the towing tank, to ensure the vessel motions are the result of similar wave environments. This data was also used to investigate the produced wave spectra as it develops at different locations along the tank.

3.2 Facility

The Australian Maritime College towing tank is 100m long and 3.55m wide with a maximum water depth of 1.5m. For these tests, since large motions were expected the water depth was reduced to 1.4m to avoid the model striking the underside of the carriage. A wet dock is located at the northern end of the tank; this section has Perspex sides which aids the observation of the trim and heel of the model. A large beach is located at the wet dock end of the tank in an attempt to reduce reflections from the wave maker. Retractable beaches are also located along the eastern side of the tank. These beaches can be lowered between runs via a remote control and pneumatic system to help reduce the water settling time and are retracted again prior to conducting each run.

A wave making machine is installed at the southern end of the tank. The wave maker consists of a single paddle, hinged at the bottom of the tank. It is driven hydraulically and can be remotely controlled from the carriage. The software controlling the wave maker was developed by HR Wallingford for the AMC; it is capable of producing regular waves of a given frequency and amplitude, standard idealised irregular wave spectra such as the JONSWAP or Bretschneider spectra, or non-standard wave forms. The wave maker is capable of producing only one wave train representative of a given condition, however it is possible to start the machine at a different point through its predefined script. Therefore the wave maker was set to commence making irregular waves at a different starting point for each run in the towing tank to be sure that the model encountered a different wave environment in each test.

A towing carriage is mounted on rails above the tank and is free to traverse the entire length of the tank. The velocity of the carriage can be varied up to a maximum of 4.6m/s. The carriage carries its own on-board DAQ and signal conditioning systems with the capacity to record up to 16 channels. The model is attached to the carriage by two tow posts which are free to move vertically. The tow posts are fixed to the model via ball joints with the aft post also mounted on a slide, allowing the model to pitch and roll freely. Both tow posts have linear voltage displacement transducers (LVDT) mounted on them. The LVDTs measure the vertical displacement of each post, allowing the heave and pitch motions of the model to be determined.

3.3 Test Objectives

These tests were planned to gather data for two primary objectives: the validation of the irregular version of the time-domain seakeeping method, and the compilation of a slam event database for an in-depth investigation into slam characteristics and kinematics for the basis of the empirical slam module. These objectives are briefly introduced below. Other secondary objectives were also identified, including: the determination of vertical bending moments in the demihulls for different conditions, ascertaining surface pressure records during centre bow slamming and measuring the generated wave spectra.

3.3.1 Validation of the Irregular Version of the Time-Domain Seakeeping Code - Test Set 1

In order to validate the time-domain seakeeping code, seakeeping measurements were conducted using a 2.5m hydroelastic segmented catamaran model. Standard JONSWAP (Joint North Sea Wave Project) sea spectra were selected to model conditions representative of operating environments for the 112m Incat ferry. The JONSWAP spectrum has a limited fetch, where the spectrum is never fully developed [51]. This makes it useful for modelling partly sheltered, limited fetch coastal conditions, such as the sea routes in Japan and the English Channel where the 112m Incat vessels have been deployed. Relatively small significant wave heights were also chosen in this investigation to ensure the absence of slamming as the investigation of ship motions was the primary goal of this objective. Tests were conducted at two vessel speeds: 20kts and 38kts; these are standard operating speeds for the 112m class vessel. The tests to achieve these goals are referred to as Test Set 1.

3.3.2 Characterisation of Slam Events - Test Set 2

The second primary objective was an investigation into the slamming of the 112m Incat hull form in irregular waves. These tests, referred to as Test Set 2, involved the collection of ship motions, slam loads, locations and wave profile data at different locations to aid the development of an empirical slam module. Once again, JONSWAP spectra were chosen to represent typical sea conditions encountered by this design. From previous investigations into slamming of the catamaran model it was found that the modal period of the encountered wave spectrum had a large influence on the slam occurrence rates of a vessel. Significant wave height is also influential; however it is proposed that the occurrence rates and magnitude of slam loads are more sensitive to the period of the encountered waves, particularly if the modal period of the encountered wave spectrum is in the vicinity of the resonant peak of the vessel's response.

Previous investigations into the motions and loads of the 2.5m hydroelastic segmented model have focused on two operating speeds: 20kts and 38kts full scale. The forward speed of the vessel has been found to be an important parameter in the magnitude and location of slam loading

during a slam event. Earlier work conducted by the investigation team [10, 77] suggested that as the forward speed of the vessel increased, the slam location tended to move further aft on the vessel. When trying to incorporate forward speed into an empirical slam model one can only assume a linear relationship exists between the vessel's forward speed and slam load or location if model testing is conducted at only two speeds. Therefore, a third vessel speed was investigated. This was chosen as 28kts since Incat is proposing this speed as an additional operating speed on medium-speed vessels.

Wave spectra measurements (known as Test Set 3) were conducted during May 2010 to investigate the accuracy with which the towing tank wave maker can reproduce given ideal sea spectra. All wave conditions were repeated in the absence of the model, and wave elevations were measured at various static locations along the towing tank. These measurements are used to support the Test Set 1 and 2 objectives.

3.4 Model Details

The vessel used in these experiments was a hydroelastic segmented model (HSM) of Incat Hull 064. Figure 3.2 is a photo of the model in the AMC towing tank and Figure 3.3 shows the 112m full scale ship. Before the UTAS team designed the catamaran, an existing monohull model was modified by cutting it in half and re-joining it with an aluminium elastic hinge such that the effects of stiffness and mass distribution on the frequency response of the model could be investigated. The NPL 6A hullform was selected because it resembles a catamaran demihull [45, 46]. Experience gained from the preliminary segmented monohull experiments, as well as acknowledging the work of others in slamming investigations using segmented models, such as the 4.1m catamaran model developed at Norwegian Marine Technology Research Institute (MARINTEK) [29, 57] and the segmented fast ferry monohull used by Dessi et al. [19, 20], aided in the design and construction of the hydroelastic segmented model. The HSM was designed to have similar frequency response characteristics as the full scale vessel. However since the full scale vessel was not built at the model design stage, the target resonant frequency of the model was based on FEA results of Incat Hull 064 [45].

The demihulls consist of three segments, thus allowing the measurement of bending moments at two locations. The ability to determine vertical bending moments is critical for ship design [38]. The centre bow was also isolated from the rest of the vessel to allow the measurement of slam loads (Figure 3.4 shows a schematic of the model layout). Two different centre bow segments were also constructed: a standard one and one containing 84 pressure tappings over the starboard arch extending from frame 55 to frame 82 with reference to the full scale vessel. Since the bow containing the pressure tappings is substantially heavier than the normal bow, the centre bows can be interchanged when pressure measurements are not desired.

The model was constructed using carbon fibre and Divinycell foam sandwich to obtain light-weight yet high hull segment stiffness. The demihull segments are joined by aluminium elastic

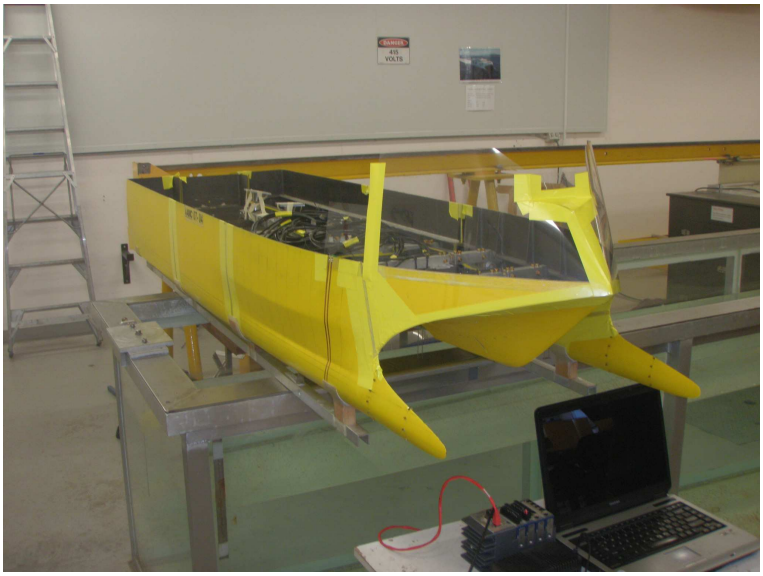

Figure 3.2: 2.5m hydroelastic segmented model representing Incat Hull 064. The cRIO DAQ unit can be seen at the bottom of the photo, next to the laptop.

Figure 3.3: Incat Hull 064, *Natchan Rera* as she passes under the Tasman Bridge, Hobart, Tasmania, during sea trials

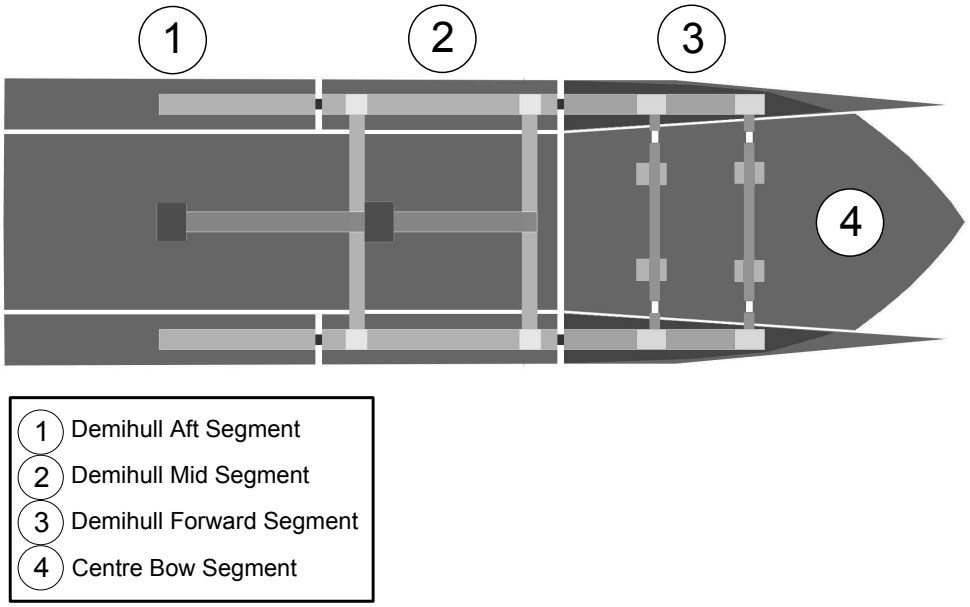

Figure 3.4: Diagram of the 2.5m segmented catamaran model (model number 07-04).

links, and aluminium square hollow section backbone beams are fitted into both demihulls to provide mounting points for the aluminium links. The links were designed to slide inside the backbone beam and are held in place by aluminium bolts. The centre bow was located by two square hollow section aluminium beams connected transversely to the forward most demihull backbone beam segment via pin joints. These beams were cut in two places and re-joined with aluminium links in a similar manner to the demihulls so that loads on the centre bow segment could be determined.

Three sets of links of differing stiffnesses were constructed for the demihulls: 9,903 Nm/rad, 12,378 Nm/rad and 14,854 Nm/rad. It was found that the 12,378 Nm/rad links modelled the frequency response of the full scale vessel most accurately when the model is in water loaded to 27.43kg displacement (2,500t full scale) [47]. These links were used in most previous tests, when the pressure bow was not installed. Rigid links were installed for pressure mapping tests conducted by Amin [1] to reduce the influence of the flexibility of the model on pressure measurements.

During the experiments presented here, the heavier pressure bow was installed and in order to maintain a realistic and achievable radius of gyration in pitch, the overall displacement of the model was raised to 30kg. This represents a full scale displacement of 2,764t which is a realistic overload condition. The pitch radius of gyration was estimated by using the bifilar method, similar to the method described in Lloyd [51], and adjusted by shifting the ballast until the desired radius of gyration was obtained.

The stiffer 14,854 Nm/rad links were also fitted in the demihulls to increase the natural frequency of the model. This was done in an attempt to emulate the natural frequencies of

later 112m class vessels which had an extra vehicle deck installed. At the time of testing, the natural frequency of the later 112m class vessel was not known.

Table 3.1 summarises the scale model's particulars compared with the full scale equivalents where possible.

Table 3.1: Main particulars of the 2.5m HSM. Full scale equivalents are shown where possible.

Model number	07-04
Model scale	1:44.8
Configuration	Pressure bow Transverse centre bow segment beam
Displacement	30kg/2764 tonnes
Trim	Level
Radius of gyration in pitch	640mm (25.6%L)
Trim tab angle	7 degrees
Centre bow truncation from transom	1902mm/85.2m
Fwd tow post from transom	956mm
Aft two post from transom	527mm
LCG from transom	954mm/42.7m
Fwd tow post from LCG	2mm
Aft tow post from LCG	427mm
Centre bow truncation to LCG	948mm/42.5m
Fwd tow post to CBT	946mm
Max arch height from undisturbed CWL	76.4mm/3.4m

3.4.1 Scaling Effects

The model was scaled according to Froude's law. Similarity in the Froude number between full and model scale, as opposed to Reynolds number, was chosen because Froude's law ensures that the correct relationship between inertial and gravitational forces are maintained [24]. Reynolds scaling fixes the relationship between inertial and viscous forces. It is virtually impossible to achieve both Reynolds and Froude scaling in towing tank model tests, and the Froude number is more appropriate since ship slamming is dominated by gravitational and inertial forces.

Differences in the Reynolds number between model and full scale are not significant since the flow in the area of interest (the archway) is naturally turbulent. Even if the flow was not turbulent in this region, turbulence stimulators were installed on the demihulls and centre bow to ensure that it is.

It is proposed that model scale slam characteristics can be scaled to full scale satisfactorily. In a previous experiment with the same model, the distribution of model scale slamming characteristics in irregular seas, analysed by Thomas et al. [65], were compared to full scale measurements on a similar catamaran [67]. They found that the varying slam load magnitude was similar to the full scale slam measurements.

3.5 Instrumentation

3.5.1 Data Acquisition

Due to the number of channels required during these tests, two DAQ systems were used; the carriage-borne system and the compact RIO system. The carriage DAQ system can acquire data on 16 channels, which is saved on a PC running a LabView program located on board the carriage. For these tests the carriage-mounted DAQ system was used to acquire carriage speed, ship motions, wave profiles and pressure readings.

The National Instruments (NI) cRIO (Compact Reconfigurable Input Output) data acquisition system was used primarily to record strains via strain gauges fixed on the aluminium links on the model. The controller is the NI cRIO-9004 model; it contains a 200MHz Pentium processor and a Field Programmable Gate Array (FPGA) programmed by the NI LabView software. The chassis (cRIO-9101) has four slots in which four modules are inserted. Two 4-Channel, 16-bit, $\pm$10V Analog Input Modules (NI-9215) and two 4-Channel, 24-Bit Simultaneous Bridge Modules (NI-9237) are available. The simultaneous bridge modules (Channels 8-15 in Tables 3.2 and 3.3) are used exclusively to record strains. The other channels are general purpose.

A simple push button trigger device supplying a DC signal from a 9V battery was recorded on both DAQ systems. The DAQs were then easily synchronised (even though they acquired data at different sample frequencies) by matching this signal in the initial phases of analysis. The LVDTs were recorded on both systems as a contingency in case the trigger failed; however the trigger system was found to be the most convenient synchronisation method. During past experimentation, synchronisation using the time varying oscillating LVDT signals proved to be difficult because both DAQ systems contained their own noise and sampled at different frequencies. Synchronisation was made much easier by the sudden sharp change in signal that the trigger provides.

Tables 3.2, 3.3 and 3.4 contain the allocation of channels on both the carriage and cRIO DAQ systems during the April/May 2010 testing period. Descriptions of the various instrumentation follows.

Two digital video cameras and one still frame camera were also used during testing. One video camera and the still frame camera were set up so that the bow was in frame and the second camera captured the starboard side of the model.

3.5.2 Pressure Transducers

Pressure transducers were used to record surface pressures at different locations along the starboard arch of the model. The pressures were measured by piezoresistive transducers manufactured by Endevco (model 8510C-50). This transducer model has a high resonance frequency of 320Hz, making them suitable for dynamic applications. The project team conducted two dimensional drop tests of Incat-style wave piercing centre bows and the maximum measured

Table 3.2: Data acquisition - Test Set 1 (motions objective).

DAQ System	Channel	Description
CARRIAGE	0	Carriage speed
	1	Forward LVDT
	2	Aft LVDT
	3	Capacitance moving wave probe in plane with **LCG** (WP1)
	4	Acoustic moving wave probe in plane with **LCG** (WP6)
	5	Pressure sensor 2 (ID11232)
	6	Pressure sensor 3 (ID11302)
	7	Pressure sensor 4 (ID11258)
	8	Pressure sensor 5 (ID11257)
	9	Pressure sensor 6 (ID11253)
	10	Pressure sensor 7 (ID11222)
	11	Pressure sensor 8 (ID11304)
	12	Pressure sensor 9 (ID11300)
	13-15	N/A
cRIO	0	N/A
	1	Forward LVDT
	2	Aft LVDT
	3	Capacitance moving wave probe in plane with **LCG**
	4	Boat mounted wave probe (WP2) (furthest forward)
	5	Boat mounted wave probe (WP3) (in plane with **CBT**)
	6	Boat mounted wave probe (WP4) (aft of **CBT**)
	7	Boat mounted wave probe (WP5) (behind **CBT**)
	8	Strain gauge - Demihull port fwd
	9	Strain gauge - Demihull port aft
	10	Strain gauge - Demihull starboard fwd
	11	Strain gauge - Demihull starboard aft
	12	Strain gauge - Centre bow port fwd
	13	Strain gauge - Centre bow port aft
	14	Strain gauge - Centre bow starboard fwd
	15	Strain gauge - Centre bow starboard aft

Table 3.3: Data acquisition - Test Set 2 (slamming objective).

DAQ System	Channel	Description
CARRIAGE	0	Speed
	1	Forward LVDT
	2	Aft LVDT
	3	Capacitance moving wave probe in plane with **CBT** (WP1)
	4	Acoustic moving wave probe in plane with **CBT** (WP6)
	5	Trigger (for synchronisation)
	6	Pressure sensor 1 (ID11255)
	7	Pressure sensor 2 (ID11232)
	8	Pressure sensor 3 (ID11302)
	9	Pressure sensor 4 (ID11258)
	10	Pressure sensor 5 (ID11257)
	11	Pressure sensor 6 (ID11253)
	12	Boat mounted wave probe (WP2) (furthest forward)
	13	Boat mounted wave probe (WP3) (in plane with **CBT**)
	14	Boat mounted wave probe (WP4) (aft of **CBT**)
	15	Boat mounted wave probe (WP5) (behind **CBT**)
cRIO	0	N/A
	1	Forward LVDT
	2	Aft LVDT
	3	Trigger (for synchronisation)
	4-7	N/A
	8	Strain gauge - Demihull port fwd
	9	Strain gauge - Demihull port aft
	10	Strain gauge - Demihull starboard fwd
	11	Strain gauge - Demihull starboard aft
	12	Strain gauge - Centre bow port fwd
	13	Strain gauge - Centre bow port aft
	14	Strain gauge - Centre bow starboard fwd
	15	Strain gauge - Centre bow starboard aft

Table 3.4: Data acquisition - Test Set 3 (wave spectra measurements).

DAQ System	Channel	Description
CARRIAGE	0	Speed (not used)
	1	Wave probe 40m from beach
	2	Wave probe 65m from beach
	3	Wave probe (foil) 65m from beach
	4	Wave probe 91.5m from beach
	5	Wave probe 15m from beach
	6-15	N/A

pressures were found to be in the range of 170kPa [75]. When these loads are scaled to full scale they exceeded the largest measured slams by a factor of approximately three [16]. Therefore it is expected that three dimensional effects present in scale model seakeeping tests would reduce the maximum measured slam pressures to that of less than that of the dimensional drop tests. The Endevco model 8510C-50 maximum output is 50psi (344.75kPa).

For Test Set 1 (the motions objective) nine pressure transducers were used since minimal slamming was expected in these relatively mild conditions. One pressure sensor was sacrificed (pressure sensor 1, see Table 3.2) to allow for an acoustic wave probe, leaving eight transducers on the carriage DAQ. For Test Set 2 (slamming objective), the boat mounted wave probes were also moved onto the carriage DAQ system, leaving six pressure transducers on the carriage DAQ system (see Table 3.3). The locations of the pressure sensors can be seen in Figure 3.5.

3.5.3 Wave Probes

Six wave probes were used during testing: five capacitance types (one mounted on a foil) and one acoustic probe. The capacitance wave probes consist of two steel probes that are partway inserted into the water. The potential difference across the probes varies linearly with the amount of submersion of the probes. Previous observations on these probes has shown that they tend to disturb the wave surface, producing 'up run' on the wave probe, resulting in an offset of the wave profile measurement. This is particularly evident when they are used at speed [77]. The acoustic wave probe model (UltraLab ULS-40D) was installed in-line with the moving foil-mounted capacitance wave probe in an attempt to compare and correct for the wave probe run up.

For the motions objective, the foil-mounted capacitance wave probe and an acoustic probe (WP1 and WP6 in Table 3.2) were fixed to the carriage floor in plane with the model's longitudinal centre of gravity. These measurements were used in RAO calculations along with vessel motions measured by the LVDTs. When slamming investigations commenced, WP1 and WP6 were moved from the LCG to in plane with the centre bow truncation, as wave profiles at the CBT were of more interest for the slamming investigations. These measurements can be

Test Set 1. Conditions 81-84.

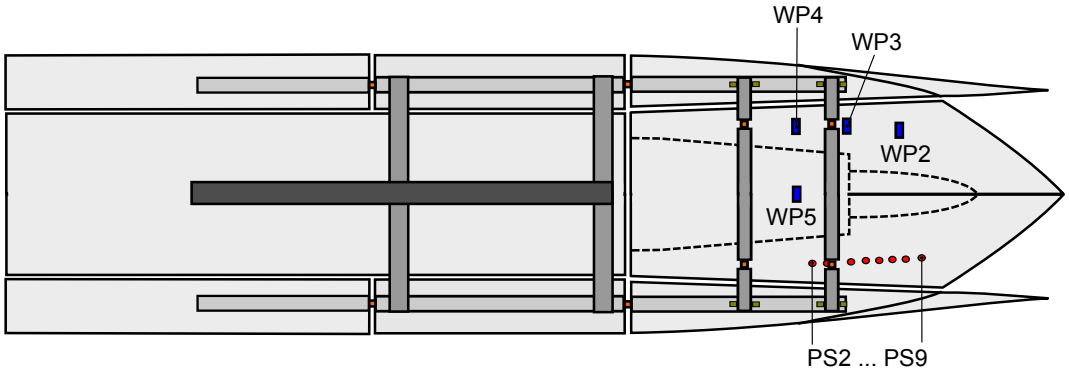

Test Set 2. Conditions 85-101.

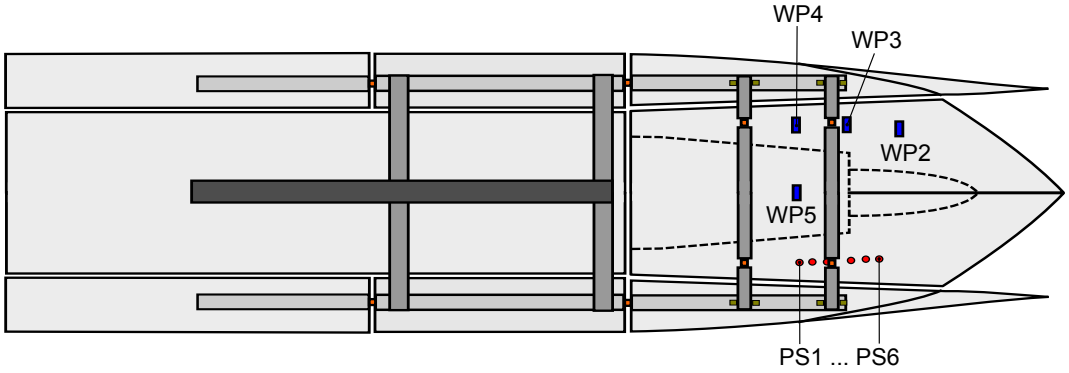

Test Set 2. Conditions 102-111.

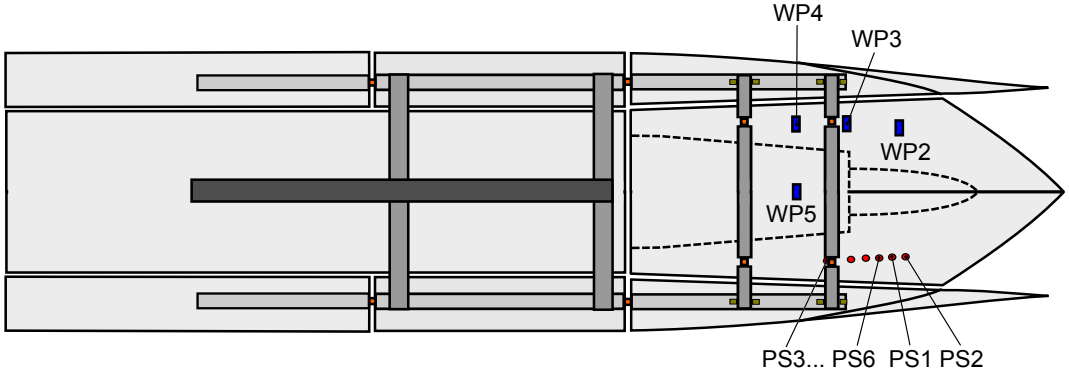

Figure 3.5: Diagrams showing the locations of the pressure transducers (PS1-PS6) and boat mounted wave probes (WP2-WP5) during experimentation.

compared with those from WP3 which was mounted in plane with the CBT but inside the arch tunnel.

The four other probes are shortened versions of capacitance probes and were installed on the bow segment of the model. The probes protruded 140mm from the surface of the wetdeck, perpendicular to the calm water line, see Figure 3.6. These probes were used to gather wave profile information for use in the empirical slam module. Three probes were mounted on the port side of the centre bow longitudinally along the maximum arch height, WP3 in plane with the centre bow truncation, WP2 was 120mm forward of WP3 and WP4 120mm aft of WP3. The fifth wave probe (WP5) was mounted in the centerline of the model, aft of the centre bow truncation in plane with the port wave probe furthest aft (WP4).

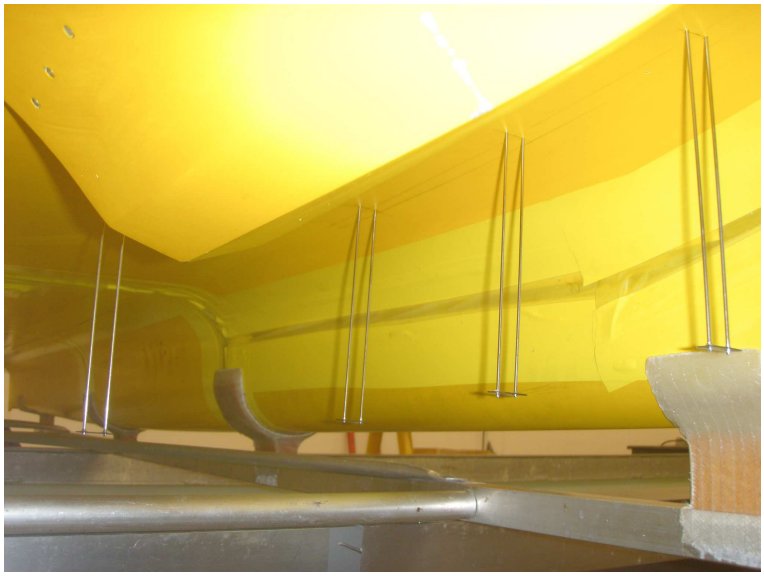

Figure 3.6: Underside of the model showing the four boat mounted wave probes (from left to right WP5, WP4, WP3 and WP2). Three pressure tappings can be seen on the centre bow in the top left corner. Also visible in this photo are the centre bow truncation and sealing of the segment gaps with latex and yellow tape.

It was soon found that calibrating the boat mounted wave probes on the cRIO was not as reliable as the carriage DAQ system since the carriage system contained pre-implemented calibration software, whereas the cRIO did not. Also the carriage DAQ system was found to be more reliable than the cRIO; data storage issues were apparent when the sample rate for the cRIO was set too high for extended runs of 30-40s. The decision was therefore made to move the wave probes to the carriage system as they were more valuable with regards to the development of the slamming module than pressure readings.

3.5.4 LVDTs

The vertical motion of the model was measured at each of the two tow posts using linear voltage displacement transducers (LVDT). This provided data to calculate model heave and pitch motions as well as vertical acceleration.

3.6 Test Procedure

The development of a statistical model describing the behaviour of a particular vessel requires a large amount of experimental data to build a sufficient distribution of typical slam events. Not only is a 'statistically sufficient' amount of experimental data required, but it is required over a range of conditions to gain a complete picture of the vessel's behaviour. For the time allocated for access to the towing tank facility, a compromise between the number of conditions and the number of runs in each condition needed to be made. Lloyd recommends at least 100 pairs of peaks and troughs should be encountered to obtain reasonable estimates of rms motions [51]. Therefore the minimum run time, T_H, is given by:

$$T_H = \frac{100\bar{T_P}}{60} \text{ minutes}, \tag{3.1}$$

where $\bar{T_P}$ is the mean period of the peaks for the chosen motion. This value is the absolute minimum, Lloyd suggests adding an additional 10 minutes (full scale) to T_H as a contingency [51].

Lloyd's approach was taken when considering the number of runs required to obtain an accurate RAO in the towing tank. This equates to roughly eight towing tank runs in each condition. This is appropriate for spectral analysis, but for slamming investigations, a large number of slam events need to be collected. Therefore the number of slams per run was observed to ensure that sufficient slam events were obtained in order to perform a statistical analysis. Slam rate calculations conducted by Dove [21] from past irregular sea tests using the 2.5m HSM are shown in Table 3.5. Based on these observations, four conditions were selected for testing to investigate the motion of the model in the absence of slamming (see Table 3.6. Note: since this is a continuation of an existing project, the condition numbers are carried on from past tests).

Table 3.5: Slam rates for HSM catamaran (from Dove [21]). All conditions are JONSWAP spectra, modal period of 8s full scale (1.2s model scale).

Vessel speed		**Sig. wave height**		**Slam rate**
full scale	**model scale**	**full scale**	**model scale**	**slam/hr**
20kts	1.54m/s	1.49m	30mm	3
20kts	1.54m/s	1.95m	45mm	3
20kts	1.54m/s	2.64m	60mm	63
38kts	2.92m/s	1.49m	30mm	0
38kts	2.92m/s	1.95m	45mm	0
38kts	2.92m/s	2.64m	60mm	27

After these conditions were completed, an investigation into the pressure transducers and the required sample rate of the carriage DAQ system to adequately capture pressure peaks commenced. Several calm water runs were conducted and the pressure signals were examined

for any abnormalities, then the model was subjected to regular waves where the ship motion response was known to be large. The sample rate of the carriage DAQ was systematically altered from 500Hz to 5kHz and the pressure signals were inspected at the end of each run. Figure 3.7 shows the minimum, maximum and average pressures measured during runs at different sampling frequencies in the same conditions. Even though these tests were in regular waves, a significant variation in peak pressures was observed. Repetitions of runs showed variations in maximum and minimum recorded pressure peaks. The second highest sampling rate (4kHz) captured the greatest pressure peak of all the sampling rates. Therefore it was decided to set the carriage DAQ system to sample at 5kHz; this sampling rate gave good resolution of pressure traces (see Figure 3.8 for an example pressure trace sampled at 5kHz for a significant slam event) without producing unwieldy data files; the data file from a 40s run was approximately 30.5MB. The carriage sampling rate was set at 5kHz for Test Set 2 (Conditions 90-111).

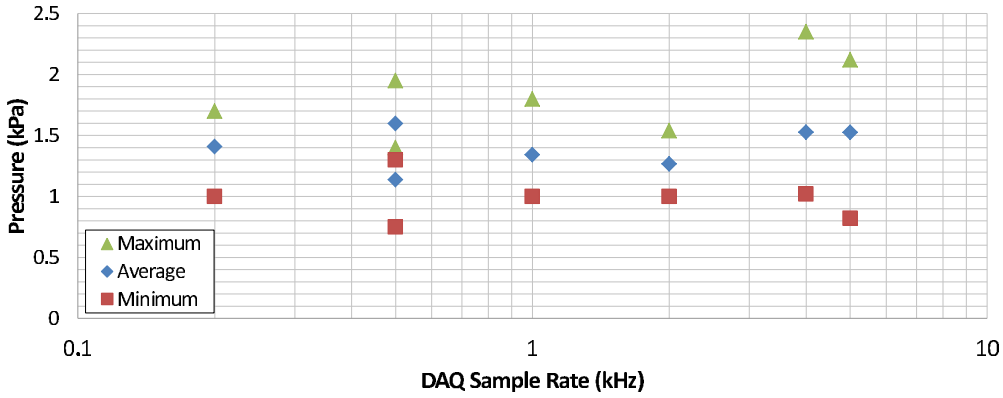

Figure 3.7: Measured minimum, maximum and average pressure peaks against DAQ sample rate (regular wave, vessel speed = 1.45m/s, $f_w = 0.7$Hz, $H_w = 60$mm)

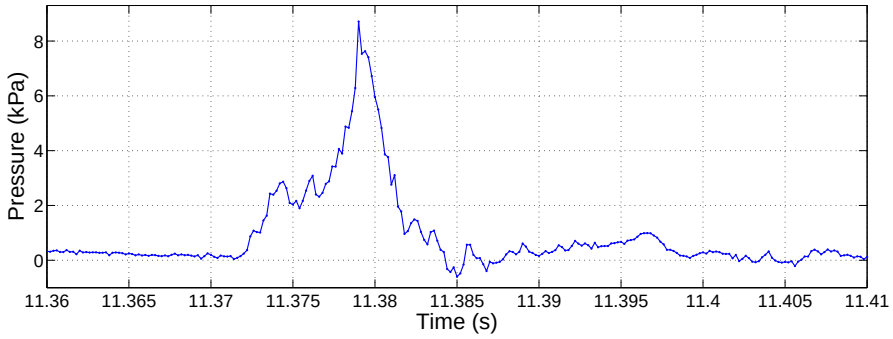

Figure 3.8: Pressure time trace for a slam event in an irregular sea. DAQ sample rate 5kHz. Note the duration of the entire event is no more than 0.015s.

To determine the number of slamming conditions that would be realistically tested within the allocated three week testing window, the test variables needed to be identified. Too many test variables would result in too many conditions and thus not enough testing time in each condition. 48 runs were allocated to Test Set 1 (36 runs) and the pressure investigation (12

Table 3.6: Test matrix for Test Set 1 (motions objective), JONSWAP wave spectra.

	Model Scale			Full Scale			Sample Rates	
Cond.	**Sig. Wave Height (mm)**	**Modal Period (s)**	**Speed (m/s)**	**Sig. Wave Height (m)**	**Modal Period (s)**	**Speed (kts)**	**Carriage (Hz)**	**cRIO (Hz)**
81	25.0	1.2	1.54	1.12	8	20	500	100-500
82	25.0	1.2	2.92	1.12	8	38	500	100-500
83	50.0	1.2	1.54	2.24	8	20	500	100-500
84	50.0	1.2	2.92	2.24	8	38	500	200

Table 3.7: Test matrix for the pressure investigation, regular waves.

	Model Scale			Full Scale			DAQ Sample Rates	
Cond.	**Wave Height (mm)**	**Period (s)**	**Speed (m/s)**	**Wave Height (m)**	**Period (s)**	**Speed (kts)**	**Carriage (Hz)**	**cRIO (Hz)**
85	0.0	N/A	1.54	0.0	N/A	20	500-5k	200-500
86	0.0	N/A	2.92	0.0	N/A	38	500-5k	500
89	60.0	1.4	1.54	2.69	9.57	20	500-5k	500

runs). As discussed in Section 3.3.2, there was principally an interest in the effect of the speed of the vessel and the modal period of the irregular sea. Three vessel speeds, three modal periods and two significant wave heights resulted in 18 conditions. Eight runs in each condition were estimated to provide sufficient slam events. This gave a total of 192 runs over the allocated testing period. Table 3.8 shows the test matrix for the Test Set 2.

3.7 Calibrations

During the testing period, the LVDTs and all wave probes were calibrated every morning prior to testing. This is a straightforward procedure on the carriage DAQ system; the LVDTs and wave probes are recorded at 'zero' position, then they are adjusted up and down from zero at known increments and the resulting voltage output is recorded by the carriage calibration software. The program then conducts a linear regression between instrument position and resulting voltage output and the relationship between position and output is obtained. The carriage speed was not calibrated during the testing time and it was assumed that the variation of carriage speed was minimal.

The most efficient way to calibrate the boat mounted wave probes was simultaneously using the carriage DAQ system. This was done by placing additional ballast in the boat when it was connected to both carriage tow posts and fixing the boat at 10mm sinkage increments via the tow post pins. It is understood that some deflections in the centre bow section may have

Table 3.8: Test matrix for Test Set 2 (slamming objective), JONSWAP wave spectra.

	Model Scale			Full Scale			Sample Rates	
Cond.	**Sig. Wave Height (mm)**	**Modal Period (s)**	**Speed (m/s)**	**Sig. Wave Height (m)**	**Modal Period (s)**	**Speed (kts)**	**Carriage (Hz)**	**cRIO (Hz)**
90	78.1	1.0	1.54	3.5	7.0	20	5k	200
91	78.1	1.0	2.15	3.5	7.0	28	5k	500
92	78.1	1.0	2.92	3.5	7.0	38	5k	500
93	78.1	1.3	1.54	3.5	8.5	20	5k	200
94	78.1	1.3	2.15	3.5	8.5	28	5k	500
95	78.1	1.3	2.92	3.5	8.5	38	5k	500
96	78.1	1.5	1.54	3.5	10.0	20	5k	200
97	78.1	1.5	2.15	3.5	10.0	28	5k	500
98	78.1	1.5	2.92	3.5	10.0	38	5k	500
99	89.3	1.0	1.54	4.0	7.0	20	5k	200
100	89.3	1.0	2.15	4.0	7.0	28	5k	500
101	89.3	1.0	2.92	4.0	7.0	38	5k	500
102	89.3	1.3	1.54	4.0	8.5	20	5k	200
103	89.3	1.3	2.15	4.0	8.5	28	5k	500
104	89.3	1.3	2.92	4.0	8.5	38	5k	500
105	89.3	1.5	1.54	4.0	10.0	20	5k	200
106	89.3	1.5	2.15	4.0	10.0	28	5k	500
107	89.3	1.5	2.92	4.0	10.0	38	5k	500
108	67.0	1.3	1.54	3.0	8.5	20	5k	200
109	67.0	1.3	2.92	3.0	8.5	38	5k	500
110	55.8	1.3	1.54	2.5	8.5	20	5k	200
111	55.8	1.3	2.92	2.5	8.5	38	5k	500

Table 3.9: Test matrix for Test Set 3 (wave spectra measurements), JONSWAP wave spectra.

	Model Scale		Full Scale		
Condition	**Wave Height (mm)**	**Period (s)**	**Wave Height (m)**	**Period (s)**	**Sampling Rate (Hz)**
123	83.7	1.2	3.75	8.0	20
124	78.1	1.0	3.50	7.0	20
125	78.1	1.3	3.50	8.5	20
126	78.1	1.5	3.50	10.0	20
127	89.3	1.0	4.00	7.0	20
128	89.3	1.3	4.00	8.5	20
129	89.3	1.5	4.00	10.0	20
132	67.0	1.3	3.00	8.5	20
133	55.8	1.3	2.50	8.5	20

occurred when the centre bow was immersed deeply into the water. However the coefficient of determination (R^2) was greater than 0.9 for all calibrations. Therefore the deflection of the centre bow section was considered to be negligible.

Calibrations of instruments measured on the cRIO DAQ system were complicated by the fact that regression software is absent from the cRIO DAQ system and no quick calibration system was available. Therefore the centre bow and demihull strain gauges were not calibrated every morning but twice during the testing session. The following sections outline the procedure taken during the demihull and centre bow calibrations. The calibration factors determined during these tests were found to be comparable with past calibrations [45, 77].

3.7.1 Demihull Calibration

The demihull calibrations were conducted by applying loads to the segments while the model was held in place in a cantilever fashion (see Figure 3.9 for a schematic of the calibration procedure). The model was placed across the wet dock so that the forward segment was protruding off the wet dock edge and the aft and centre segments were supported. A zero strain reading was taken by having the cRIO acquire data for five seconds. Next, a known load was applied to both port and starboard demihull backbone beams simultaneously and the cRIO acquired data once again. This process was repeated six more times for the forward demihull with increasing loads. The same process was then repeated for the aft demihull links, and a total of five calibration loads were applied to the aft demihull.

A regression analysis of the resulting data was completed and calibration factors for each demihull link were determined and applied to the measured moments to produce the calibrated moments. Figures 3.10 and 3.11 shows the calibration results. The demihull links were found to give good predictive qualities between applied and measured load. Only the forward starboard

demihull link showed minor divergence, this was corrected with the application of the calibration factor.

3.7.2 Centre Bow Calibration

The centre bow was calibrated by turning the model upside down and laying it on a flat table with the centre bow segment overhanging the table edge. This restrained the demihull segments but allowed the centre bow to deflect freely. A shaped polystyrene block was placed on the up-turned centre bow to provide a flat mounting point and the centre bow segment was then loaded with known calibration masses at known locations and the strain response was recorded on the cRIO DAQ system. Masses were stacked on the mount at three positions in increments of 5kg, to a maximum of 20kg. All masses were applied on the centreline of the model.

The four centre bow elastic links were removed from the model and calibrated individually by Matsubara [53] during 2008, they were not calibrated individually during the 2010 testing session. Matsubara's calibration factors were used to convert the strain gauge voltage signal to moments. Moment, M at link i is given by the following relationship:

$$M_i = C_i S_i, \tag{3.2}$$

where S_i is the i^th strain gauge signal and C_i is the individual elastic link calibration factor.

Figure 3.12 shows a schematic diagram of the force acting on the centre bow segment forward transverse beam. The beam was pinned at A and B. Strain gauges were mounted on each of the elastic links separated by a distance, l_2. The strain gauges were located l_1 distance from the pinned joints at A and B.

The force on the forward (F_f) and aft (F_a) transverse beams can be found by considering reaction forces and moments around one link. The following equations result:

$$F'_f = \frac{2M'_1}{l_1} + \frac{2(M'_1 - M'_2)}{l_2} \tag{3.3}$$

$$F'_a = \frac{2M'_3}{l_1} + \frac{2(M'_3 - M'_4)}{l_2} \tag{3.4}$$

the dashes in Equations 3.3 and 3.4 represent non-calibrated quantities.

Figure 3.13 shows a diagram of the forward and aft transverse beams; w_2 is the distance between the beams. The total slam force acting on the centre bow, F'_c , is simply the sum of the forces acting on the forward and aft transverse beam, F'_f and F'_a respectively:

$$F'_c = F'_f + F'_a \tag{3.5}$$

The total load is corrected by applying a calibration factor found by regression analysis, see Equation 3.6. Figure 3.14 shows the influence of the correction factor on the measured load.

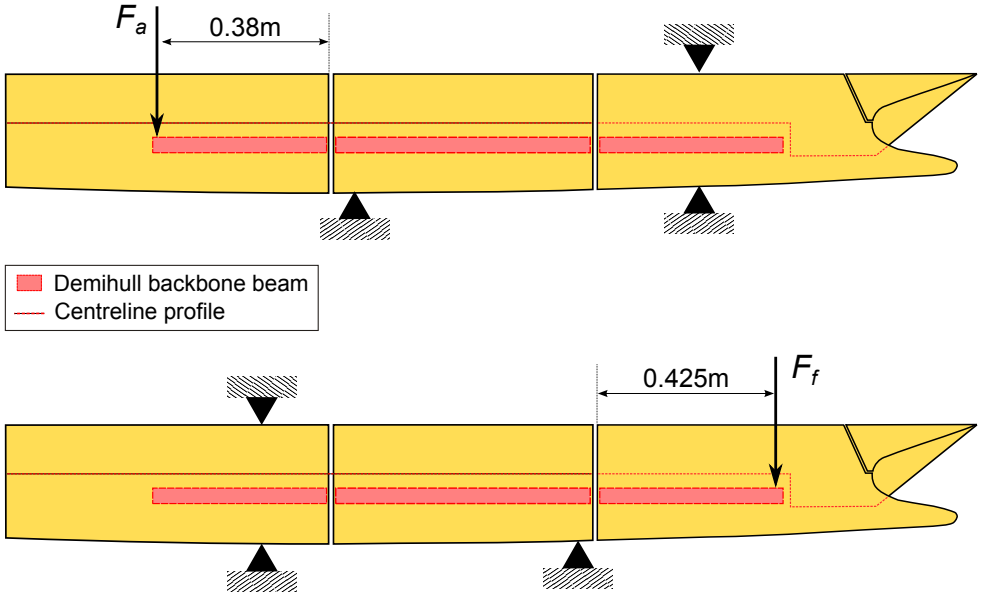

Figure 3.9: Demihull calibration procedure. Top: calibration of the aft demihull links. Bottom: calibration of the forward links.

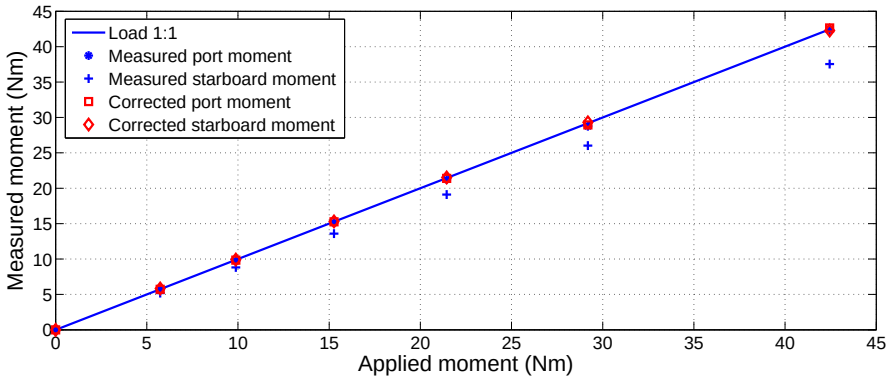

Figure 3.10: Forward demihull: Applied moment and the resulting measured and calibrated moments.

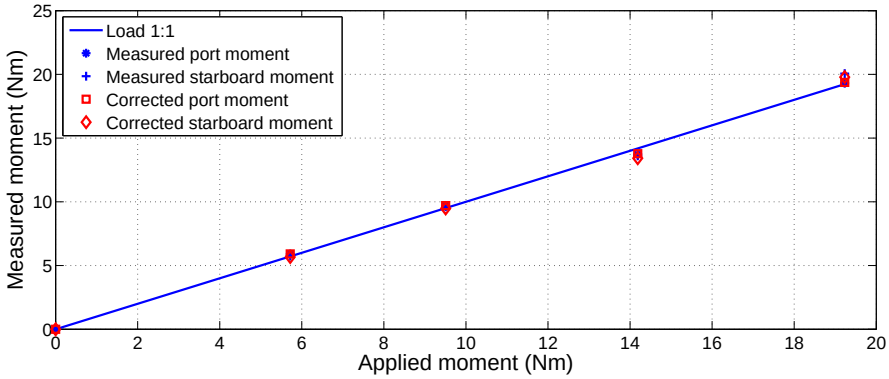

Figure 3.11: Aft demihull: Applied moment and the resulting measured and calibrated moments.

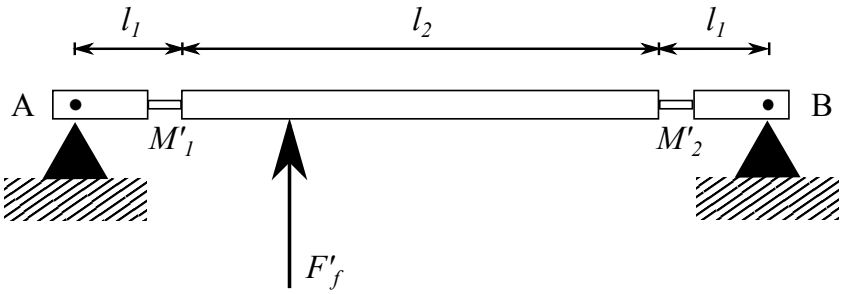

Figure 3.12: Slam force acting on the forward centre bow transverse beam.

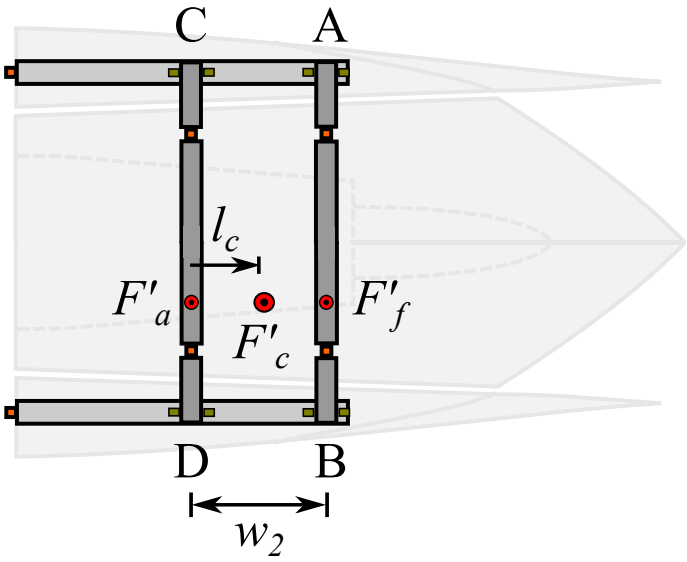

Figure 3.13: Centre bow transverse beam configuration.

$$F_c = C_c F'_c \tag{3.6}$$

The location of the load from the aft transverse beam l_c can be calculated by Equation 3.7:

$$l_c = \frac{F_f}{F_c} w_2 \tag{3.7}$$

Where F_f is the corrected load applied to the forward transverse beam. This shows that the location of the measured load can be determined be considering the ratio of load taken by the forward transverse beam to the entire applied load. F_f is corrected in a similar manner to Equation 3.6, i.e.:

$$F_f = C_f F'_f \tag{3.8}$$

This calibration can be seen in Figure 3.15. The '+', 'o' and '*' symbols represent locations calculated using the un-calibrated loads at three different locations. The 'x', square and

diamond symbols show the locations determined by applying the corrected loads in Equation 3.7. Although some spread is still present, the calibrated location calculation method shows an improvement over the non-calibrated calculation.

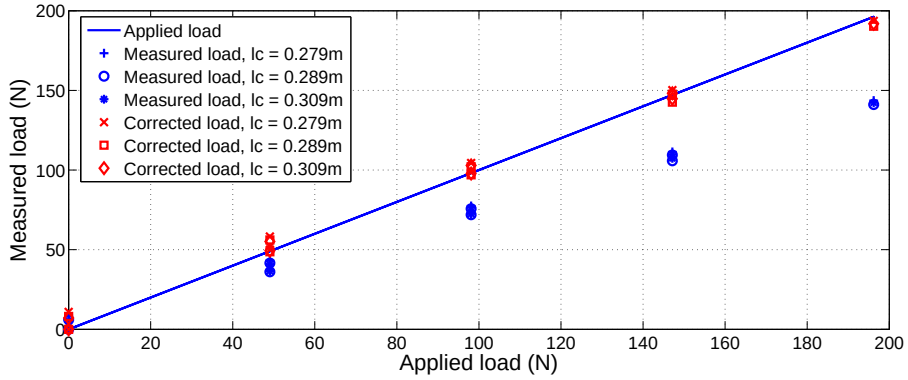

Figure 3.14: Centre bow load calibration: Applied load against measured load (F_c') also shown is the corrected calibrated load F_c.

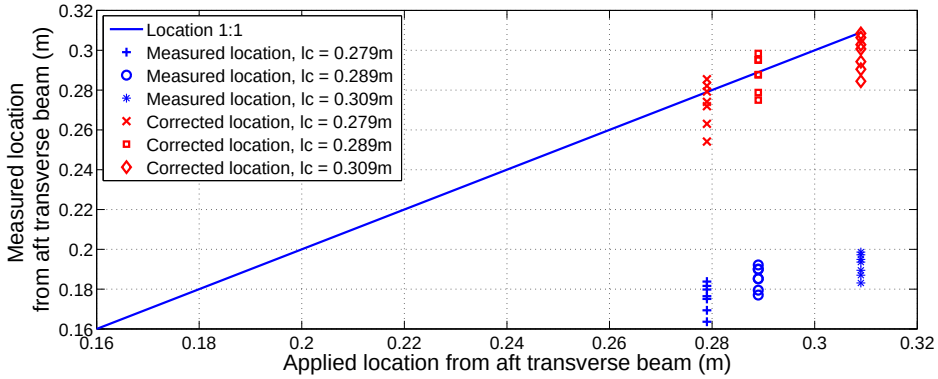

Figure 3.15: Centre bow load location calibration: Applied location against measured location l_c', also shown is the corrected location l_c.

3.8 Summary

A 2.5m hydroelastic segmented catamaran model representative of the 112m class Incat design was tested in the AMC towing tank with the goals of investigating ship motions in irregular waves in the absence of slamming (Test Set 1) and investigating the characteristics of slam events in irregular waves with the intention of developing an empirical slam module (Test Set 2). The wave environment produced by the AMC towing tank wave maker was also measured (Test Set 3) to complement the previous test sets. Test Set 1 consisted of four conditions (two speeds, two significant wave heights and one modal period). Test Set 2 consisted of eighteen conditions (three speeds, two significant wave heights and three modal periods) plus a bonus four conditions (two extra significant wave heights at two speeds and one modal period). All wave conditions were repeated with no model and static wave probes installed at various locations along the towing tank during Test Set 3.

The model was extensively instrumented with LVDTs, wave probes mounted both on the model itself and alongside, strain gauges located on the demihull and centre bow segments to measure vertical bending moments and centre bow slam loads respectively and pressure sensors located on the centre bow segment archway.

An investigation into the DAQ sample rate required to capture peak pressures was conducted with the conclusion that a 5k Hz sample rate is capable of recording maximum slamming pressures. Two DAQ systems were used to record all the instruments, the carriage mounted DAQ recorded at 5kHz, while the portable cRIO system acquired data at either 200 or 500Hz depending on the length of the run.

LVDTs and wave probes were calibrated each morning as part of the operating procedure. The strain gauges were calibrated twice during the testing period. The demihull strain gauges were calibrated by loading the demihull in a cantilever fashion and recording strain measurements. The centre bow was calibrated by upturning the model and placing masses on the centre bow segment at known locations, so that the centre bow load and load location could be determined.

Chapter 4

Motions

4.1 Introduction

The fundamental base of slamming prediction is the ability to accurately model the motions of the model. A two-dimensional time-domain strip theory optimised for high Froude numbers is used to predict vessel motions in this project. The algorithm was originally developed for regular waves, however it was soon expanded to predict motions in an irregular seaway. This extension, combined with the ability to model slamming is vital for any realistic long term loading investigation.

Following the discussion in Section 2.2, there are many motion prediction methods available to the ship designer/researcher, each with the same end goal but varying in approach. However, due to the inherent limiting assumptions these methods make, no 'perfect' seakeeping method has been developed as yet and this is particularly evident when predicting motions of high-speed catamarans.

The seakeeping theory introduced below was developed at the University of Tasmania, Australia, by Holloway [34] and it forms the motions and global load prediction tool into which the empirical slam module developed in this project will be installed. This method is formally introduced in Section 4.2 and the extended irregular sea theory is described in the following section. The irregular wave version of the time-domain seakeeping method optimised for high Froude numbers is verified and validated in Sections 4.5 and 4.6 by performing a series of program tests and by comparing scale model experimental results from Test Set 1 and wave spectra measurements (Test Set 3) with predicted motions and wave spectra produced by the seakeeping program.

4.2 Time-Domain Strip Theory Description

A two-dimensional time-domain strip theory seakeeping program is used to predict the motions and global wave loads of large high-speed catamarans. It is based on the transient Green

function solution for strips of water which are fixed in space and perpendicular to the direction of motion. The solution for each strip starts when the bow enters the strip, and finishes when the stern leaves the strip. The Green function used satisfies the linearised free surface boundary condition; therefore if the water depth is considered to be deep, it is only necessary to place sources on the hull surface. This has the advantage of reducing the number of sources (and thus number of computations) required for a solution.

Large amplitude motions and irregular incident waves can be simulated realistically with this model because the hull is panelled at the instantaneous incident wave free surface at each time step. This requires the sources to be redistributed on the wetted hull surface at each time step. It is important to remember that the Green function linearises the free surface boundary condition, so any non-linear effects resulting from large motions of the free surface are not modelled. The Green function solution determines the local pressures on each hull surface panel and the total force on the hull is found by integrating over the hull surface at each time step. The hull is then treated as a rigid body and instantaneous accelerations in heave, pitch, yaw and sway are determined. It is then possible to integrate the accelerations to determine the motion of the vessel through time [34, 35, 36].

4.2.1 Governing Fluid Equations

Strip theory seakeeping computations are built upon potential flow assumptions and boundary element methods. Therefore the problem can be solved by considering only the boundary conditions; no knowledge of the flow field inside the fluid is required. The total linear velocity potential (Φ) of the fluid is the sum of three component potentials (Equation 4.1): radiation (ϕ_r) (waves generated by the body by oscillating in still water), diffraction (ϕ_d) (the incident waves that have interacted with the body) and the incident wave potential (ϕ_i). The sum of the radiation and diffraction potential is known as the disturbance potential (ϕ, Equation 4.2) as these potentials are generated by a disturbance disrupting the free surface.

$$\Phi = \phi_r + \phi_d + \phi_i \tag{4.1}$$

$$\phi = \phi_r + \phi_d \tag{4.2}$$

Consider a right-handed coordinate system as shown in Figure 4.1. Axes (x_0, y_0, z_0) are fixed in space, the (x_0, y_0) plane lies on the still water surface. x_0 is positive in the direction of wave propagation and z_0 is directed upwards. Another coordinate system is fixed on the vessel, x is in the direction of vessel motion, y is positive to port and z is directed upwards.

Now consider a rigid body floating in a ideal fluid with harmonic waves. The time average of motions in all directions is zero. In order to simplify notation, the (x, y, z) coordinate system is assumed to be identical to the (x_0, y_0, z_0) system.

By definition of the velocity potential, the velocity of the water particles can be found:

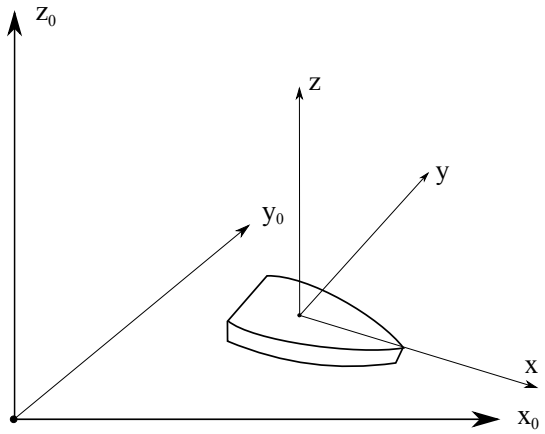

Figure 4.1: Coordinate system.

$$v_x = \frac{\partial \Phi}{\partial x}, \qquad v_y = \frac{\partial \Phi}{\partial y}, \qquad v_z = \frac{\partial \Phi}{\partial z}.$$

Since the fluid is assumed incompressible and homogeneous, the continuity equation applies:

$$\frac{\partial v_x}{\partial x} + \frac{\partial v_y}{\partial y} + \frac{\partial v_z}{\partial z} = 0. \tag{4.3}$$

This leads to the Laplace equation:

$$\nabla^2 \Phi = \frac{\partial^2 \Phi}{\partial x^2} + \frac{\partial^2 \Phi}{\partial y^2} + \frac{\partial^2 \Phi}{\partial z^2} = 0 \tag{4.4}$$

$$\nabla^2 \Phi = \frac{\partial^2 \Phi}{\partial y^2} + \frac{\partial^2 \Phi}{\partial z^2} = 0 \qquad \text{in two dimensions.} \tag{4.5}$$

The pressure at any point within the fluid can be described by the linearised form of Bernoulli's equation:

$$p = -\rho \frac{\partial \Phi}{\partial t} - \rho g z. \tag{4.6}$$

This can be written as:

$$\frac{\partial \Phi}{\partial t} + g \cdot \zeta = \frac{p}{\rho} \tag{4.7}$$

where $z = \zeta(x, y, z, t)$ at the free surface, and the pressure p is constant.

Because of the linearisation, the vertical velocity of a water particle can be described as:

$$\frac{dz}{dt} = \frac{\partial \Phi}{\partial z} \approx \frac{\partial \zeta}{\partial t}. \tag{4.8}$$

Derive Equation 4.7 w.r.t. t and then substitute Equation 4.8:

$$\frac{\partial^2 \Phi}{\partial t^2} + g \cdot \frac{\partial \Phi}{\partial z} = 0 \qquad \text{for} \quad z = 0, \tag{4.9}$$

which is the free surface boundary condition. Since higher order terms in Bernoulli's equation (Equation 4.6) were neglected, Equation 4.9 represents the linear free surface boundary condition. For linearisation of the free surface boundary condition to be meaningful it is assumed that firstly there is deep submergence of the body, secondly the body is slender and lastly the motions of the body are assumed to be small enough not to create a disturbance of the free surface. The linear assumption fails when vessel motions become very large.

In shallow water conditions, (typically when the depth of the water $(-h)$ is less than 0.03λ [51]) the boundary condition for the sea bed can be written as:

$$\frac{\partial \Phi}{\partial z} = 0 \qquad \text{for} \quad z = -h. \tag{4.10}$$

The disturbance potential tends to zero in the far field ($\nabla\phi_r \to 0$ and $\nabla\phi_d \to 0$), hence the far field boundary condition can be stated as:

$$\nabla\Phi \to \nabla\phi_i \quad \text{in the far field.} \tag{4.11}$$

The boundary condition at the surface of the floating body is given by:

$$\nabla\Phi \cdot \mathbf{n} = v_n(x, y, z, t) = \mathbf{v} \cdot \mathbf{n}, \tag{4.12}$$

where $\mathbf{n}$ is a unit vector normal to the surface of the floating body. The velocity (v_n) of a water particle in contact with the surface of the body is equal to the velocity of the body.

4.2.2 High Froude Number Time-Domain Strip Theory based on a Green Function Solution

Frequency-domain methods commonly adopt a reference frame moving with the mean speed of the ship (the x, y, z coordinate system in Figure 4.1). In order to solve the disturbance potential in frequency-domain methods, it is essential that the disturbance potential is separated into its radiation and diffraction components ($\phi = \phi_r + \phi_d$). However in a time-domain solution the disturbance potential can be more efficiently solved simultaneously [36]. By retaining this distinction the boundary condition on the surface of the floating body can be re-written as:

$$\nabla\phi \cdot \mathbf{n} = (\mathbf{v} - \nabla\phi_i) \cdot \mathbf{n}. \tag{4.13}$$

Now assume the waves generated due to a disturbance are long crested and perpendicular to the hull centreline (i.e. $v_x = 0$). These assumptions are valid for slender vessels and allows the water to be divided into two-dimensional strips and the boundary conditions solved in two-dimensional planes normal to the vessel direction of travel. This means n_x in Equation 4.13

is assumed to be small as wave propagation in the direction of travel is ignored and the two dimensional form of the Laplace equation (Equation 4.5) governs the fluid domain.

Because the disturbance potential is not separated into components, the linear free surface boundary condition (Equation 4.9) can be expressed as:

$$\frac{\partial^2 \phi}{\partial t^2} + g \cdot \frac{\partial \phi}{\partial z} = 0 \qquad \text{for} \quad z = 0. \tag{4.14}$$

Equation 4.14 has been linearised in this method; this is not strictly necessary however, by using a time-domain solution other nonlinear effects can be resolved, such as the change in hull immersion [35]. Equation 4.14 also contains no longitudinal derivatives and so it is fully three-dimensional. In fact, the assumption that $n_x << 1$ in Equation 4.13 and the two-dimensional form of the Laplace equation are the only features that prevent this method from being fully three-dimensional

It is also important to remember that this method assumes potential flow. Therefore viscous effects are neglected. At the moment an empirical viscous correction factor is implemented (see Appendix B for a description of this factor), with the knowledge that further investigation is required into the physics of viscous damping and its application into potential flow models.

A boundary element method based on a free surface Green function is used to solve the two-dimensional problem defined by Equations 4.5, 4.11 and 4.14. The source function used can be found in Wehausen and Laitone [73], a hand book containing many Green functions of different source types. Equation 4.15 is the transient two-dimensional source function used in the present method.

$$\begin{aligned} f(z,t) \quad = \quad & \frac{Q(t)}{2\pi} ln(z - c(t)) - \frac{Q(t)}{2\pi} ln(z - \bar{c}(t)) \\ & - \frac{g}{\pi} \int_0^t Q(\tau) \int_0^\infty \frac{1}{\sqrt{gk}} e^{-ik(z-\bar{c}(\tau))} \sin\left[\sqrt{gk}(t-\tau)\right] dk d\tau \end{aligned} \tag{4.15}$$

where $Q(t)$ is the real source strength, $c = a + ib$, for $b < 0$ is the source location, $\bar{c}$ its complex conjugate and $z = x + iy$ the field position and g is gravitational acceleration. Note z is redefined as a complex number representing spatial coordinates, the imaginary part being vertical.

Equation 4.15 automatically satisfies the 2D Laplace equation (4.5) as well as the far field and free surface boundary conditions (Equations 4.11 and 4.14 respectively) and because of linearity, so will any combination of sources distributed over the instantaneous wetted hull surface boundary (Equation 4.12), which is not satisfied by the source function. For finite depth, the sea bed also requires sources distributed along it to satisfy boundary condition 4.10.

The problem now is to solve for the vector of source strengths $\mathbf{Q}(t)$ distributed on the wetted hull surface that satisfies boundary condition 4.12. The velocity at any point $W = u - iv$ is obtained from Equation 4.15 due to sources integrated over all elements. This allows the boundary condition to be written in matrix form as $[A]\{Q\} = \{R\}$. Terms in Equation 4.15

independent of $\mathbf{Q}(t)$ are moved to the right hand side of the equation and are expressed in $\{R\}$, therefore this term contains the convolution integral, resulting in:

$$A_{ij} = -\mathrm{Im}\left\{\frac{e^{i\alpha}}{2\pi}\left[e^{-i\beta}\ln\left(\frac{z-c_1}{z-c_2}\right) - e^{i\beta}\left(\frac{z-\bar{c}_1}{z-\bar{c}_2}\right)\right]\right\} \tag{4.16}$$

and

$$\begin{aligned} R_i &= (\mathbf{v} - \nabla\phi_i)\cdot\mathbf{n} \\ &\quad -\mathrm{Im}\left\{e^{i\alpha}\left[i\sqrt{\frac{g}{\pi}}\sum_{j=1}^{n}\int_0^t e^{i\beta(\tau)}Q_j(\tau)\left[\frac{e^{w^2}\mathrm{erf}w}{\sqrt{i[z-\bar{c}(\tau)]}}\right]_{w_1}^{w_2}\right]d\tau\right\}, \end{aligned} \tag{4.17}$$

where c_1 and c_2 are the end points of element j, α and β are the slopes of the hull surface at i and j respectively, $w_k = \frac{i(t-\tau)}{2}\sqrt{\frac{-ig}{z-\bar{c}_k}}$ and the convolution integral is evaluated numerically by known discrete values of Q, z, c, and β at previous time intervals Δt.

Pressures (and thereby forces) are determined at each element i by summing the contributions of all other elements j by $p_{ij} = -\rho\frac{\partial\phi_{ij}}{\partial t}$:

$$\begin{aligned} p_{ij} &= -\rho\mathrm{Re}\left\{\frac{e^{-i\beta}}{2\pi}\left[(A_k + (z-c_k)B)\ln(e^{-i\gamma}(z-c_k))\right]_{k=1}^{2}\right. \\ &\quad -\frac{e^{i\beta}}{2\pi}\left[(\bar{A}_k + (z-\bar{c}_k)\bar{B})\ln(z-\bar{c}_k)\right]_{k=1}^{2} \\ &\quad \left.+\frac{2ig}{\sqrt{\pi}}\int_0^t e^{i\beta(\tau)}Q(\tau)\int_{w_1}^{w_2}\left(e^{w^2}\mathrm{erf}w + \frac{1}{w\sqrt{\pi}}\right)dwd\tau\right\}, \end{aligned} \tag{4.18}$$

where $A_k = Q\frac{dc_k(t)}{dt}$, $B = -\frac{dQ}{dt} + iQ\frac{d\beta}{dt}$ and $\gamma = \arg(z - \frac{1}{2}(c_1) + c_2)$ or $\arg(c_2 - c_1)$ if $z = \frac{1}{2}(c_1) + c_2)$, all evaluated at time t. Discussions on methods to solve these equations accurately and efficiently are given in [35].

Linearised hydrodynamic forces acting on the hull in heave and pitch (from a fixed reference frame, and in the time domain) are:

$$F_3 = \left\{\int_{stern}^{bow} pdx\right\} \tag{4.19}$$

and

$$F_5 = \left\{\int_{stern}^{bow} xpdx\right\} \tag{4.20}$$

where p is the vertical component of the sectional pressure i.e. $p = -\rho\int_{section}\frac{\partial\phi}{\partial t}n_z dl$ and the subscript 3 and 5 represents heave and pitch respectively. The rigid body equations of motion for heave and pitch are:

$$\left[F_{3,\text{Froude-Krylov}} + F_3(\xi_3, \xi_5)\right] = M\ddot{\xi}_3 \quad (4.21)$$

$$\left[F_{5,\text{Froude-Krylov}} + F_5(\xi_3, \xi_5)\right] = I_5\ddot{\xi}_5 \quad (4.22)$$

M and I_5 are the mass and pitch moment of inertia respectively, and ξ_3 and ξ_5 are heave and pitch displacements.

Unlike classical strip theories in the frequency domain, it is not necessary to separate the potential function (ϕ) into components dependant and independent of vessel motion at this point, as all force components fall on the left hand side of the equation and all components of ϕ can be solved simultaneously. Therefore the concepts of added mass and damping are not required in the application of this method. However care must be taken when integrating time domain equations of motion to avoid instability resulting from implied acceleration feedback (associated with added mass in the frequency domain approach) in the hydrodynamic force. Holloway [33] presented a procedure to stabilise these equations by estimating the implied acceleration based on an extrapolation of prior motions. This method was found to be successful for ship motion applications.

4.3 Predictions of Motions in Irregular Seas

In order to simulate realistic seakeeping scenarios, the method should be able to predict motions in irregular seaways. Because this method is formulated in the time-domain and instantaneous wave heights are determined at all strips of water and at each time step, it is possible to use the principle of linear superposition of regular waves to create an irregular wave field. This assumes that nonlinear interactions of regular waves are negligible. An array of wave heights, frequencies, phases and headings are required in this method. Surface displacements, velocities and Froude-Krylov forces are calculated for each regular wave component at each water section and then summed to give the total surface displacement, velocity and Froude-Krylov forces.

4.3.1 Incident Irregular Wave Definition

The potential function for the j^{th} regular wave component is:

$$\phi_j = \frac{H_{wj}\omega_{0j}}{2k_{0j}} e^{k_{0j}z} cos(k_{0j}x + \omega_{0j}t) \quad (4.23)$$

Linear superposition of individual wave components is used to obtain the total potential function for the irregular wave:

$$\phi = \sum_{j=1}^{n} \phi_j = \sum_{j=1}^{n} \frac{H_{wj}\omega_{0j}}{2k_{0j}} e^{k_{0j}z} cos(k_{0j}x + \omega_{0j}t) \quad (4.24)$$

for n regular waves.

The wave elevation associated with the j^{th} wave component is:

$$\eta_j = \frac{H_{wj}}{2}\sin(k_{0j}x + \omega_{0j}t). \tag{4.25}$$

Total wave elevation is simply the sum of these components ($\eta = \sum \eta_j$).

The hydrodynamic component of pressure head and vertical velocity can now be determined:

$$\begin{aligned} \frac{p}{\rho g} + z &= -\frac{1}{g}\frac{\partial \phi}{\partial t} \qquad (4.26)\\ &= \sum_{j=1}^{n} \frac{H_{wj}}{2} e^{k_{0j}z}\sin(k_{0j}x + \omega_{0j}t) \\ &= \sum_{j=1}^{n} \eta_j e^{k_{0j}z} \\ w &= \frac{\partial \phi}{\partial z} \qquad (4.27)\\ &= \sum_{j=1}^{n} \frac{\partial \eta_j}{\partial t} e^{k_{0j}z}. \end{aligned}$$

Equations 4.23 through to 4.27 assume that the waves are travelling in the $-x$ direction, however these equations can be further generalised to represent any heading by replacing x by $(x\cos\theta + y\sin\theta)$. Each wave component can also be given a different phase by simply including phase angle γ in the $(k_0x + \omega_0 t)$ term. The following sections present a method in which to represent any given wave spectra as a sum of regular wave components.

4.3.2 Simulating Idealised Wave Energy Spectra

Many idealised wave energy spectra have been developed over the years to represent real ocean wave systems and aid in the ship design process. They are often defined by a small number of parameters (usually significant wave height and modal period) so that vessel reactions can be analysed when certain sea parameters are varied.

The spectra considered here are: Joint North Sea Wave Project (JONSWAP), Bretschneider (otherwise known as the ITTC two-parameter spectrum), one-parameter Bretschneider, Pierson-Moskowitz and the general spectrum used by Det Norske Veritas (known here on as DNV). The JONSWAP and Bretschneider spectra are special cases that fit within the DNV general spectra. Even though the JONSWAP spectra was chosen as the primary spectra for the scale model experiments (see Section 3.3.1) and therefore all the results presented in this work involves the JONSWAP spectrum, the method used to create idealised wave spectra is general and able to produce all of the spectra discussed here.

The Bretschneider wave energy spectrum is a wide band spectrum and is representative of

open ocean wave conditions; in contrast, the JONSWAP spectrum is often used to represent coastal waters where fetch is limited [51]. Although it must be remembered that an idealised spectrum is only an approximation of real ocean wave conditions, the 15th ITTC (International Towing Tank Conference) recommended the use of the Bretschneider spectrum to model average open ocean wave conditions when more appropriate spectra are not known [48]. The Bretschneider spectrum has been found to be most useful in engineering applications.

The Pierson-Moskowitz spectrum differs from the other spectra mentioned above as it is defined by wind speed alone (not significant wave height or modal period like the other common spectral families). It was originally developed for oceanographic applications, such as the prediction of storm waves. The Pierson-Moskowitz spectrum assumes a fully-developed sea (fetch and duration are not restrained), and so its use in ship design is limited as the idealised Pierson-Moskowitz spectrum is approached asymptotically with extended periods of steady winds and no swell interference from outside areas [48].

Ideal wave energy spectra are described by the following general formula:

$$S(\omega) = \frac{A}{\omega^5} e^{\left(\frac{-B}{\omega^4}\right)} \gamma^C, \tag{4.28}$$

where the coefficients A, B, C and the peak enhancement factor, γ, are defined by the type of idealised spectrum.

For all spectra (JONSWAP, Bretschneider (ITTC), DNV, one-parameter Bretschneider, Pierson-Moskowitz):

$$C = e^{\left[\frac{-1}{2\sigma^2}\left(\omega\frac{T_0}{2\pi}-1\right)^2\right]}. \tag{4.29}$$

Where,

$$\sigma = \begin{cases} 0.07 & \text{if} \quad \omega < \frac{2\pi}{T_0} \\ 0.09 & \text{if} \quad \omega > \frac{2\pi}{T_0} \end{cases} \tag{4.30}$$

and the peak enhancement factor, γ, is given as:

$$\gamma \quad = \quad \begin{cases} 1.0 & \text{for Bret., 1P Bret. and P-M spectra} \\ 3.3 & \text{for JONSWAP spectra} \end{cases} \tag{4.31}$$

and for the more general DNV spectrum:

$$\gamma = \begin{cases} 1.0 & \text{if} \quad \frac{T_0}{\sqrt{H_{1/3}}} > 5.0 \\ e^{\left(5.75-1.15\frac{T_0}{H_{1/3}}\right)} & \text{if} \quad 3.6 < \frac{T_0}{\sqrt{H_{1/3}}} \leq 5.0 \\ 5.0 & \text{if} \quad \frac{T_0}{\sqrt{H_{1/3}}} \leq 3.6 \end{cases} \tag{4.32}$$

By assigning a peak enhancement factor of 1.0, parameter C is effectively ignored (see Equation 4.29).

For a JONSWAP, Bretschneider, or DNV spectrum A and B are:

$$A = 5\pi^4 (1 - 0.287 \ln(\gamma)) \frac{H_{1/3}^2}{T_0^4}, \quad \text{and} \tag{4.33}$$

$$B = \frac{20\pi^4}{T_0^4} \tag{4.34}$$

and for the Pierson-Moskowitz or one-parameter Bretschneider spectrum:

$$A = 8.11 \times 10^{-}3g^2, \quad \text{and} \tag{4.35}$$

$$B = \frac{0.74g^4}{U_{wind}^4}, \quad \text{(Pierson-Moskowitz)}, \tag{4.36}$$

$$B = \frac{3.11}{H_{1/3}^2}, \quad \text{(one-parameter Bretschneider)}. \tag{4.37}$$

The Pierson-Moskowitz is unique from the other spectra as wind speed is the only defining parameter. The nominal wind speed is measured in units of metres per second, and is taken by convention to be at a height of 19.5m above the sea surface [26]. Philp's constant (Equation 4.35) is used by both the one-parameter Bretschneider and Pierson-Moskowitz to define parameter A. Thus the one-parameter Bretschneider is defined by significant wave height only.

The peak enhancement factor γ of an idealised spectrum is an indicator of the 'broadness' of the spectrum. Table 4.1 summarises the different spectra analysed.

Table 4.1: Summary of idealised wave energy spectra.

Spectrum	**Bandwidth**	**Use**
Bretschneider	'Broad' ($\gamma = 1.0$)	Open ocean conditions
JONSWAP	'Narrow' ($\gamma = 3.3$)	Coastal conditions
DNV	Function of T_0 and $H_{1/3}$ ($1.0 \leq \gamma \leq 5.0$))	General
1P Bretschneider	'Broad' ($\gamma = 1.0$)	Open ocean
Pierson-Moskowitz	Not applicable	Open ocean, oceanographic

4.3.3 Representing Sea Spectra by Superposition of Regular Waves

An ideal wave spectrum can be represented by a series of regular waves of varying frequencies and amplitudes depending on the energy distribution of the wave spectrum. The average energy ($\bar{E}$) over a wavelength is given by Equation 4.38:

$$\bar{E} = \frac{\rho g \zeta_0^2}{2}. \tag{4.38}$$

Figure 4.2 shows a wave energy spectrum that has been divided into a number of bands. The solid lines represent the boundaries of the frequency bands and the dotted lines show the mid-point, each band is represented by one regular wave. The area under the wave energy spectrum is proportional to the energy multiplied by density and gravitational acceleration. Therefore the n^{th} regular wave component of the spectrum can be found by applying Equation 4.39, where the frequency of the regular wave is the mid-point and its amplitude represents the average energy over the frequency band.

$$\zeta_n = \sqrt{\frac{2\bar{E}}{\rho g}} \tag{4.39}$$

In order to avoid repetition of the wave pattern in time, the wave spectrum is not divided by a constant frequency spacing but by constant amplitude. Each wave component represents a constant amount of energy in the spectrum, therefore in regions of little energy, the frequency spacing between wave components is greater than at the energy peak where the regular wave components are more concentrated. This can be seen in Figure 4.2, each frequency band represents the same amount of energy (and thus area under the curve). The spectrum shown in Figure 4.2 is divided into fifty waves for clarity, the spectra used in the simulations presented in Section 4.6 are divided into five hundred wave regular wave components.

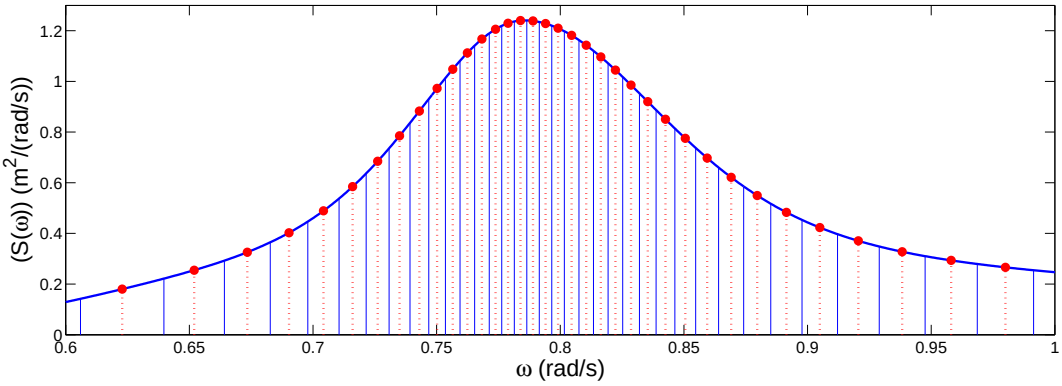

Figure 4.2: A JONSWAP wave spectrum illustrating the constant energy method of separating the spectrum into a series of regular waves. The dashed lines and circles show the mid-point of each energy band, a regular wave of this frequency represents the energy within the associated band. ($H_{1/3} = 2.24m$, $T_0 = 8s$).

4.4 Ship Motions in Irregular Waves

Response amplitude operators (RAOs) are determined for heave and pitch to show the ship motion response in irregular waves. For the case of heave, this is done by calculating the encountered wave spectrum from time domain measurements of the encountered wave elevation and the motion spectrum from the heave response of the vessel. A Fourier analysis was used to determine the motion and wave spectra and the ratio of these spectra provides the RAO for

that particular condition.

The motion RAO for heave is given as the square root of the ratio of the heave spectrum, $S_{x_3}(\omega_e)$, to the measured encountered wave elevation spectrum, $S_\zeta(\omega_e)$ and similarly the pitch RAO is given as the square root of the ratio of the wave slope pitch spectra:

$$\frac{x_{30}}{\zeta_0} = \sqrt{\frac{S_{x_{30}}(\omega_e)}{S_\zeta(\omega_e)}} \tag{4.40}$$

$$\frac{x_{50}}{k\zeta_0} = \sqrt{\frac{S_{x_{50}}(\omega_e)}{S_\alpha(\omega_e)}} \tag{4.41}$$

Variances in the motions and wave spectra were reduced by applying Bartlett's method of ensemble averaging to reduce spectral leakage into other frequency bins. Instead of separating the runs into K segments before applying the Fourier analysis, each run was considered individually and the resulting spectra for all K runs in the condition were averaged (see Equation 4.42). Bartlett's method was also applied to the time domain simulation data; a series of $K = 20$ runs were conducted and ensemble averaging smoothed the resulting spectra.

$$S = \frac{1}{K}\sum_{i=1}^{K} S_i. \tag{4.42}$$

To ensure that the same wave train was not encountered twice, a random phase was applied to each regular wave component when constructing the irregular was spectrum in the time domain, before it was input into the seakeeping program.

4.5 Verification

A series of system tests were devised to verify the operation of the extended seakeeping code. All solutions were computed on the AMC cluster (a Linux cluster of 128 cores on 32 nodes) with the freeware FORTRAN compiler, gfortran. All pre and post processing of the data presented here was carried out with MATLAB on a Windows PC. Table 4.2 summarises the tests undertaken. These tests ranged from simple checks such as observing motions in extremely long waves (test 1) and comparing motions in a single regular wave with that of the same wave composed of two wave components of identical frequency (test 2) to developing an operating strategy regarding simulating idealised sea spectra (tests 6-8). The influence of the modal period and significant wave height of the encountered wave spectrum on the resulting motions of the vessel are of particular interest and so are shown here. Also of interest are the characteristics of the regular wave components that make up the irregular spectrum.

Table 4.2: Summary of verification tests.

Test #	Program Check
1	Single long period wave
2	Superposition of regular waves
3	Compiler comparison
4	Spectral tests
5	RAOs for varying T_0 and $H_{1/3}$
6	Spectra with varying number of waves
7	High frequency investigation
8	Simulation time

4.5.1 RAOs for Varying Modal Period

Heave and pitch RAOs were calculated for the wave-piercing catamaran for JONSWAP and Bretschneider spectra of varying significant wave height and modal period. The influence of wave height (and the presence of the centre bow) on the resulting heave and pitch RAOs is further discussed in Appendix B. Figure 4.3 shows the heave RAO for two encountered JONSWAP wave spectra with a significant wave height of 2m and different modal periods. The encountered wave energy spectrum is overlaid on the RAO plot emphasising the region of maximum energy relative to the peak vessel response frequency. The frequency and magnitude of the peak vessel response does not change significantly with the encountered wave spectra's modal period. Some noise can be seen in the low frequency response of the vessel ($\omega_e^* < 3$) for the 9s period spectrum where there is very little low frequency energy in the wave spectrum.

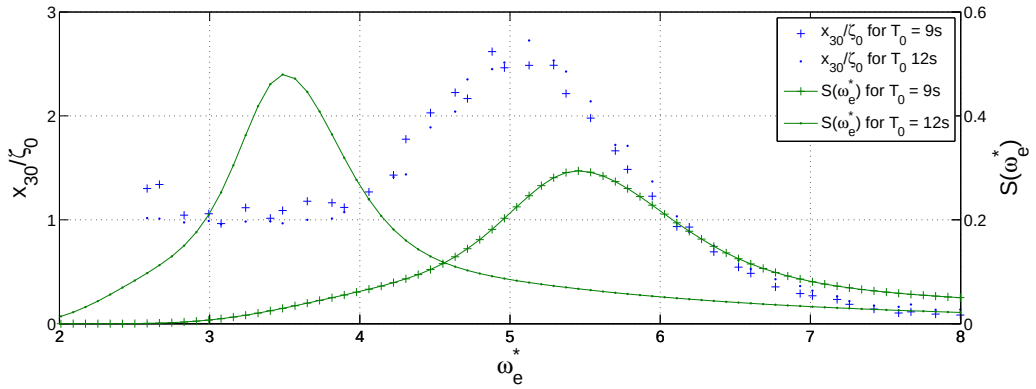

Figure 4.3: Heave RAOs and two encountered wave spectra of different modal periods (JONSWAP spectra, $H_{1/3} = 2$m and vessel speed 38kts (from test 5).)

Figure 4.4 compares the motion response for similar wave spectra, both spectra are Bretschneider (2.5m significant wave height, 12s modal period, vessel speed 38kts) one spectra consisted of 192 regular wave components while the other was identical to the first, except that wave components with an encounter frequency greater than 10 were removed from the simulation. Very high frequency wave components are seen to contribute little to the vessel motions at

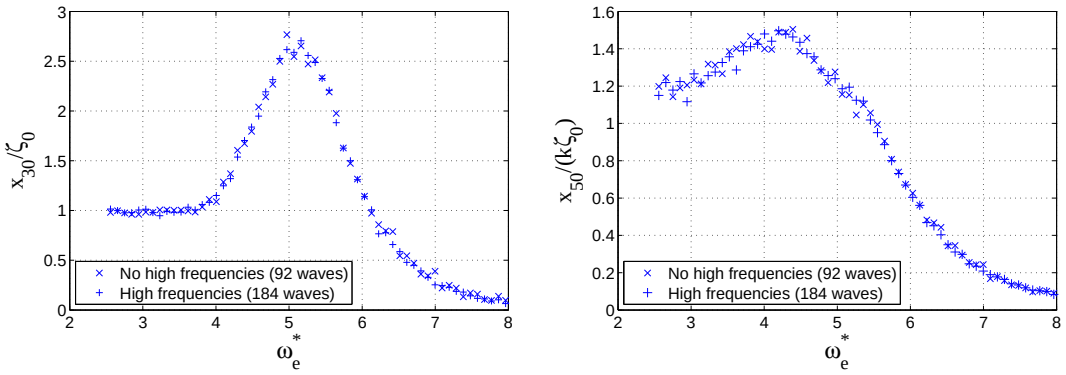

Figure 4.4: Heave and pitch RAO for two similar spectra (one has the frequencies above $\omega_e^* = 10$ excluded) (from test 7).

lower frequencies, therefore there is no advantage in including regular wave components with encounter wave frequencies greater than $\omega_e^* = 8$.

4.5.2 Simulation Time

The required solution time is a function of the number of sections in the vessel geometry file, number of panels per section, number of wave components and of course the total number of time steps simulated. It was found that 10-12 time steps (approximately 0.6s simulated time) were computed per minute real time for a geometry file containing 80 sections and 14 panels per section. Increasing the number of regular wave components in the simulation increases the required simulation time by 3% for every 100 regular wave components. The code may compute 600 time steps per hour for a single regular wave, simulating motions in a spectrum represented by 500 wave components may reduce the time step output to 510 time steps per hour for example. This linear trend was observed for wave spectra consisting of up to 800 wave components.

Altering the number of panels per section has a more drastic effect on the simulation time. A square relationship was found between simulation time and number of panels per section; doubling the number of panels increases the required computational time fourfold. From previous investigations involving a relatively simple hull form (the NPL), 14 panels around each section was found to give a solution within 3% of the solution for a large number of panels. Appendix B contains a brief investigation on the effect of the number of panels on the resulting predicted motions of the vessel.

Bartlett's method of ensemble averaging (Equation 4.42) was used to reduce spectral leakage (error). The number of data points to be used in each discrete Fourier transform (DFT) and the number of solutions to average to obtain a realistic RAO was investigated. Figure 4.5 shows the effect ensemble averaging on the resulting RAO. The right hand plot is of particular interest; the average peak dimensionless heave is shown on the y-axis, and the number of solutions averaged on the x-axis (K in Equation 4.42). There was found to be little gain from running

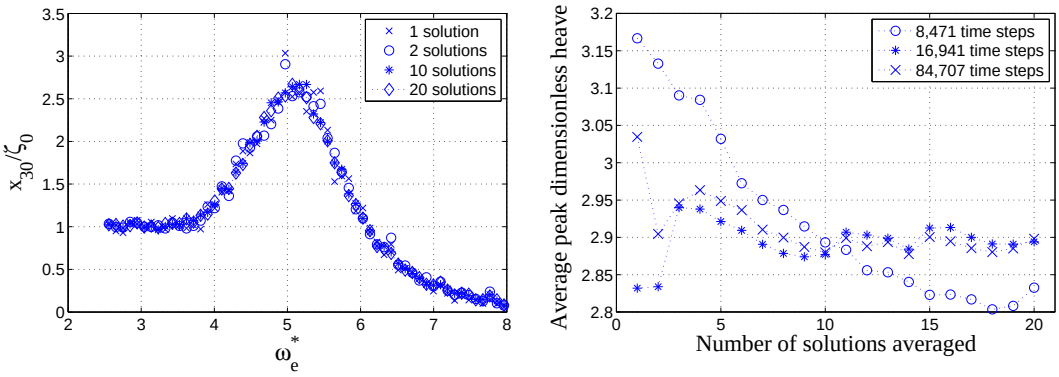

Figure 4.5: Heave RAO (left) determined by averaging a different number of solutions, each solution contained 84,707 time steps, and (right) the peak dimensionless heave with solution time expressed as the number of simulations averaged (from test 8).

excessively long simulations, seventeen thousand data points (roughly 17 minutes of simulated time) per DFT is more than ample, ensemble averaging of 10 or so solutions providing sufficient convergence of the peak dimensionless motions.

4.6 Validation

Validation of the seakeeping code is primarily carried out by comparing predicted motion from the seakeeping code against scale model experimental test results (from Test Set 1). In place of attempting to recreate the scale model test environment exactly in the computational domain (i.e. match time histories of wave elevations with the scale model experiments) a statistical approach was taken and a series of wave systems representative of each condition in Test Set 1 were developed using the method outlined in Section 4.3.3. Twenty of these systems were constructed and ship motions were predicted using the seakeeping program for each one. A Fourier analysis on wave elevation and ship motion time traces were conducted using Bartlett's method of ensemble averaging over the twenty runs representing each test condition. The resulting encountered wave elevation and slope spectra were compared with those measured experimentally during Test Set 1. Predicted heave and pitch spectra were divided by the respective wave elevation or slope spectra to obtain RAOs and these were also compared with Test Set 1 results.

Encountered wave elevation and slope spectra from the model experiments and the seakeeping prediction code were compared with the ideal spectra for every condition (even Test Set 2, the slamming conditions) to ensure that a viable comparison could be made between experimental and numerically predicted motions. Figures 4.6 and 4.7 show the encountered wave elevation and slope spectra for Conditions 81 and 82 compared with the ideal spectra (the solid line). The dot-dashed line is the spectrum produced from the seakeeping prediction while the dashed line represents the spectrum measured during experiments. Good correlation can be

seen between the ideal and measured spectra, allowing viable comparisons between predicted and experimentally measured ship motions. Wave spectra plots for all the other conditions can be found in Appendix A. The wave making machine was generally able to represent the desired spectra, however some discrepancy was observed the shorter period waves (see Figures A.3, A.11 and A.12 on pages 170, 178 and 179 respectively). Appendix A also contains RAO plots for all the other test conditions compared with previous regular sea scale model test results presented by Lavroff [45]. The regular sea tests were carried out with a vessel displacement of 27.43kg compared with the larger 30kg displacement used in these tests necessitated by the presence of the heavier pressure bow, however it can be seen from these plots that the RAO determined from the irregular sea tests falls within the 'envelope' of the regular results, as expected.

Figures 4.8 to 4.11 compare heave and pitch RAOs for Test Set 1 (JONSWAP wave spectra: significant wave height $25 - 50$mm modal period 8s and vessel speed $20 - 30$kts). Since strip theories inherently ignore viscous effects, a vertical damping force coefficient is introduced to model vertical damping (see Appendix B), the results presented in Figures 4.8 to 4.11 use a damping coefficient of 0.08. The peak heave RAO magnitude for Condition 81 (Figure 4.8) matches well with experimental results. If the significant wave height is increased to 2.24m, as shown in Figure 4.10, the predicted heave motions are much greater than expected. This shows that damping effects become significant in larger waves and slower speeds. The peak heave response magnitude also increases with forward speed for both measured and predicted motions, emphasising the non-linearity of this hull form.

There is a discrepancy in the predicted and measured motion frequency, both predicted heave and pitch RAOs appear to be 'shifted' to the right by approximately $0.8\omega_e^*$. This has also been observed when comparing full scale motions data with the simulation [39]. A short investigation into the behaviour of the code was conducted and can be found in Appendix B. A number of possible causes of this error were identified, ranging from the action of the centre bow to the added mass calculations at the transom stern. The irregular wave analysis method was not found to be the cause of this problem as regular wave solutions compared with regular wave model test results still showed the frequency offset in peak motions.

It was seen in Section 4.5.1 that the encountered model period of the sea spectrum does not significantly alter the frequency response of vessel motion. However if the modal period of the encountered wave spectrum coincides with the peak heave response frequency, then greater motions (and slam loads) will be expected. Therefore when considering the application of this seakeeping prediction tool in a real-life scenario, the model period of the sea condition must be carefully selected to give realistic motion results.

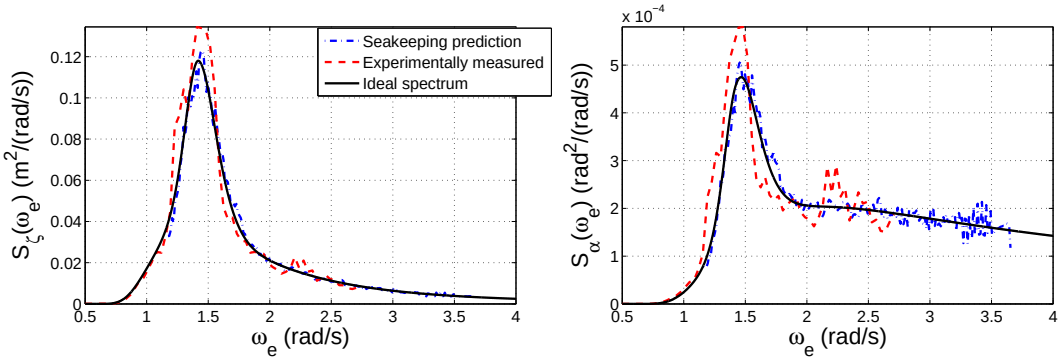

Figure 4.6: Encountered wave spectra (numerical and experimental) compared with the ideal for Condition 81 (JONSWAP, $H_{1/3} = 1.12$m, $T_0 = 8$s, $U = 20$kts (25mm, 1.2s, 1.53m/s model scale)).

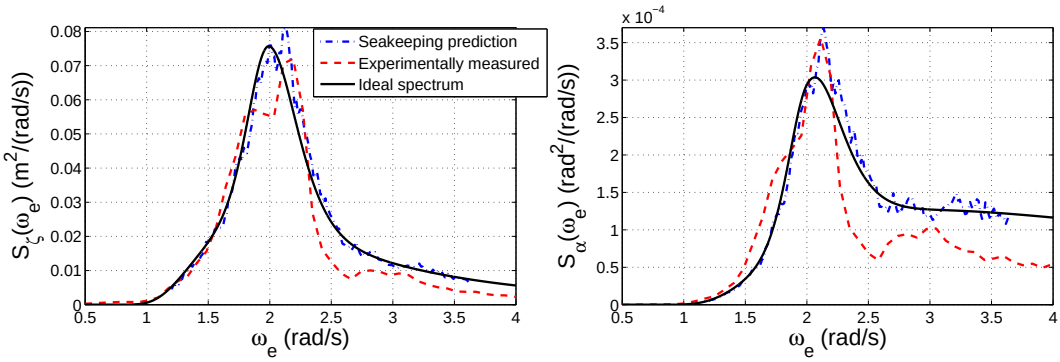

Figure 4.7: Encountered wave spectra (numerical and experimental) compared with the ideal for Condition 82 (JONSWAP, $H_{1/3} = 1.12$m, $T_0 = 8$s, $U = 38$kts (25mm, 1.2s, 2.98m/s model scale)).

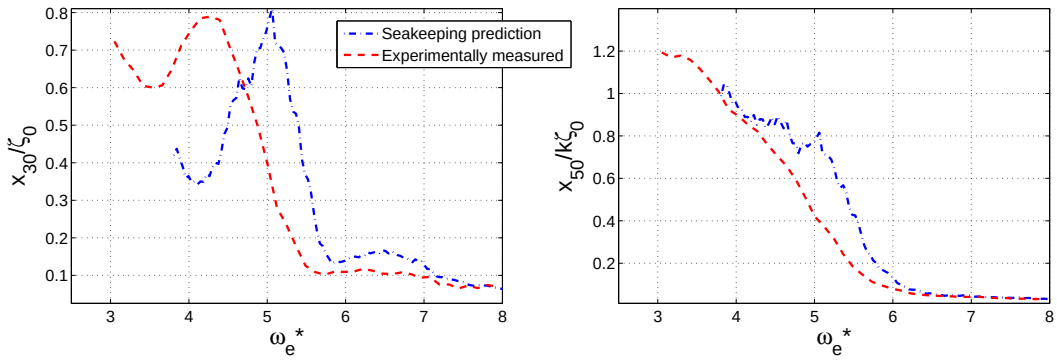

Figure 4.8: Comparison between experimental and predicted heave and pitch RAOs (Condition 81, JONSWAP, $H_{1/3} = 1.12$m, $T_0 = 8$s, $U = 20$kts (25mm, 1.2s, 1.53m/s model scale)).

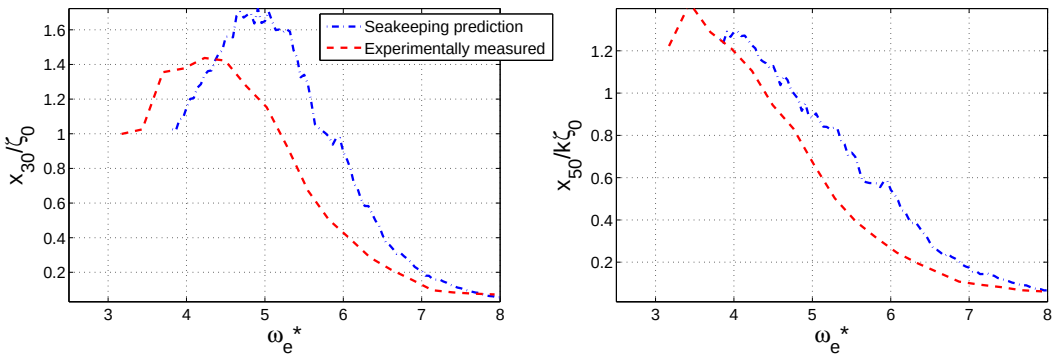

Figure 4.9: Comparison between experimental and predicted heave and pitch RAOs (Condition 82, JONSWAP, $H_{1/3} = 1.12$m, $T_0 = 8$s, $U = 38$kts (25mm, 1.2s, 2.98m/s model scale)).

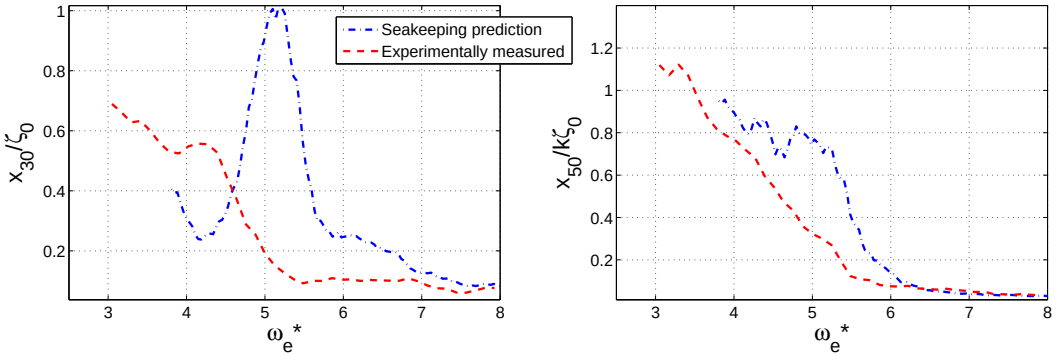

Figure 4.10: Comparison between experimental and predicted heave and pitch RAOs (Condition 83, JONSWAP, $H_{1/3} = 2.24$m, $T_0 = 8$s, $U = 20$kts (50mm, 1.2s, 1.53m/s model scale)).

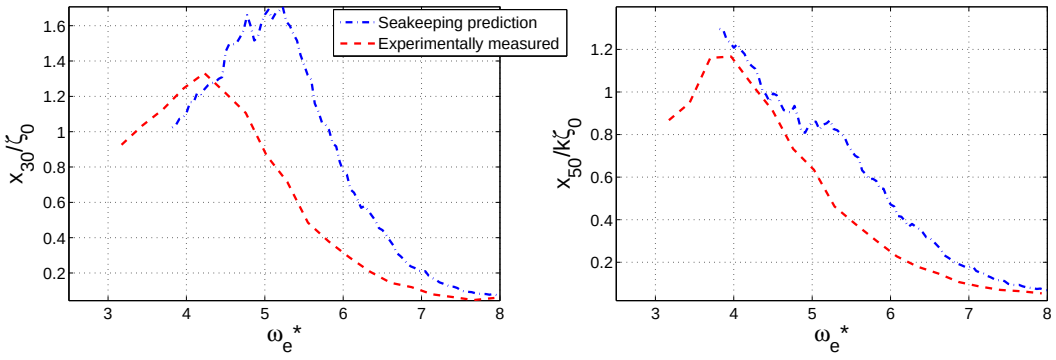

Figure 4.11: Comparison between experimental and predicted heave and pitch RAOs (Condition 84, JONSWAP, $H_{1/3} = 2.24$m, $T_0 = 8$s, $U = 38$kts (50mm, 1.2s, 2.89m/s model scale)).

4.7 Conclusions

A description of the high Froude number time-domain strip theory was provided in Section 4.2, followed by an extension of this code to predict motions and loads in irregular seas by applying the principle of linear superposition. A method to represent idealised sea spectra as a series of regular waves was developed and successfully implemented as a pre-processing unit for the irregular wave version of the seakeeping code and is shown in Section 4.3.2. Several program tests were used to verify the operation of the code before validating the code by comparing predicted vessel motions with scale model test results. Encountered wave spectra and heave and pitch RAOs were determined from a Fourier analysis of Test Set 3 results. Comparisons between the numerical sea spectra and the spectra measured experimentally in the towing tank during Test Set 3 were made to ensure that an appropriate comparison can be made between the predicted and experimentally measured ship motions. Experimentally measured RAOs and predicted RAOs from the seakeeping code are compared to validate the seakeeping simulation.

Motions of the 2.5m hydroelastic catamaran model were measured in relatively mild conditions during experimental Test Set 1 and the same conditions were emulated in the time domain seakeeping code in order to validate the prediction method. Fourier analyses were used to estimate spectral densities of vessel motions and wave elevations and slopes for the purpose of creating RAOs from the irregular motions data. Although the behaviour of the seakeeping code captured nonlinear trends identified in the model test results, an offset in the predicted peak motion frequency was observed, this issue is further discussed Appendix B.

Chapter 5

Slam Event Characteristics

5.1 Introduction

The results from Test Set 2 (the slam conditions, introduced in Chapter 3), are presented in this chapter. Firstly slam events are identified in the recorded data, then important slamming parameters are identified and obtained for each identified event. The general analysis procedure is demonstrated by considering one sample run, which is then repeated for every run and then distributions of slam events resulting from the analysis of the entire data set (2,103 slam events) are shown. These slam characteristic distributions are further developed for implementation in the time-domain code in Chapter 6.

Previous scale model slamming investigations undertaken by this project team have taken a regular wave deterministic approach. The deterministic approach is usually unavoidable when testing in regular waves but it is an inherently unrealistic situation where every slam event in a given condition is similar to the one that precedes it. In previous regular wave investigations (such as Lavroff [45]), 'typical' (one value, be it mean, median or maximum) slam kinematics were presented for each condition. If the opposite (probabilistic) approach was taken, each slam event, no matter how similar it was to the preceding one, would be preserved and the slam kinematic distribution would be presented in place of the typical kinematic. The typical (average, or more robust median) kinematics could still be obtained from the kinematic distribution. This is the approach taken during this work, since the project involves irregular sea conditions it cannot be avoided in one respect, however it is considered better practice to present slam parameter distributions as well as the typical statistic.

5.2 Slam Identification

In previous experiments, slams have been identified by defining two slam event criteria, namely a threshold and rate of change of load. In the investigation presented by Thomas et al. [65], a slam was said to have occurred if the peak load was greater than 10 N (model scale) and the

rate of change exceeded the threshold criterion of 5,000 N/s (model scale). Another method, implemented by Amin [1] and Matsubara [53] with the goal of slam identification involved conducting a form of Fourier transform on the time-domain strain gauge data, known as wavelet analysis. When the required parameters are properly selected, wavelet analysis promises to be a powerful tool to identify both slam events and the subsequent whipping behaviour. However, in this study a more convenient technique to identify slam events was found by using the pressure transducer data. The pressure data clearly showed the presence of a peak value when the water surface impacted with the underside of the hull in the archway. This meant that a slam criterion was not necessary, instead only a peak detection method was required to identify peak pressures and thus slam events. This process was semi-automated: once the data was scanned though and the majority of events identified, the data was then manually examined to ensure all events were identified and to remove any non-slams that had been erroneously selected. It did mean that all impacts of the water surface with hull were identified as slam events as no threshold limit on the magnitude of the slam load was used. A total of 2,103 slam events were identified in the 22 test conditions. The pressure transducer closest to the centre bow truncation was used as the reference location.

Figure 5.1 shows time traces of the surface pressure and centre bow load data from a typical test run. Slams can be identified from the pressure trace or the centre bow load. An upwards load on the centre bow is defined as negative on the centre bow load trace. Slam events can be seen from the centre bow load trace by a sudden change in load followed by an oscillatory whipping response; however they are more easily identifiable from the centre bow surface pressure trace by the distinctive and sudden spikes in pressure. Circles are used to highlight the identified slams when the measured surface pressure is at a maximum, and they are also reproduced on the centre bow load trace below. It is interesting to note that the pressure peaks all occur just prior to the maximum measured slam load. The pressure peak at 17.5s is deliberately not identified as a slam event as it occurs at the very end of the run.

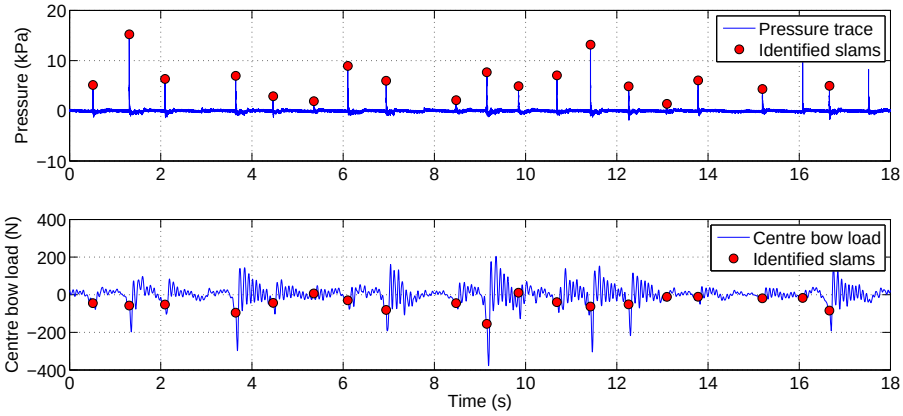

Figure 5.1: Pressure and centre bow load trace with identified slams highlighted with circles (negative load is up on the centre bow). Condition 97, Run 137 $T_0 = 1.5$s, $H_{1/3} = 78.1$mm, $U = 2.15$m/s.

5.3 Slam Load

From a design perspective, it is important to consider the maximum load the vessel structure will likely be exposed to. However, the aim of this analysis was to isolate the slam load from the global wave loads. The resulting slam load component can then be used in a regression analysis for development of the slam module (see Chapter 6) or even applied to a dynamic finite element model in future analysis.

The measured load is considered to consist of three separate load components: inertial, global wave and slam loads. A diagram showing the different load components can be seen in Figure 5.2. Since the time-domain code is currently able to predict the inertial and global wave components, these components must be removed from the experimentally measured loads to isolate the slam force. Slam forces are induced by water impact on the centre bow archway and wetdeck, low frequency global forces are due to the immersion of the centre bow (a cyclic load that coincides with the encountered wave frequency) and the inertial force is proportional to the acceleration of the centre bow segment.

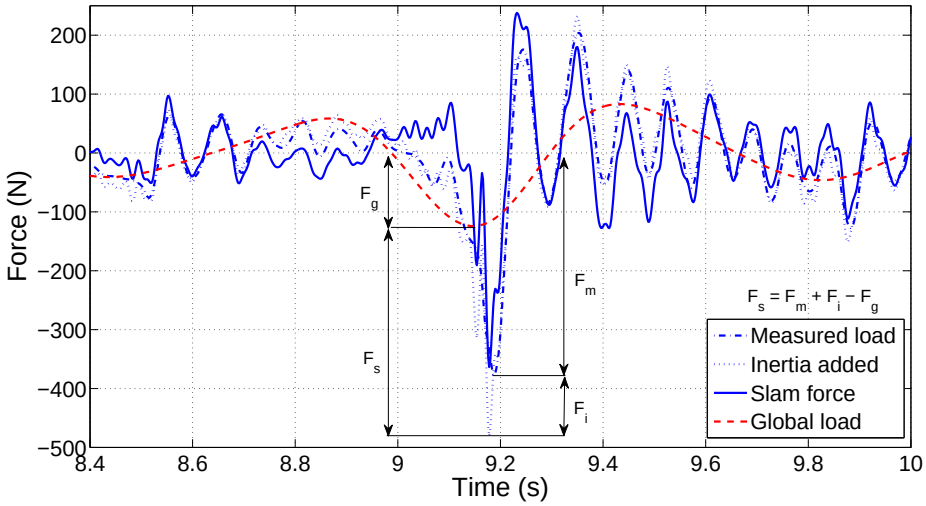

Figure 5.2: Measured centre bow load decomposed into force components: slam force, low frequency global load and inertial force. Structural vibrations, or whipping, of the model can be seen after the slam at 9.2s.

5.3.1 Inertial Loads

A brief investigation into the inertia of the centre bow during slamming was conducted by Lavroff [45]. The Lavroff experiments (and the experiments presented in this thesis) were carried out with no instruments to measure bow accelerations directly. Therefore he neglected inertial loads during his analysis, assuming they were small enough to be ignored. However the inertial load magnitude was quantified by examining results from tests conducted by Amin [1] on the same model. An Endevco accelerometer was installed on the forward transverse beam during investigations on the effect of hull stiffness on pressure measurements. Incidentally it

was concluded that the stiffness of the segmentation links had little effect on measured centre bow pressures and accelerations, however the whipping behaviour and thus the hydroelasticity of the model was more strongly influenced by the link stiffness. Lavroff used the accelerometer measurements from these tests and estimated that inertial forces during slamming could be as much as 17% of the measured peak slam load; a significant proportion of the total load [45].

Since no channels were allocated for acceleration measurements during Test Set 2, the acceleration of the bow was estimated by assuming the boat is a rigid body and differentiating the vertical displacement at the centre bow truncation with respect to time twice. To test the suitability of this method, the Amin test set was revisited once again. Bow accelerations were calculated from the LVDT signals and compared with those measured from the accelerometer, shown in Figure 5.3. The accelerations derived from the global motions of the boat are seen to correlate well with the accelerations measured by the accelerometer (correlation coefficient, $r = 0.8536$, at the 95% confidence interval), thus providing confidence in using the LVDT signal to determine the acceleration on the centre bow. The relatively large amplitude oscillations found in the LVDT trace could be attributed to noise in the signal, vibrations in the tow posts recorded by the LVDTs or the motions of the wetdeck segment of the model.

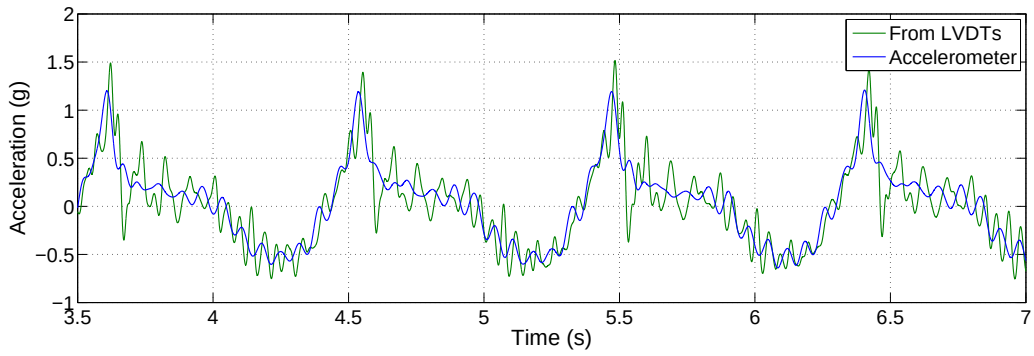

Figure 5.3: Comparison between accelerations measured from accelerometer and those derived from LVDT signals (accelerometer data from [1], Run 22, regular 120mm wave height, 0.65Hz wave frequency, vessel speed 1.53m/s ($\omega_e^* = 3.27$))

The inertial load can be calculated simply from Newton's Second Law of Motion, $F = ma$, where the mass m relates to the mass of the centre bow segment and all other associated material on the centre bow (the transverse beams, aluminium nuts and bolts, pressure transducers, cable masses etc.) and the acceleration a is the acceleration of the centre of mass of the said body. A least-squares correlation between the measured loads and the derived accelerations was employed to determine the inertial load. Accelerations were calculated at the centre bow truncation and the loads were determined from the calibrated strain gauges. Although there was variation from run to run, the unknown parameter (comparable to the mass in Newton's Second Law of Motion) determined from the regression analysis was always within the vicinity of the estimated mass of the centre bow ($\pm 0.5kg$). This gave confidence in the correlation

method for determining inertial loads. Figure 5.4(a) illustrates the proportion of acceleration loads compared with measured loads. The resulting total load is shown in Figure 5.4(b).

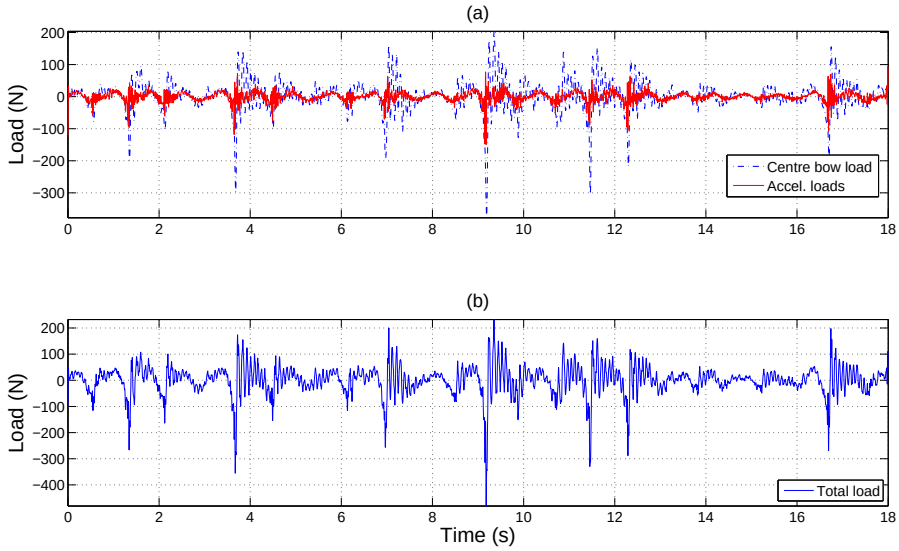

Figure 5.4: (a) A comparison between the measured vertical load on the centre bow and the acceleration load. (b) The resulting load once the acceleration loads has been included. Condition 97, Run 137 $T_0 = 1.5$s, $H_{1/3} = 78.1$mm, $U = 2.15$m/s.

Figure 5.5(a) shows the absolute displacement (with reference to calm water) for the same test run as shown in Figure 5.1. Figures 5.5(b) and (c) show the velocity and accelerations derived from the displacements. Again, identified slam events are displayed as circles on these plots. Slams are seen to occur when the centre bow truncation vertical displacement is at a minimum and when accelerations are at a maximum.

5.3.2 Low-Frequency Global Load

Low frequency global loads measured by the centre bow segment strain gauges are induced by the centre bow entering and leaving the water and so are considered to have similar loading frequencies as the encountered wave frequency. Although these tests were conducted in irregular waves, the dominant encountered wave frequency can be estimated by considering the modal period of the spectrum. The wave celerity, c, is defined by (assuming deep water):

$$c = \frac{T_0 g}{2\pi}, \tag{5.1}$$

where T_0 is the period of the wave (modal period in this case). By knowing the speed of the model, U, the encountered wave frequency can be estimated by applying a Doppler shift:

$$f_e = \frac{U + c}{cT_0}. \tag{5.2}$$

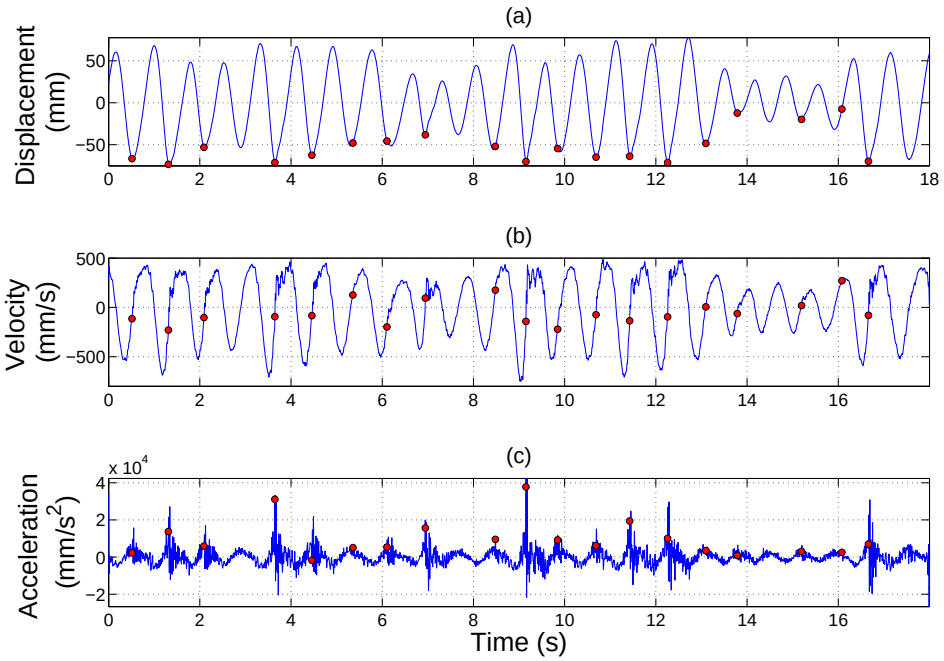

Figure 5.5: Centre bow truncation vertical displacement (a), vertical velocity (b) and vertical acceleration (c) calculated from the LVDTs. Identified slam events are highlighted with circles. Condition 97, Run 137 $T_0 = 1.5$s, $H_{1/3} = 78.1$mm, $U = 2.15$m/s.

A Butterworth low-pass filter was used to isolate the wave components associated with global wave loading. These loads could then be subtracted from the total centre bow load to provide the slam load alone. An investigation into the sensitivity of the cut-off frequency on the resulting slam load was undertaken to determine the appropriate cut-off frequency. The cut-off frequency is defined as the frequency where half the signal power is attenuated (-3dB). Since a series of sea conditions with varying modal periods and vessel speeds and thus encounter frequencies was tested, the cut-off frequency was defined as a multiple of the encountered modal frequency for a given condition.

Figure 5.6 shows the root mean square (rms) difference between the filtered and unfiltered centre bow load signal for a series of different test conditions and cut-off frequencies (f_c). As the cut-off frequency increases, naturally the residual (the difference between the filtered and unfiltered signals) decreases, however a plateau can be seen in all shown conditions, starting approximately when the cut-off frequency is twice that of the estimated encountered frequency. This observation is further supported in Figure 5.7, where the slam load is normalised by calculating the average slam load in the filtered data for a particular run and dividing it by the average unfiltered slam load. As the cut-off frequency is increased, the filtered signal approaches the unfiltered signal and thus the averaged slam load ratio is expected to approach 1.0. All examined runs exhibited the same trend when n is less than two. When the cut-off frequency is $2fe$, the average global load can be expected to be about 30 to 40% of the total load when

a slam occurs.

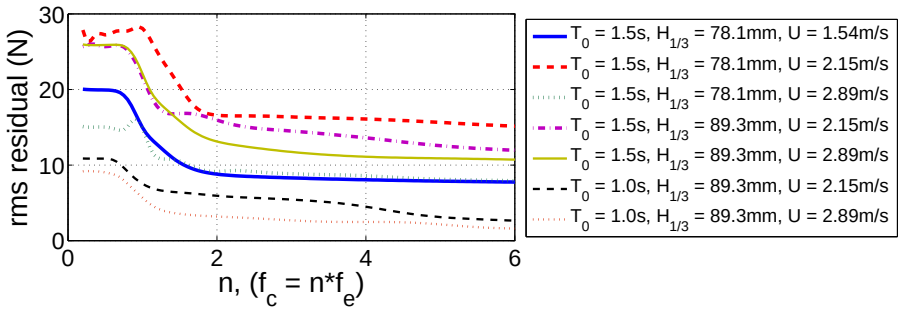

Figure 5.6: Root mean square residual of a low-pass Butterworth filter with the cut-off frequency expressed as a function of encountered wave frequency.

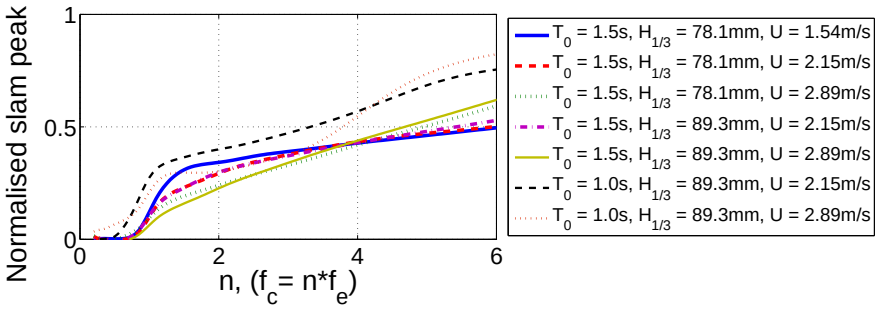

Figure 5.7: Normalised slam peak (mean filtered slam peak / mean unfiltered slam peak) against cut-off frequency as a function of encountered wave frequency (low-pass Butterworth filter).

Data from an example test run is shown in Figure 5.8, where the global load is overlaid on the total vertical load on the centre bow in plot (a). Plot (b) shows the resulting load with the global load removed. It is important to note that the resulting slam load time trace also contains the dynamic structural response of the model (whipping) after a slam has occurred. These fluctuations are at a similar frequency to the slam load frequency, but since the maximum load when a slam occurs is of primary interest, the whipping behaviour was kept in the signal with the acknowledgement that whipping behaviour could be the focus of a future investigation.

5.4 Slam Characteristics

Based on previous investigations into slamming behaviour in irregular waves [65], several key parameters were identified during the planning stage of the experiments for further examination. In particular the importance of bow immersion, the vertical velocity of the bow relative to the vertical velocity of the wave, the wave peak slam force and location are investigated.

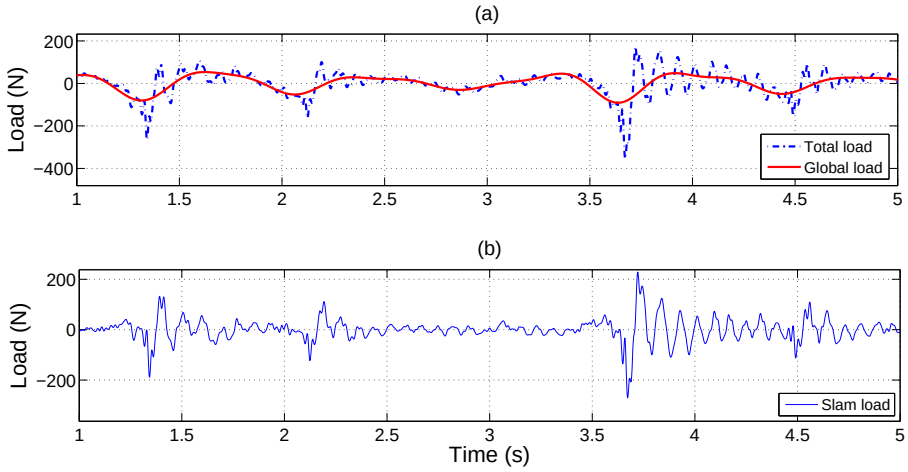

Figure 5.8: (a), A comparison between the total vertical load on the centre bow and the low-frequency global load. (b), The resulting slam load (plus structural response) once the global load has been removed. Condition 97, Run 137: T0 = 1.5s, H1/3 = 78.1mm, U = 2.15m/s.

5.4.1 Slam Magnitudes

The largest recorded slam was 388.6 N (model scale), equivalent to 132% of the displacement of the model. The largest slam reported in previous scale model tests in irregular seas was 70% of the model displacement [65], that data set analysed two conditions and identified 284 slam events. Of the 2,103 slam events identified in the present investigation, fourteen (0.67%) had a magnitude exceeding the total displacement of the model. Severe slam magnitudes of the order of the total vessel displacement are not surprising; full scale strain measurements of a 96m Incat catamaran were used in conjunction with a finite element model estimated a severe slam to be 93% of the vessel displacement [66].

Figures 5.9 to 5.11 show the distribution of slam loads when the data is grouped by Froude number, significant wave height and model period respectively. The left hand figures are box-and-whisker plots (also known as box plots) that represent the probability density functions (pdf)[1] of the parameters shown on the x-axis and the right side contains the corresponding cumulative distribution function (cdf). The area under the probability density function is unity, the cdf plot shows the 'area so far' under the pdf if it is integrated successively from left to right. Probabilities can be quickly estimated from the cdf plot, as they are represented by the height of the cdf curve, as opposed to the area under the pdf.

The box plot is a useful tool to compare distributions as it lays them side by side, as opposed to viewing the pdf as a histogram or frequency polygon. The interquartile range (IQR) is shown by the 'box', this is the difference between Q_3 (the upper quartile, or the 75^{th} percentile) and Q_1 (lower quartile, or the 25^{th} percentile), hence 50% of the measurements fall within the box. The middle line, dividing the box in two, is the median value of the data set. Therefore visual

[1]The probability density function plots of these parameters have been included in Figures C.1 to C.3 in Appendix C on page 198.

comparisons of the median, IQR, outliers or even skewness of the distributions can be made directly by investigating box plots. *Whiskers* (the dashed lines) extend above and below the boxes to enclose the lowest and highest datum within 1.5 of the interquartile range (i.e. the 'height' of the box). Data outside of this range can be considered as outliers.

The model scale slam load appears to be independent of Froude number, as seen in Figure 5.9. The distributions for all three Froude numbers are quite spread, with numerous outliers. The cdf also show little deviation between the slam load distributions. Figure 5.10 on the other hand, displays a clear trend between significant wave height and slam load. This is not surprising as it has been previously observed in regular wave tests [45, 53]. Although exceptionally large and small slams are present, there is a general increase in the median slam magnitude when significant wave height is increased. The IQR also becomes larger with significant wave height, suggesting that the variance of the distribution is also a function of $H_{1/3}$. The cdf clearly demonstrates the increase in slam load severity with significant wave height as well.

With reference to Figure 5.11, the conditions with a modal period of 1.0s (model scale) appears to be much less severe than the other two model periods tested; the median slam magnitude of the 1.0s period condition lies around the 25 percentile of the other two conditions. The 1.3s and 1.5s modal period conditions are quite similar in distribution except that the 1.5s modal period condition contains a significant number of outliers, this can be seen in the tail end of the cdf.

Figure 5.12 illustrates the distribution of slam severity for each approximate dimensionless wave encounter frequency. The encountered wave frequency was estimated using the same method described in the section 5.3.2; the wave celerity was estimated by Equation 5.1 and then the encountered frequency was given by Equation 5.2. This was then made non-dimensional by converting it to angular frequency and then multiplying by the square root of L/g, where $L = 2.5$m and $g = 9.81m/s^2$ as shown in Equation 5.3. Table 5.1 summarises the test conditions and the corresponding calculated dimensionless encountered wave frequencies for convenience when observing Figure 5.12. The amount of recorded slam events in each condition are also shown in Table 5.1, the sample size of each group varies from condition to condition but generally contains more than 80 slam events.

$$\omega_e^* = 2\pi f_e \sqrt{\frac{L}{g}} \tag{5.3}$$

Figure 5.12 (a) shows the slam magnitude distribution for 78.1mm significant wave height (3.5m full scale) and (b) slam distribution for $H_{1/3} = 89.3$mm (4m full scale). Immediately clear from these plots are the increase in median slam magnitude around the modal frequency of the model, where vessel motions are greatest. Also apparent is that the median slam magnitudes for the 4.0m sea conditions are larger than the corresponding 3.5m conditions. The IQR is also larger in Figure 5.12 (b), suggesting that the slam load magnitudes are more spread than the smaller wave condition. Even though the slams tend to be more severe in plot (b), the largest

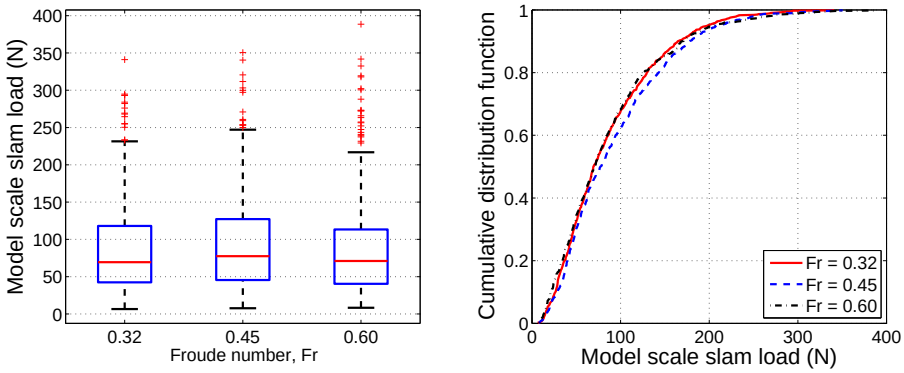

Figure 5.9: Distributions of slam load magnitude for differing Froude number.

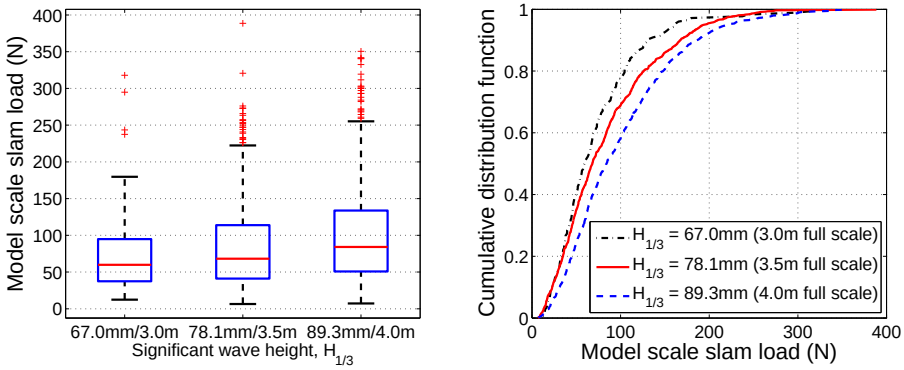

Figure 5.10: Distributions of slam load magnitude for differing significant wave height.

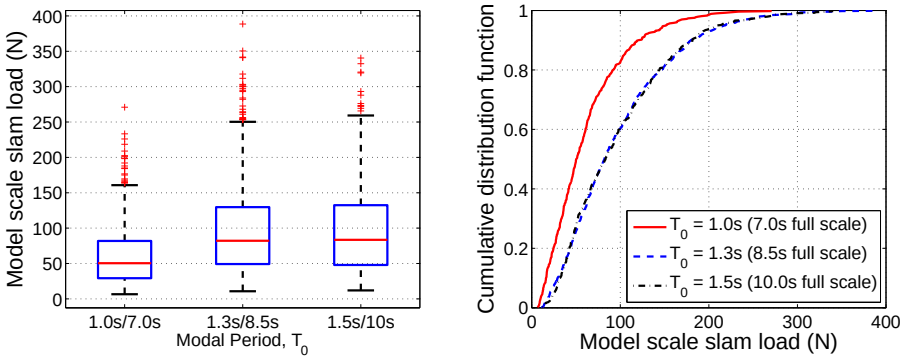

Figure 5.11: Distributions of slam load magnitude for differing modal period.

Table 5.1: Test conditions, the corresponding dimensionless encounter frequency (ω_e^*) and the number of slams per condition.

Model Scale		Full Scale			# Slams ($H_{1/3}$)	
T_0 (s)	U (m/s)	T_0 (s)	U (kts)	ω_e*	3.5m	4.0m
1.5	1.54	10.0	20	3.50	83	82
1.5	2.15	10.0	28	4.06	110	100
1.3	1.54	8.5	20	4.28	131	171
1.5	2.92	10.0	38	4.72	90	66
1.3	2.15	8.5	28	5.02	132	137
1.3	2.92	8.5	38	5.91	98	86
1.0	1.54	7.0	20	6.28	97	83
1.0	2.15	7.0	28	7.54	101	106
1.0	2.92	7.0	38	9.04	83	58

individual slam (4 times the median) was recorded in the 3.5m condition, $\omega_e^* = 5.91$ ($T_0 = 8.5$s, $U = 38$kts). This observation highlights the importance of taking a statistical approach when investigating slamming, especially in irregular conditions. A *typical* slam magnitude could be defined as the median (the median statistic is a better choice opposed to the mean, as the median is robust to outliers). However extreme events need to be also considered as extreme slams up to four times the median have been measured (for example $\omega_e^* = 7.54$ and 9.04 for both significant wave heights).

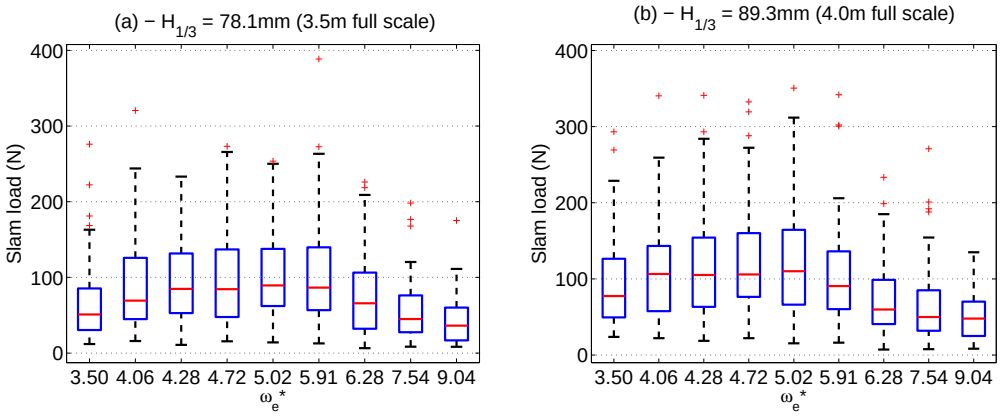

Figure 5.12: Box plots describing the distributions of slam load against dimensionless encounter frequency. (a) $H_{1/3} = 78.1$mm (3.5m full scale). (b) $H_{1/3} = 89.3$mm (4.0m full scale).

5.4.2 Relative Vertical Velocity

Since the maximum relative vertical velocity does not coincide with the maximum surface pressure when a slam occurs, two relative vertical velocities were considered during this investigation: the maximum relative vertical velocity prior to the slam (this is the standard approach), and the instantaneous relative velocity at the time when the maximum centre bow pressure was

recorded. Figure 5.13 shows the relative immersion and vertical velocity for a sample run. Also included in this figure is the immersion and velocity when the maximum pressure was recorded (denoted by squares), local maxima are identified by circles.

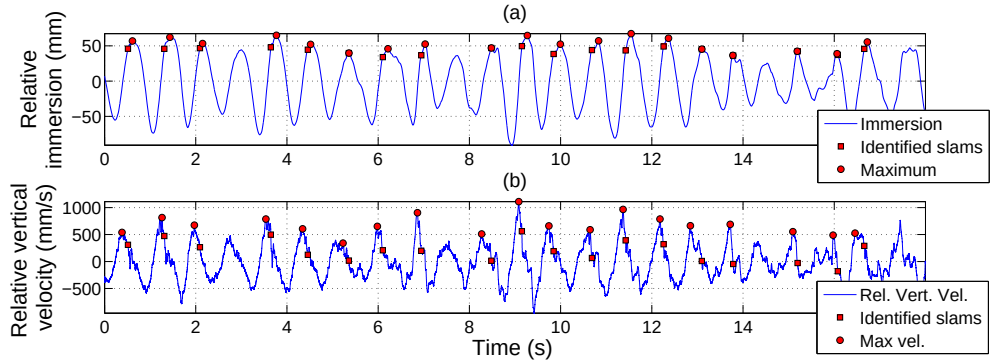

Figure 5.13: (a) Relative immersion of the catamaran model at the CBT. (b) Relative vertical velocity at the CBT. Identified slam events are highlighted with squares, and local maxima are highlighted circles. Condition 97, Run 137: $T_0 = 1.5$s, $H_{1/3} = 78.1$mm, $U = 2.15$m/s.

Scatter plots comparing the slam load distribution for these two relative vertical velocities can be seen in Figures 5.14 and 5.15. The relative vertical velocities prior to slam are shown in Figure 5.14 on the x-axis and the relative velocity at the slam event time are plotted in Figure 5.15. Data is grouped by Froude number. Whilst there is a weak relation between the peak relative vertical velocity and slam load, there appears to be a clearer trend between the instantaneous velocity and slam load. This observation is supported by a correlation coefficient, r, of 0.58 for relative velocity at the recorded slam instant compared to a correlation coefficient of 0.45 for the maximum relative velocity prior to the slam event. This implies that the relative vertical velocity at the time of impact is a somewhat better indicator of slam magnitude than the peak relative vertical velocity prior to the slam. The relation between relative vertical velocity at impact and the maximum prior to impact was investigated, but no correlation was identified ($r = 0.19$), however it is noted that the velocity at the time peak pressures are measured could be sensitive to the physical location of the pressure transducer. If the transducer is mounted away from the actual slam location, then there will be a delay between the time when the slam event occurs and when the pressure transducer records a pressure spike. That being said, the seemingly better correlation between relative vertical velocity when the pressure peak is measured and slam load may simply be coincidental.

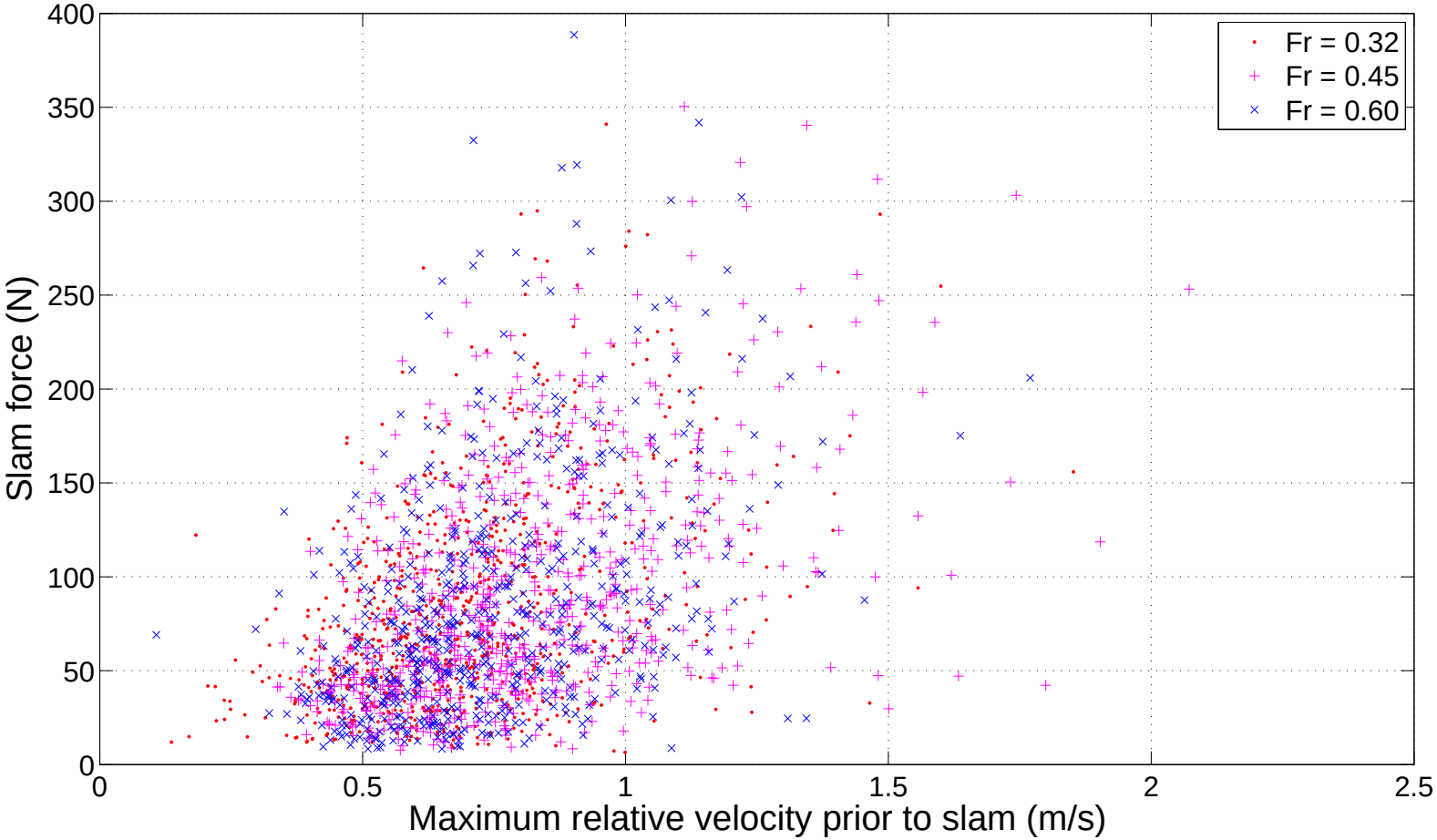

Figure 5.14: Maximum relative velocity prior to slam event against slam load. Data grouped by Froude number.

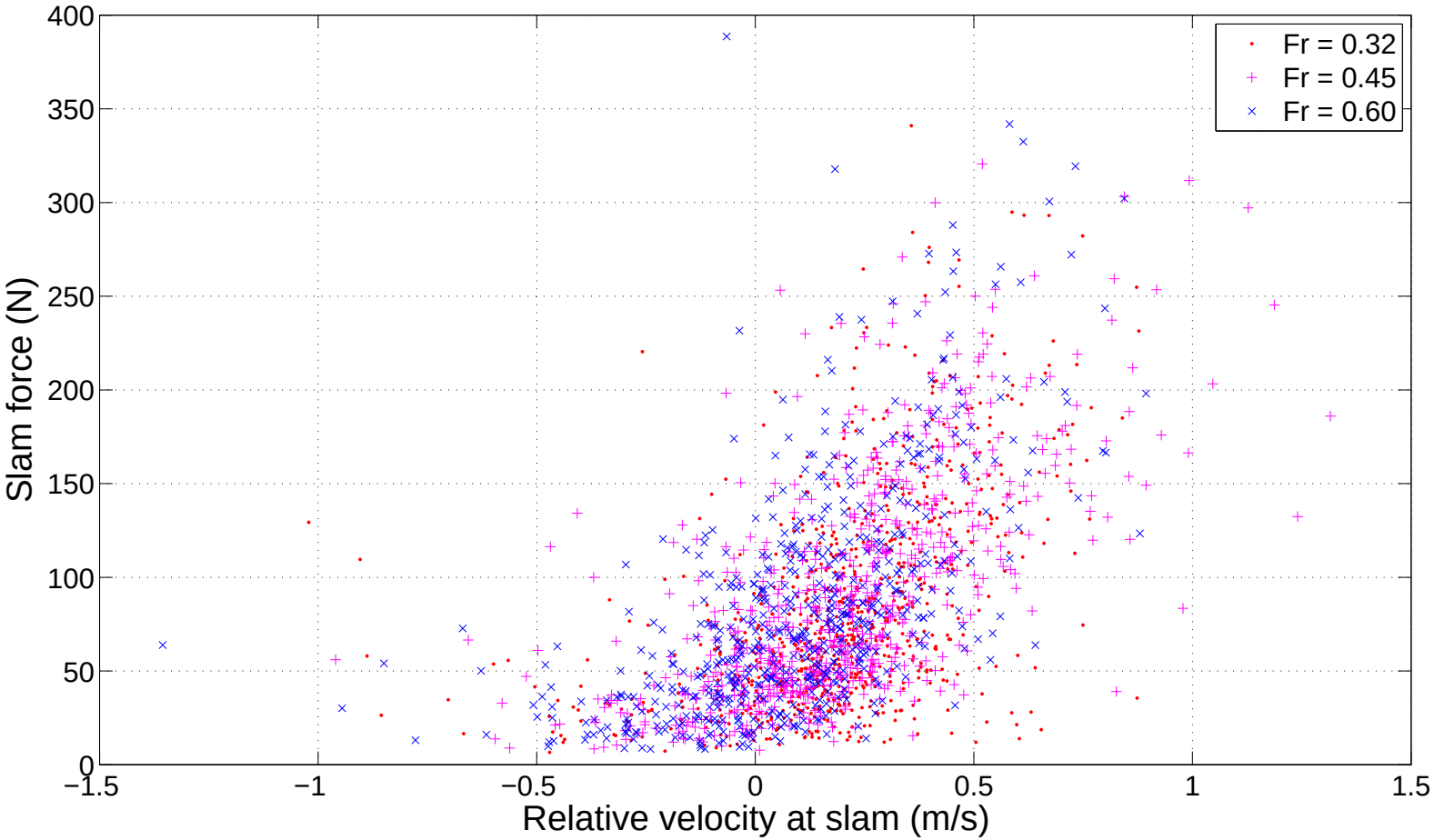

Figure 5.15: Relative velocity when slam occurred against slam load. Data grouped by Froude number.

It is apparent from these plots that for a particular relative vertical velocity (either the maximum prior or the velocity at the recorded event), there are a range of possible slam force magnitudes. Previous investigations have already observed a weak association between velocity and slam load, for a given relative velocity a large range of possible slam loads could result [27, 65]. Therefore the slam load cannot be determined by relative vertical velocity alone - other parameters may be involved. It is quite possible that there is some random variation in the resulting slam load from seemingly identical conditions; however, one aim of this investigation is to attempt to identify the important parameters and thus reduce the spread of the slam load distribution, ultimately making the slam load as predictable as possible.

Figures 5.16 to 5.19 sort the relative vertical velocity data by different parameters: modal period and significant wave height respectively. Figures 5.16 and 5.17 are particularly interesting as they reveal a trend between modal period, relative vertical velocity and slam load. For a given maximum velocity prior to the slam, the shorter 1.0s (7.0s full scale) modal period waves result in a lower slam load than the longer waves, this has been previously observed in Figure 5.11. Figure 5.17 displays a clear distinction between the 1.0s and 1.5s (10.0s full scale) modal period conditions. Many of the slams that were recorded during the $T_0 = 1.0$s conditions occurred when the relative velocity was negative, that is, the boat and wave were moving apart at the reference point (the CBT). However if the slam occurs at a location other than the CBT, the relative vertical velocity at the actual slam location would be positive. Therefore it is expected that the slam locations of the 1.0s conditions occur on a different part of the wave, or a different wave entirely, away from the centre bow truncation (this is best seen in Figure C.18 on page 203, where the 1.0s modal period conditions tend to occur aft of the CBT when compared with the other conditions). The relative velocity at the slam event is skewed to the right in the longer wave conditions, this means that the boat and wave surface are still moving together when a slam occurs. It is also apparent that the distribution of relative velocities at the slam time straddles zero; slams occur around the point where the relative motions of boat and water surface change directions, when accelerations are the greatest. If a slam occurs before this change takes place (the relative velocity is positive), the resulting slam load is greater.

The data is grouped by significant wave height in Figures 5.18 and 5.19. The slams recorded during the 67.mm/3.0m significant wave height conditions are included in these plots. These conditions were limited compared to the other wave heights tested (only two speeds and one modal period, compared with the nine conditions tested for the other wave heights), therefore their distribution is sparse. It is difficult to discern any noticeable differences in these distributions alone; the box plots produced in Appendix C and discussed below, provide more insight into centre bow velocity characteristics.

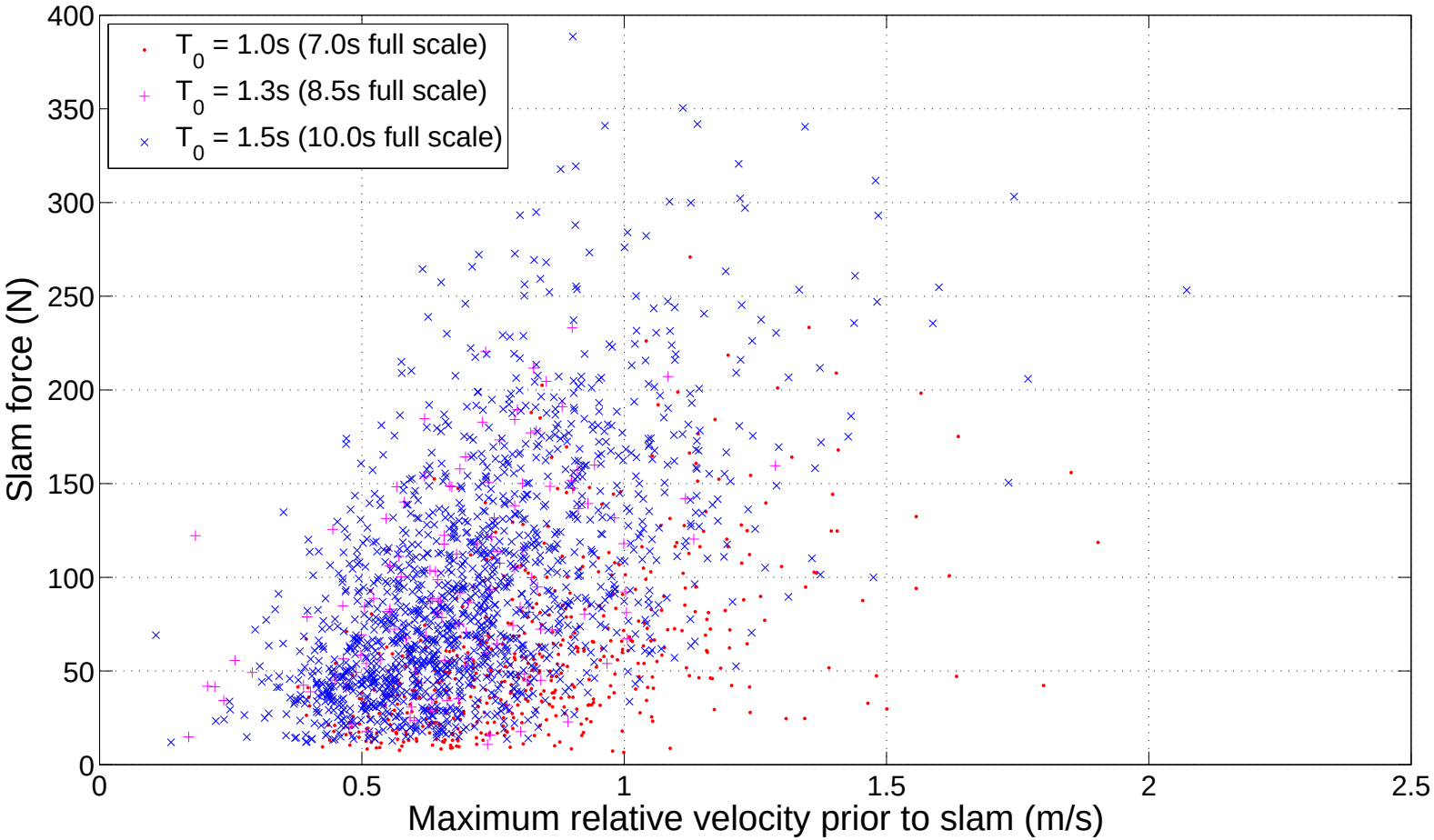

Figure 5.16: Maximum relative velocity prior to slam event against slam load. Data grouped by modal period.

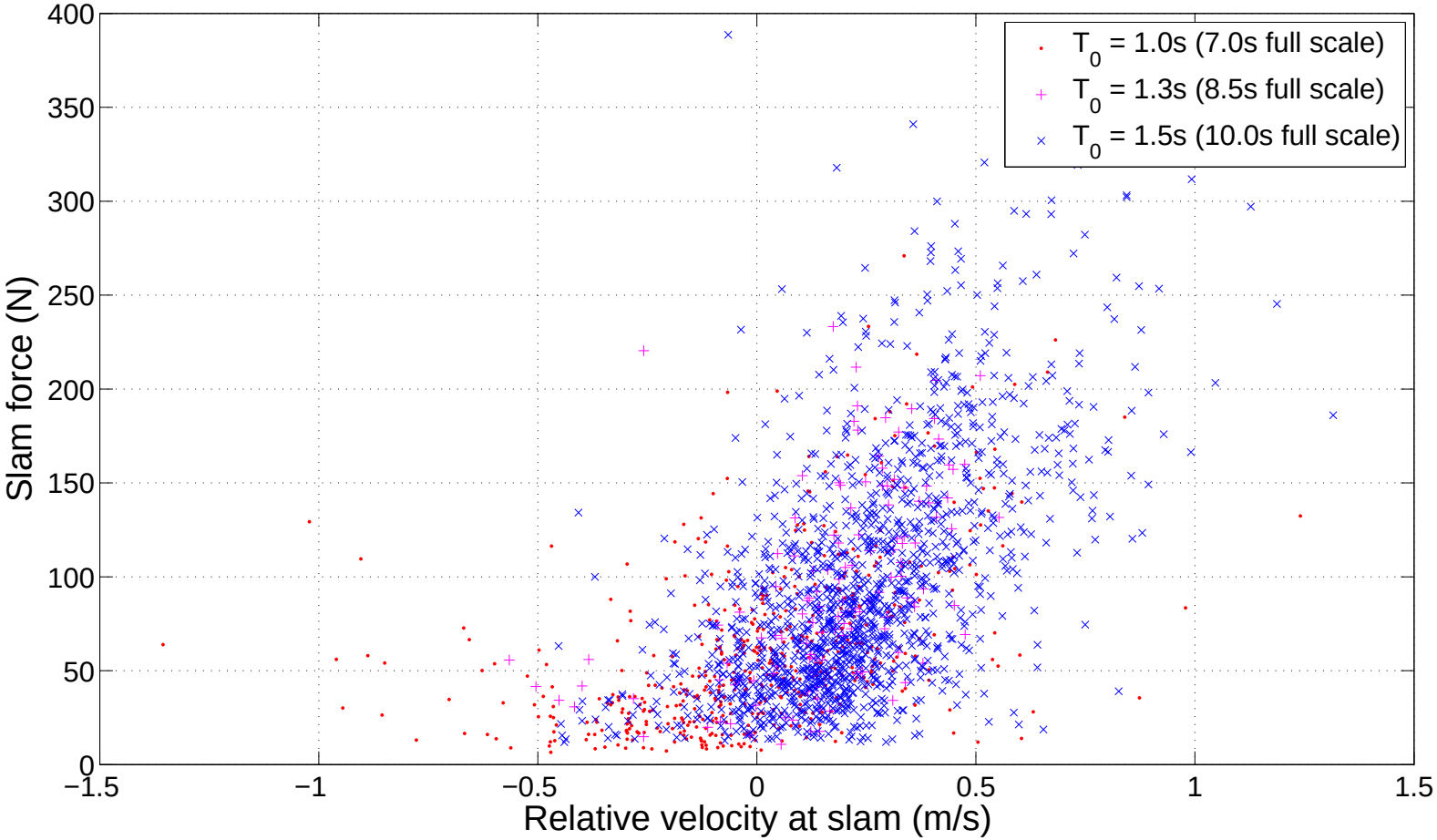

Figure 5.17: Relative velocity when slam occurred against slam load. Data grouped by modal period.

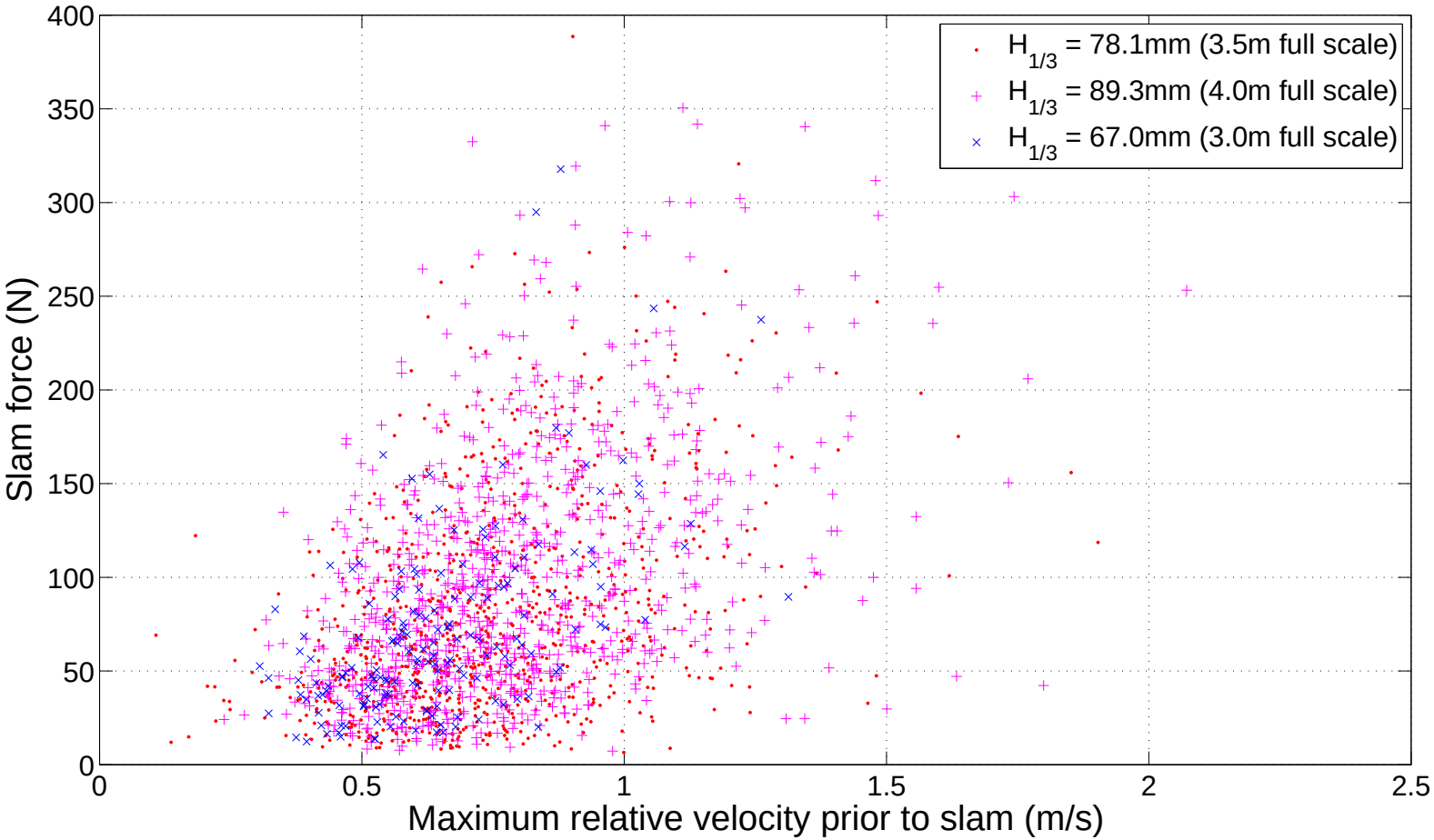

Figure 5.18: Maximum relative velocity prior to slam event against slam load. Data grouped by significant wave height.

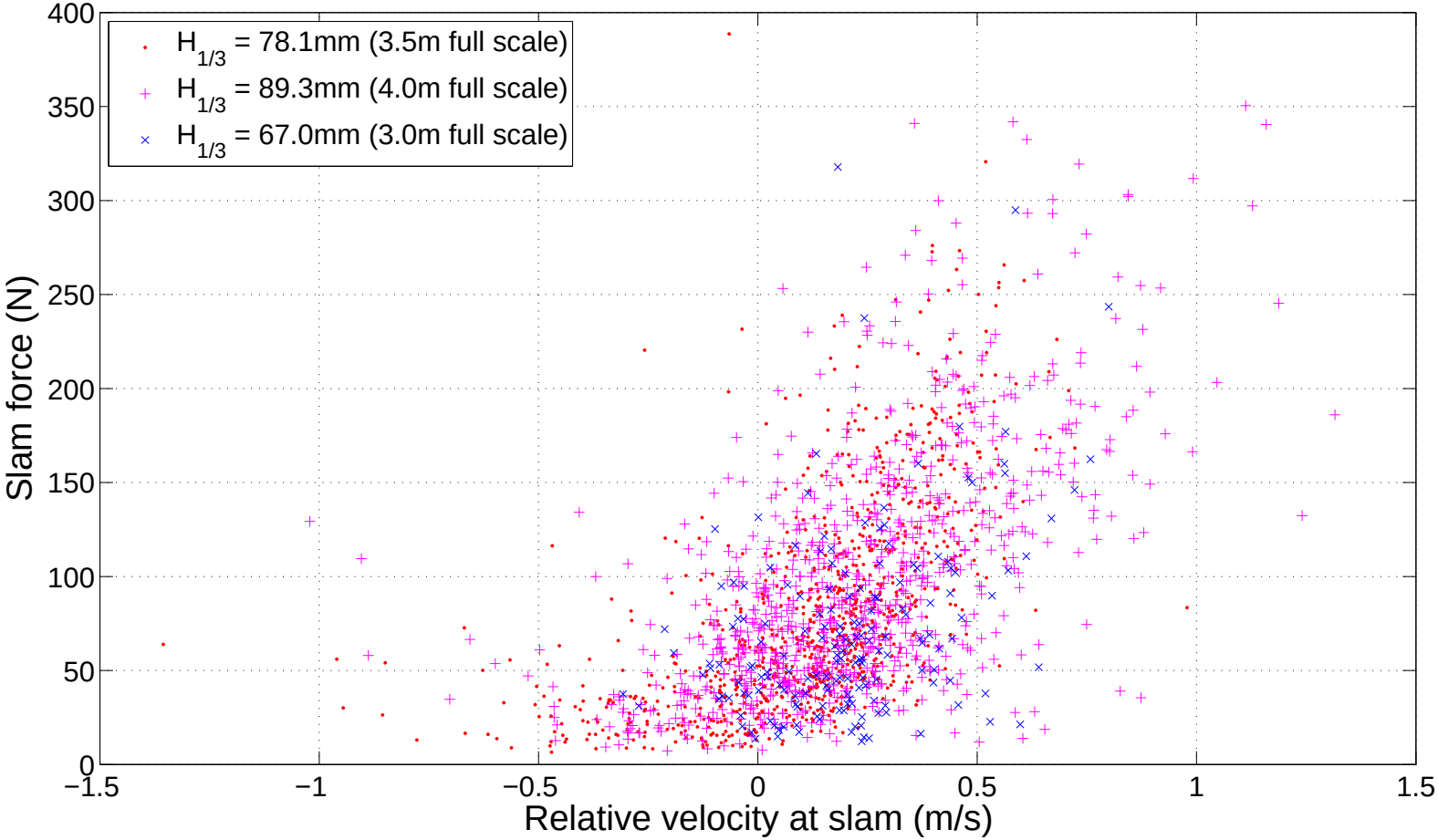

Figure 5.19: Relative velocity when slam occurred against slam load. Data grouped by significant wave height.

Figures C.4 to C.9 found in Appendix C (pages 199 and 200) show the distributions the maximum velocity prior to slam and the velocity at the slam instant for data grouped by Froude number, modal period and significant wave height in a similar fashion to the slam load distributions shown in the previous section (Figures 5.9 to 5.11). Figure C.4 illustrates that larger maximum velocities prior to slamming tend to occur at the medium vessel speed, and Figure C.6 suggests at shorter wave periods as well. The maximum vertical velocities are also likely to increase with significant wave height (Figure C.5). When the relative velocity at the slam event is considered, the variance of the distribution somewhat increases with Froude number and significant wave height (Figures C.7 and C.8). The relative vertical velocities at the pressure maximum are seen to straddle, but are not centred on 0m/s (when bow acceleration is thought to be the greatest). The median velocity at the slam instant tends to be greater than 0m/s. This can be clearly seen in Figure 5.20 where the data is grouped by dimensionless encountered wave frequency; the higher frequencies are more likely to result in negative relative vertical velocities at the slam time. The IQR for $\omega_e^* = 9.04, H_{1/3} = 78.1$mm/3.5m is almost entirely negative (greater than 50% of slams are negative). This observation supports the notion that slams tend to be located away from the CBT at higher vessel speeds. Figure 5.21 shows the distributions of maximum relative vertical velocity prior to the slam event. Maximum relative velocities tend to increase with ω_e^* and then plateau at the higher dimensionless encounter wave frequencies. Interestingly, at the very high encounter frequencies, where heave and pitch motions are small (see Section 4.6 for RAOs) and slam loads are relatively mild (see Figure 5.12), and the maximum relative vertical velocity prior to slamming distributions are similar to more severe motions and slamming conditions.

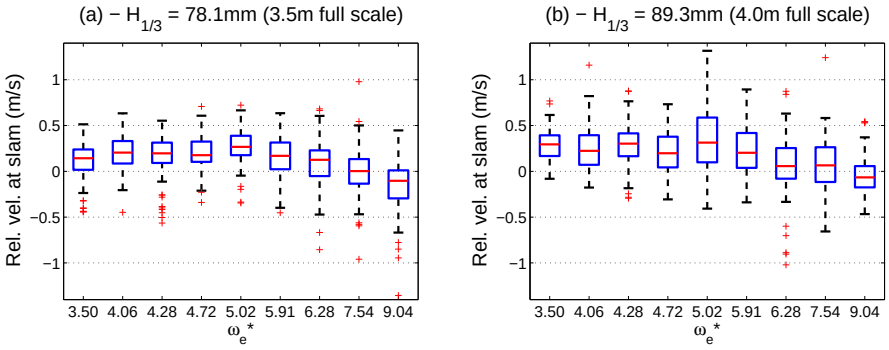

Figure 5.20: Box plots describing the distributions of relative vertical velocity at the maximum pressure instant against dimensionless encounter frequency. (a) $H_{1/3} = 78.1$mm (3.5m full scale). (b) $H_{1/3} = 89.3$mm (4.0m full scale).

5.4.3 Centre Bow Immersion and Archway Wave Elevations

Wave elevations under the archway were measured by three wave probes. A fourth probe was located on the centre line of the model, 120mm aft of the centre bow truncation. A time trace of the different wave elevations under the bow archway and the calculated centre bow immersion

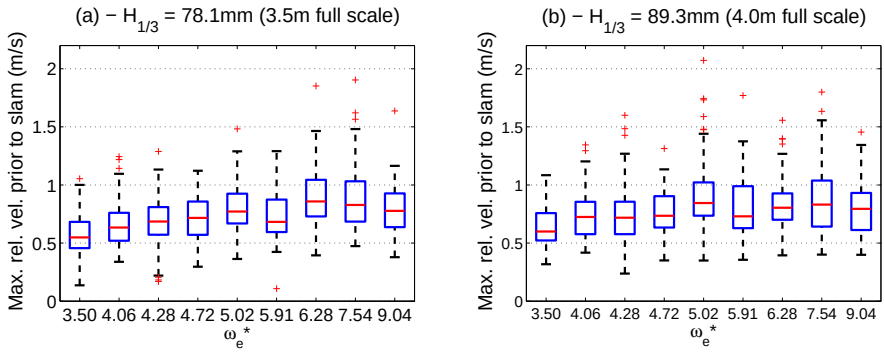

Figure 5.21: Box plots describing the distributions of maximum relative vertical velocity prior to slamming against dimensionless encounter frequency. (a) $H_{1/3} = 78.1$mm (3.5m full scale). (b) $H_{1/3} = 89.3$mm (4.0m full scale).

at the CBT is shown in Figure 5.22. Figure 5.22(a) shows relative immersion at the centre bow truncation (calculated by taking the difference between the displacement at the CBT and the wave elevation measured by a wave probe located in plane but transversely offset from the CBT). Slam events are shown by circles. Figure 5.22(b), (c) and (d) show wave elevations between the demihulls. The wave probes occasionally come completely out of the water; this is most evident by the flat bottoms in Figure 5.22(b) where the probes emerge on almost every wave. This probe is mounted the furthest forward on the bow, and thus it is the highest relative to the calm water line. Wave probe emergence has been captured in several still camera photos; Figure 5.23 shows one instance where wave probes 2 and 3 (120mm forward of the CBT and in plane with the CBT respectively) have completely emerged from the water.

Note in Figure 5.22 the measured wave elevations within the archway tunnel at the identified slam events. The maximum archway height (at the CBT) is shown in the plots with a solid line. The archway does not appear to be completely filled when a slam occurs, and the events always occur prior to the maximum recorded relative wave height. This could happen if the slam occurred at a different location from where the wave probes are mounted. Figure 5.22(c) is of particular interest, because this is the reference point for the '2D filling height'. The 2D filling height is defined as the height of a rectangle with a breadth equal to the two-dimensional area underneath the centre bow arch at the centre bow truncation [45], as shown in Figure 5.24. This parameter is based on the observation that slam events seemed to occur prior to the archway filling completely with water. It attempts to account for water displaced by the centre bow when the bow is immersed. For this model configuration, the 2D filling height is approximately 50mm from the calm water line at the CBT. For the condition shown in Figure 5.22(c), the majority of slam events occur when the recorded wave elevation is between 40-50mm, close to the 2D filling height parameter.

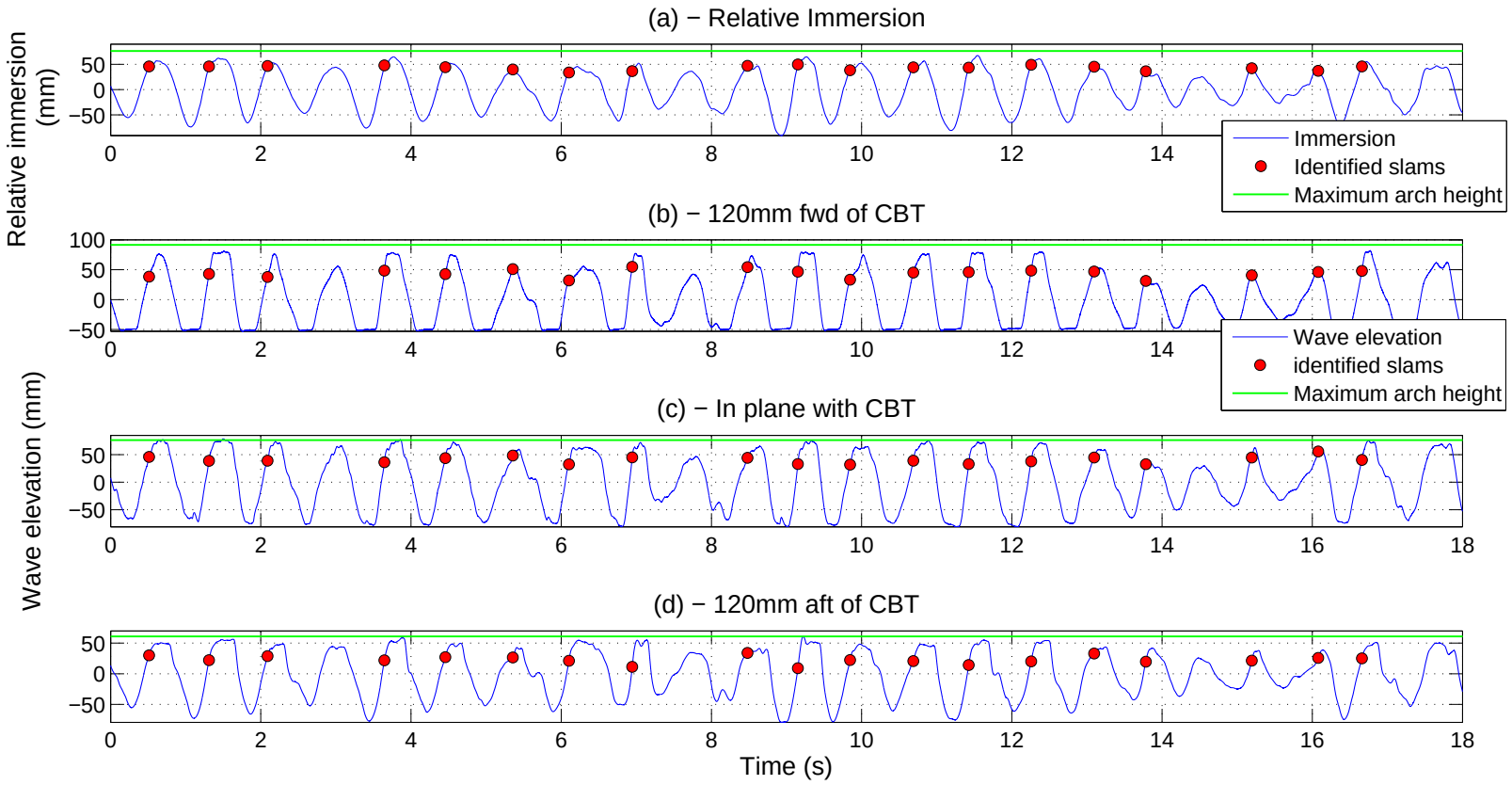

Figure 5.22: Wave elevations for one run. Identified slam events are shown with circles. (a) Relative immersion at the CBT. (b) Surface elevation 120mm forward of the CBT. (c) At the CBT. (d) 120mm aft of the CBT. Wave probes at (b), (c) and (d) are located in line with the maximum archway. Note the wave probes can be seen to come out of the water in (b) and (c), complete archway filling is also shown. Condition 97, Run 137 $T_0 = 1.5$s, $H_{1/3} = 78.1$mm, $U = 2.15$m/s.

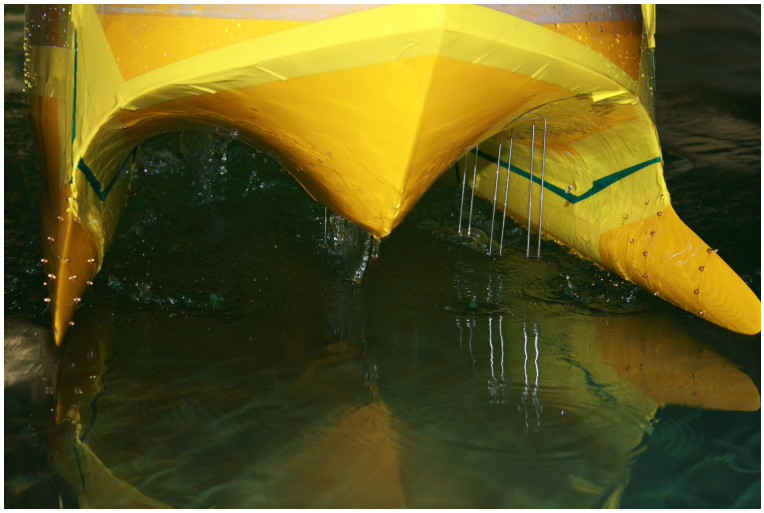

Figure 5.23: Still photograph of the centre bow, taken during experimental tests. The wave-piercers have completely emerged from the water as well along with two boat mounted wave probes (WP2 and WP3). A glimpse of WP5, mounted in the centreline of the model, 120mm aft of the centre bow truncation, can be seen.

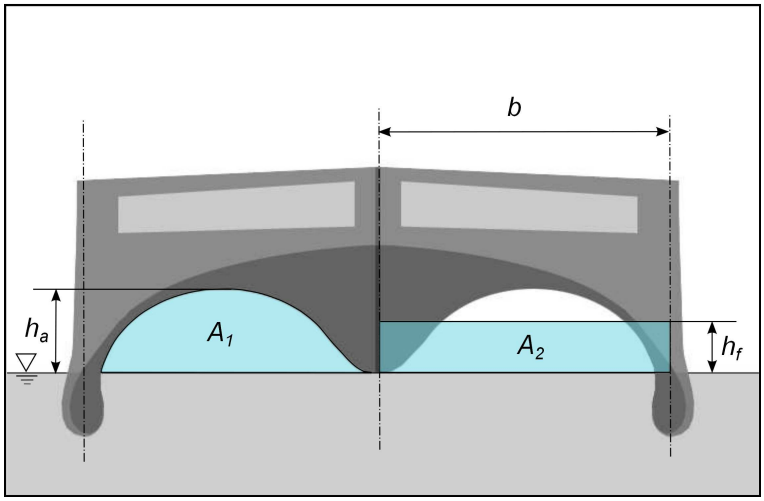

Figure 5.24: Definition of the 2D filling height. $A_1 = A_2$, h_f is the 2D filling height.

The immersions at the slam instant (when the centre bow pressure is maximum at the reference location, in line with the CBT) and the maximum immersion post-slam were recorded for each slam event. The sample run shown in Figure 5.13(a) highlights the immersions at the identified slam instant and the subsequent maximum immersion. Figures C.10 to C.12 in Appendix C (page 201) illustrate immersion distributions at the CBT and the time when slams occur. Data is grouped by Froude number, significant wave height and modal period respectively. Maximum immersion distributions are found on page 202 in Figures C.13 to C.15.

Immersions at the slam time tend to generally decrease with forward speed (Figure C.10), however the variance of the distribution increases. Four slams with negative immersions (i.e. the centre bow was completely out of the water) at the CBT were recorded for Froude numbers of 0.32 and 0.6, suggesting that these slams occurred a significant distance from the CBT.

Also apparent from the cdf is that slams at low Froude numbers tend to occur at deeper immersions. The maximum arch height is also included in these figures, it can be seen that the vast majority of slams occur well before the bow is immersed to the maximum archway. The 2D filling height for this model configuration is approximately 50mm at the CBT; although judging from these distributions, the 2D filling height cannot be declared as a strict threshold condition for slam occurrence predictions, as slam events tend to occur around the 2D filling height. The distribution of immersions for the 1.0s/7.0s modal period conditions (Figure C.12) is interesting in that it is much more spread than the longer period conditions and locations tend to occur further aft than other modal periods.

The maximum immersion distributions shown in Figures C.13, C.14 and C.15 reveal that some immersions exceed the maximum arch height. This is particularly evident for the larger wave heights and longer modal periods. Although outliers are present for all Froude numbers, a strong trend is identified between maximum immersion and forward speed; slams occur at shallower immersions at high Froude numbers. The median maximum immersions for all slam events is closer to the 2D filling height than the immersion distributions at the slam time.

Figures 5.25 and 5.26 sort the immersion and maximum immersion distributions by dimensionless encountered frequency and significant wave height. Here the maximum arch height and the 2D filling height are included in the plots. From Figure 5.25 it can be seen that the majority of slams occur at immersions less than the 2D filling height, with the exceptions of $\omega_e^* = 4.28$ and 6.28. Also apparent in these plots are the low immersions at higher encounter frequencies and the slam events almost always occur at immersions less than the maximum arch height. However in Figure 5.26 the maximum immersion has exceeded the maximum arch height on several occasions, particularly in the larger wave height conditions.

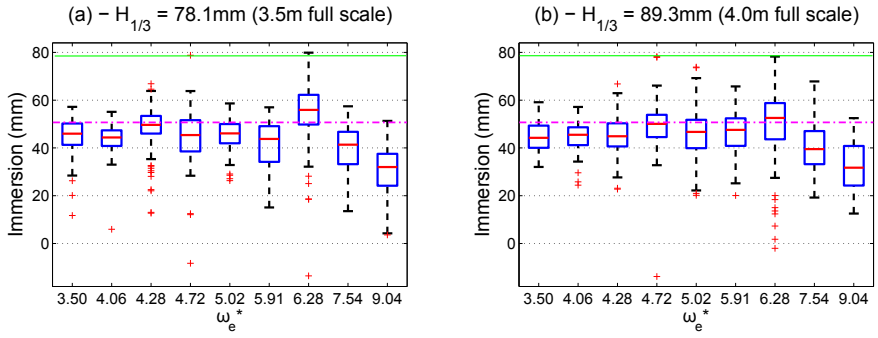

Figure 5.25: Box plots describing the distributions of immersion at the centre bow truncation against dimensionless encounter frequency. (a) $H_{1/3} = 78.1$mm (3.5m full scale). (b) $H_{1/3} = 89.3$mm (4.0m full scale). The maximum arch height at this location (solid line) and the 2D filling height (dotted line) are also shown.

5.4.4 Slam Location and Centre Bow Pressure Distribution

Pressure mapping was accomplished by analysing peak pressures during slam events. Pressure distributions for one sample run is shown in Figure 5.27, each line represents the peak pressures

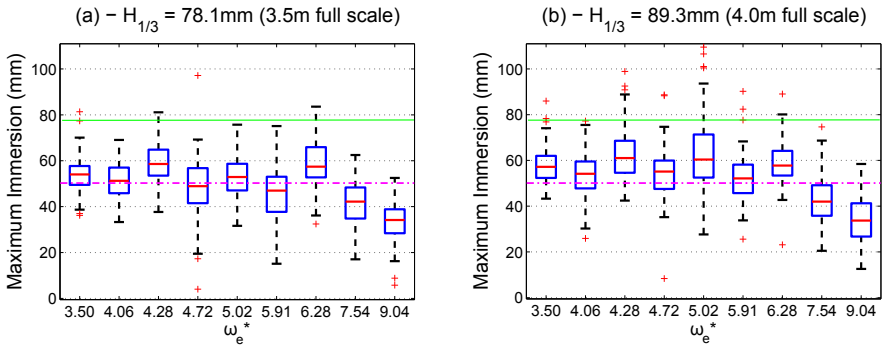

Figure 5.26: Box plots describing the distributions of maximum immersion at the centre bow truncation against dimensionless encounter frequency. (a) $H_{1/3}$ = 78.1mm (3.5m full scale). (b) $H_{1/3}$ = 89.3mm (4.0m full scale). The maximum arch height at this location (solid line) and the 2D filling height (dotted line) are also shown.

recorded for one slam event during that run (the centre bow truncation is at frame 71). For this particular condition, the centre of pressure, and thus the slam location, generally occurs forward of the centre bow truncation, however some slams are centred quite aft of the CBT, around frames 67 and 68.

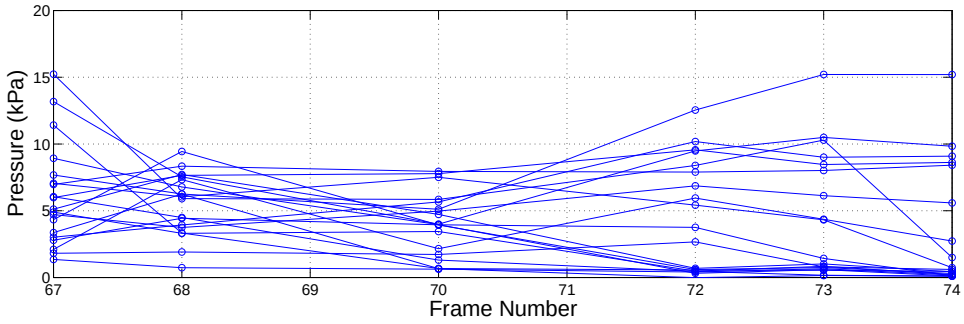

Figure 5.27: Peak centre bow archway pressure distribution for one sample run. Frame 74 is towards the bow. The centre bow truncation is located at frame 71. Condition 97 Run 137, T_0 = 1.5s, $H_{1/3}$ = 78.1mm, U = 2.15m/s.

Figure 5.28 presents a box plot displaying the distribution of surface pressures during slamming. The median slamming pressure is relatively small and consistent along the entire archway, however, large pressures, eight to ten times the magnitude of the median have been recorded at each frame. This observation has important design implications: designers must prepare their centre bow and wetdeck arrangement to withstand occasional excessive impulse loading throughout all locations along the wetdeck structure.

In a previous irregular sea investigation, Thomas et al. [65] found a correlation between vessel speed and slam location: at higher speeds, slams tend to occur further aft and at a shallower centre bow immersion than the lower speed case. Slam locations for each slam event, derived from the proportion of slam load measured by the forward and aft centre bow transverse beams (see Section 3.7.2 for a description of the method), were determined and examined.

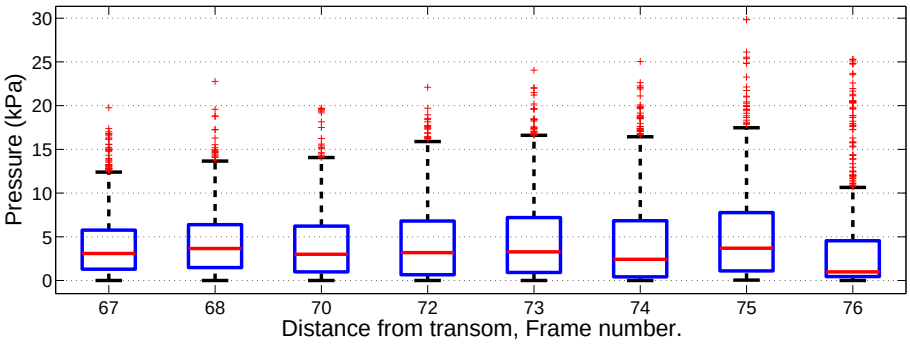

Figure 5.28: Box plot describing the centre bow arch pressure distribution during slamming.

Scatter plots, Figures 5.29 and 5.30, compares slam location on the x-axis with immersion (at the slam instant) at the centre bow truncation on the y-axis. The location of the centre bow truncation and the 2D filling height are also included in these figures. Scatter plots of the maximum immersion can be found in Appendix C (Figures C.19 and C.20) for completeness. The slams are grouped into Froude numbers: 0.32, 0.45 and 0.60 in Figure 5.29 and in Figure 5.30 they are grouped by modal period. From Figure 5.29, slams seem to occur at lower immersions as the forward speed is increased, as noticed in the previous section; but from these plots alone, the slam locations do not appear to move further aft with forward speed in accordance with the earlier observation. The 2D filling height, shown as a black spot, fits close to the centre of the observed location cluster.

When the data was grouped according to modal period in Figure 5.30, the slams tend to occur mostly aft of the centre bow truncation for the shorter modal period but significant data scatter is still present.

Distributions of slam locations, with reference to the transom of the model, when the data is grouped by Froude number, significant wave height and modal period can be found in Appendix C (Figures C.16, C.17 and C.18 respectively, on page 203) Again, the majority of slams are found to fall in the vicinity of the CBT, (or just aft) and it appears that the slam location is independent of forward speed, contrary to previous observations [65]. However, if the data is sorted by dimensionless encountered frequency (from Table 5.1), as shown in Figure 5.31, then the slam location distributions are seen to be shifted slightly aft of the CBT for high encountered frequencies, $\omega_e^* > 6$.

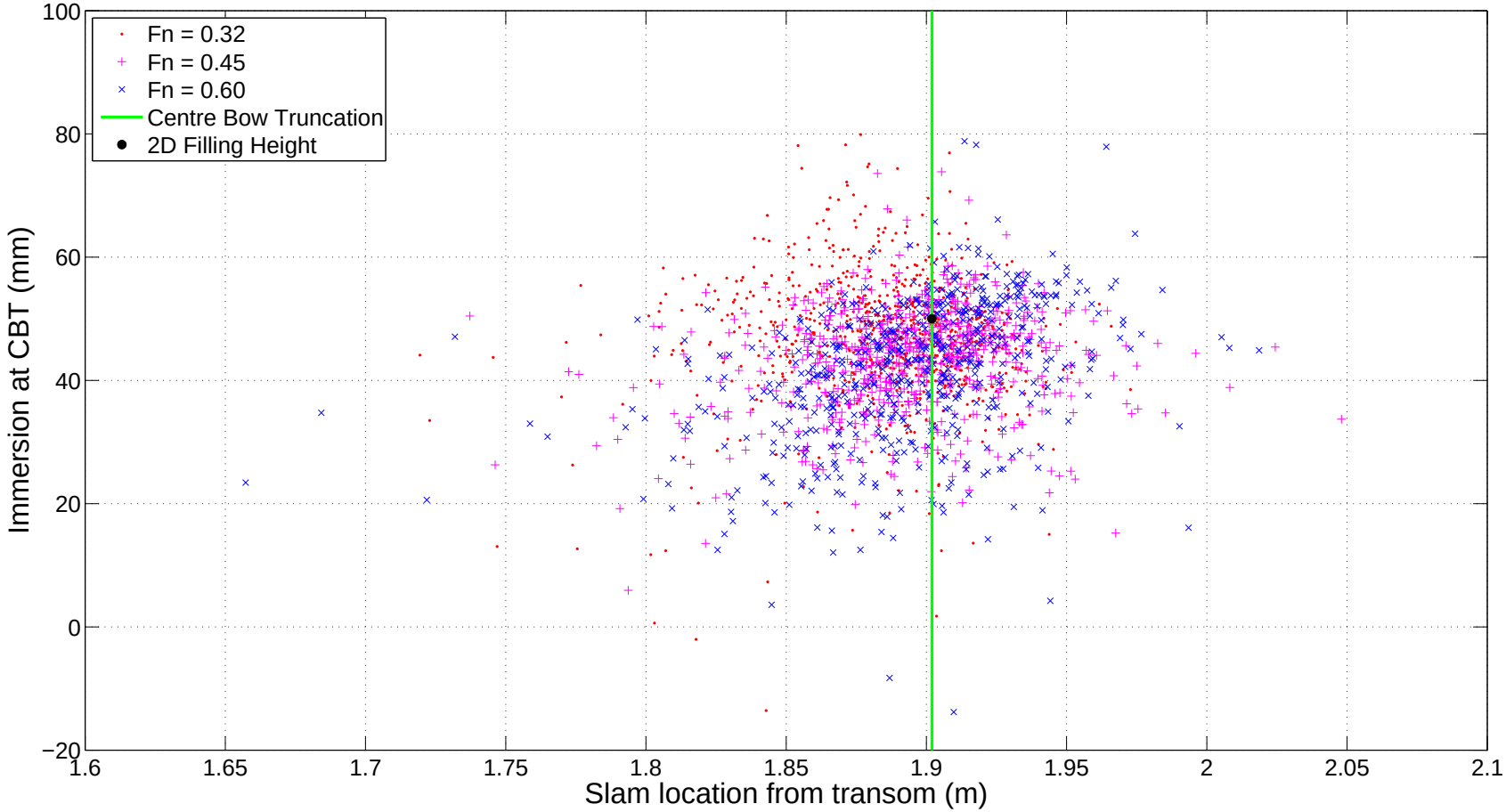

Figure 5.29: Slam location against immersion at the centre bow truncation, location of the CBT and the 2D filling height is included. Data grouped by Froude number.

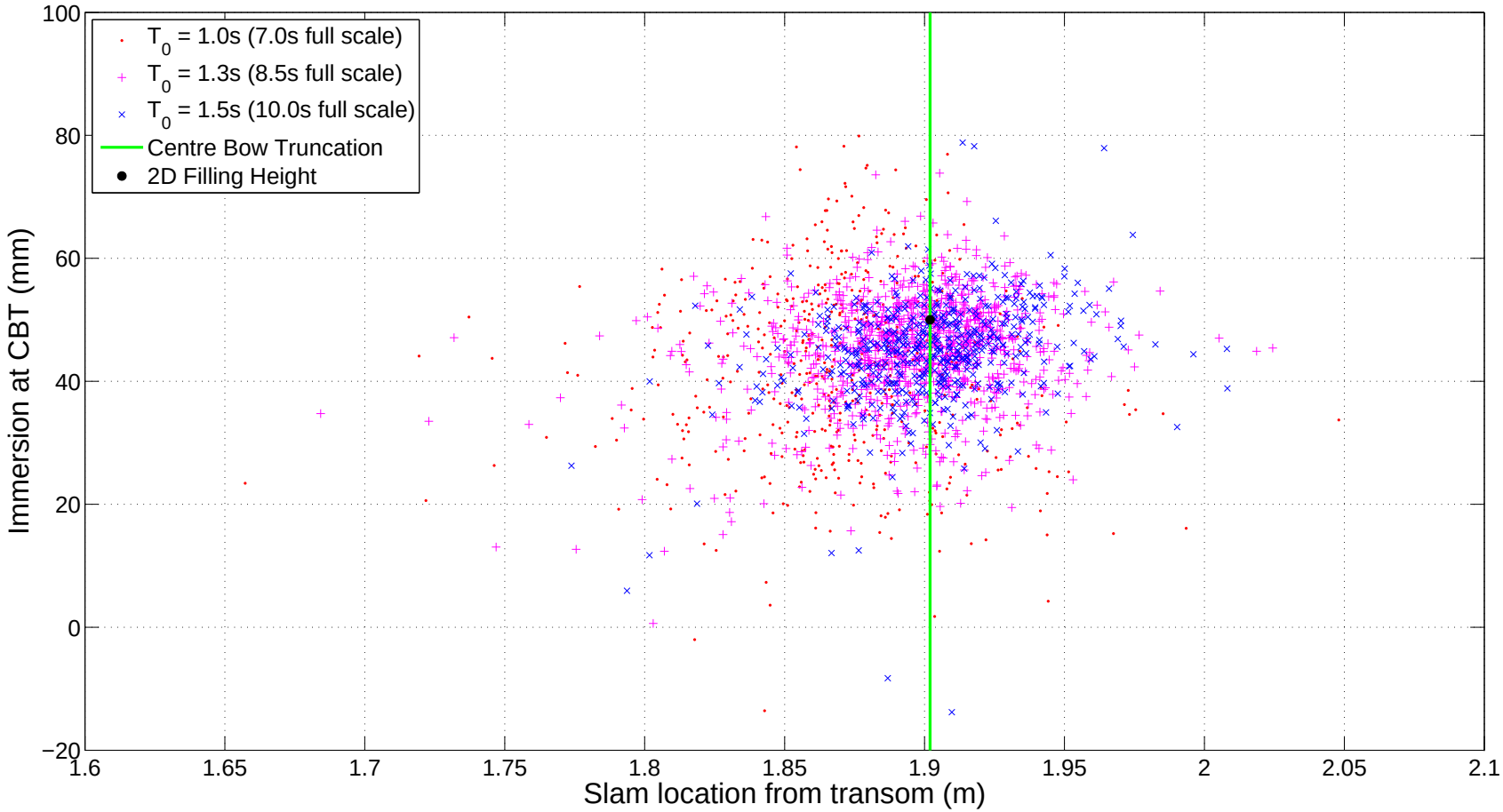

Figure 5.30: Slam location against immersion at the centre bow truncation, location of the CBT and the 2D filling height is included. Data grouped by modal period.

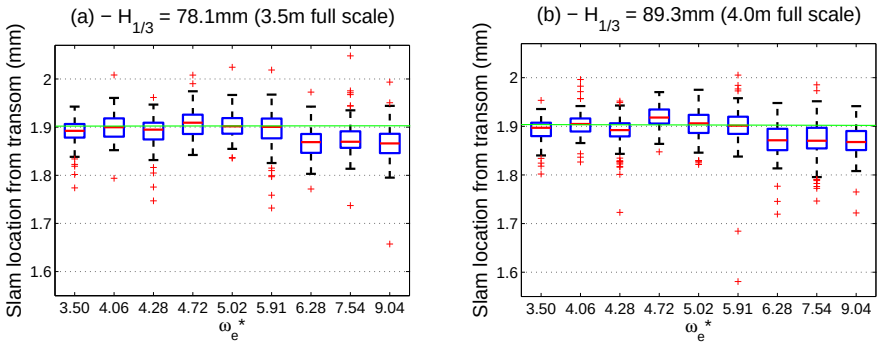

Figure 5.31: Box plots describing the distributions of slam location against dimensionless encounter frequency. (a) $H_{1/3} = 78.1$mm (3.5m full scale). (b) $H_{1/3} = 89.3$mm (4.0m full scale). The location of the centre bow truncation is also highlighted.

Some discrepancy in slam locations has arisen during previous experimentation resulting from the method used to calibrate the centre bow strain gauges for determining slam locations. The analysis conducted by Lavroff [45] in regular waves reports that the slam locations are almost exclusively found in the vicinity of the CBT, whereas Matsubara [53] conducted extensive calibrations of the system and developed a two stage slam load location calculation method, ultimately resulting in slam locations much further forward on the centre bow segment than Lavroff. The calibration method described in Section 3.7.2, and used in this thesis is similar in approach to the method used by Lavroff.

As a result of this contradiction, pressure mapping was undertaken to determine whether slam locations can be estimated based on the pressure data. First, the slam location was assumed to be closest to the pressure tapping that recorded the greatest pressure for a particular slam. With that in mind, each slam event was scanned and the transducer with the highest recorded pressure was noted. A two dimensional normalised histogram was then constructed showing the maximum pressure distribution as a function of dimensionless encounter frequency and location (distance from transom). This process was carried out for the two significant wave heights and is shown by the contour plots in Figures 5.32 and 5.33.

Figure 5.32 shows the maximum pressure density for the 78.1mm/3.5m significant wave height. Locations of the pressure transducers are shown by the circles, the contours are the result of interpolation between these measurement locations. It can be seen from this plot that the pressure transducers aft of the centre bow truncation (located at frames 67, 68 and 70) recorded the larger pressures. Exceptions to this observation are when $\omega_e^* = 3.5$ and 4.28. At $\omega_e^* = 3.5$, 30% of the recorded slams were located at frame 74, and another 40% were located around the CBT (frames 70 and 72). There is a more obvious discrepancy at $\omega_e^* = 3.5$, where 70% of the slams at this encountered frequency were measured to be forward of the CBT. This is an interesting result, as an encountered frequency of 4.28 is close to the resonance frequency of the model (see the motion RAOs in Section 4.6). This may imply that the slams that occur at this band of encounter frequency are of a different nature to the slams at other encountered

frequencies, the enhanced motions of the boat inducing slams further forward on the centre bow section. However the forward nature of the slam location at this encounter frequency is not supported by the location calculations based on the centre bow strain gauge readings. According to Figure 5.31(a), slam locations measured at $\omega_e^* = 4.28$ are centred just aft of the CBT (at frame 71), when the pressure data is clearly recording the largest pressures well forward of the CBT in Figure 5.32.

The maximum pressure density for the larger 89.3mm/4.0m significant wave height conditions are shown in Figure 5.33. During these tests larger pressures were noticed further forward on the centre bow segment, therefore the pressure transducers mounted at frame 67 and 68 were moved forward to frames 75 and 76 (see Figure 3.5, page 30). Again, at high encounter frequencies slams tend to occur further aft on the centre bow section. Interestingly, at moderate to low encountered frequencies (less than $\omega_e^* = 6$) slams are found to be centred around frame 75, although it is difficult to gain an insightful picture from these conditions, as only one pressure transducer is located aft of the CBT.

As well as considering only the location that recorded the greatest pressure, a second analysis investigated the distribution of median slam pressures. The median statistic was chosen rather than the mean or maximum, since it is the measurement of the 50^{th} percentile and less influenced by extreme pressures. Figure 5.34 shows the median pressure distribution for the 78.1mm/3.5m significant wave height conditions. Relatively large pressures are recorded on the aft transducers at higher encountered wave frequencies. The pressure distribution at $\omega_e^* = 4.72$ is surprising; all measured pressures appear to be lower than their neighbours by a factor of two. It is currently not clear whether this is a real phenomenon or if the gathered pressure magnitudes are unreliable for that condition. Ninety slams were recorded for this condition and the strain gauges did show considerable slam loads (some in excess of 200N, see Figure 5.12).

Large pressures were recorded at frame 73, $\omega_e^* = 4.28$, forward of the CBT at the location highlighted in Figure 5.32, supporting the case that slam loading occurred forward of the CBT for that condition, contrary to strain gauge results in Figure 5.31. High pressures are then found aft of the CBT at frame 67-68 for $\omega_e^* = 4.06$.

Figure 5.35 presents the median slam pressures for the 89.3mm/4.0m significant wave height conditions. Once again large pressures are found at high encountered frequencies, and from the data gathered at lower encountered wave frequencies, generally forward of the CBT up to frame 75 (approximately 100mm forward of the CBT), however more data should be gathered at frames 67 and 68 to completely resolve the pressure map (pressure transducers cannot be located at frames 69 or 71 as these are obscured on the model by the centre bow forward transverse beam).

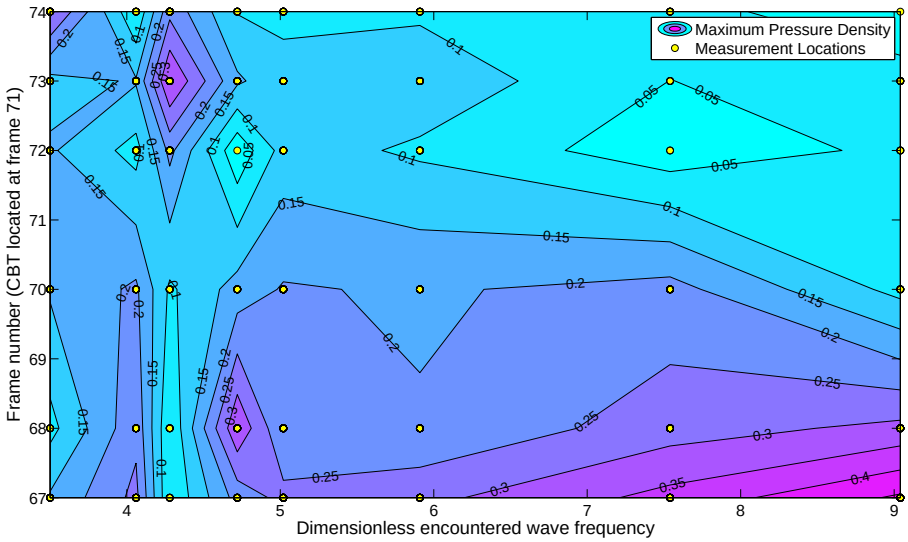

Figure 5.32: Maximum pressure location density; 78.1mm/3.5m significant wave height. The centre bow truncation is located at frame 71. Yellow spots identify the locations of the pressure transducers.

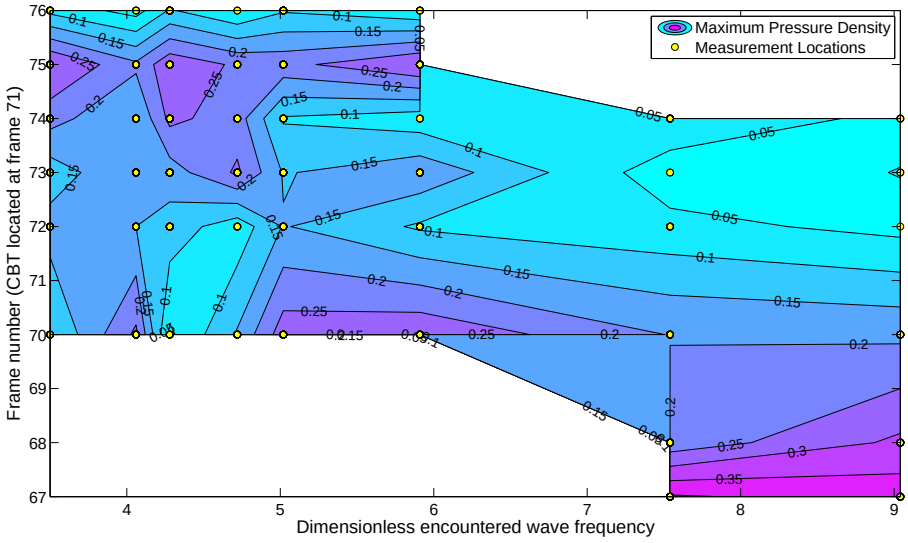

Figure 5.33: Maximum pressure location density; 89.3mm/4.0m significant wave height. The centre bow truncation is located at frame 71. Yellow spots identify the locations of the pressure transducers.

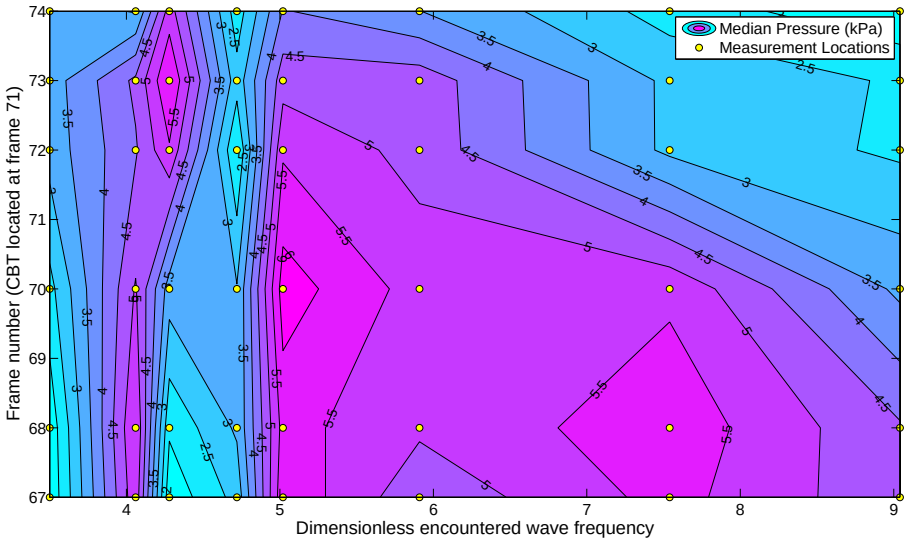

Figure 5.34: Median pressure distribution for the 78.1mm/3.5m significant wave height conditions. The centre bow truncation is located at frame 71. Yellow spots identify the locations of the pressure transducers.

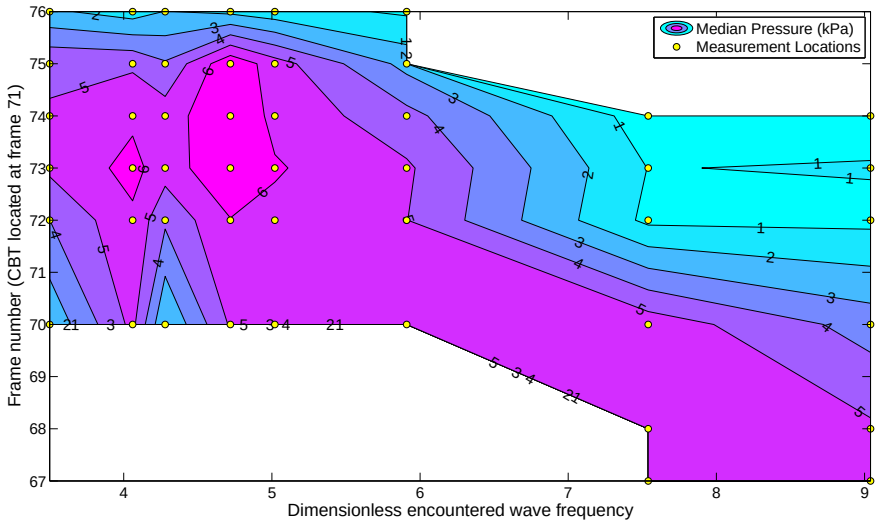

Figure 5.35: Median pressure distribution for the 89.3mm/4.0m significant wave height conditions. The centre bow truncation is located at frame 71. Yellow spots identify the locations of the pressure transducers.

5.4.5 Slam Duration

The duration of slam loading is of interest in the development of the empirical slam module for the time-domain simulation. It is envisioned that the slam load would be applied over several time steps in the computer simulation. The slam load duration was collected for each slam event identified in the experimental data. Slam duration was defined as the time between the slam load changing signs, therefore the slam duration contains two phases: the loading phase, and the unloading phase. Figure 5.36 shows the slam time tends for all slam events during one run. The slam load and duration were normalised in an attempt to identify trends. Normalisation of load was done by dividing the measured slam load by the maximum load for that particular slam event. Time was normalised by dividing by the total slam duration. Plot (a) displays the raw loading data with no normalising, plots (b) and (c) show the same data with time and load normalised respectively. In plot (d), both parameters have been normalised. Double peaks were observed for many slam events, at a frequency of approximately 11Hz. No correlation was found between slam duration and the resulting slam load ($r = 0.16$).

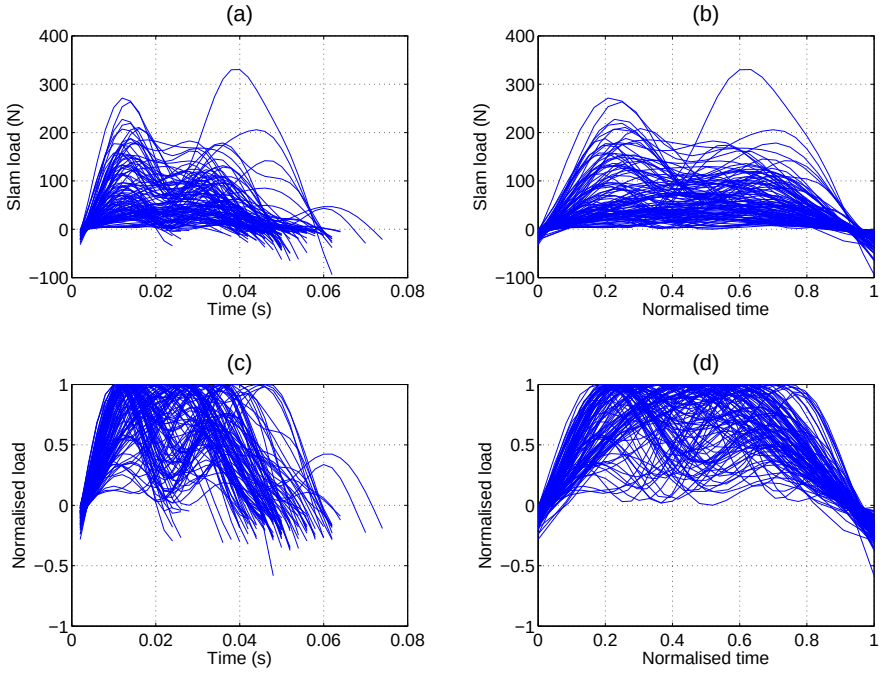

Figure 5.36: Slam durations for Condition 97. (a) duration against slam load, (b) normalised duration against slam load, (c) duration against normalised load and (d) normalised duration against normalised load.

The time at the end of the loading phase, when the centre bow load has reached a maximum, is defined as the rise time. Slam duration has been plotted against rise time in Figure 5.38. A solid line showing when the rise time is half of the slam duration is also included in this figure. Distributions of rise time and duration can be seen adjacent to the relevant axis in Figure 5.38. The apparent regular spacing of the data is an artefact of the data acquisition

unit; slam durations are relatively short in time (the median slam duration is 0.05s) and the DAQ used to gather load data from the centre bow strain gauges was limited to a sample rate of 200 - 500Hz.

The same data has been plotted in Figure 5.39, this time showing the rise time in a non-dimensional form by expressing it as a fraction of the total duration, . The dimensionless rise time falls around the 50% of the total duration with a second concentration close to 30%. Since Figures 5.38 and 5.39 do not show the number of data points that fall on the same location (this is quite possible due to the coarseness of the DAQ sample rate).

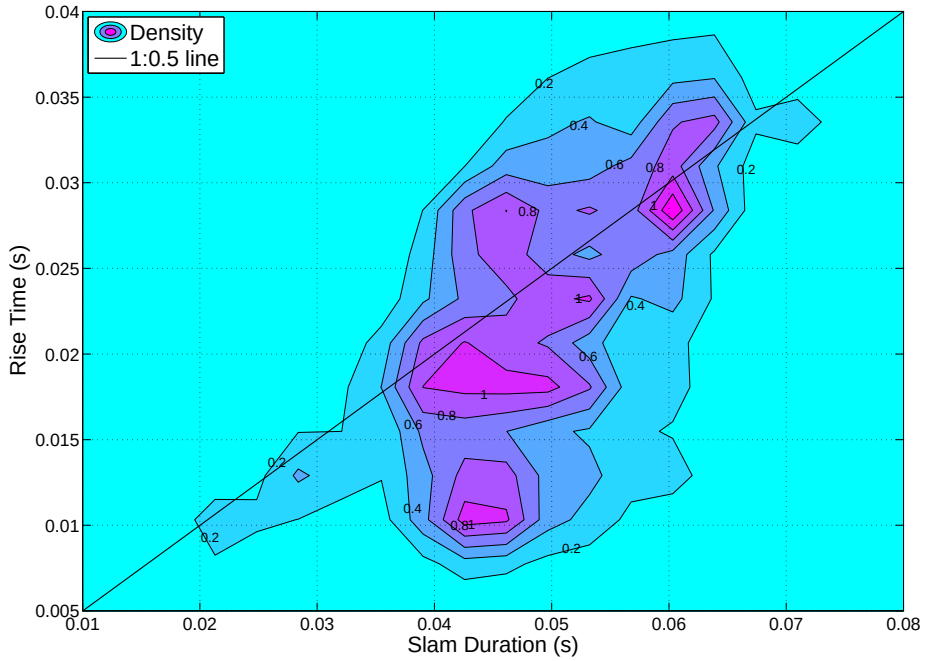

Figure 5.37: Slam time trends against maximum slam load contour plot highlighting the distribution density.

Figure 5.37 is a contour plot representing the occurrence density of slam duration against rise time[2]. Of particular note in this plot is the three apparent peaks around a vertical slice taken at slam duration = 0.04 to 0.05. These peaks are separated by approximately 0.09s in rise time (11Hz); therefore it appears that vibration of the structure at its natural frequency is occurring even as the slam load is ramping up (post pressure peak). The fact that rise time peaks are found at 0.011, 0.019 and 0.027 suggests that vibrations are enhancing the resulting measured slam load. These dual peaks can be seen in the time traces shown in Figure 5.36. It is also interesting to note that when the slam duration was 0.06s, few slams were measured with a 0.2s rise time (30% of the slam duration).

[2]It is actually a re-plot of Figure 5.38.

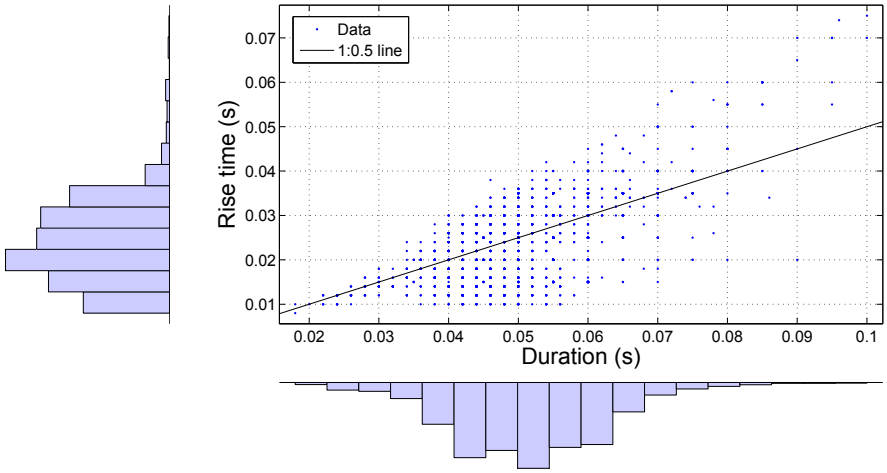

Figure 5.38: Slam duration against rise time, with a 1:0.5 line also shown. Histograms showing the distributions of slam duration and rise time are shown next to the x and y axis respectively.

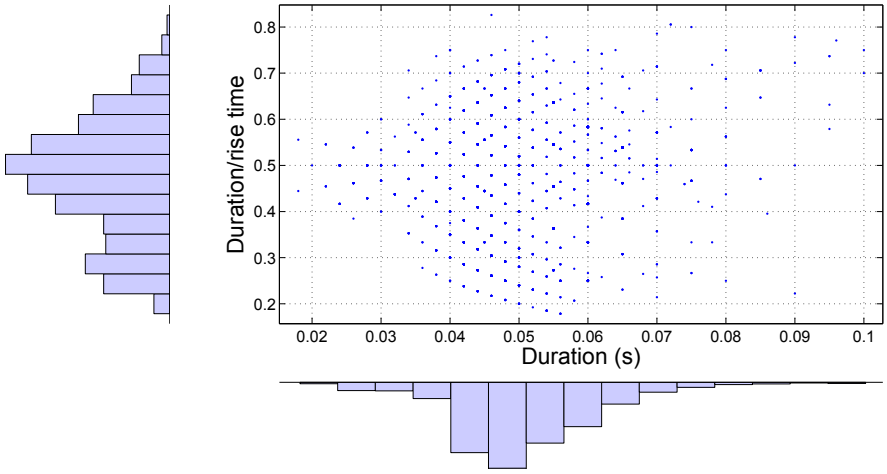

Figure 5.39: Slam duration against rise time (as a percentage of slam duration). Histograms showing the distributions of slam duration and dimensionless rise time are shown next to the x and y axis respectively.

5.4.6 Vertical Bending Moments

Maximum vertical bending moments (VBM) at the demihull links were recorded for each slam. The maximum slam induced vertical bending moment was determined using a similar peak finding method to that used to find peak relative vertical velocities (Section 5.4.2). Slam events were identified via a peak detection method on the centre bow surface pressure trace and that identified time index was used to centre a search window (of $\pm 0.2s$) in the VBM time trace and then peak hog and sag VBMs were determined for the forward and aft demihull links.

Maximum hog and sag vertical bending moments during slamming are plotted against slam load for the forward and aft demihull links in Figures 5.40 and 5.41 respectively. Figure 5.40 shows a clear trend between slam load and VBM; if the slam magnitude is known, then the VBM (on the forward part of the vessel at least) can be estimated. This also suggests that a large amount of slam energy is transferred to the demihulls. The trend is not so defined in the aft links (Figure 5.41). The VBM in the aft demihull links during slamming is generally smaller than the forward ones, this is expected as the aft links are further away from the slam location and the sagging VBM is generally larger than hog for a given centre bow slam load. This is also expected as the sagging load is an external slam load and hogging is the subsequent structural response.

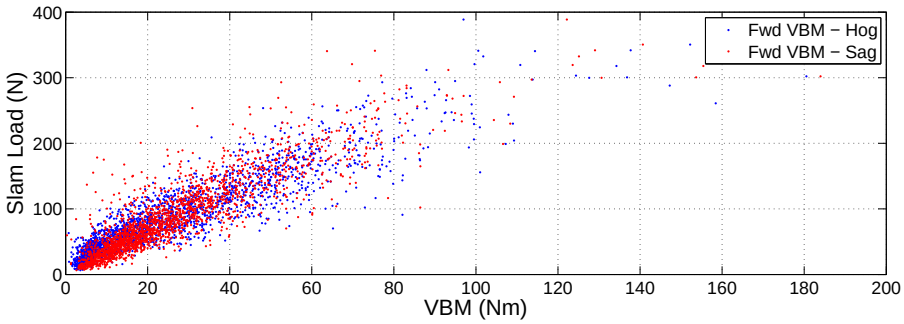

Figure 5.40: Hog and sag slam induced vertical bending moment against slam load. Forward links.

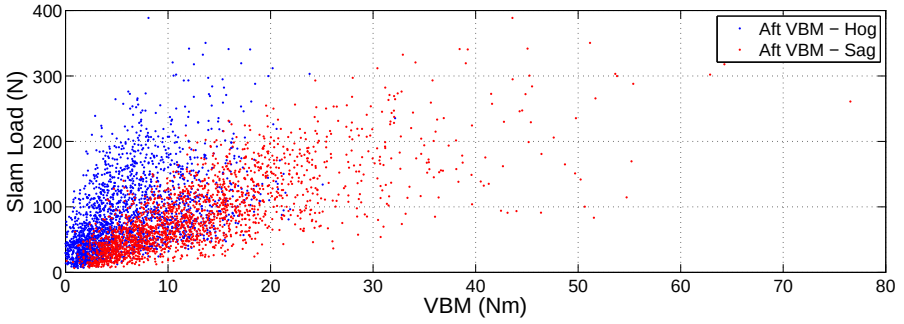

Figure 5.41: Hog and sag slam induced vertical bending moment against slam load. Aft links.

The relationship between slam load and vertical bending moment appears linear for the

forward links. It is observed that the gradient of this trend has units of distance which could relate the slam location with the slam load and resulting demihull vertical bending moments. The location of each slam was determined relative to the forward segmentation cut and a 'slam moment' was defined as the product of the slam load and the distance from the forward segmentation cut to the slam location. Figure 5.42 the relation between the VBM at the forward links and the slam moment. A line representing a 1:1 relation is also plotted for reference. If the slam moment and the vertical bending moment were closely related, then ideally they should fall on the 1:1 line. The slam moment is seen to be generally higher than the demihull bending moment and a least squares line of best fit reveals a gradient of 1.34 for the sagging bending moment trend. This confirms that the slam load magnitude can be used as a first-pass estimator for vertical bending moments at the forward end of the demihull.

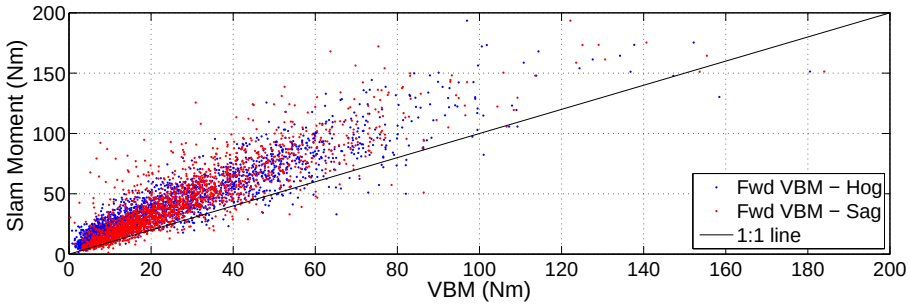

Figure 5.42: Hog and sag slam induced vertical bending moment against slam moment for the forward links. Slam moment was calculated by multiplying the slam load by the slam location relative to the forward segmentation links.

Figures 5.43 and 5.44 provide some insight into the distributions illustrated in Figures 5.40 and 5.41. Figure 5.43 (a) represents the probability density function (pdf) of the forward VBM for hog and sag. The measured VBM is placed into bins (shown on the x-axis) and the percentage of occurrence on the y-axis. Figure 5.43 (b) displays the box plot for the pdf shown in (a). It can be seen from plot (b) that the medium VBM are very similar for hog and sag, although the hogging VBM appears to be more broadly distributed, shown by the IQR (inter quartile range - the box). Figure 5.44 show the pdfs for the aft demihull links. The aft hogging VBM is much smaller than sag, with the medium VBM being approximately half of the sag.

Figure 5.45 presents the cumulative distribution functions (cdf) for the previous pdfs. The VBM cumulative distribution function is useful in showing the percentage of VBMs with magnitudes within a given range. For example, from Figure 5.45, 80% of the recorded sagging vertical bending moments in the aft demihull links were less than 20Nm. If this figure is enlarged, it can be seen that 5% of the sagging VBM magnitudes are greater than approximately 68 Nm and 5% of the corresponding hogging VBMs are greater than roughly 70 Nm. Interestingly, there is a greater tendency to have a larger hogging moment than sagging at the forward links, this can be seen the cdf plot, and it was suggested by the wider distribution observed in Figure 5.43 (b).

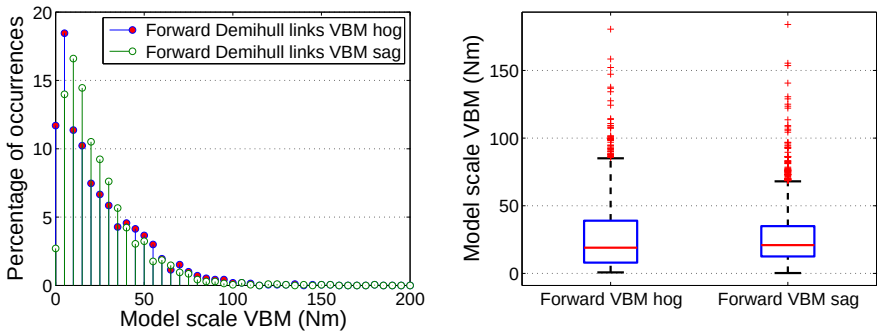

Figure 5.43: (a) Hog and sag slam induced vertical bending moment distributions. Forward links. (b) Box plots representing the distributions in (a).

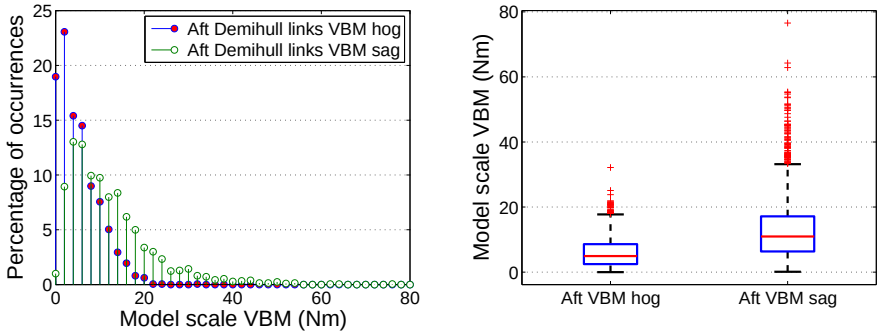

Figure 5.44: (a) Hog and sag slam induced vertical bending moment distributions. Aft links. (b) Box plots representing the distributions in (a).

The correlations between vertical bending moments and the centre bow slam loads are shown in Table 5.2; correlations between VBM and slam load are clearly apparent. This further supports the observation that measurements of the vertical bending moments can be used to indicate the magnitude of centre bow slamming. Notice how the VBM at the aft link does not correlate well with any other variable. Wave contact with the aft wetdeck has been proposed as one cause of this problem[3]. Figure 5.46 shows a slam on the aft wetdeck with exaggerated bending in the demihulls, since the wetdeck is one continuous piece, a lever effect is induced, potentially contaminating VBM measurements at the demihull links. At the time of writing, a new model has been designed with a segmented wetdeck in order to realistically model and isolate wave contact effects on the aft wetdeck.

[3]The model was constructed with a single (unsegmented) wetdeck extending from the aft of the centre bow segment to the transom of the model (see Figure 3.4 on page 24 for a schematic of the model).

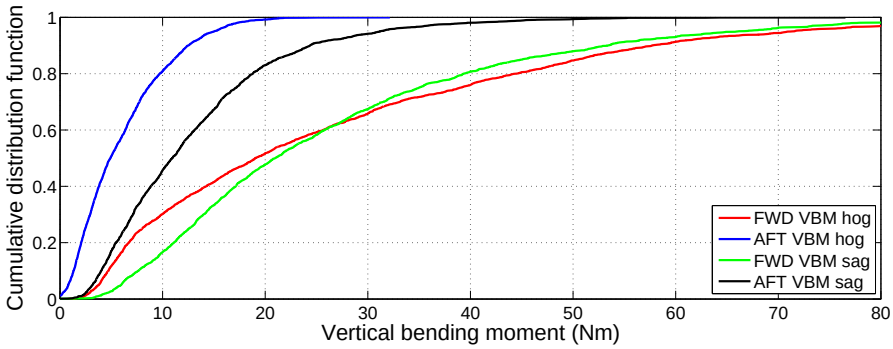

Figure 5.45: Cumulative distribution function for hog and sag slam induced demihull VBM at the forward and aft elastic links.

Table 5.2: Correlation coefficients, r, for centre bow loads and demihull vertical bending moments.

		VBM			
	F_s	fwd hog	aft hog	fwd sag	aft sag
F_s	1.00				
VBM fwd hog	0.91	1.00			
VBM aft hog	0.52	0.55	1.00		
VBM fwd sag	0.88	0.88	0.47	1.00	
VBM aft sag	0.76	0.86	0.59	0.74	1.00

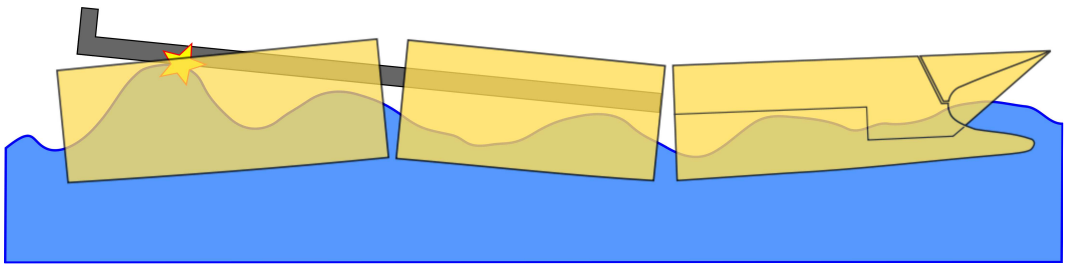

Figure 5.46: Slam on the aft wetdeck with exaggerated bending in the demihulls.

5.4.7 Occurrence Rates

Figures 5.47 and 5.48 compares slam occurrence rates (scaled to full scale) for different speeds and modal periods. Occurrence rates are found to increase with forward speed, as more waves are encountered per hour at higher speeds. Slams are most common when the vessel motions are greatest, for this particular model configuration, the 8.5s modal period conditions tended to give the greatest motions and thus slam rates. The most severe slamming condition for both tested significant wave heights is 8.5s modal period and a vessel speed of 38kts, with more than 500 slam events occurring per hour (approximately one slam every 6.5s). This may seem excessive, and it is indeed unlikely that a ship operator would be sailing at 38kts in these conditions, however it is important to remember that a ride control system is installed on the full scale ship; the scale model did not incorporate any ride control system at all. Therefore the slam occurrence rates for the real vessel will be expected to be lower than those presented here.

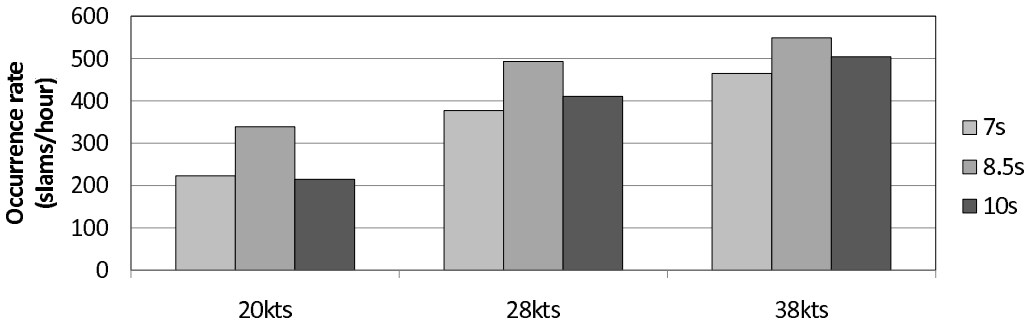

Figure 5.47: Slam occurrence rates for 3.5m significant wave height and various speeds and modal periods.

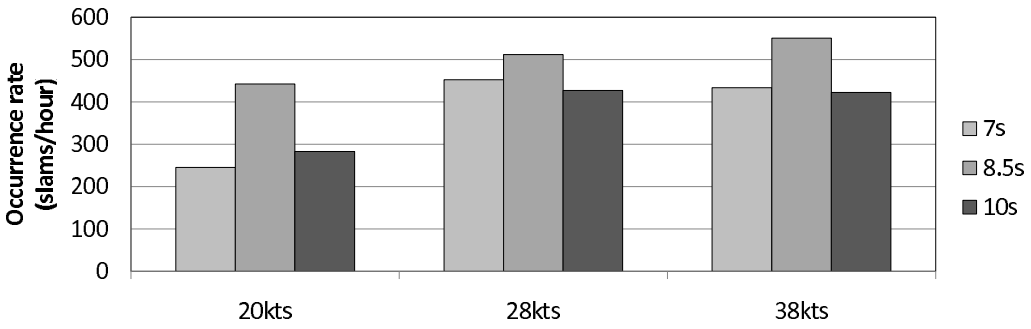

Figure 5.48: Slam occurrence rates for 4.0m significant wave height and various speeds and modal periods.

Figures 5.50 and 5.51 confirm that the occurrence rate is proportional to significant wave height, though there is expected to be a minimum threshold wave height (dependent on encountered wave frequency) below which vessel motions are not great enough to induce slamming. The maximum occurrence rate of course would equal the number of waves encountered per hour, if a slam occurred on every wave. Interestingly there was a decrease in the slam occurrence rate for the 38kts conditions at 4.0m significant wave height compared with the 3.5m conditions.

Figures 5.52 and 5.53 contain the same data shown in Figures 5.50 and 5.51 however the slam occurrence rates are normalised by expressing them as a percentage of the total encountered waves. This shows the slam rates as a function of encountered waves, rather than a number of slams per hour, where higher slam rates would be expected at higher vessel speeds simply because the ship encounters more waves per hour. This can be seen by comparing the two worst conditions for two different speeds: 8.5s modal period, 4.0m significant wave height at 20kts and 38kts in Figures 5.50 and 5.51. The slam occurrence rates for these two speeds were found to be 430 slams/hour and 540 slams/hour respectively. This is quite a noticeable difference, however if the occurrence rates are calculated as percentage of encountered waves, the difference is much closer, at 35% and 32% respectively (see Figures 5.52 and 5.53). This Reveals that the slam occurrence rate, in terms of encountered waves, are quite similar, resulting in one about slam in every three waves.

It can also be seen from Figures 5.52 and 5.53 that increasing the speed *does* increase the slam occurrence percentages; slams were found to occur on 16-19% of the encountered waves at 20kts for the 7s period and 3.5-4.0m significant wave heights (Figure 5.52) compared to 24% slam occurrence rate for the same wave conditions at 38kts.

The observed proportionality between slam occurrence rate and significant wave height was examined for the 8.5s modal period cases shown in Figures 5.50 and 5.51. Slam occurrence rates for these conditions are shown in Figure 5.49 and linear least squares trends are extrapolated down to the x-intercept representing a slam occurrence rate of zero. The maximum significant wave height when no slams occur is defined as the threshold significant wave height. From Figure 5.49 the threshold wave height for both 20kts and 38kts vessel speed in 8.5s modal period conditions is in the vicinity of 1.5m (the slam occurrence threshold for 20kts was found to be 1.43m and for 38kts it was 1.51m).

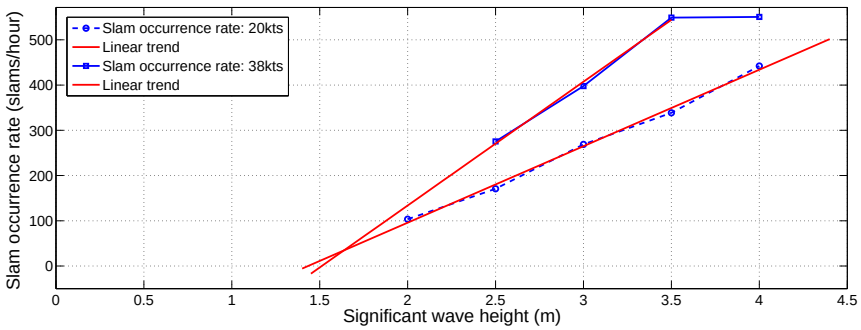

Figure 5.49: Significant wave height against slam occurrence rates for the $T_0 = 8.5$s conditions, linear trend lines are extrapolated down to the x-intercept to show an estimated slam occurrence threshold of 1.43m when the vessel speed is 20kts and 1.51m for the 38kts conditions.

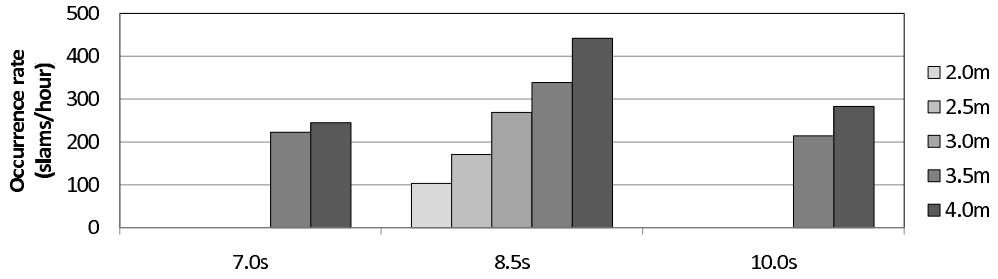

Figure 5.50: Slam occurrence rates for vessel speed of 20kts. Data is grouped by significant wave height and modal period.

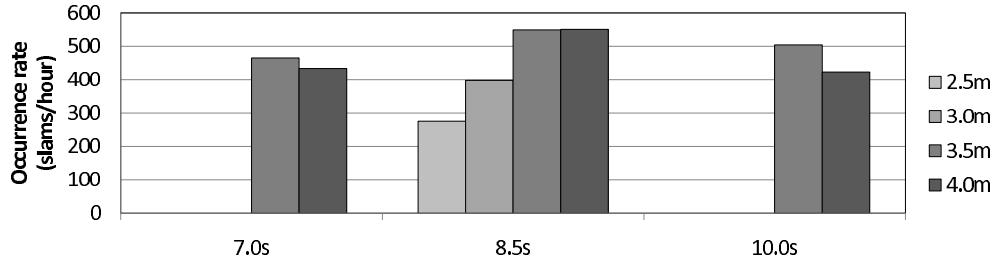

Figure 5.51: Slam occurrence rates for vessel speed of 38kts. Data is grouped by significant wave height and modal period.

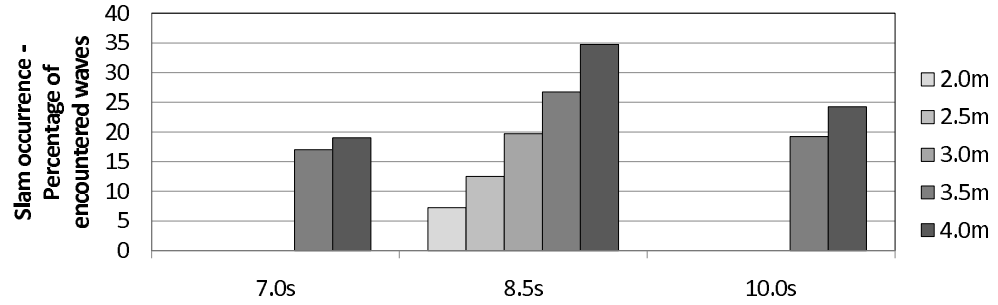

Figure 5.52: Slam occurrence rates for vessel speed of 20kts, shown as a percentage of encountered waves. Data is grouped by significant wave height and modal period.

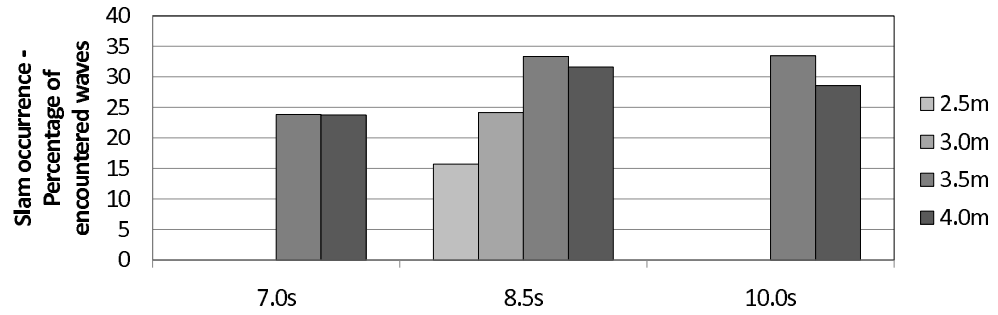

Figure 5.53: Slam occurrence rates for vessel speed of 38kts, shown as a percentage of encountered waves. Data is grouped by significant wave height and modal period.

5.5 Conclusions

Slam parameters and characteristics were identified by testing a hydroelastic scale model of a 112m Incat catamaran. A total of 2,103 slam events were identified over 22 different conditions; each condition containing a minimum of 10 minutes full scale equivalent sea time. Centre bow slam loads were determined by analysing strain gauge signals mounted on the centre bow transverse beams. 0.67% of the slams measured had a magnitude exceeding the displacement of the model; the largest slam recorded was equivalent to 132% of the model displacement. The encounter wave frequency is as an important parameter with regard to centre bow slamming; slam loads, although scattered, tends to follow motion RAO trends. The distribution of slam magnitudes showed that the median is a function of significant wave height and encountered wave frequency, however many outliers were detected and extreme slam events (of the order of 4 times the median) were recorded for most conditions. Statistical investigations of slamming phenomena such as slam loading and the resulting influence on the demihull vertical bending moment are useful as it gives an indication of not only the mean, or typical observations, but also their distribution and the likelihood of extreme events.

Slams at higher encountered frequencies $\omega_e^* > 7$ are found to differ from 'normal' slams; they are characterised by a small, often negative, relative vertical velocity at the CBT when the maximum pressure is recorded, small immersion at the CBT and are located further aft on the centre bow segment than other encountered frequencies. Slam loads at higher encountered wave frequencies are also generally lower than other conditions. It can be concluded that these types of slams are primarily the result of wave impacts on the vessel, with little vessel motion contributing to the relative motions of ship and wave as opposed to slams at lower encounter frequencies where the vessel impacts on the wave, with vessel motions contributing significantly to the relative motions of ship and wave.

The 2D filling height, previously defined from regular sea tests, was considered and compared with centre bow immersions during slamming. Slams were found to start before immersion of the centre bow reached the maximum arch height at the CBT, and were also generally concluded before immersions reached the maximum arch height, with the exception of the 89.3mm/4.0m significant wave height conditions, some extreme slams resulted in immersions up to twice the maximum arch height at the centre bow truncation. Scatter of the immersion data showed that the 2D filling height cannot be used as an exact threshold for centre bow slamming, however it is a step in the direction of understanding the onset conditions for slamming predictions.

Pressure investigations revealed that the cross-deck structure was exposed to large local pressures at all locations measured, meaning ship designers should ensure the structure is able to withstand large local loads all the way along the length of the bow.

Slam locations were determined by analysing the centre bow strain gauge signals. Locations were found to generally fall within 100mm of the centre bow truncation, with slams at the high encounter frequencies shifted noticeably aft. Pressure mapping was conducted to confirm

the slam locations determined via the strain gauge method. Higher pressures were generally found at the pressure transducer locations aft of the CBT; however the number of measurement locations are quite sparse to draw firm conclusions based off these tests alone. Slams were found to be concentrated at frame 73 (approximately 55mm forward of the CBT) for $\omega_e^* = 4.28$ for the 78.1mm/3.5m significant wave height conditions, in contrast to surrounding conditions. Pressure magnitudes for $\omega_e^* = 4.72$ for the same wave height were two to three times lower than expected; the measured pressure magnitudes are questionable for that condition, pending repeated tests.

Slam durations are defined as the time required to apply a load from zero Newtons to some maximum load and back to zero again. Slams are short in duration; the median slam duration was measured at 0.05s for these experiments. The DAQ system used to measure slam loads is limited to 500Hz, resulting in a coarse resolution of slam load over time. Vibration of the model is detected in the slam load data even at the slam load is ramping up to a maximum. In future experimentation, centre bow loads will be able to be measured on the AMC carriage DAQ, allowing 5kHz sample rates and thus better resolutions of centre bow load applications in time.

Vertical bending moments at the forward links are shown to be consistent with the centre bow segment slam load; if the demihull VBM is measured at a point close to the bow, the centre bow load could be estimated and vice versa. Trends in the aft links were not as defined, the maximum hog VBM was generally less than the maximum sag VBM for a given slam. This could be the result of a lever-action induced by the continuous aft wetdeck section. Future tests with an improved scale model will further investigate this observation.

Slam occurrence rates are a function of encountered wave frequency (modal period and vessel speed) and significant wave height. If the encountered wave frequency falls in the vicinity of the modal frequency of the vessel motions and thus the slam occurrence rate will increase. In this situation, the operator would alter the encountered wave frequency, most likely by slowing down or changing heading to reduce motions and slamming. A slam occurrence threshold was identified by extrapolating experimentally measured slam occurrence rates for a range of significant wave heights and two vessel speeds. Slams are determined not to occur at significant wave heights less than 1.5m for 20kts to 38kts vessel speed and modal period of 8.5s.

This chapter illustrates the first step in developing a statistical slam prediction module. Chapter 6 continues the analysis of the identified slam parameters using statistical methods with the aim of developing a predictive slam load module. Ideally, given a set of conditions, the resulting slam load can be determined exactly if all relevant slam parameters are known. Admittedly, this is probably impossible to achieve realistically, as slam loading could well be an inherently non-deterministic process, however further parameter identification and regression could make predicting slam loading as deterministic as possible.

Chapter 6

Development of an Empirical Slam Module

6.1 Introduction

This chapter aims to develop and install a module for the time-domain seakeeping code introduced in Chapter 4 capable of identifying slam events and applying the resulting slam load on-line during the simulation. This module is to be empirical in nature, using the slam characteristics investigated in Chapter 5 as a basis. The slams analysed in the previous chapter were used to establish a database of slam events with varying characteristics. A total of 28 possible slamming variables were collected for each of the 2,103 identified slams. These variables are used as a basis for a stochastic prediction model developed in this chapter. Not all of the potential slam variables are included in the final module; a correlation analysis is applied to remove irrelevant variables. Slam identification involves defining a location dependent immersion threshold based on the 2D filling height concept combined with a stochastic permutation from experimental observations. Slams are identified by checking relative wave elevations between the ship and the wave at these locations. If the immersion threshold is exceeded at any location, a slam is said to have occurred where the threshold was first exceeded. The maximum slam load consists of a deterministic element resulting from a regression on experimental data and a stochastic element based on the distribution of the regression residuals. The slam load is then applied over a number of time steps based again on the experimental observations presented in the previous chapter.

Initially a preliminary off-line slam model was developed, based on a previous set of slam load measurements in irregular seas. To aid in illustrating the general mechanics of the final stochastic on-line slam module, this simplified model will be explained in the next section. A statistical investigation into the slam characteristics developed in Chapter 5 is found in Section 6.2 followed by the development of the final on-line slam module in Section 6.3.

6.1.1 Slam Module Mechanics: Preliminary Off-line Model

A preliminary off-line slam module was developed in 2010 by using slam data gathered by Chamberlin in 2008 [10] and analysed by Winkler in 2009 [77] (and subsequently published, by Thomas et al. [65]) as a basis. This slam module was presented at the Seventh International Conference on High-Performance Marine Vehicles in October 2010 (HIPER'10) [27]. A brief description of that model is provided here as many features of its routines are applicable to the one presented later in this thesis.

The aim of the model was to first identify slam events as they occur in the time-domain simulation and then calculate the resulting slam load. The slam identification criterion and slam load prediction method were based on results from model experiments.

Slam events were identified in the simulation by using the two-dimensional filling height criterion (see Section 5.4.3 and Figure 5.24 for details). A slam event was said to have occurred when the relative immersion at the CBT equals or exceeds the 2D filling height. Figure 6.1 demonstrates the application of the 2D filling height slam identification trigger. A 112m catamaran is simulated in the time-domain seakeeping method, sailing at 38kts in a JONSWAP spectrum with significant wave height of 3m and modal period of 7s (headseas). The 2D filling height and maximum arch height at the CBT are included in the plot. The 2D filling height can be seen to be exceeded three times during this short section of simulation, therefore, according to the 2D filling height criterion, three slams have occurred over the 70s of simulated time. Circles on the relative velocity plot denote the relative vertical velocity subsequently used in the slam load calculations.

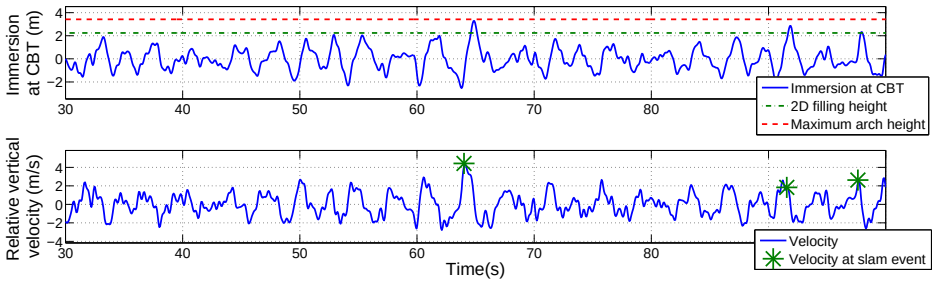

Figure 6.1: Time-domain simulation of a 112m wave-piercing catamaran sailing at 38kts in head seas represented by a 3m, 7s JONSWAP wave spectrum. Relative immersion and vertical velocity (+ve represents the ship and wave moving towards one another) time traces are shown. The circles on the velocity plot highlight identified slam events.

The slam load calculation is based on a regression analysis of scale model testing in irregular seas. The dataset used for this regression consisted of a total of 284 slams from one sea condition (a JONSWAP spectrum with a significant wave height of 3.75m and a modal period of 8s, full scale) and two vessel speeds (20 and 38kts full scale).

The only explanatory variable considered in this model is the maximum relative vertical velocity at the centre bow truncation prior to the slam. A quadratic least-squares fit is applied

to the experimental data; the quadratic is forced through the origin (when relative vertical velocity is zero, the slam load is also zero), therefore the predicted load basis equation can be written as:

$$L_p = a_1 v_{rel} + a_2 v_{rel}^2 \tag{6.1}$$

where the coefficients a_1 and a_2 are determined by a regression analysis of the irregular slam load data. Figure 6.2 shows the measured slam data with this line of best fit representing the predicted slam load ($L_{predicted}$). It is clear from this plot that the data is weakly associated; for a given relative vertical velocity, a range of slam load magnitudes were measured. The slam load mechanism is not yet clear, therefore a random permutation is introduced to emulate the distribution of slam loads for a given relative vertical velocity.

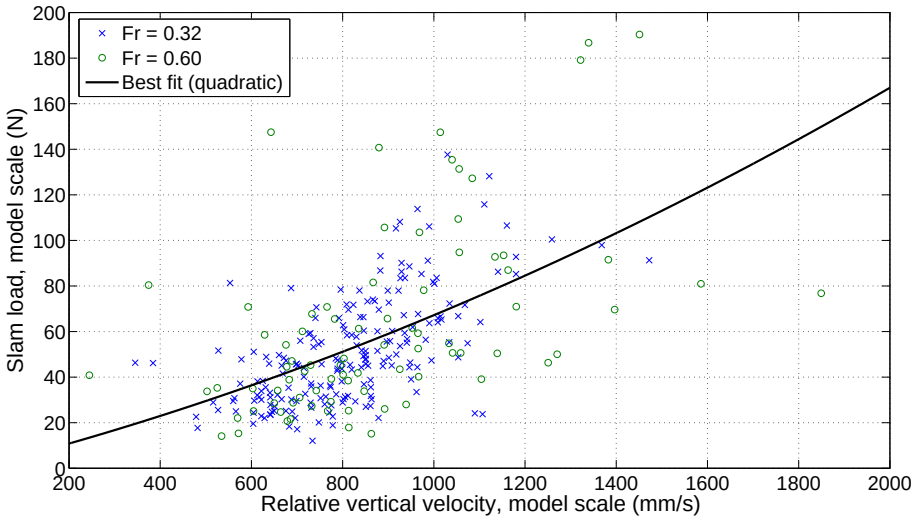

Figure 6.2: Line of best fit through the slamming data for two vessel speeds.

Analysis of the slam load residual suggested that the total slam load, L_{slam}, could be defined as:

$$L_{slam} = F_{slam} L_p. \tag{6.2}$$

Here F_{slam} is defined as:

$$F_{slam} = (1 + \varepsilon) \tag{6.3}$$

and ε is an independent and identically distributed random number based on the observed distribution of the residuals of the experimental data. The experimental residual, e, is defined as:

$$e = \frac{(L_{measured} - L_p)}{L_p} \tag{6.4}$$

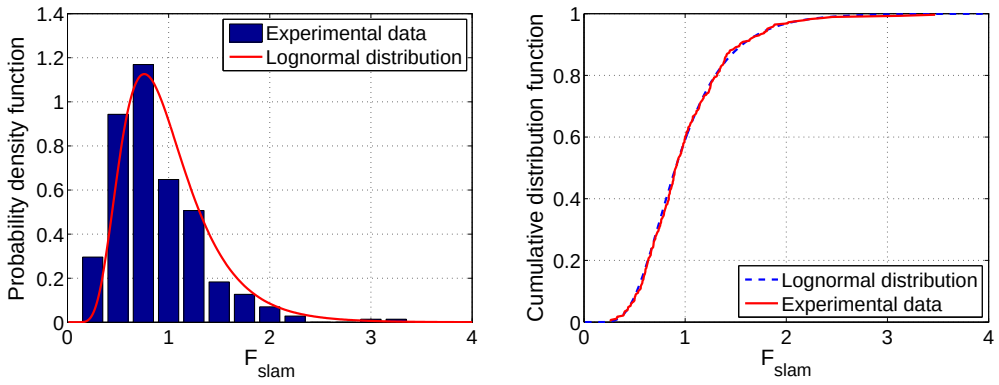

Figure 6.3: Probability density function and cumulative distribution function of $F_{slam} = (1 + \epsilon)$ compared with the lognormal distribution.

Inspection of the distribution for slam factors computed from the experimentally measured load residuals suggested that it can be approximated by a lognormal distribution (see Figure 6.3). In this form, the slam factor distribution will have a mean of 1.0 and a standard deviation, calculated from the data, of 0.4763. To determine whether the slam factor distribution is lognormal, a chi-square goodness-of-fit test was performed. For this arrangement, $\chi^2 = 6.29$, which falls well within the 95% confidence level, with the conclusion that the hypothesis cannot be rejected. Therefore, when a slam event occurs in the simulation, the slam load is predicted from the basis equation (Equation 6.1) and then multiplied by a random factor derived from the appropriate lognormal distribution to give the actual slam load.

This is an off-line model, where the motion history of the vessel is predetermined before the addition of slamming loads and slam loads are assumed not to influence the overall motion of the vessel. This is a standard assumption in many seakeeping codes; however it is unrealistic. Upon implementation in the time-domain simulation, it is envisioned that slamming loads will have some modest impact on subsequent vessel motions. Other limitations of this model is the small data set from which the slam load model was derived; slam data was analysed for only one irregular sea condition and two vessel speeds, making inferences to slamming behaviour in other conditions difficult. The following work involves a much larger data set.

6.2 Statistical Investigation

The previous section introduced the experimental basis for the basic method employed to model slam events in the time domain. The dataset used in that method came from a relatively small investigation into slamming in irregular waves. In comparison, the dataset collected during this project for the purpose of developing an extended on-line slam model is significantly larger. Chapter 5 presented the characteristics of slam events from a kinematic perspective and in this section, the slam characteristic distributions from the 2,103 recorded slam events are investigated and compared in preparation for a regression analysis.

Note that in keeping with statistical terminology and to avoid confusion, the 'slam parameters' discussed in the previous chapter will be now referred to as *variables* or *explanatory variables*. A *parameter* in statistical terminology refers to a characteristic of a population (the average of a population for example), whereas a *statistic* refers to a characteristic of a sample. This chapter will involve mainly *variables* and *statistics*.

6.2.1 Objective

It is essential to identify the aims of any statistical analysis before carrying out any detailed work. Statistical analysis is employed for three main objectives: data summary, prediction and process studies [74]. The focus of this investigation is the prediction of slam events, slam loads, locations, and durations by regression of experimental data. That being said, Wetherill [74] reminds the analyst not to restrict themselves to the primary objective, instead all relevant statistical tests should be undertaken to maximise the information that the data can give. Like all analytical methods, it is also vitally important to understand the assumptions and limitations of the chosen statistical methods and not follow them blindly.

6.2.2 Data Exploration

Wetherill [74] also defines some features to be aware of when exploring characteristics of the data; some of these are briefly described below. Not all of the features are applicable to the current study, however they have been kept in mind when examining the slam data. If any of these features are identified, it is best practice to attempt understand why that particular feature is present and tailor the regression to suit the nature of the data if necessary.

Linear relationships between explanatory variables is a common issue in regression analysis. There are several methods to combat multicollinearities among the variables; with careful selection of variables it is not thought to be a significant issue in this project.

Replication of observations refers to repeating observations in the response variable space. This can be useful in estimating the variance of the underlying error; an indication of repeatability. This feature has been observed in the experimental data, for example a given slam load has resulted from a range of relative vertical velocities. This large variance of observed data is not the result of measurement error, it is rather an indication of the non-deterministic

nature of attempting to predict the slam load from relative vertical velocity alone, and other variables may be required to reduce the error variance.

Slam events could possibly be influenced by **time trends** to some extent. Slam events have been visually noticed to occur on consecutive waves in packets of three or four with the vessel motions becoming more violent after each wave encounter until the final, most severe slam effectively halts the heave and pitch motions of the vessel. This suggests that slams do influence motions and a periodic factor could be included in the slam model to emulate this observation if necessary. This observation is purely subjective at the moment; a future study focusing on 'slam clusters' would be valuable in investigating this phenomenon further.

Boundary points within the data should also be identified. One obvious boundary is the slam load; it is never observed to be negative. The regression model must be examined carefully to ensure it behaves correctly close to the boundary regions, if it does not then the model may require modification, or sections of data should be ignored to prevent poor fitting in these regions. An example of a poor-fitting model can be seen in Figure 6.4; relative vertical velocity at the encountered slam instant is used to predict the slam load in a linear fashion. On the occasions when the relative vertical velocity is negative (less than -3m/s) a negative slam load results. Additionally, unrealistic outcomes must be avoided; if the model shown in Figure 6.4 is to be used, a piecewise function could be applied where a second model is applied outside of the 'operating point' of the first model.

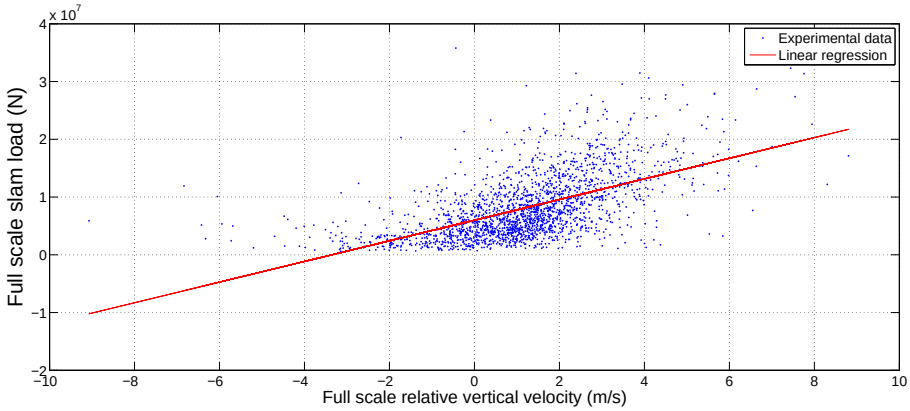

Figure 6.4: A poor regression model showing unrealistic negative slam loads when the relative vertical velocity at slam instant is less than -3m/s.

In some analyses **system change points** are apparent, this occurs when the system response changes at some point. In these cases a better approach may be to alter the regression model to account for this change, or have multiple models, one for each system. An example of this is the modified Wagner method proposed by Whelan [75] (recall Section 2.2.1 and Figure 2.5) where one model is applied during the first stages of the method and a separate one is applied for the second stage.

Outliers are data points that are found far away from the sample median. They are either

the results of measurement error or when sampling from a population with a heavy tailed distribution. Care must be taken when analysing data with outliers, the outlying points may be neglected or robust methods employed. In this work outliers in the data are intentionally included in the regression analysis as the primary goal of the work is to model the slam behaviour, which was found to be inherently heavy tailed.

The chosen potential slam prediction variables are shown in Table 6.1. Originally 25 different variables were collected, such as forward and aft demihull VBM, maximum elevations measured on the boat mounted wave probes prior to and at the slam instant, and the maximum immersion at the CBT after a slam event. Preliminary correlation analysis, inappropriateness and difficulties in adapting the variable for use in the time-domain method quickly eliminated some variables, leaving ten potentially important indicators of slam characteristics. For example the vertical bending moment was shown to be a good indicator of slam load (see Section 5.4.6), however it is more of an output parameter; the resulting demihull vertical bending moment is caused by the centre bow slam load and not vice versa. The ten remaining variables, shown in Table 6.1 include: the maximum slam load on the centre bow (once inertia and the global load is accounted for, see Section 5.3), the relative displacement of the wave surface and centre bow truncation at the slam instant (immersion, measured in metres), the instantaneous (at slam instant) and maximum relative vertical velocity at the CBT, the pitch angles and pitch velocity prior to and at the slam event, the location of the slam (measured from the transom) and the vessel speed.

All variables requiring a reference point shown in Table 6.1, such as relative vertical velocity and immersion are taken from the centre bow truncation by convention. Variables referring to a maximum are always measured *prior* to the slam, while all others are at the instant the slam is identified (at the time when the surface pressure was measured to be maximum, see Section 5.2 for the slam identification procedure). Variables that appear post-slam are neglected (such as maximum immersion after the slam event) because they are inappropriate in a time-domain method as only past and present data is known.

A preliminary correlation analysis was conducted on all 25 variables by calculating Pearson's correlation coefficient, r, and Spearman's rank correlation coefficient, ρ, for each variable against each other variable. This is a first-pass indicator of the importance of a particular variable with regards to slam load and it was also used to identify correlations between other explanatory variables. If high correlations exist between the explanatory variables, then multicollinearity may become an issue, resulting in unstable estimated regression coefficients. The effects of multicollinearity can be reduced by using a ridge regression technique.

Perhaps the most important axiom to remember when performing a statistical analysis is "Correlation does not imply causation" [74]. If a strong correlation is detected between two variables, it cannot be concluded from the correlation analysis alone that one variable causes the other one. Other variables that have not been included in the analysis may be responsible for the observed correlation, or the variables may be collinear.

Table 6.1: Slam characteristic variables.

F_s	Slam load on centre bow	N
I	Centre bow immersion at slam instant	m
V	Relative vertical velocity at slam instant	m/s
V_{max}	Maximum relative vertical velocity prior to slam event	m/s
x_{50}	Pitch angle at slam instant	rad
x_{50max}	Maximum pitch angle prior to slam event	rad
$\dot{x}_{50}$	Pitch velocity at slam instant	rad/s
$\dot{x}_{50max}$	Maximum pitch velocity prior to slam event	rad/s
Loc	Slam location from transom	m
U	Vessel speed	m/s

Spearman's rank correlation method has the advantage over Pearson in that it is better suited to detecting non-linear trends in data. Where Pearson's r is a reflection of the linear relationship between two variables, Spearman's ρ describes the degree in which the variable's relationship monotonically increases (or decreases). However some information is lost in Spearman's method as the magnitude of the data is not considered, only its rank within the data set, this does make it more robust to outliers however.

The Pearson product-moment correlation coefficient, r, determines the degree in which a linear relationship exists between two variables (the predictor variable X, and the criterion variable, Y). The definition formula for the Pearson product-moment correlation coefficient is given by Equation 6.5:

$$r_{XY} = \sum^{N} \frac{(x_i - \bar{x})\,(y_i - \bar{y})}{N s_X s_Y}. \tag{6.5}$$

Here N is the number of observations, x_i and y_i are the i^{th} observation of X and Y respectively, $\bar{x}$ and $\bar{y}$ are the means, and s_X and s_Y are standard deviations of X and Y.

The correlation coefficient r is an estimate of the correlation of the population which the variables where sampled from, it always falls within the range $-1 \leq r \leq +1$. The absolute value of r indicates the 'strength' of correlation between the two variables, as $|r| \to 1$ the linear relationship becomes stronger. As $|r| \to 0$ the predictive relationship decreases and the use of the X to predict Y may be no more accurate than a prediction based on a random process. The sign of r shows the direction of the relationship, a positive r implies a positive association whereas a negative r suggests a negative association.

The Pearson product-moment correlation coefficient method assumes a linear association (i.e. $y = mx + c$) exists between the two variables. If the relationship is better described by a higher order function, the value of r may not represent the true extent of correlation between the variables. That being said, if the computed r is close to 0, the possibility of a higher order correlation is very unlikely [61].

The assumptions of the Pearson product-moment correlation coefficient are:

1. The sample of n measurements are randomly selected from the population it represents.
2. The two variables have a bivariate normal distribution.
3. Homoscedasticity[1].
4. Nonautoregression (autocorrelation or serial correlation).

These assumptions are quite standard in statistical analysis, similar assumptions are made when applying OLS (ordinary least squares) regression models. Heteroscedasticity was detected in the preliminary slam module described in Section 6.1.1 and an attempt was made to correct this by scaling the residuals with the predicted slam load.

It is important to remember that the correlation coefficient is not a robust statistic, therefore r can be greatly influenced by high leverage points (outliers) and some caution must be exercised when excluding potential explanatory variables from the regression analysis based primarily on r values. The correlation coefficient table of all the chosen variables in Table 6.1 is shown in Table 6.2. These variables are the most likely candidates for inclusion in the slam module. Slam load, F_s, displays the highest correlation to relative vertical velocity (V) and it also has moderate correlations with pitch angle (both maximum and instantaneous) and maximum pitch velocity prior to slam ($\dot{x}_{50max}$). Vessel speed, U, has negligible correlation with slam load and poor correlation with the other variables. This is attributed to testing only three different speeds, however it will be included in the slam load prediction method as it is found that the inclusion of this variable reduces the residual variance [27].

Table 6.3 shows Spearman's rank correlation coefficients for all the chosen variables. As noted above, these coefficients represent the degree in which one variable monotonically increases (or decreases) with another. Comparing Table 6.2 with Table 6.3 it can be seen that if two variables are moderately correlated according to Pearson, they generally achieve a similar Spearman coefficient as well. One notable exception is centre bow immersion, I; the Pearson correlation coefficient is rather small (0.36) while the Spearman coefficient is considerably greater (0.68), suggesting that although the slam load tends to increase with immersion, the relation is not modelled well with linearly.

[1]Homoscedasticity refers to the distribution of residuals. The Pearson correlation coefficient assumes that the variance of residuals is constant, this means the strength of correlation between X and Y is equal along the entire range of both variables [61]. If this is not so, then the data can be said to be heteroscedastic. Heteroscedasticity does not cause OLS regression coefficient estimates to be biased, however it may cause the standard error of the estimate to be biased. This makes obtaining inferences from the data unreliable.

Table 6.2: Pearson product-moment correlation coefficients, r, for some selected variables. Correlations greater than 0.4 are highlighted in bold.

	F_s	I	V_{max}	V	Loc	x_{50}	x_{50max}	$\dot{x}_{50}$	$\dot{x}_{50max}$	S
F_s	**1.00**									
I	0.36	**1.00**								
V_{max}	**0.45**	0.27	**1.00**							
V	**0.58**	0.31	0.19	**1.00**						
Loc	0.28	0.16	0.06	0.23	**1.00**					
x_{50}	**-0.48**	-0.26	-0.07	**-0.49**	**-0.41**	**1.00**				
x_{50max}	**-0.46**	-0.25	0.05	**-0.44**	-0.39	**0.93**	**1.00**			
$\dot{x}_{50}$	0.17	0.24	-0.26	-0.01	0.18	0.05	-0.18	**1.00**		
$\dot{x}_{50max}$	**-0.54**	-0.32	-0.17	**-0.49**	**-0.42**	**0.94**	**0.89**	0.02	**1.00**	
U	0.00	-0.21	0.08	-0.15	0.10	0.28	0.30	0.21	0.21	**1.00**

Table 6.3: Spearman's rank correlation coefficients, ρ, for some selected variables. Correlations greater than 0.4 are highlighted in bold.

	F_s	I	V_{max}	V	Loc	x_{50}	x_{50max}	$\dot{x}_{50}$	$\dot{x}_{50max}$	S
F_s	**1.00**									
I	**0.68**	**1.00**								
V_{max}	**0.44**	0.26	**1.00**							
V	**0.61**	**0.61**	0.17	**1.00**						
Loc	0.29	0.29	0.03	0.24	**1.00**					
x_{50}	**-0.48**	**-0.54**	-0.06	**-0.49**	**-0.44**	**1.00**				
x_{50max}	**-0.46**	**-0.57**	0.06	**-0.46**	**-0.45**	**0.94**	**1.00**			
$\dot{x}_{50}$	0.18	0.18	-0.28	0.01	0.22	0.00	-0.20	**1.00**		
$\dot{x}_{50max}$	**-0.54**	**-0.56**	-0.15	**-0.49**	**-0.45**	**0.94**	**0.90**	-0.02	**1.00**	
U	0.00	**-0.42**	0.10	-0.17	0.12	0.29	0.30	0.19	0.22	**1.00**

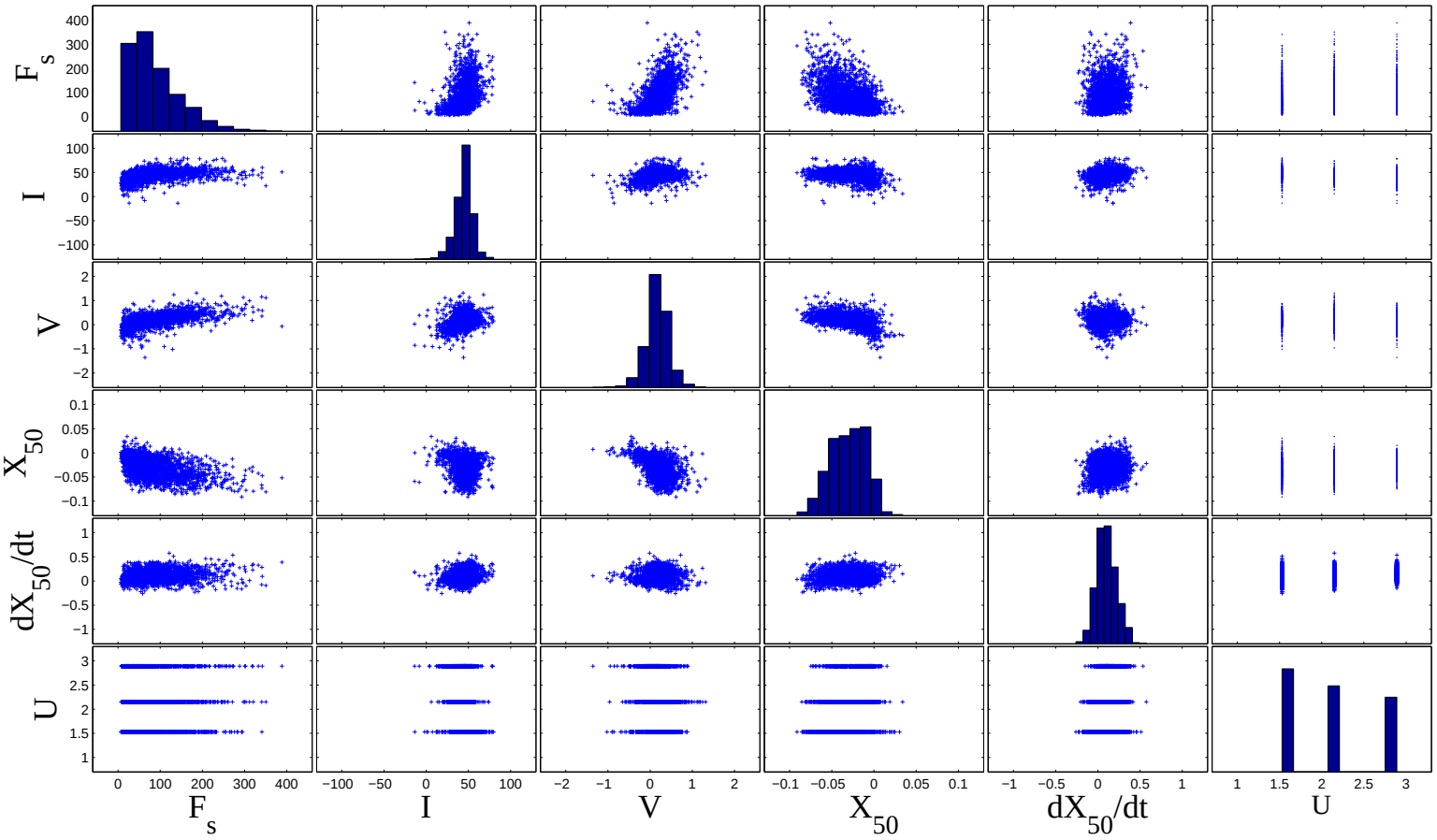

Figure 6.5: Scatter plots comparing variable correlations with each other. The diagonal plots show histograms of each variable, giving an indication of its distribution.

'Instantaneous' variables are chosen over the 'maximum prior to slam' variables as it is more realistic, and preferable, to be able predict the slamming behaviour of the vessel purely by the current state of the ship as opposed to recalling its past state. Relationships between the instantaneous variables are shown graphically in Figure 6.5 where all variables of note are plotted against each other, forming a matrix of plots. For the case where a variable is to be plotted against itself, a histogram showing the distribution of the variable is shown instead.

Further to the correlation coefficients, basic statistics of the chosen variables are shown in Tables 6.4 and 6.5. These tables effectively show a summary of each variable's distribution. The minimum, maximum, range and upper and lower quartiles (25th and 75th percentile respectively) are included in Table 6.4, while the IQR (interquartile range), median, mean, variance and standard deviation statistics are shown in Table 6.5.

Table 6.4: Basic statistics of selected slam variables

					Quartiles	
Variable	Units	Minimum	Maximum	Range	Lower	Upper
F_s	N	6.5186	388.60	382.08	42.7380	118.65
I	mm	-13.8229	79.8825	93.7054	39.1547	50.7344
V	m/s	-1.3554	1.3154	2.6708	0.0218	0.3285
x_{50}	rad	-0.0913	0.0339	0.1252	-0.0460	-0.0129
$\dot{x}_{50}$	rad/s	-0.2592	0.5750	0.8343	0.0974	0.1778
U	m/s	1.5400	2.9200	1.3800	1.5400	2.9200

Table 6.5: Basic statistics of selected slam variables - continued

		Inter-				Standard
Variable	Units	quartile range	Median	Mean	Variance	deviation
F_s	N	75.9090	72.1030	87.6750	3583	59.8580
I	mm	11.5797	45.3780	44.2985	107.2347	10.3554
V	m/s	0.3067	0.1794	0.1741	0.0711	0.2666
x_{50}	rad	0.0331	-0.0291	-0.0303	0.00045	0.0211
$\dot{x}_{50}$	rad/s	0.1543	0.0974	0.1044	0.0135	0.1163
U	m/s	1.3800	2.9200	2.1294	0.3129	0.5594

When selecting variables for the regression analyses detailed the following sections, the tables of correlations (Tables 6.2 and 6.3) and statistics (Tables 6.4 and 6.5) along with the features described above are revisited to ensure appropriateness or be aware of any limitations of a linear regression.

6.3 Slam Module Development

On-line implementation of the slam module involves several stages. Figure 6.6 is a flow chart illustrating the slam identification and application procedure as implemented in the time-domain seakeeping code. Conditions for slamming involve the immersion of the vessel at the centre bow truncation I_{CBT} and the change in immersion at this position relative to the previous time step dI_{CBT}/dt. A slam event is possible when and only when the immersion at the CBT and the change in immersion over one time step are positive (i.e. the CBT must be immersed and it must be 'immersing'). This is to prevent slams occurring at unrealistic phases of the ship motion. If these two conditions are fulfilled a slam event is not guaranteed however; a threshold immersion, (see Section 6.3.1) is applied to determine if a slam event occurs.

If the above conditions are met, and a slam event has occurred, a second subroutine (labelled Slam Module in Figure 6.6) is called. This subroutine determines the maximum slam load, location (if the identification method does not account for that), duration and rise time of the slam. It sets a counter variable (Slam count) to by-pass the slam module until the current slam is completely resolved and it also assigns a logical flag (New slam ready) to false to prevent a new slam occurring during the current cycle of motion. The logical flag is changed to true when the change in immersion over time is negative, that is, the bow and wave start to move apart. Note according to the condition $dI_{CBT}/dt > 0$, a new slam cannot occur until the bow begins immersing again.

The slam load and moment are applied to the LCG of the vessel. Currently only a heave load and pitch moment are applied on-line; however, in the event of modelling oblique seas the model can be extended to apply roll, sway and yaw loads in accordance with the actual slam location. However some approximations would be required for this extension, as no experimental data has yet been gathered for oblique, quartering or following seas. Once the slam load is applied, slam data is written to an output slam file for further analysis.

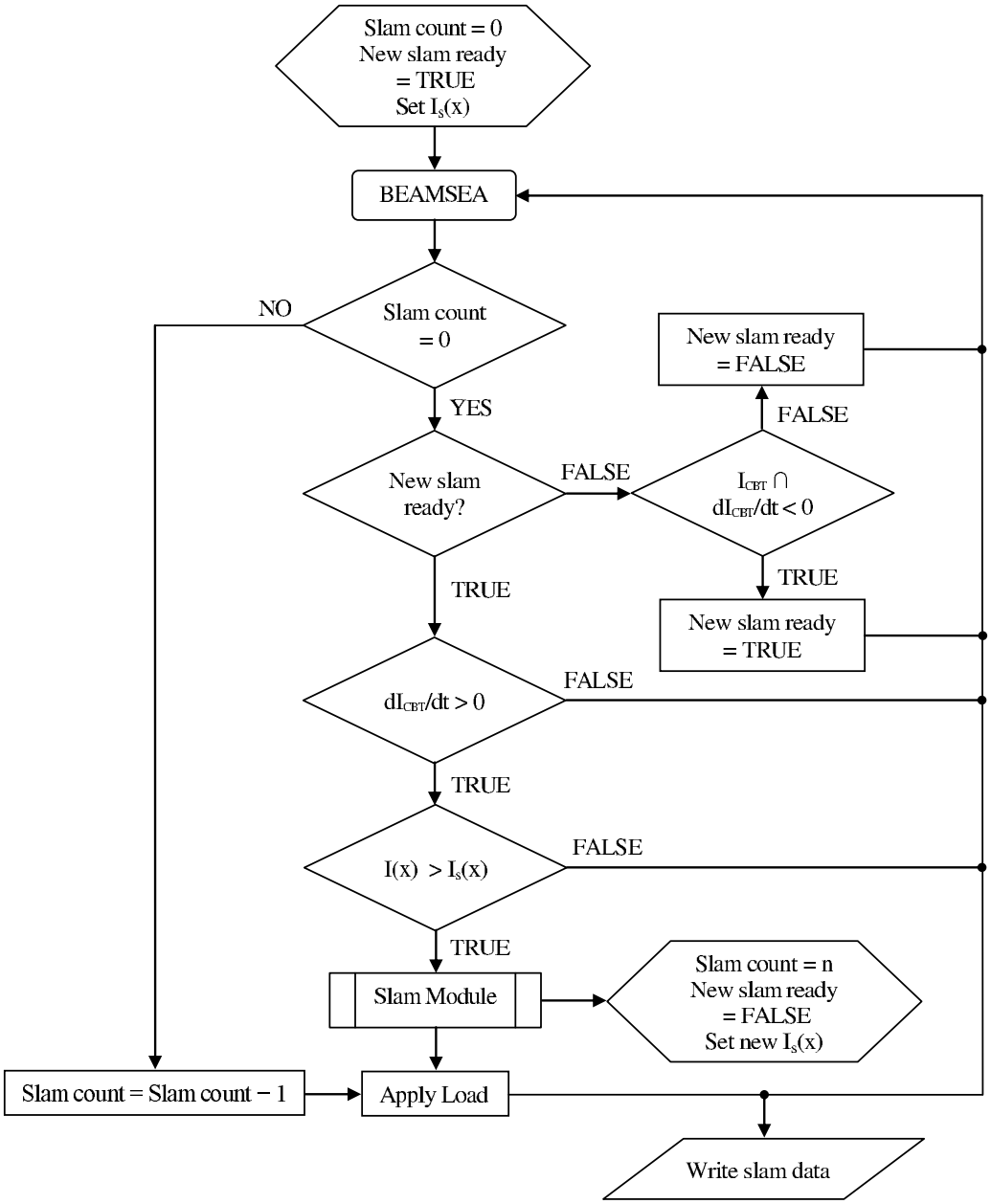

LEGEND	
Slam count	= Integer representing slam duration in time steps.
New slam ready	= Boolean, TRUE if a new slam is possible.
I_{CBT}	= Immersion at the centre bow truncation.
dI_{CBT}/dt	= Rate of change in immersion at centre bow trucntion.
$I_s(x)$	= Immersion required for a slam event at location x.
I(x)	= Immersion at location x.

Figure 6.6: Slam module flowchart.

6.3.1 Slam Identification

The ability to produce a realistic slam identification method is vital to the validity of the slam model. The simplest slam identification method is to apply a slam load when the oncoming wave contacts the surface of the vessel[2], however previous observations [45, 75, 77] and the slam characterisation undertaken in this project show that the peak centre bow slam loads occur prior to the archway becoming completely filled. Therefore an abstract slam identification algorithm is required to simulate the occurrence of slam events according to this observation.

Three different slam identification methods were developed and implemented in the time-domain seakeeping code. Comparisons of occurrence rates with experimental results, presented in Section 5.4.7, were used as the primary indicator of the methods' ability to emulate the slamming behaviour of the vessel.

The list below introduces the three different slam identification methods and a brief description of each method is given in the following sections. Each method involves measuring the difference between the local wave elevation and the calm waterline at one or more reference points along the vessel and setting a threshold immersion slam criterion. Slams were found to occur well before the relative immersion of the centre bow suggests that the archway is completely filled. Three-dimensional effects, such as splashing, run-up the archway and jetting of water are thought to significantly contribute to early filling of the archway and/or the onset of slam events. This observation led to the proposition of the 2D filling height as a tool (see Section 5.4.3) for estimating the amount of immersion of the centre bow required for centre bow slamming in head seas.

(a) Fixed threshold immersion criterion (2D filling height) at the centre bow truncation.
(b) Variable threshold immersion criterion at the centre bow truncation.
(c) Variable threshold immersion criterion at a number of sections along the vessel.

Two-Dimensional Filling Height Method

The Two-Dimensional Filling Height Method is identical to the slam identification method described earlier in Section 6.1.1. It involves applying a single immersion threshold criterion at the centre bow truncation. When the immersion of the vessel surpasses this threshold (the 2D filling height) at the reference point (the CBT), a slam is said to have occurred in the simulation. The disadvantage with this method is that slam events are identified at only one reference point on the vessel; a method to determine the actual location of the maximum slam load needs to be also applied as it is unrealistic to apply all slam loads at the reference point.

[2]Indeed this approach has been applied in an unpublished attempt to model slam loading in this seakeeping code. A 'wetdeck' file was specified, giving coordinates for potential slam positions relative to the vessel geometry file (points on the wetdeck). During the course of the simulation, local wave elevations are computed and compared with these wetdeck points, and if the wave elevation equals or exceeds the wetdeck location, a slam is said to have occurred.

Variable Threshold Immersion Criterion Methods

The Variable Threshold Immersion Criterion at the Centre Bow Truncation Method is an evolution of the 2D Filling Height Method. In place of having a fixed slam trigger criterion, a variable threshold criterion is applied. The concept of a variable threshold criterion is supported by Figure 5.25 on page 86; where slam events are seen to occur over a range of centre bow immersions for different conditions.

Distributions of CBT immersion when slams are identified during the experimental tests are used to estimate the average immersion at the CBT when slamming occurs. From the conditions tested, this was found to be generally less than the 2D filling height. A linear regression analysis including the forward speed of the vessel, U, (assumed to be time independent, i.e. constant during the seakeeping simulation) is undertaken to predict the average immersion required for a slam event to occur as shown by Equation 6.6:

$$I_\mu = a_0 + a_1 U \tag{6.6}$$

The residual of this regression, Figure 6.7, approximates a normal distribution. The variance of this normal distribution is used to modify the threshold immersion criterion, therefore:

$$I_s = I_\mu + \varepsilon. \tag{6.7}$$

Here I_s is the slam trigger immersion threshold, I_μ is the predicted mean immersion at the CBT for slamming to occur and ε is an independent and identically distributed random number based on the observed residual distribution of the OLS fit (this distribution is shown in Figure 6.7). In the seakeeping simulation, I_s is assigned first in the preliminary section of the code, then it is kept until the immersion of the vessel at the reference point equals or exceeds the slam trigger threshold. Once this criterion is met, a slam event is triggered and a new target immersion threshold is generated by drawing another random number (ε) and applying Equation 6.7 once more. This effectively creates a step-function trigger criterion, emulating the slam immersion distribution observed from the experimentation. The disadvantage with this method, like the Two-Dimensional Filling Height Method, is it relies on one reference point in space for slam identification. Therefore the actual slam location on the vessel requires further consideration.

In order to account for the location of slam loading during the identification process, and thus improve the realism of the slam identification algorithm in general, the method was extended by assigning target threshold immersions a series of locations along the centre bow and checking relative immersions at each location at every time step in the simulation (when a slam event is possible). Two different approaches were considered when determining the location-dependent immersion threshold: a method based on experimental measurements and a geometrically based, extended two-dimensional filling height method.

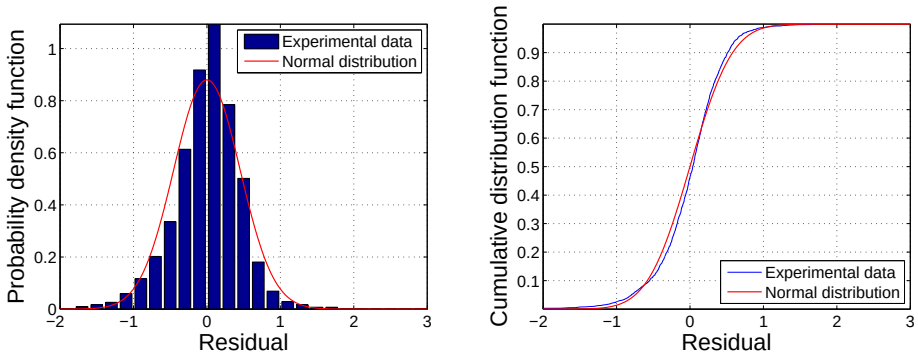

Figure 6.7: Probability density function and cumulative distribution function of the residual from an ordinary least squares regression of Equation 6.7 compared with the respective normal distribution.

For the first method, the boat mounted wave probe data were used to identify relative archway wave elevations at three locations during slam events. The median wave elevations from this analysis were used to fit a quadratic equation representing a simplistic immersion criterion at different locations along the vessel. Figure 6.8 shows the quadratic fit through the boat mounted wave probe data. Distance from transom is plotted on the x-axis, while immersion is shown on the y-axis (both have been scaled to full scale). The full scale two-dimensional filling height parameter is also included.

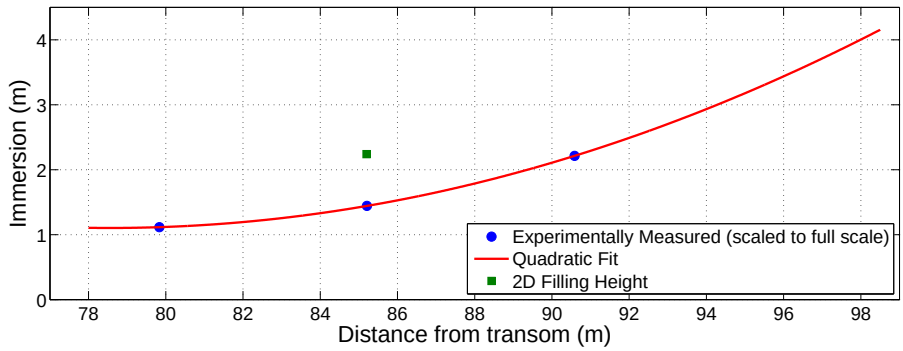

Figure 6.8: Slam trigger immersion threshold as a function of location along the vessel: experimental data method. The two-dimensional filling height is also shown.

The curve shown on this plot represents the threshold immersion as a function of position along the vessel. It can be described by Equation 6.8:

$$I(x) = c_0 + c_1 x + c_2 x^2, \tag{6.8}$$

where c_0, c_1, c_2 are coefficients from the OLS regression and x is distance from transom. This regression trend is shifted in the y-direction by reintroducing the variable offset (ε) concept from Equation 6.7. During the simulation immersions are calculated at 24 locations along the vessel bow. As soon as the immersion criteria is fulfilled at any one of these locations, a slam event is triggered and no more slams are possible until the current event is completely

resolved. Therefore slam events are limited to one during a given immersion cycle (note that the slam load is ramped up to a maximum and then down again over a number of time steps, as described below in Section 6.3.3). The slam load is applied at the location where the slam was first triggered.

The second method is an extension of the two-dimensional filling height concept, where the cross-sectional 2D filling height is calculated at locations forward and aft of the centre bow truncation (where the 2D filling height is originally defined). This was achieved by taking two dimensional cross sections and calculating tunnel areas from a computer-drafted three dimensional model drawn by Matsubara [53] during the initial stages of the scale model design. Figure 6.9 shows a piecewise quadratic trend highlighting pre and aft-CBT two dimensional filling heights. The 2D filling heights were calculated from the 3D computer model between 82 and 88m (full scale) from the transom. The trends shown in Figure 6.9 are an extrapolation of the measured 2D filling heights. The discontinuity in the trend arises from the sudden termination of the centre bow, resulting in an increased two-dimensional filling height as the location moves further aft. The maximum archway in the centre bow tunnel continues to decrease further aft, explaining the reducing filling height trend aft of the CBT.

The slam identification curve from the boat mounted wave probe trend is also included in Figure 6.9 for comparison, it can be seen that both methods show similar trends between 85 and 90m (if the vertical offset is ignored); this is the region where most of the slam action is thought to occur. The discontinuity in the geometric method results in very few slams occurring aft of the CBT.

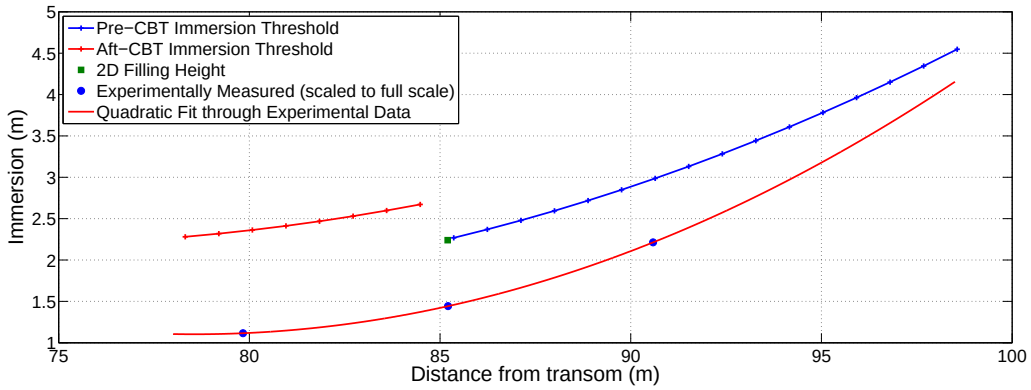

Figure 6.9: Piecewise slam trigger immersion threshold as a function of location along the vessel: geometry method. The 2D filling height and the experimentally based slam trigger from Figure 6.8 is also shown for comparison.

Section 6.4 explains the tuning of the slam identification model by replicating the slam occurrence rates measured experimentally. Comparisons between slam locations from the two slam identification methods are also shown.

6.3.2 Slam Load Magnitude

The slam load prediction method is very similar to that developed in the preliminary slam model shown in Section 6.1.1. The slam load calculation procedure consists of two components; a deterministic part and a stochastic element based on the residual of the deterministic fit. The predicted load equation was extended from the preliminary slam load prediction equation based primarily on relative vertical velocity at the centre bow truncation (Equation 6.1). Forward speed is the only other variable included in the new prediction equation. Pitch angle, pitch velocity and centre bow immersion were all considered and found to not enhance the regression.

$$L_p = a_0 + a_1 V_{rel} + a_2 V_{rel}^2 + a_3 U. \tag{6.9}$$

Here a_0, a_1, a_2 and a_3 are all regression coefficients, V_{rel} is the relative vertical velocity and U the forward speed of the vessel. V_{rel} differs from the preliminary model in that it is the relative vertical velocity at the slam event time and location, as opposed to the maximum relative vertical velocity at the centre bow truncation prior to the slam event. Applying the instantaneous relative velocity at the slam location is a more realistic approach.

Figure 6.10 shows the predicted slam load for three different speeds as a function of relative vertical velocity, also highlighted on this plot are potential outlying data points. These outliers were detected by normalising the residuals by 'studentising[3]' them and then investigating the resulting residual distributions. If a residual was found to be larger than expected in 95% of new observations, then it can be considered as an outlier. The identified outliers are retained in the regression as is it desired to attempt to model extreme events.

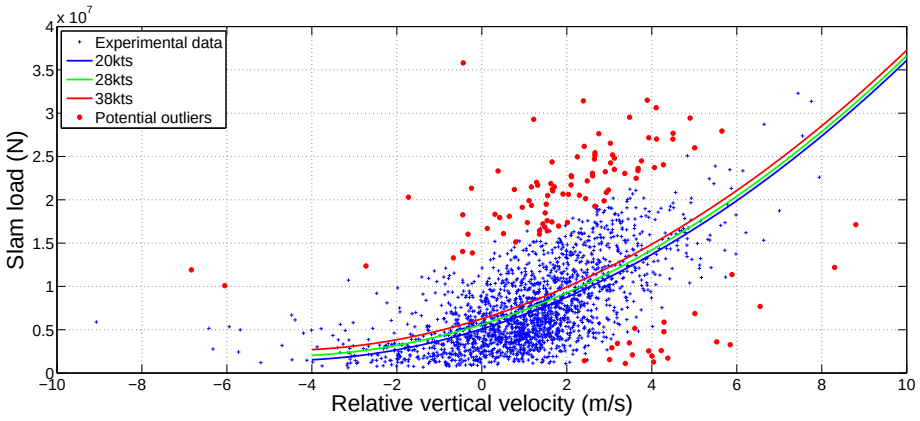

Figure 6.10: Slam load scatter plot, showing the slam load prediction equation (Equation 6.9) for three different vessel speeds. Outlier events are also highlighted by the red coloured dots.

Similar to the preliminary slam algorithm, the residual from this multi-dimensional fit is scaled by the predicted load (see Equation 6.4) and is used to form the stochastic element of the slam model. Figure 6.11 shows the scaled residual distribution compared with the corresponding

[3]Residuals are studentised by diving the residual by its standard deviation. This is done because the standard deviation of residuals are typically unequal from data point to data point [54].

lognormal distribution. In this case the fit is poor, although both the scaled residual and the lognormal distribution have identical means and standard deviations, there is a clear miss-match between the distributions. When the lognormal distribution is used to adjust the predicted load according to Equation 6.10, the resulting slam loads, L_{slam} were found to be generally smaller than the experimental results. This is due to the stochastic slam factor, F_{slam} being less than expected. Therefore in this case, the residual distribution cannot be successfully modelled by a lognormal distribution. There are two options available to improve the results, firstly choose another distribution, such as the Weibull or Rayleigh distributions, or secondly draw from the empirical cumulative distribution itself.

$$L_{slam} = F_{slam} L_p. \tag{6.10}$$

The second option is advantageous in that if the underlying population distribution is unknown, then drawing directly from the sample distribution is most likely more accurate than applying an ill-fitting distribution. The empirical cumulative distribution function was discretised, shown in Figure 6.12 and input into the time domain seakeeping code. A table containing the discrete empirical distribution is included in Table 6.6. When a slam occurs, a uniformly distributed random number is generated and the resulting stochastic slam factor is interpolated from the sample empirical cumulative distribution function. This approach is also more flexible than drawing from a standard distribution as the empirical cdf is input into the program from an input file; alternate empirical distributions can easily be applied without being locked into drawing from a given distribution.

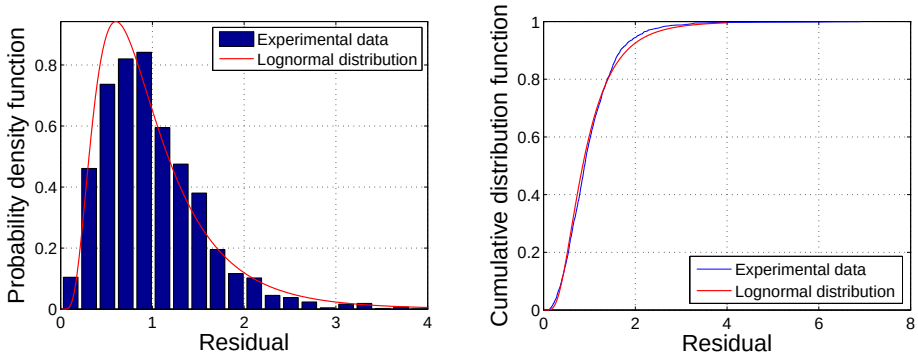

Figure 6.11: Probability density function and cumulative distribution function of the scaled residual of the predicted slam load compared with the respective lognormal distribution.

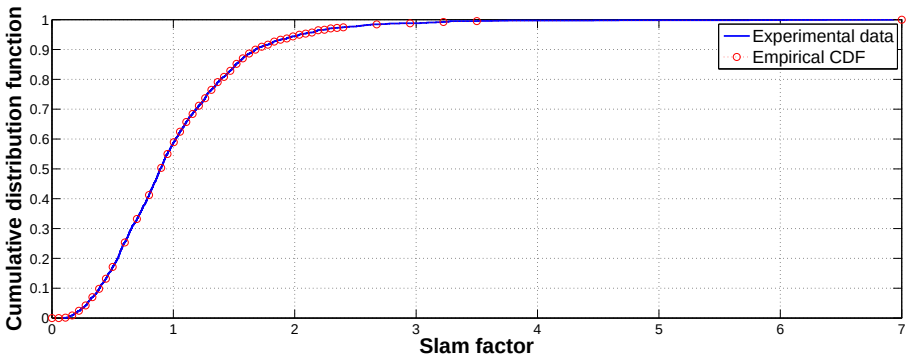

Figure 6.12: Empirical cumulative distribution function of the scaled residual of the predicted slam load.

Table 6.6: Slam factor table. F_{slam} is the slam load multiplying factor which is interpolated from a uniformly distributed random number between points shown in column ε.

ε	F_{slam}	ε	F_{slam}
0.0013	0.1111	0.8704	1.5724
0.0088	0.1667	0.8864	1.6241
0.0245	0.2222	0.8995	1.6759
0.0424	0.2778	0.9094	1.7276
0.0701	0.3333	0.9162	1.7793
0.0980	0.3889	0.9266	1.8310
0.1319	0.4444	0.9328	1.8828
0.1713	0.5000	0.9372	1.9345
0.2533	0.6000	0.9438	1.9862
0.3320	0.7000	0.9495	2.0379
0.4123	0.8000	0.9534	2.0897
0.5034	0.9000	0.9569	2.1414
0.5499	0.9517	0.9644	2.1931
0.5894	1.0034	0.9662	2.2448
0.6246	1.0552	0.9708	2.2966
0.6572	1.1069	0.9724	2.3483
0.6842	1.1586	0.9743	2.4000
0.7117	1.2103	0.9743	2.4000
0.7368	1.2621	0.9841	2.6750
0.7649	1.3138	0.9879	2.9500
0.7907	1.3655	0.9921	3.2250
0.8083	1.4172	0.9952	3.5000
0.8287	1.4690	1.0000	7.0000

6.3.3 Slam Duration

A similar method used for the slam load is utilised to determine slam durations: a prediction was made, then it was modified by an experimentally based stochastic factor. Mild correlation was found between slam duration and immersion at the centre bow truncation ($r = 0.39$), and duration and forward speed ($r = -0.513$). Inclusion of the immersion variable in the regression analysis reduced the variance of the scaled residuals by 3%, therefore it was included as an explanatory variable for the slam duration time. An ordinary least squares regression was used to calculate the predicted slam duration:

$$t_p = a_0 + a_1 U + a_2 I, \tag{6.11}$$

U is the forward speed of the vessel and I is the immersion at the centre bow truncation at the time that the slam is identified.

When scaled in a similar manner as described in Section 6.1.1 (Equation 6.4), the residuals of this least squares fit approximates a lognormal distribution, shown in Figure 6.13.

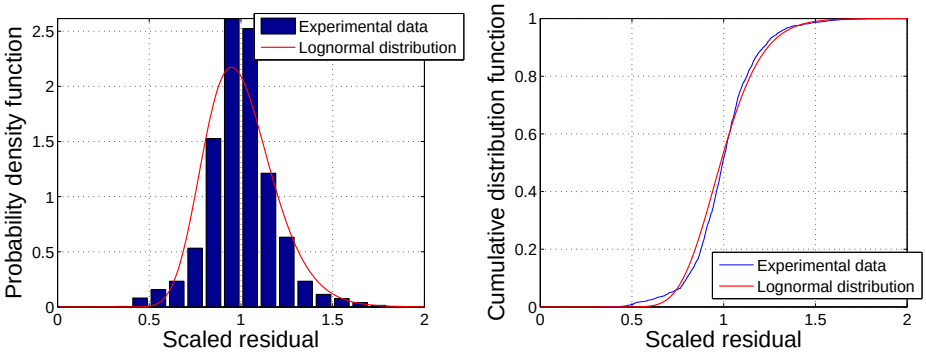

Figure 6.13: Probability density function and cumulative distribution function of the scaled residual of the predicted slam duration compared with the respective lognormal distribution.

Therefore when a slam is identified in the simulation, the slam duration can be predicted by Equation 6.11, and then modified by a factor derived from the scaled residual distribution shown in Figure 6.13, resulting in Equation 6.12:

$$t = (a_0 + a_1 U + a_2 I)\,\varepsilon, \tag{6.12}$$

where a_0, a_1 and a_2 are coefficients from an ordinary least squares regression, U and I are the forward speed of the vessel and immersion at the centre bow truncation respectively, and ε is an independent and identically distributed random number based on the observed distribution of the scaled residuals of the OLS fit. Table 6.7 shows the (full scale) parameters that represent the experimental distributions. From the signs of these parameters, the slam duration tends to increase with immersion and decrease with forward speed. It can also be estimated from Equation 6.11 that when the vessel is sailing at 38kts (19.55m/s), the predicted slam duration

is roughly 0.3s and from the standard deviation (σ) the permutation factor (ε) generally falls between 0.6 and 1.4, therefore the slam duration is expected to be in the range of 0.18 to 0.42s. The time step applied in the time domain seakeeping code is in the vicinity of 0.06s (for the 38kts case[4]), therefore a typical slam event occurs over 3 to 7 time steps. During this time, the slam load is ramped from zero up to a maximum and then back to zero. It may be recalled that the slam load traces displayed double peaks (attributed to vibration of the model, see Section 5.4.5), however due to the relatively coarse time resolution, there is no need to model this nonlinear behaviour.

Table 6.7: Parameters used to determine the slam duration.

a_0	0.3944	s
a_1	-0.0085	s^2/m
a_2	0.0279	s/m
μ	1.0168	s
σ	0.1900	s

Rise Time

The rise time (expressed as a percentage of slam duration) is based purely on the observed rise time distribution with no deterministic (regression) element. The rise time distribution, seen in Figure 6.14, appears to be bimodal with distinct local maxima at 0.25 and 0.5, these modes can be attributed to the double peaks seen in the time traces (refer to Figure 5.36) and the vibratory response of the model, observed in Section 5.4.5. The relative dominance of the first or second peak appears to be arbitrary.

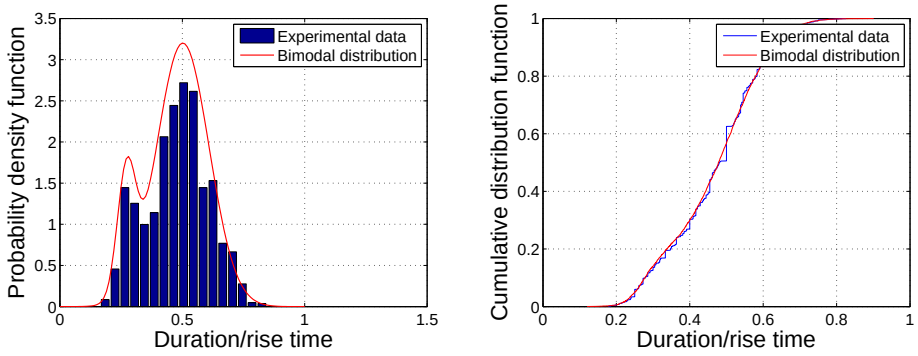

Figure 6.14: Probability density function and cumulative distribution function of the rise time (shown as a fraction of slam duration) compared with a bimodal distribution representing the observed distribution.

The pdf of the observed distribution can be represented by the following equation:

[4]Although not essential, to avoid the need to interpolate between strips, the time step in the seakeeping code is fixed such that the vessel advances one strip per time step. The governing equation is $dt = \mathrm{LOA}/(\mathrm{ns}U)$ where LOA is the overall length of the vessel, ns is the number of strips and U is the vessel speed. Therefore increasing the vessel speed and/or the number of strips modelling the vessel decreases the time step.

$$M = p\phi_1 + (1-p)\phi_2, \tag{6.13}$$

where ϕ_1 and ϕ_2 are normal distributions representing the two modes of the distribution and the mixing proportion p represents the relative dominance of each distribution. The approximate bimodal distribution was determined by applying an iterative expectation maximization (EM) algorithm. In this case, the mixing proportion p was found to be 0.14, therefore 14% of slam rise times are drawn from the first distribution with the remainder determined from the other.

With the slam duration and rise time known, a piecewise linear function is introduced to ramp the maximum slam load F_s (determined in Section 6.3.2) from zero at the start of the slam event to a maximum at the rise time and back to zero at the end of the slam duration. Since a constant slam load must be applied over each time step, the piecewise linear function is divided and averaged over each time steps, effectively becoming a vector of slam load weights, see Equation 6.14.

$$F_{slam}(i) = R(i)F_s, \tag{6.14}$$

here $F_{slam}(i)$ and $R(i)$ are the slam load and slam weight at time step i respectively and $F(s)$ is the maximum slam load.

Figure 6.15 shows a typical step rise slam load ramp up and down. The slam load, shown on the y-axis, has been non-dimensionalised. In this case the load reached a peak at about 0.07s, and a secondary peak can be found at 0.21s. The secondary peak has been neglected when determining the linear ramp up and down. The total duration of the slam is divided into a number of time steps, in this particular instance the seakeeping code time step is 0.06s and the measured slam duration is 0.29s, therefore the slam duration is rounded to the next whole time step (0.32s) and the slam load is ramped linearly up to the time of maximum load and back to zero at the end of the slam duration. In this example the total slam duration is five time steps long. The histogram in Figure 6.15 represents the equivalent constant slam load applied over each time step ($R(i)$ in Equation 6.14).

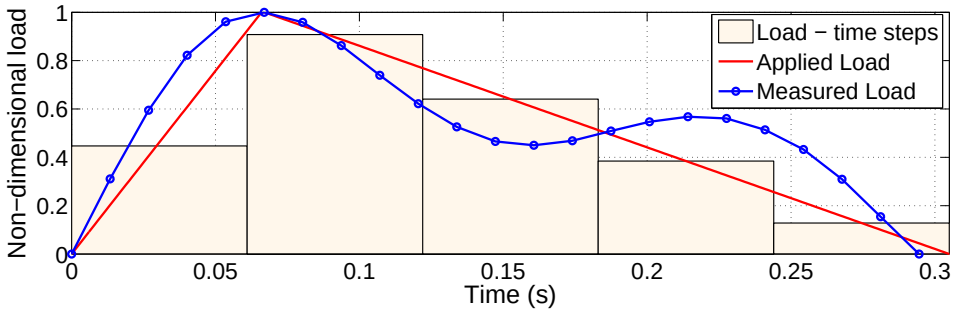

Figure 6.15: Typical step rise slam load ramp up and down. Measured experimental data is shown along with the linear approximation. The histogram represents the slam load weighting factor for a given time step in the time-domain simulation.

6.4 Slam Module Validation

For the slam module to be performing correctly, it should be able to predict slam loads, locations and occurrence rates representative of actual ship behaviour. Since the time-domain seakeeping code used in this project is inherently a two-dimensional strip theory; a three-dimensional correction factor could be introduced in order to account for three-dimensional effects not considered in the two-dimensional analysis.

The first characteristic to be verified is slam occurrence rates. Two parameters can be altered to control the occurrence rates: the vertical damping force coefficient introduced in the seakeeping code itself, and the mean slam immersion threshold criterion. The vertical damping force coefficient was originally developed as an empirical method to model viscous damping in order to match resonant responses with scale model experiments [15] (this factor is further discussed in Appendix B). Although raising the vertical damping coefficient will reduce the motions of the vessel (and thus slam occurrence rates), care must be taken when altering this parameter, as it is important to maintain realistic motions.

The second parameter mentioned raises or lowers the slam threshold shown in Figure 6.9 (by adding an extra constant to Equation 6.6). This extra constant can be thought as a 'three-dimensional correction factor' since the two-dimensional assumption inherent in strip theories neglects the fully three-dimensional fluid dynamics observed during slamming.

Figure 6.16 compares the slam occurrence rates determined by the three slam identification methods described in Section 6.3.1 with the scale model occurrence rates measured experimentally (from Section 5.4.7). Three conditions are shown: significant wave height 4.0m, speed 38kts and modal periods 7, 8.5 and 10s. The occurrence rates were calculated by summing the number of identified slams over a 20 minute simulated time period and dividing by the total simulation time. The vertical damping force coefficient was set at 0.08; matching the motions with model scale as much as possible, even though the shift in the vessel response frequency is still present (see the discussion in Section 4.6). The filling heights are also set as default, in the case of the 2D filling height methods at the CBT, this is as calculated from the 3D computer model and for the filling heights calculated at different locations, this is based on experimental measurements and on the geometry of the vessel respectively.

It can be seen that every identification method over predicts slam occurrences. Figures 6.17 and 6.18 shows how the filling height criterion and vertical damping force coefficient affects the resulting slam occurrence rates. The slam identification model used in Figure 6.17 is the geometry-based 2D filling height at different locations along the vessel, this model was chosen over the experimentally-based method as it is more intuitive as it follows the form of the vessel. There is a linear trend between filling height and slam occurrence rate. However, the filling height correction required to match scale model results appears to be a function of condition. For example to correct for the 7s modal period condition, a filling height correction of +0.2m would suffice, but for the 10s modal period condition in excess of +0.8m is required (probably

+0.9 to +1.0m).

Figure 6.18 shows the influence of the vertical damping coefficient on slam occurrence rates. It may be remembered from Chapter 4 that a damping coefficient of 0.08 to 0.10 is required to match the magnitude of the peak dimensionless heave and pitch motions for the 112m Incat vessel. The damping coefficient/occurrence rate trend is as clear for the 7s modal period condition as the 10s condition, but what is apparent from this plot is the relatively large damping coefficient required to reduce the slam occurrence rates to match the experimental measurements: a damping coefficient roughly ten times that required to match the motions. This is unacceptable as it has a detrimental effect on the predicted motion RAOs, therefore the filling height criterion is used as the primary occurrence rate correction factor.

A sample of slam locations are shown in Figure 6.19. Slam location (distance from transom in metres) is shown on the x-axis and normalised occurrence frequency is plotted on the y-axis Three frequency polygons are shown comparing slam location distributions of the two variable location slam identification methods, discussed in Section 6.3.1, with experimental data. The centre bow truncation is located 85m from the transom. The polygon highlighted with circles comes from the quadratic fit through the boat mounted wave probe data seen in Figure 6.8, whereas the second polygon represents the location distribution from the piecewise geometry-based method shown in Figure 6.9. The third polygon marked with plus-signs is from experimental data.

A difference is seen between predicted and experimentally measured slam locations. For the condition shown (4m wave height, 7s modal period, 38kts vessel speed), the experimental results suggest most slams occur aft of the centre bow truncation. Both slam identification (the quadratic line-of best-fit and the geometry based 2D filling height) methods identify the majority of slams forward of the centre bow truncation, the piecewise geometry-based method exclusively forward of the CBT for this particular set of runs.

Slam location analysis requires further investigation, as some discrepancy has arisen with regards to slam location measurements conducted previously by Lavroff [45], Matsubara [53] and the work presented in this thesis (further discussion on this issue can be found in Section 5.4.4). It has been noticed that the slam location distributions presented here and in Lavroff [45] are centred on the centre bow truncation (indeed this is the location where the 2D filling height was defined, as it was believed that the majority of slam events occurred in this area). This could possibly be due to the arrangement of the experimental system rather than the actual location of the slam load. At the time of writing, a new segmented model (the same scale as the existing one) representing the 112m Incat catamaran has been constructed with a different configuration designed to accurately measure slam locations. More on this new model can be found in Section 8.3.

A section of heave and pitch time traces from the simulation are shown in Figures 6.20 to 6.25. The vessel is sailing at 38kts in 4m waves of modal period 10s. Each dot on the plots represent a time step where slamming is occurring. During the 20s of data shown, three slams

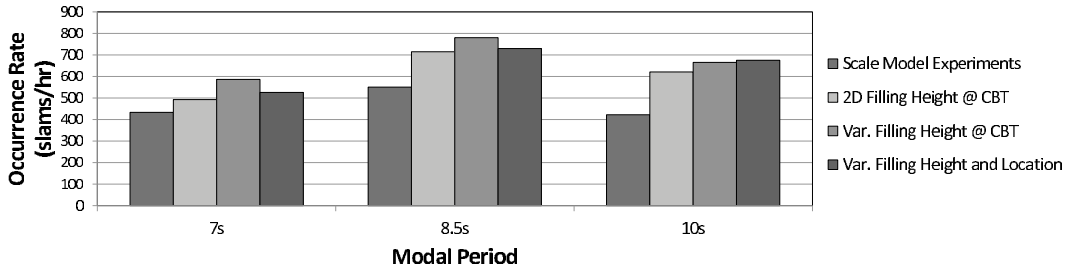

Figure 6.16: Slam occurrence rates for the four slam identification methods. Data grouped by modal period. Significant wave height 4.0m, speed 38 knots. Default filling heights and damping coefficients.

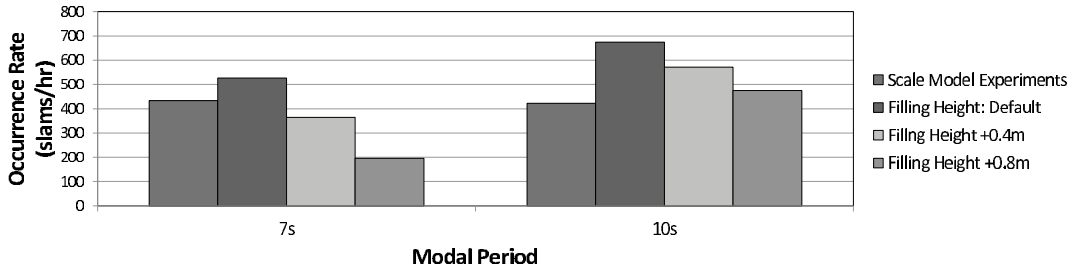

Figure 6.17: The influence of the filling height criterion on slam occurrence rates. Variable threshold immersion criterion method at a 24 locations. Data grouped by modal period. Significant wave height 4.0m, speed 38 knots. Default damping coefficient (0.08).

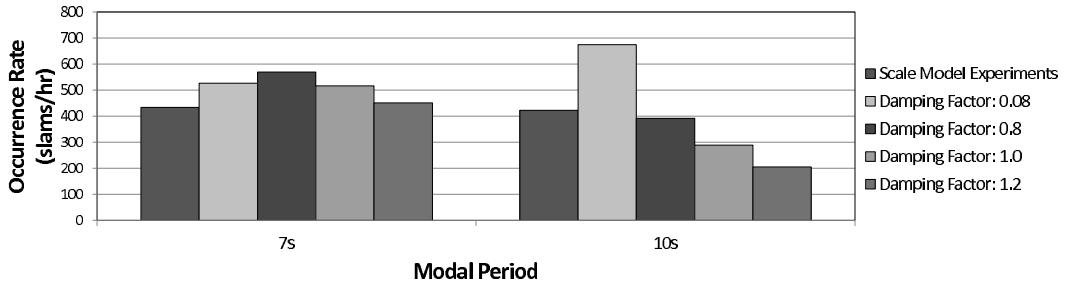

Figure 6.18: The influence of the sectional vertical damping coefficient on slam occurrence rates. Variable threshold immersion criterion method at a 24 locations. Data grouped by modal period. Significant wave height 4.0m, speed 38 knots. Default filling height.

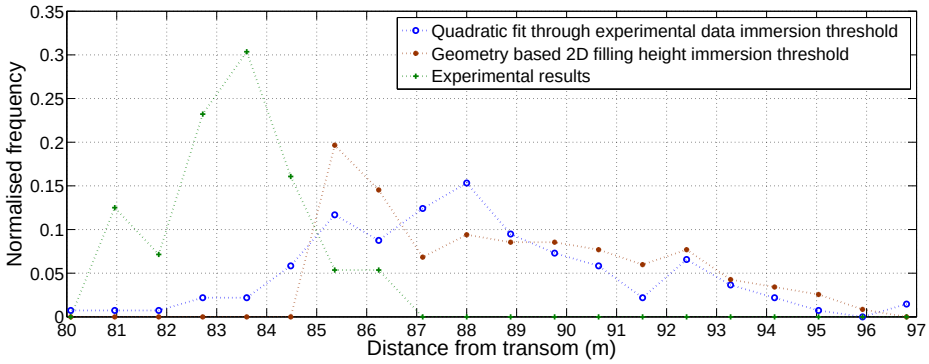

Figure 6.19: Frequency polygon of slam locations comparing the two variable location slam identification methods with experimental results. The CBT is located 85m from the transom.

have occurred on three consecutive waves; at 131s, 135.4s and 138.9s. The first two slams are six time steps in duration (0.22s duration) and the third one has a duration of five time steps (0.18s). The second slam event is the largest, applying a slam load of 5.8MN at its peak. The maximum load of the first slam is 2.4MN and the third slam is relatively minor at 1.0MN.

The slam events are too short in duration to significantly change the global motion of the ship, as shown in the heave and pitch time traces (Figures 6.20 and 6.23 respectively). However their influence can be seen in the heave velocity (Figure 6.21) and pitch velocity 6.24, the effect of the second slam in the series is particularly noticeable. Although none of these slams explicitly change the direction of motion of the vessel, significant deceleration is observed, particularly in heave.

Figure 6.26 presents comparisons between experimentally measured (shown in plot (a)) and simulated relative vertical velocity at the slam instant distributions (plot (b)) for two conditions, 7s and 10s modal periods (significant wave height 4m and vessel speed is 38kts for both conditions). The experimental data (plot (a)) shows that slams tend to occur in the 7s period condition when the relative vertical velocity is small and often negative (the ship and wave are moving apart at the CBT), whereas the 10s period has a greater variance and the majority of slam events occur when the wave and ship are moving together at the CBT. Plot (b) shows that slams occur in the simulation at a greater relative vertical velocity during the 10s period compared with the 7s condition, as observed in the experimental data. However when the distributions from experimental results are compared with the simulation, the simulation tends to predict larger relative vertical velocities at the slam instant, resulting in larger slam loads than the simulation (as shown in Figure 6.27).

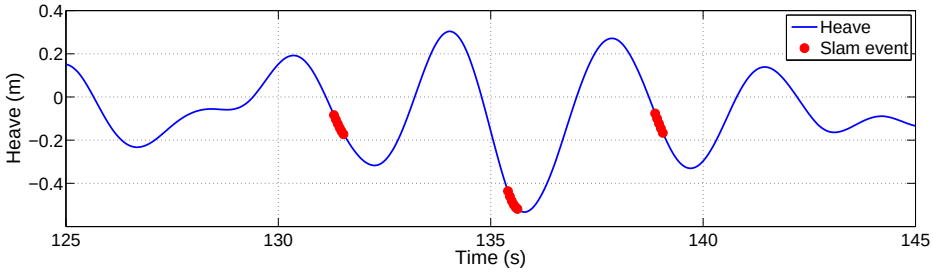

Figure 6.20: Heave time trace, three slam events at 131s, 135.4s and 138.9s are highlighted. Condition 107: $H_{1/3} = 4.0$m, $T_0 = 10.0$s, U =38kts.

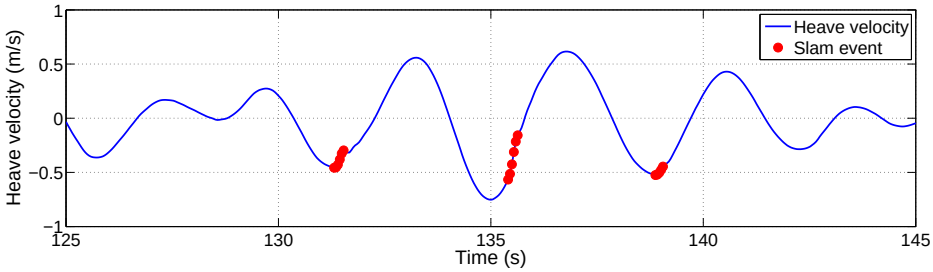

Figure 6.21: Heave velocity time trace, slam events at 131s, 135.4s and 138.9s are highlighted. Condition 107: $H_{1/3} = 4.0$m, $T_0 = 10.0$s, U =38kts.

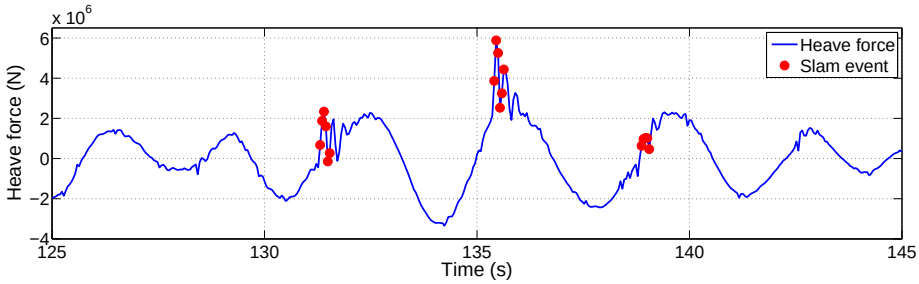

Figure 6.22: Heave force time trace, slam events at 131s, 135.4s and 138.9s are highlighted. Condition 107: $H_{1/3} = 4.0$m, $T_0 = 10.0$s, U =38kts.

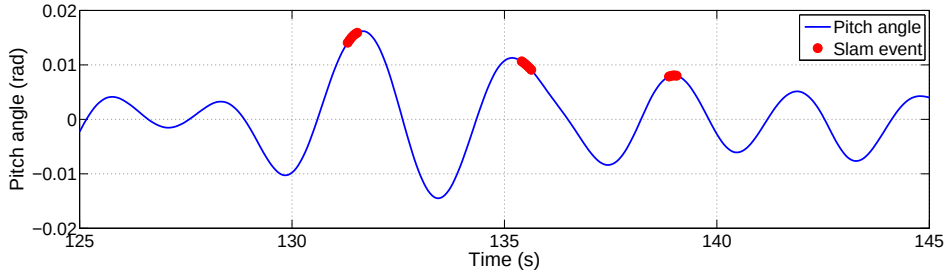

Figure 6.23: Pitch angle time trace, three slam events at 131s, 135.4s and 138.9s are highlighted. Condition 107: $H_{1/3} = 4.0$m, $T_0 = 10.0$s, U =38kts.

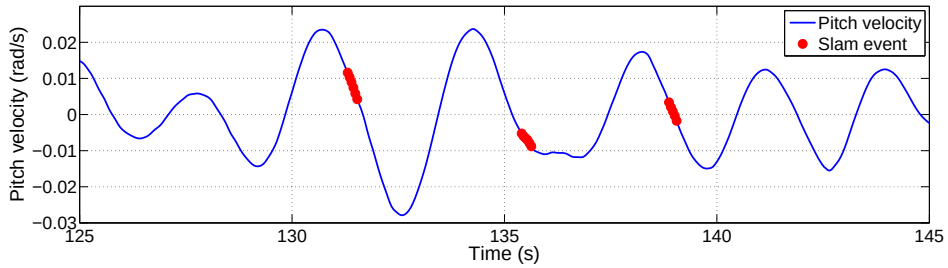

Figure 6.24: Pitch velocity time trace, slam events at 131s, 135.4s and 138.9s are highlighted. Condition 107: $H_{1/3} = 4.0$m, $T_0 = 10.0$s, U =38kts.

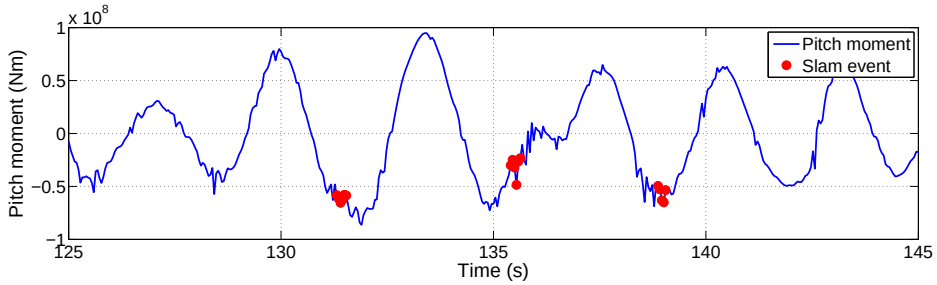

Figure 6.25: Pitch moment time trace, slam events at 131s, 135.4s and 138.9s are highlighted. Condition 107: $H_{1/3} = 4.0$m, $T_0 = 10.0$s, U =38kts.

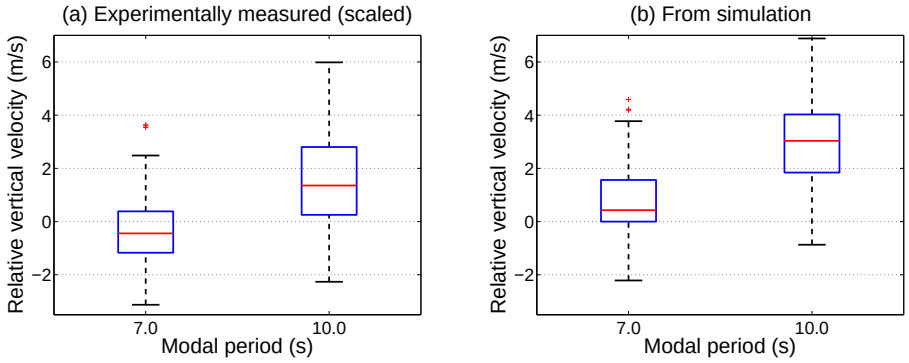

Figure 6.26: Comparison between (a) experimentally measured and (b) simulated relative vertical velocity distributions at the CBT when slams are identified (significant wave height 4m, vessel speed 38kts).

The slam load distributions are shown in Figure 6.27. Plot (a), experimental data, shows relatively small slam loads for the 7s condition and larger slams at 10s, with two extreme events detected in the latter condition. Plot (b) shows the slam load distributions resulting from the simulation. Both slam load distributions from the simulation are more spread than the experimentally measured results (and more outliers are present). The median slam load from the simulation also exceeds the experimentally measured median. The 7s modal period condition has a smaller variance and median than the 10s condition, which can be attributed to the smaller variance and median of relative vertical velocity distribution in Figure 6.26. This verifies that the slam module is behaving as expected, however the seakeeping simulation has a tendency to over predict relative vertical velocities and thus slam loads.

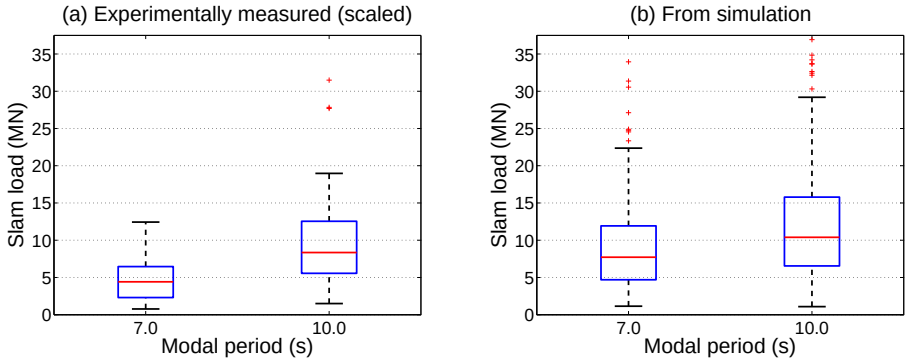

Figure 6.27: Comparison between (a) experimentally measured and (b) simulated slam loads (significant wave height 4m, vessel speed 38kts).

6.5 Summary and Conclusions

An on-line time-domain slam model has been developed, based on scale model experimental results. Slam identification involves defining a location dependent immersion threshold based on the 2D filling height concept combined with a stochastic permutation from experimental observations. Slams are identified by checking relative wave elevations between the ship and the wave at these locations. If the immersion threshold is exceeded at any location, a slam is said to have occurred at the location where the threshold was first tripped.

The maximum slam load consists of two components: a deterministic part resulting from a regression on experimental data and a stochastic part based on the scaled residuals of the regression. Forward speed and relative vertical velocity at the CBT are two variables used to predict the slam load. Once the maximum slam load is predicted, it is multiplied by a factor drawn from an empirical cumulative distribution function. This emulates the observed slam distribution from scale model experiments.

Slam loads are applied over a number of time steps. The slam load starts at zero and is ramped to a maximum then ramped down to zero again when the event is finished. The durations are determined by following a similar method to the maximum slam load calculation method. Durations are assumed to be a function of vessel forward speed and immersion at the centre bow truncation. The duration is predicted via a regression of experimental data and then modified by applying a random factor drawn from lognormal distribution based on experimental observations. The time when the maximum load is applied is also determined purely from the experimental data, this time a bimodal distribution is used. The slam load is assumed to ramp linearly to a maximum and back to zero and since the time-domain simulation is time-stepped, the average slam load for each time step is applied.

The slam identification, maximum load and duration calculations are all based on experimental data for one particular hull form. If the seakeeping analysis was to be performed on a different hull form, a different slam prediction equation (or regression coefficients) and a slam factor cumulative distribution function may need to be developed. It is thought that similar hull forms (such as the wave piercer catamaran) would require only minor adjustments, however, it would be important to conduct a series of preliminary scale model tests on a different design just to determine the sensitivity of hull form on the resulting empirical slam parameters. For different but similar hull forms, altering the empirical functions or regression coefficients for different applications is not an issue as the program has been coded with this functionality in mind.

The slam module assumes headsea conditions as the experiments were all conducted at headseas, the model can be extrapolated to predict slamming in oblique and quartering seas by identifying slams in the centre of each demihull archway and applying a slam roll moment by assuming that the slam is offset from the centreline of the vessel, however, additional scale model tests are required at bow quartering seas to confidently extend the slam module further.

Chapter 7

Case Study: Tsugaru Strait

Figure 7.1: Hakodate ferry terminal with 112m Incat catamaran *Natchan World*. Image from Google Maps.

7.1 Introduction

An application of the integrated motions and loads prediction tool developed over the course of this project is presented in this chapter. An actual high-speed ferry service route is selected and real wave data used to determine the expected wave environment for this route. The computer simulation is run for a range of sea conditions and slam events are identified. The slam event statistics are then extrapolated to produce long term loading expectations.

Figure 7.2: Regional map showing the Tsugaru Strait route between Aomori, Honshū to Hakodate, Hokkaidō. Image from Google Maps.

7.2 Route and Wave Data

The service route chosen for this case study is the Tsugaru Strait, located between the main island of Japan, Honshū and the northern island, Hokkaidō. Two 112m class Incat vessels operate in this strait; *Natchan Rera* (Incat hull 064, shown in Figure 3.3, the basis of the hydroelastic segmented model used in this project) and *Natchan World* (Incat hull 065). The ferries service the towns of Aomori, Honshū and Hakodate, Hokkaidō (see Figure 7.2). The route length is 113km (61 nautical miles) with an estimated average transit time of 1 hour, 45 minutes at 35kts [58].

When heading South from Hakodate the wind and wave direction is predominately bow

quartering. The route can be varied slightly for the first half of the voyage depending on prevailing weather conditions in order to minimise headseas. The second half of the route is well protected from Westerly weather. The maximum fetch to the East across Mutsu Bay is 50km and the maximum wave height expected from the East, during 30 knot winds is 2m [58].

The reverse trip, from Aomori to Hakodate, is predominately stern quartering seas and as such centre bow slamming is not expected for this leg of the trip [58].

Tsugaru Strait wave data was provided to Revolution Design Pty. Ltd. by Higashi Nihon and has been adapted for this case study. The wave data was originally used by Revolution Design for the purpose of investigating motion sickness incidence for several proposed routes in the strait [58]. Table 7.1 shows the adapted wave data used in this case study. Significant wave height and modal period are shown along the left hand side and top of the table respectively, percentage of observations are the table entries. Also included in this table are the vessel's operating speeds, shown as cell shading. In calm conditions (<0.5m significant wave height) the ferry will likely travel at 38kts safely, between 1.0m and 2.5m waves the vessel will operate at 35kts and at larger sea states the vessel will transit at 20kts. Table 7.2 summarises the significant wave heights and their expected occurrences. The wave height is less than 2m for 75% of the observations; minimal slamming is thought to occur for these conditions. Also in the higher wave height observations (particularly greater then 4m) caution is exercised and temporary suspension of the ferry service will likely occur.

Table 7.1: Wave data: significant wave heights and modal periods. The entries in the table show percentage of occurrences. The shaded cells show expected operating speeds for the different wave conditions.

Significant wave height (m) \ Modal period (s)	2	3	4	5	6	7	8	9	10	11	12
0.5		2.9	10.5	6.2	1.7	0.5					
1		1.4	11.0	11.9	5.3	1.2	0.1				
1.5			2.4	8.0	8.2	3.2	0.5	0.1	0.2		
2				3.9	5.2	2.8	0.8				
2.5				0.3	2.3	2.9	0.9				
3						1.3	0.8	0.2			
3.5						0.3	0.7	0.2			
4							0.9	0.3	0.1		
4.5							0.2				
5								0.3	0.1	0.1	
6								0.1			

Operating Speeds

38kts

35kts

20kts

As noted above, the average transit time per trip is estimated to be 1 hour and 45 minutes.

Assuming the vessel makes three round trips per day, seven days a week, 48 weeks a year (4 weeks are reserved for maintenance duties), this means the ship is crossing the strait for 3,528 hours each year and 70,560 hours in twenty years.

Table 7.2: Summary of significant wave heights and their occurrence.

Wave height	Occurrence %
<2m	75.3
2m-3m	19.1
3m-4m	4.8
>4m	0.8

7.3 Long Term Statistics

Long term loading characteristics can be investigated by applying statistical methods commonly used when forecasting extreme natural events such as storms, floods or earthquakes. In order to take this approach, the slam load probability density functions for each condition are weighted according to the expected the percentage of occurrences shown in Table 7.1 and then summed to create a single slam load probability density function representative of the total slam properties[1]. The weighted probability density function can then be integrated to give the cumulative distribution function.

This method allows great flexibility as the gathered data is not limited to this route, it is possible to model slamming behaviour of the vessel in any given route (provided the type of sea spectra used in the simulation, e.g. JONSWAP, is valid) by reallocating the sea state occurrence weights to suit a new sea route environment. This allows for the recycling of the collected data, which can be stored in a database and added to future simulations for use in other scenarios. With more simulation time and slam events, future predictions of extreme events will have greater resolution.

In order to conduct a statistical investigation, the slam events are assumed to follow a Poisson process. The probability of obtaining exactly k observations of X, if X has a Poisson distribution with an expected frequency of λ, is given by Equation 7.1:

$$f(k;\lambda) = Pr(X = k) = \frac{\lambda^k e^{-\lambda}}{k!} \tag{7.1}$$

The probability of observing at least one event equal to or greater than a given severity is shown by Equation 7.2, the probability of exceedance P_e:

$$P_e(X) \quad = \quad 1 - f(0,\lambda)$$

[1]The same method was used to determine the rise time bimodal distribution in Equation 6.13 on page 130, in that case the weight (mixing proportion) was 0.14 for one distribution and 0.86 for the other.

$$= \quad 1 - e^{-\lambda} \tag{7.2}$$

The return period, T, for an event with an average frequency of λ and particular severity can be approximated by the inverse of the exceedance probability, Equation 7.3:

$$\begin{aligned} \lambda T &= \frac{1}{P_e} \\ \therefore T &= \frac{1}{\lambda P_e} \end{aligned} \tag{7.3}$$

The return period is defined as the average time required to observe a slam of a given severity or greater. This is not to say that a slam of this severity occurs once every T-years in this sea condition, but a T-year event has a 1/T chance of being exceeded in any given year. Actually there is a 63% probability of exceeding this slam load in a T-year period. This is explained by Equation 7.4; the encounter probability, P_E.

$$P_E = 1 - (1 - e^{-\lambda})^N \tag{7.4}$$

where N is the period in years for the event to occur (for a T-year event, $N = T$, resulting in the 63% exceedance probability mentioned above). Encounter probability curves can be produced for differing number of years. Plots generated by these methods are presented in Sections 7.4.2 and 7.4.4. From this analysis, provided sufficient slam events have been observed. it is possible to estimate magnitudes of rare slam events (10-year or 20-year slam events for example) in this environment.

7.4 Results

A series of simulations was run for each condition, starting from the worst (the bottom right conditions in Table 7.1) and working back to the more mild conditions. Since the objective of this case study is the investigation of extreme slam events, when a slam event was not detected in 15 minutes of simulated sea time, it was concluded that that particular condition is too mild for slamming and no more runs were conducted. After conducting all simulations, a total of 1,152 slams were generated over 5 hours and 38 minutes of simulated sea time. This is arguably a short amount of sea time to extrapolate long term slam load statistics, however it is sufficient to demonstrate the statistical methodology.

7.4.1 Occurrence Rates

Occurrence rates for each condition are determined by dividing the number of measured slams by the time spent in that condition. Table 7.3 shows the expected slam occurrence rates for each condition. A region of no slamming can be seen for low wave heights. Transitional conditions,

where slamming is first identified for a given modal period, are highlighted with grey shading. Slam occurrence rates increase with significant wave height, as expected. Also noticeable in this table are maximum slam occurrence rates for the 8s modal period conditions. The slam rates for 7 and 9s modal period conditions, for a given significant wave height are all less than the corresponding occurrence rate for 8s, providing evidence that resonance for this ship configuration is around that encountered frequency. Peak motions around 8s modal period were observed during scale model testing in Chapter 5, the occurrence rates compare reasonably to the scale model results from Section 5.4.7, with the occurrence rates from the simulation being slightly higher. Remember that the occurrence rates shown in Table 7.3 are headseas with ride control excluded, therefore they are considered to be greater than the real-life operations where the captain has the option to mitigate slamming by altering course and the use of ride control to reduce vessel motions. Table 7.3 includes all detected slam occurrences, a considerable number of the slam events identified are very small and insignificant, they are included nonetheless.

Table 7.3: Slam occurrence rates (slams/hour)

		Modal period (s)									
		2	**3**	**4**	**5**	**6**	**7**	**8**	**9**	**10**	**11**
Significant wave height (m)	**0.5**	-	0	0	0	0	0	-	-	-	-
	1	-	0	0	0	0	0	0	-	-	-
	1.5	-	-	0	0	0	0	23	136	102	-
	2	-	-	-	0	0	12	61	-	-	-
	2.5	-	-	-	29	26	130	271	-	-	-
	3	-	-	-	-	-	357	539	333	-	-
	3.5	-	-	-	-	-	501	515	336	-	-
	4	-	-	-	-	-	-	519	476	427	-
	4.5	-	-	-	-	-	-	618	-	-	-
	5	-	-	-	-	-	-	-	497	431	438
	6	-	-	-	-	-	-	-	508	-	-

7.4.2 Slam Loads

Measured slam loads for each condition are weighted and combined according to the method described in Section 7.3 to produce probability density and cumulative distribution functions of the slam load distribution shown in Figures 7.3 and 7.4 respectively. This figures only show the distribution of slam loads once they occur, it is not possible to learn anything about the slam occurrences from these figures alone. Slam load magnitudes are shown as multiples of total vessel displacement on the x-axis of Figure 7.3 and the y-axis of Figure 7.4.

The return period is calculated for each recorded slam event by applying Equation 7.3 and is shown in Figure 7.5. Non-dimensional slam load is shown on the y-axis and the return period (in years) is shown in log-scale on the x-axis. Due to the relatively short simulation time (5.5 hours), resolution is lost at long return periods. Therefore a logarithmic trend line (shown

as the straight line on Figure 7.5) is fitted to the data for return periods of less than 10^{-3} years and projected into the future. Figure 7.6 shows slam load encounter probabilities (from Equation 7.4) for different time periods. Since long term data is poorly defined due to the short simulation time, the trend line from Figure 7.5 is used to determine the encounter probability curves.

7.4.3 Discussion

It can be seen from Figure 7.3 that some very extreme slams, up to and exceeding twice the total vessel displacement have been detected. In fact, 35 out of 1,152, or 3% of the slams have exceeded the mass displacement of the vessel, suggesting that although the slam occurrence rates are about expected, the simulation over predicts slam loads. This can be attributed to a combination of factors relating to the motions and the slam load prediction methods.

The first source of error is an offset in motion response frequency that was previously identified in Chapter 4 and further discussed in Appendix B. The time-domain seakeeping simulation tended to predict resonant motions at higher wave encounter frequencies than model scale and full scale measurements [39]. This issue was not completely solved and it persistent during this case study. Motion magnitudes were matched with scale model experiments through the selection of an appropriate empirical damping factor, although they still occurred at a higher wave encounter frequency in the simulation. This could result in larger vertical velocities than those observed during scale model testing. Over prediction of vertical velocity was noticed in Section 6.4 where the experimentally measured median relative vertical velocity (scaled to full scale) is between 1 to 1.5m/s less than that predicted by the simulation (see Figure 6.26 on page 137). The error in velocity prediction is amplified by the quadratic relation assumed between velocity and slam load in the slam prediction equation; a 30% error in relative vertical velocity results in a 59% error in slam load.

A normalised histogram of the relative vertical velocities used in the slam prediction regression equation is shown in Figure 7.7, compared with the normalised distribution of slam velocities measured during the experimental tests. Different sea conditions than the ones tested at model scale were simulated in this case study, some conditions being more severe and others less severe, however all conditions contained in the experimental test set fitted within the envelope of the conditions shown in Table 7.1, therefore the distributions of velocities in Figure 7.7 should be similar. It can be seen that the simulation does contain more slams with a relative vertical velocity greater than 2m/s compared with those experimentally measured, and conversely it lacks slams with a negative relative vertical velocity. In fact, no slam was recorded with a velocity less than -2m/s, compared with 4.04% of the experimentally measured slams.

Another potential cause for unrealistically large slam loads is the inappropriateness of a quadratic slam load prediction equation for large relative velocities. Figure 7.8 revisits Figure 6.10 (on page 125) and visually shows the quadratic fit to the experimentally determined slam

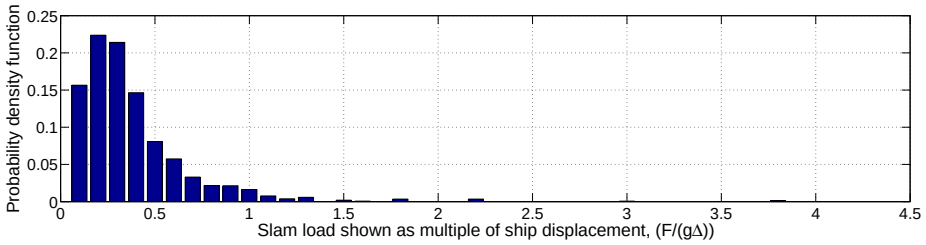

Figure 7.3: Probability distribution function for centre bow slam loads from the time-domain seakeeping code. The slam load is shown as multiples of total ship displacement ($F/(g\Delta)$).

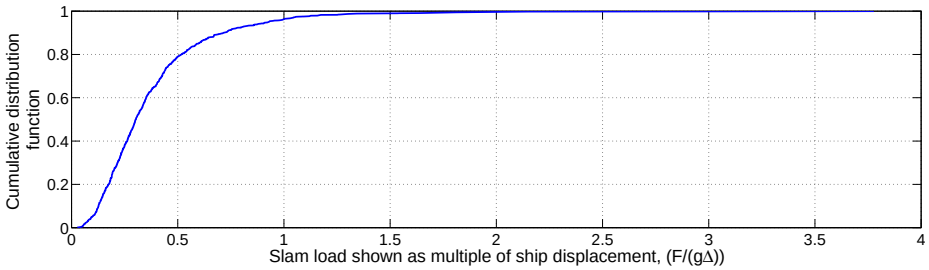

Figure 7.4: Cumulative distribution function for centre bow slam loads from the time-domain seakeeping code. The slam load is shown as multiples of total ship displacement ($F/(g\Delta)$).

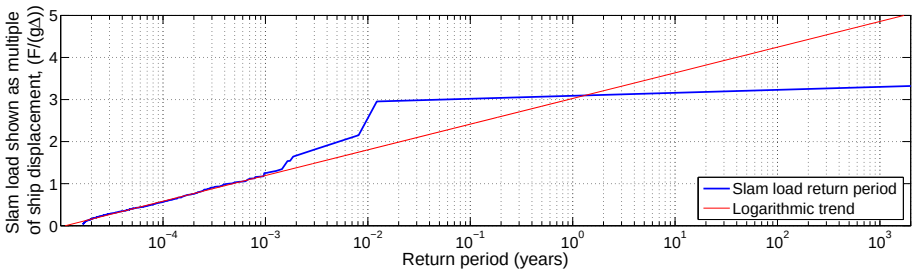

Figure 7.5: Slam load return period.

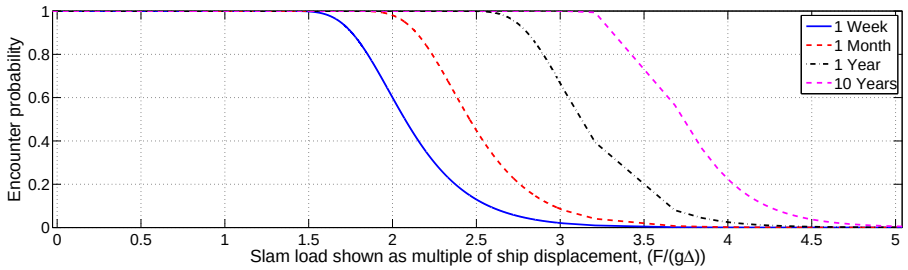

Figure 7.6: Slam load encounter probability.

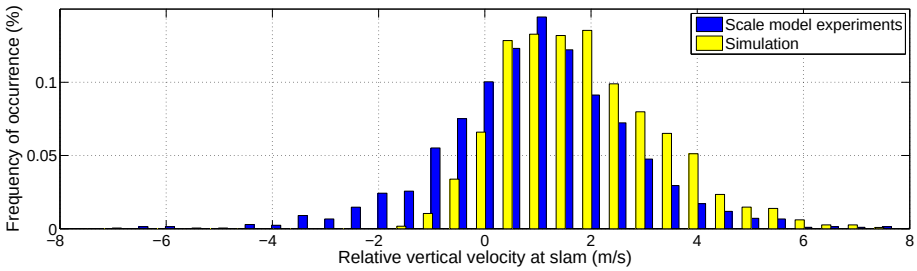

Figure 7.7: Normalised histogram of relative vertical velocities used to predict slam loading.

load data. The gradient of the fit becomes rather steep after 5m/s and very few slams have been measured within this region to draw confident inferences, however a large proportion of slams were with a relative vertical velocity greater than 2m/s were recorded from the simulation. Perhaps a different function providing an upper slam load prediction limit, or a piecewise function with a dramatically reduced gradient is best used to model this region, remembering that the slam factor empirical distribution provides an ultimate upper limit to the slam multiplier[2]. Figure 7.8 also shows a non-linear regression of a hyperbolic tangent function to the data. The hyperbolic tangent function provides a natural upper and lower limit as it is contains horizontal asymptotes at -1 and 1. Here the slam load prediction function takes the form:

$$L_p = a_1 \left(\tanh\left(\alpha V + \beta\right) + 1\right) + a_2 U \tag{7.5}$$

where U and V are the forward speed and the relative vertical velocity at the centre bow truncation respectively, a_1 and a_2 are linear regression coefficients and α and β are scaling coefficients of the hyperbolic tangent function. The hyperbolic tangent and quadratic functions are quite similar between V = -4 and 4m/s where the majority of slams are expected. Also included are the upper and lower limits on the plot where 95% of the slams are expected to fall with the addition of the random slam factor if Equation 7.5 is used to predict the slam load. Coincidently the upper limit of the predicted slam load from this function is very close to the mass displacement of the ship: (27.5 MN, mass of the overloaded ship (2,764 tonnes).

Whilst Equation 7.5 provides a maximum and minimum predicted slam load based on the measured experimental data, another method of limiting extreme slams is to introduce a limiting algorithm before or after applying the random slam factor. This algorithm would take the form of a piecewise function containing an exponential limit shown by Equation 7.6:

$$L_l = \begin{cases} L_p & \text{if} \quad L_p \leq S \\ L_m - (L_m - S)e^{(-A(L_p - S))} & \text{if} \quad L_p > S \end{cases} \tag{7.6}$$

L_p is the predicted slam load, L_m, S and A are parameters required to define the maximum

[2]Currently the upper limit of the empirical slam factor is 7; at worst case a slam can be 7 times larger than predicted by the quadratic relationship, however the probability of this occurring is very small, the upper 95% interval of the slam factor is roughly 2.4 (shown in Table 6.6 on page 127).

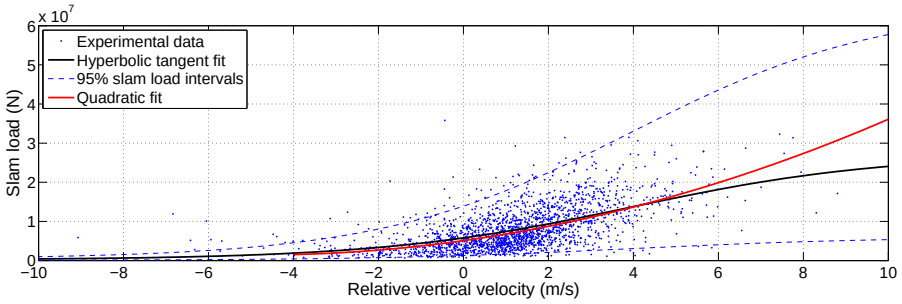

Figure 7.8: Slam load against relative vertical velocity, comparing the quadratic slam load prediction equation (Equation 6.9 on 125) with a hyperbolic tangent function (Equation 7.5) when $U = 20$kts.

allowed slam load, join point and join point smoothing constant respectively. In contrast to Equation 7.5, the coefficients that define Equation 7.6 (the maximum allowed slam load, L_m and join point S) can be intuitively selected, as they represent slam loads. For example the maximum load may be chosen to be 2,500 tonnes and the join point may be 1,500 tonnes. The coefficient A can then be determined by equating the gradients of the two piecewise functions in Equation 7.6. Figure 7.9 shows an example of this function, where $L_m = 2{,}500$ tonnes, $S = 1{,}500$ tonnes and $A = 0.001$.

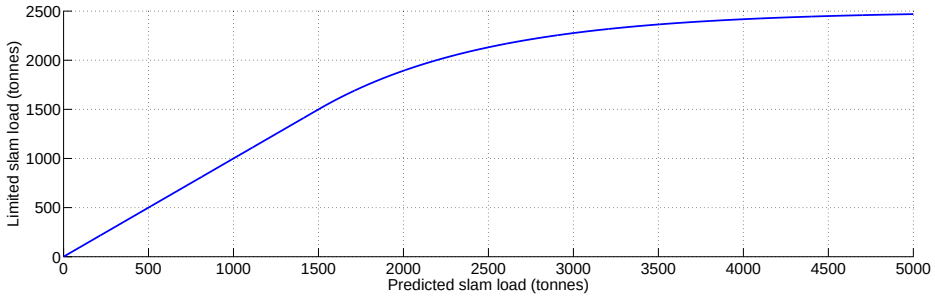

Figure 7.9: An example of the application of Equation 7.6 limiting the slam load. Here, $L_m = 2{,}500$ tonnes, $S = 1{,}500$ tonnes and $A = 0.001$.

Another difference between the simulation and experimental method is the slam identification method. During analysis of the experimental data, a slam event was identified at the moment the peak surface pressure was measured. The relative vertical velocity at the slam instant was also recorded at this moment. Slam identification in the simulation is based on a location dependant immersion threshold criterion related purely to the geometry of the centre bow archway. This criterion is offset by forward speed of the vessel (assumed constant during a particular simulation) and immersion of the bow region of the vessel. A random offset is further introduced to emulate the uncertainty observed during experimentation. Slam induced surface pressures are not explicitly calculated in the simulation, so a direct implementation of the experimental method was not possible. This slam identification approximation could have resulted in a slight misalignment of slam identification time in the simulation.

7.4.4 Vertical Bending Moments

The prediction of vertical bending moments are generally of greater importance than slam load magnitudes to the ship designer. Classification societies provide rules that detail design loads and loading conditions (such as still water, hollow landing condition etc.). Finite element analysis is commonly employed to numerically determine structural response to these prescribed loading conditions. Large high-speed catamarans are novel craft, and do not have the extensive service history to provide a large level of confidence in the class rules. For instance, a slam event measured during full scale trials of a 96m Incat catamaran exceeded the maximum sagging vertical bending moment class rule defined by Det Norske Veritas by 16% [11]. Due to the novelty of the design, the design load used by Revolution Design during the development of the 112m catamaran was determined by direct strength analysis and not the DNV design rules. This analysis resulted in a sag bending moment of 480 MNm and hog of 365 MNm.

Whilst the time-domain simulation can currently determine the longitudinal vertical bending moments due to vessel motions, the effect of the slam load on the vertical bending moment has not been integrated into the method yet. An inference between the slam load and vertical bending moment relationship observed in Chapter 5 is used to predict vertical bending moments during slamming for this case study. A future development of the time-domain simulation will be full integration of the slam loads to result in slam-induced vertical bending moments.

Figure 7.10 reproduces the scaled up experimentally measured sag slam vertical bending moments at the forward links from Figure 5.40 (page 98). A trend between slam load and vertical bending moment at the forward segmentation cut is observed. A linear, ordinary least squares tend line is superimposed on the scatter plot, showing the 'mean' relationship between the slam load and VBM. This trend line is used to convert slam magnitudes determined through the simulation to expected vertical demihull bending moments at the position of the forward segmentation cut (63.4m from the transom, full scale). The maximum vertical bending moment is usually found amidships, however in the presence of centre bow slamming the location of the maximum bending moment is shifted forward [62], suggesting that the measured vertical bending moment at the forward links is close to the maximum.

The cumulative distribution function of this new slam induced vertical bending moments distribution is shown in Figure 7.11. The uncertainty involved in applying the linear trend to model the spread of the data in Figure 7.10 is visually accounted for by the presence of the upper and lower limits encompassing 95% of the experimentally measured data represented by the dashed lines. The large uncertainty from this method, particularly for extreme slam events, is noticeable in the return period plot, Figure 7.12. The vertical bending moment return periods were determined in the same manner as the slam magnitude distributions in the previous section. Again a trend is fitted to the log-linear section of the data and extended into the future. Curves of encounter probability are shown in Figure 7.13, the upper and lower envelopes have been left off this plot to avoid clutter.

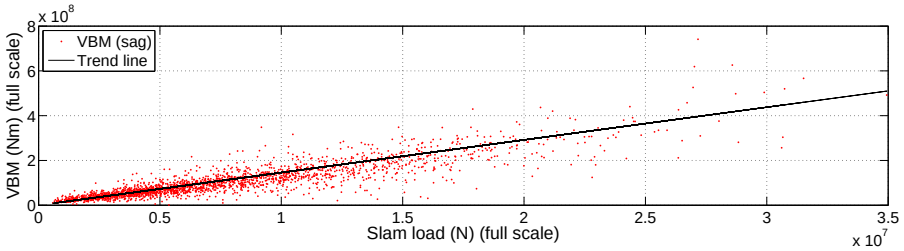

Figure 7.10: Experimentally measured vertical bending moment at the forward links (63.4m from the transom full scale) against centre bow slam load. A linear least-squares fit is also included.

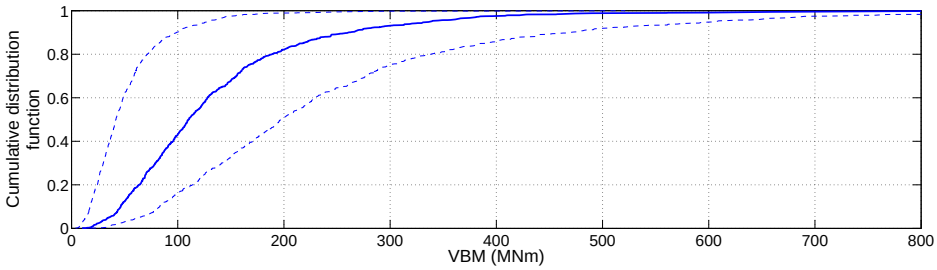

Figure 7.11: Cumulative distribution function for VBM (63.4m from transom) predicted from the slam magnitudes. Upper and lower 95% confidence intevals are also shown as the dashed lines.

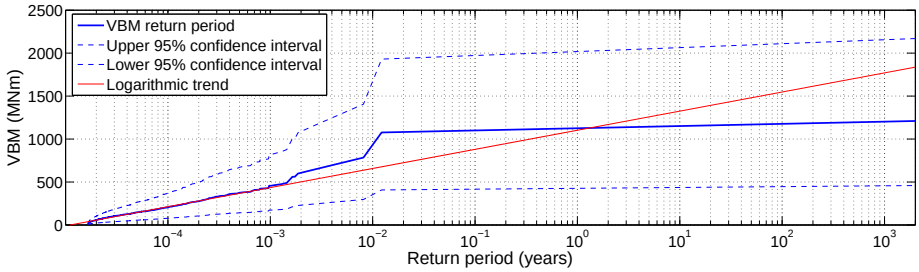

Figure 7.12: Vertical bending moment (63.4m from transom) return period. Upper and lower 95% confidence intervals are also shown as the dashed lines.

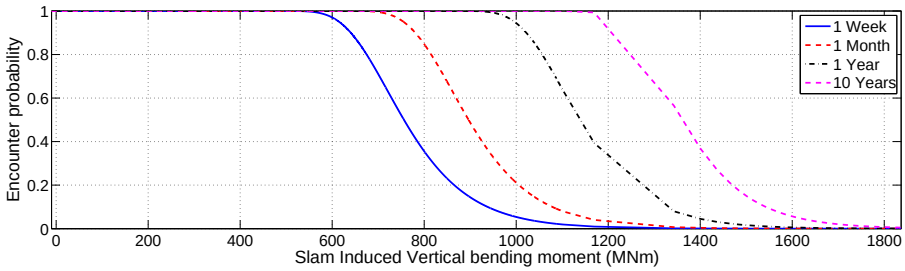

Figure 7.13: Vertical bending moment (63.4m from transom) encounter probability.

7.5 Conclusions

Wave data was used to determine the operating environment for a 112m catamaran operating in an actual high-speed ferry service route. A series of simulations was conducted and long term statistics commonly used in the prediction of extreme natural phenomena applied to predict likely extreme slam events for the purposes of developing design loads.

The slam occurrence rates for the different sea conditions supported the threshold significant wave height required for slamming proposed in Chapter 5. Resonant motions and a peak in slam occurrence rates were also observed at a model period of 8s, which were also present in the experimental results.

Long term slam load predictions of the catamaran in the overall environment were determined by weighting the slam distributions for each individual condition according to the observed sea condition occurrences. Cumulative distribution functions, return period and encounter probability plots were constructed aiding the identification of a design slam load. Of greater use to the ship designer, demihull vertical bending moments distributions can be investigated to identify the design VBM. The relationship between centre bow slam load and the demihull vertical bending moment from experimental data has been used to determine expected vertical bending moment values.

The over prediction of centre bow velocities has resulted in unrealistically common severe slam events, however with more simulation time the method is able to estimate return periods and encounter frequencies for severe slam events and from that design loads can be developed.

This method also allows the development of a motions and slam database for a vessel to be reused in any sea route, by reallocating the sea state occurrence weights when determining the slam load cumulative distribution function for that environment, provided the wave spectrum type, wave heading etc. are applicable.

Future developments including the correction of impact velocities and the implementation of VBM calculations in the seakeeping code would allow reliable direct calculation of the VBM in the time-domain. Fatigue analysis could also be conducted with this method, however it would require longer run times than presented here; to populate the slam distribution 'body' (as the smaller slams would now be of interest).

Chapter 8

Conclusions

8.1 Project Outcomes

The project aims discussed in Section 1.1 identified a shortfall in current design methodology when it comes to considering slamming implications on vessel design. Numerical seakeeping methods commonly neglect slamming altogether or they are included as simplified two-dimensional methods. Over the course of this project, an empirical slam module was developed, using extensive scale model seakeeping measurements in irregular seas as a basis.

8.1.1 Scale Model Experimentation

A 2.5m hydroelastic segmented catamaran scale model based on an Incat design was extensively tested in the AMC towing tank. The goals of these tests were to investigate motions and centre bow loads in irregular waves. Three test sets were conducted: the first investigated motions of the vessel in irregular waves in the absence of slamming, the second test set investigated characteristics of centre bow slamming. Data from this set was used to develop an empirical slam module for installation in a time-domain seakeeping code. The third test set involved measuring the wave environment produced by the AMC wave making machine, to ensure that the correct wave environment is reproduced in the seakeeping code, for validation purposes.

For the characterisation of slam events, the model was instrumented with LVDTs, wave probes mounted both on the model and alongside, at the LCG (for motion measurements) and the CBT (for slamming characterisation), strain gauges located on the demihulls and the centre bow section, for the measurement of demihull vertical bending moments and centre bow slam loads respectively and pressure sensors located on the centre bow segment archway.

8.1.2 Prediction of Ship Motions in Irregular Waves

A time-domain strip theory optimised for high Froude numbers was extended to predict motions and loads of a vessel in irregular seas. Linear superposition of regular waves was used to define

the sea spectra. The extended method was verified by applying a series of program tests. For a verification exercise, motions of the Incat catamaran were predicted in identical sea conditions to those tested with the hydroelastic segmented catamaran and the resulting heave and pitch RAOs were compared. The seakeeping code is capable of capturing non-linear trends present in the unconventional Incat hull form, however an offset in the predicted peak motion frequency was observed.

8.1.3 Characteristics of Slam Events

Slam events were characterised by testing the hydroelastic segmented catamaran model in 22 different JONSWAP irregular sea conditions. Slams were identified by analysing local centre bow pressure via pressure transducers. Centre bow slam events are easily identified by a characteristic sudden impulse of measured surface pressure. Strain gauges mounted on the centre bow transverse beams allowed the calculation of slam loads. 0.67% of the slams measured had a magnitude exceeding the displacement of the model; the largest slam recorded was equivalent to 132% of the model displacement. The distribution of slam load magnitudes showed that the median slam load is a function of wave height and encountered frequency, however extreme slam events (relative to the median measured slam load) were recorded for most conditions.

Centre bow archway surface pressure investigations revealed that the cross-deck structure was exposed to large local pressures at all locations measured meaning that ship designers should ensure that the cross-deck structure is able to withstand large loads along the length of the bow.

The immersion at the centre bow truncation during slamming was determined by calculating the relative displacements between the ship and wave. Slams events were found to commence and generally conclude before the immersion at the centre bow truncation reference point reached the maximum arch height. This observation was used to support the 2D filling height criterion, defined during tests in regular waves. However scatter of the immersion data was present, suggesting that a fixed filling height parameter is not appropriate to define the onset of slam events.

A linear trend between vertical bending moments at the forward links and the centre bow slam load was identified, allowing the prediction of vertical bending moment if the slam load is known. This trend was not identified at the aft demihull links. The unsegmented aft wetdeck section or inertia from the aft tow post could be the reason for these results.

Slam occurrence rates were found to be a function of encountered wave frequency and significant wave height. Occurrence rates were found to increase linearly for irregular JONSWAP seas between 2m and 4m significant wave height and modal period of 8.5m. This allowed the definition of a slam occurrence threshold by extrapolating the experimentally measured slam occurrence rates. For the described condition, the slam occurrence threshold was determined to be 1.5m for two vessel speeds.

8.1.4 Development of an Empirical Slam Module

A part-deterministic, part-stochastic empirical slam model has been developed relying on scale model experimental results as a basis. This model was integrated into a time-domain seakeeping code, where it can apply slam loads on-line as they occur during the simulation.

Maximum slam load magnitudes consist of two components; a deterministic part based on a regression analysis on experimental data, and a stochastic part resulting from the residual of the regression on the same data. A slam magnitude is predicted and then 'magnified' by a factor derived from the measured spread of the experimental data. The slam load is then applied over a number of time steps at the location where the slam identification mechanism first identified the event. This whole process is conducted on-line in the time-domain.

8.1.5 Case Study

A case study was presented illustrating the application of the extended seakeeping program in a design situation where a proposed vessel is tested in a known sea route. The outcome of this study is a design load (or bending moment), based on the results of long term loading statistical investigation. These results would be used as an input into a finite element model to ensure structural stresses and deflections are within acceptable limits.

8.2 Research Implications

The limitations in attempting to numerically predict slamming pressures on ships has been discussed in Chapter 2. A result of this discussion was the decision to avoid the deterministic Wagner-based potential flow methods and adopt a stochastic frame of mind to develop an empirical slam model capable of emulating experimental observations. This methodology has led to the largest collection of scale model irregular sea seakeeping data for an Incat wave-piercer to date and has therefore allowed a unique insight into the slamming characteristics of centre bow equipped wave-piercing catamarans.

Research implications of the irregular sea scale model seakeeping tests include the measurement of large local surface pressures along the length of the bow during centre bow slamming, the definition of a wave height dependant slam threshold criterion (in the absence of ride control systems) and a relation between centre bow slam load magnitudes and the resulting measured demihull vertical bending moments.

The extended time-domain seakeeping program would be a useful tool for the ship designer; it is more flexible and yet less computationally intensive than a three-dimensional finite element or computational fluid dynamics model, however, it is not intended to replace these computational methods but instead work in conjunction with them. Where an FE, or CFD model can only economically consider very few slams, the advantage of the empirical model lies in the ability to analyse a large sample of slams, giving the ability to statistically 'forecast' rare

extreme slam events. Over time, a large database of seakeeping data can be gathered and easily reused for predictions in different sea environments.

8.3 Recommendations and Future Work

The on-line implementation of the slam model was the primary goal of this project and this has been achieved. However further work is required on the on-line prediction and modelling of demihull vertical bending moments in irregular seas. This was beyond the scope of the current project and may require another round of scale model experimentation, focusing on the mass distribution of the model and the measured demihull vertical bending moments in regular and irregular waves.

The empirical slam model could be further refined by conducting extensive experimentation on one sea condition. In this project, roughly 2,000 slams were identified over 22 conditions, resulting in 80-100 slams per condition, this is perhaps limited when developing the distributions. Whilst using a test matrix over a range of conditions is a good first-pass investigative approach, now a more detailed investigation into a single condition is the next goal. By identifying several hundred slams in one key irregular sea condition, identified by the earlier investigation, a more comprehensive understanding of the slam distributions can be gained.

Another potentially important parameter that was not included in this project is the influence of hull form on the slam characteristics. The slam identification, maximum load and duration calculations are all based on experimental data for one particular hull form. If the seakeeping analysis was to be performed on a different hull form, a different slam prediction equation (or regression coefficients) and a slam factor cumulative distribution function may need to be developed. It is currently not known if these empirical components vary considerably for different designs and so a series of scale model tests using a different design should be conducted to determine the sensitivity of hull form on the resulting empirical slam parameters.

All experiments were conducted in headseas, therefore the slam module assumes headsea conditions (i.e. the slam identification trigger measures immersions on the centre line and it is assumed that no slam roll moment is generated during a slam event). The model can be extrapolated to predict slamming in oblique and quartering seas by identifying slams in the centre of each demihull archway and applying a slam roll moment by assuming that the slam is offset from the centreline of the vessel. This is not advised as it is not explicitly supported by experimental data, so scale model testing in oblique seas using the segmented catamaran model should be planned in the future.

Experiences from this project, and previous postgraduate work, are being used to further investigate the motions and loads of catamarans at the University of Tasmania and Australian Maritime College. A new segmented model has been designed and constructed. Improvements in this design are a segmented aft wetdeck, 6 degree of freedom load cells in place of the centre bow mounted strain gauges in an attempt to measure longitudinal wave and slam loads as well

as vertical. It is envisioned that this new configuration could determine centre bow locations with much more accuracy than the current method and would shed light on the slam location issue. The model has also been designed with three interchangeable centre bow sections of varying tunnel height.

An active ride control system, consisting of a T-foil mounted on the centre line at the centre bow truncation and trim tabs on the demihull transoms could be fitted to the model. These surfaces would be controlled by an in-house designed feedback system. The influence of ride control systems on motions and slamming behaviour would be investigated. The reduction of slam occurrence rates with active ride control is of particular interest.

References

[1] Amin, W. *Non-Linear Unsteady Wave Loads on Large High-Speed Wave Piercing Catamarans*. PhD thesis, University of Tasmania, 2009.

[2] Applebee, T., Crossland, P., Grigoropoulos, G., Hermanski, G., Kim, Y., Kishev, R., Matsumoto, K., Hua, J., and Fathi, D. The seakeeping committee - final report and recommendations to the 25th ittc. In *Proceedings from the 25th International Towing Tank Conference* (2008), pp. 209–262.

[3] Arai, M., Cheng, L., and Inoue, Y. A computing method for the analysis of water impact of arbitrary shaped bodies. *Journal of the Society of Naval Architects of Japan* (1994), 233–240.

[4] Arai, M., Cheng, L., and Inoue, Y. A computing method for the analysis of water impact of arbitrary shaped bodies (2nd report). *Journal of the Society of Naval Architects of Japan* (1995), 91–99.

[5] Arai, M., Cheng, L., Miyauchi, T., and Ishikawa, M. A study of slamming characteristics and optimisation of bow forms of ships. In *Practical Design of Ships and Mobile Units* (1995), pp. 1.672–1.683.

[6] Bishop, R., and Price, W. *Hydroelasticity of Ships*, first ed. Cambridge University Press, Cambridge, 1979.

[7] Bisplinghoff, R., and Doherty, C. Some studies of the impact of vee wedges on a water surface. *Journal of the Franklin Institute* (1952), 547–561.

[8] Brown, K., Wraith, R., and Joubert, P. Local pressure on hull plating due to slamming. In *FAST '99* (1999), pp. 947–956.

[9] Cappelletti, A., Pino, E., Sebastiani, L., Boccalatte, C., Viviani, M., Bruzzone, D., and Brizzolara, S. Experience on the application and validation of the theoretical methods for the seakeeping prediction of fast ships. In *FAST '03* (2003), vol. 2, pp. 37–42.

[10] Chamberlin, K. Characterisation of high-speed catamaran slam events in irregular waves. B.eng thesis, Australian Maritime College, 2008.

[11] Davidson, G., Roberts, T., and Thomas, G. Global and slam loads for a large wavepiercing catamaran design. In *FAST '05* (2005).

[12] Davis, M., Amin, W., Lavroff, J., Holloway, D., Thomas, G., Matsubara, S., and Roberts, T. Global and slam load model testing to support developing hsmv operations in severe sea conditions. In *International Conference for Innovation in High Speed Marine Vessels* (Fremantle, Australia, January 2009).

[13] Davis, M., and Holloway, D. Effect of sea, ride controls, hull form and spacing on motion and sickness incidence for high speed catamarans. In *FAST '03* (2003), vol. 3, pp. 1–10.

[14] Davis, M., Thomas, G., Holloway, D., Lavroff, J., Amin, W., Matsubara, S., and Roberts, T. Slamming and whipping of wave-piercing catamarans. In *Hydroelasticy in Marine Technology* (2009).

[15] Davis, M. R., and Holloway, D. S. The influence of hull form on the motions of high speed vessels in head seas. *Ocean Engineering 30* (2003), 2091–2115.

[16] Davis, M. R., Whelan, J. R., and Thomas, G. A. Computational modeling of wet deck slam loads with reference to sea trials. In *FAST '07* (2007), pp. 616–624.

[17] Dawson, C. A practical computer method for solving ship-wave problems. In *Proceedings from the 2nd Conference on Numerical Ship Hydrodynamics* (1977), pp. 30–38.

[18] Dessi, D., and Mariani, R. Analysis and prediction of slamming-induced loads of a high-speed monohull in regular waves. *Journal of Ship Research 52*, 1 (2008), 71–86.

[19] Dessi, D., Mariani, R., Coppottelli, G., and Rimondi, M. Experimental identification of wet bending modes with segmented model tests. In *FAST '05* (2005).

[20] Dessi, D., Mariani, R., La Gala, F., and Benedetti, L. Experimental analysis of the wave-induced response of a fast monohull via a segmented-hull model. In *FAST '03* (2003), vol. 2, pp. 75–82.

[21] Dove, T. Slamming of high-speed catamarans in irregular waves. B.eng thesis, Australian Maritime College, 2007.

[22] El Moctar, O., Brunswig, J., Brehm, A., and Schellin, T. Computation of ship motions in waves and slamming loads for fast ships using ranse. In *FAST '05* (2005).

[23] Faltinsen, O. Interpretation of full-scale tests of wetdeck slamming. In *HIPER '99* (1999), pp. 62–71.

[24] Faltinsen, O. *Hydrodymanics of High-Speed Marine Vehicles*. Cambridge University Press, 2005.

[25] Faltinsen, O., and Zhao, R. Numerical predictions of ship motions at high forward speed. In *Philosophical Transactions of the Royal Society: Physical and Engineering Sciences* (1991), vol. 334.

[26] Formation Design Systems Pty Ltd. *Seakeeper Windows Version 12, Users Manual*, 2006.

[27] French, B., Thomas, T., Davis, M., Holloway, D., and Mason, L. Time-domain simulations of wet deck slamming - a hybrid theoretical and empirical approach. In *Seventh International Conference on High-Performance Marine Vehicles (HIPER'10)* (Melbourne, Florida, October 2010), pp. 123–134.

[28] Fu, T., Fullerton, A., Terrill, E., Faller, W., Lada, G., Hess, D., and Minnick, L. Measurement and modeling of the motions of a high-speed catamaran in waves. In *28th International Conference on Ocean, Offshore and Arctic Engineering, OMAE 2009* (June 2009).

[29] Ge, C. *Global Response to Catamarans due to Wet Deck Slamming*. PhD thesis, Norwegian University of Science and Technology, 2002.

[30] Ge, C., Faltinsen, O., and Moan, T. Global hydroelastic response of catamarans due to wetdeck slamming. *Journal of Ship Research 42*, 1 (2005), 24–42.

[31] Hermundstad, O., Aarsnes, J., and Moan, T. Hydroelastic analysis of a high speed catamaran in regular and irregular waves. In *Fourth International Conference on Fast Sea Transportation, FAST'97* (Sydney, Australia, 1997), N. Baird and A. Jeffs, Eds., pp. 447–454.

[32] Hess, J., and Smith, A. Calculation of potential flow about arbitrary bodies. *Progress in Aeronautical Sciences 8* (1966), 1–138.

[33] Holloway, D. Numerical stabilisation of motion integration. In *Australia and New Zealand Industrial and Applied Mathematics* (July 2007), ANZIAM, pp. C249–C263.

[34] Holloway, D. S. *A High Froude Number Time Domain Strip Theory Applied to the Seakeeping of Semi-SWATHs*. PhD thesis, University of Tasmania, 1998.

[35] Holloway, D. S., and Davis, M. R. Green function solutions for the transient motion of water sections. *Journal of Ship Research 46*, 2 (2002), 99–120.

[36] Holloway, D. S., and Davis, M. R. Ship motion computations using a high froude number time domain strip theory. *Journal of Ship Research 50*, 1 (2006), 15–30.

[37] Hudson, D., Turnock, S., and Lewis, S. Predicting motions of high-speed rigid inflatable boats: Improved wedge impact prediction. In *9th International Conference of Fast Sea Transportation, FAST07* (Shanghai, China, 2007), pp. 377–383.

[38] Hughes, O. F., McNatt, T., and Spradbrow, B. J. Structural design of large, fast marine vehicles based on first principles. In *Proceedings of the Second International Conference on Fast Sea Transportation (FAST'93)* (Yokohama, Japan, December 1993), pp. 489–500.

[39] Jacobi, G. High-speed catamaran motion response and slamming behaviour during full scale trials. Diploma of engineering (naval architecture) thesis, Australian Maritime College, University of Tasmania, April 2011.

[40] Jacobi, G., Thomas, G., Davis, M., Holloway, D., Davidson, G., and Roberts, T. Full-scale motions of a large high speed catamaran. the influence of wave environment, speed and ride control system. *International Journal of Maritime Engineering (RINA Transactions), in press* (2012).

[41] Kara, F., and Vassalos, D. Time domain prediction of steady and unsteady motion of high speed craft. In *FAST '03* (2003), vol. 2, pp. 27–36.

[42] Korvin-Kroukovsky, B. V., and Jacobs, W. R. Pitching and heaving motions of a ship in regular waves. In *SNAME* (1957), vol. 65.

[43] Kring, D., Huang, Y., Sclavounos, P., Vada, T., and Braathen, A. Nonlinear ship motions and wave induced loads by a rankine method. In *Twenty-First Symposium on Naval Hydrodynamics* (1997), pp. 45–63.

[44] Kvalsvold, J., and Faltinsen, O. Hydroelastic modelling of slamming against wet-decks. In *Water Waves and Floating Bodies* (1993), pp. 57–60.

[45] Lavroff, J. *The Slamming and Whipping Vibratory Response of a Hydroelastic Segmented Catamaran Model*. PhD thesis, University of Tasmania, 2009.

[46] Lavroff, J., Davis, M., Holloway, D., and Thomas, G. Experimental analysis of the wet flexural mode response of an npl 6a hydroelastic segmented model. In *HIPER '06* (2006), pp. 179–190.

[47] Lavroff, J., Davis, M. R., Holloway, D. S., and Thomas, G. The whipping vibratory response of a hydroelastic segmented catamaran model. In *FAST '07* (2007), pp. 600–607.

[48] Lewis, E., Ed. *Principles of Naval Architecture*, second ed., vol. three. The Society of Naval Architects and Marine Engineers, 1989.

[49] Lin, W., Collette, M., Lavis, D., Jessup, S., and Kuhn, J. Recent hydrodynamic tool development and validation for motions and slam loads on ocean-going high-speed vessels. In *Practical Design of Ships and Other Floating Structures* (2007), American Bureau of shipping.

[50] Lindemark, T., Kamsvag, F., and Valsgard, S. Fatigue analysis of gas carriers. In *RINA '04* (2004).

[51] Lloyd, A. *Seakeeping: Ship Behaviour in Rough Weather*. Ellis Horwood, 1989.

[52] Marcer, R., Berhault, C., de Jouëtte, C., Moirod, N., and Shen, L. Validation of cfd codes for slamming. In *5th European Conference on Computational Fluid Dynamics (ECCOMAS CFD 2010)* (Lisbon, Portugal, June 2010).

[53] Matsubara, S. *Ship Motions and Wave-Induced Loads on High Speed Catamarans*. PhD thesis, Australian Maritime College, 2011.

[54] Myers, R. *Classical and Modern Regression Analysis with Applications*, second ed. PWS-KENT Publishing Company, 1990.

[55] Nakos, D., and Sclavounos, P. On steady and unsteady ship wave patterns. *Journal of Fluid Mechanics 215* (1990), 263–288.

[56] Newman, J. *Marine Hydrodynamics*. MIT Press, Cambridge, Massachusetts, 1977.

[57] Okland, O., Zhao, R., and Moan, T. Numerical assessment of segmented test model approach for measurement of whipping responses. In *FAST '03* (2003), vol. 2, pp. 87–94.

[58] Roberts, T. Route assessment for higashi nihon line. Tech. rep., Revolution Design, 2005.

[59] Sahoo, P. K., and Doctors, L. J. Theoretical and experimental study of motion characteristics of high-speed catamaran hull forms. In *Practical Design of Ships and Other Floating Structures* (2004).

[60] Salvesen, N., Tuck, E. O., and Faltinsen, O. Ship motions and sea loads. *Society of Naval Architects and Marine Engineers* (1970).

[61] Sheskin, D. *Handbook of Parametric and Nonparametric Statistical Procedures*. CRC Press, Florida, USA, 1997.

[62] Thomas, G. *Wave Slam Response of Large High Speed Catamarans*. PhD thesis, University of Tasmania, 2003.

[63] Thomas, G., Davis, M., Holloway, D., and Roberts, T. The influence of slamming and whipping of the fatigue life of a high-speed catamaran. In *FAST '05* (2005).

[64] Thomas, G., Davis, M., Holloway, D., Roberts, T., Matsubara, S., Lavroff, J., Amin, W., Chamberlin, K., and Dove, T. Characterisation of slam events of a high-speed catamaran in irregular waves. In *FAST '09* (October 2009), pp. 177–188.

[65] Thomas, G., Winkler, S., Davis, M., Holloway, D., Matsubara, S., Lavroff, J., and French, B. Slam events of high-speed catamarans in irregular waves. *Journal of Marine Science and Technology 16* (2011), 8–21.

[66] Thomas, G. A., Davis, M. R., Holloway, D. S., and Roberts, T. J. Transient dynamic slam response of large high speed catamarans. In *FAST '03* (2003).

[67] Thomas, G. A., Davis, M. R., Holloway, D. S., Watson, N. L., and Roberts, T. J. Slamming response of a large high-speed wave-piercer catamaran. *Marine Technology 40*, 2 (2003), 126–140.

[68] Veen, D., and Gourlay, T. Sph study of high speed ship slamming. In *3rd ERCOFTAC SPHERIC workshop on SPH applications* (Lausanne, Switzerland, June 2008).

[69] von Karman, T. The impact on seaplane floats during landing. Tech. rep., National Advisory Committee for Aeronautics, 1929.

[70] Wagner, H. über stoss- und gleitvergänge an der oberflache von flüßigkeiten. *Zeitschrift für Angewandte Mathematik und Mechanik 12* (1932), 192–235.

[71] Watanabe, I., Takemoto, H., and Mitamoto, T. Use of an elastic model in studying wave loads on a ship in waves and its verification by a full scale measurement. In *International Symposium on Scale Modelling* (1988), Japan Society of Mechanical Engineers: Tokyo, pp. 47–55.

[72] Weems, K., Zhang, S., Lin, W., Bennett, J., and Yung-Sup, S. Structural dynamic loadings due to impact and whipping. In *Practical Design of Ships and Mobile Units* (1998), Elsevier Science.

[73] Wehausen, J. V., and Laitone, E. V. Surface waves. In *Handbuch der Physik* (1960), S. Flügg, Ed., vol. 9, pp. 445–814.

[74] Wetherill, G. *Regression Analysis with Applications.* Chapman and Hall Ltd, London, 1986.

[75] Whelan, J. *Wetdeck Slamming of High-Speed Catamarans with a Centre Bow.* PhD thesis, University of Tasmania, 2004.

[76] Whelan, J., Holloway, D., Roberts, T., and Davis, M. Wetdeck slamming of high-speed catamarans with a centre bow. In *FAST '03* (2003), vol. 2, pp. 33–40.

[77] Winkler, S. Classification of high-speed catamaran slam events in irregular waves. Diploma of engineering (naval architecture) thesis, Australian Maritime College, University of Tasmania, August 2009.

[78] Ye, H., and Hsiung, C. Time domain motion computations of twin and mono hull ships in head seas. *International Shipbuilding Progress 46*, 445 (1999), 91–123.

[79] Zhao, R. A nonlinear time domain simulation for predicting wet-deck slamming of catamaran. In *FAST '03* (2003), vol. 2, pp. 95–102.

[80] Zhao, R., Faltinsen, O., and Aarsnes, J. Water entry of arbitrary two-dimensional sections with and without flow separation. In *21th symposium on Naval Hydrodynamics* (1997), pp. 408–423.

Appendix A

Motions and Wave Spectra Plots

The following 22 pages present experimentally measured ship motion results for all the test conditions undertaken during the scale model experimentation. The top two plots show experimentally measured wave elevation and slope energy spectra measurements compared with the ideal JONSWAP spectra. Dimensionless encountered wave frequency is plotted on the x-axis, this has been done to enable direct comparison with the bottom two plots: heave and pitch RAOs.

The heave and pitch motions plots compare the measured irregular sea RAOs (the solid lines) with regular wave data from Lavroff [45]. Since regular wave data was collected for 1.54 and 2.92m/s (model scale) and wave heights of 60mm and 90mm, the 1.54m/s regular wave RAOs are shown on the 1.54m/s irregular conditions and similarly for the 2.92m/s conditions. In the case of the 2.15m/s conditions, since no regular motions data has been collected, all regular motions RAOs have been included for comparison.

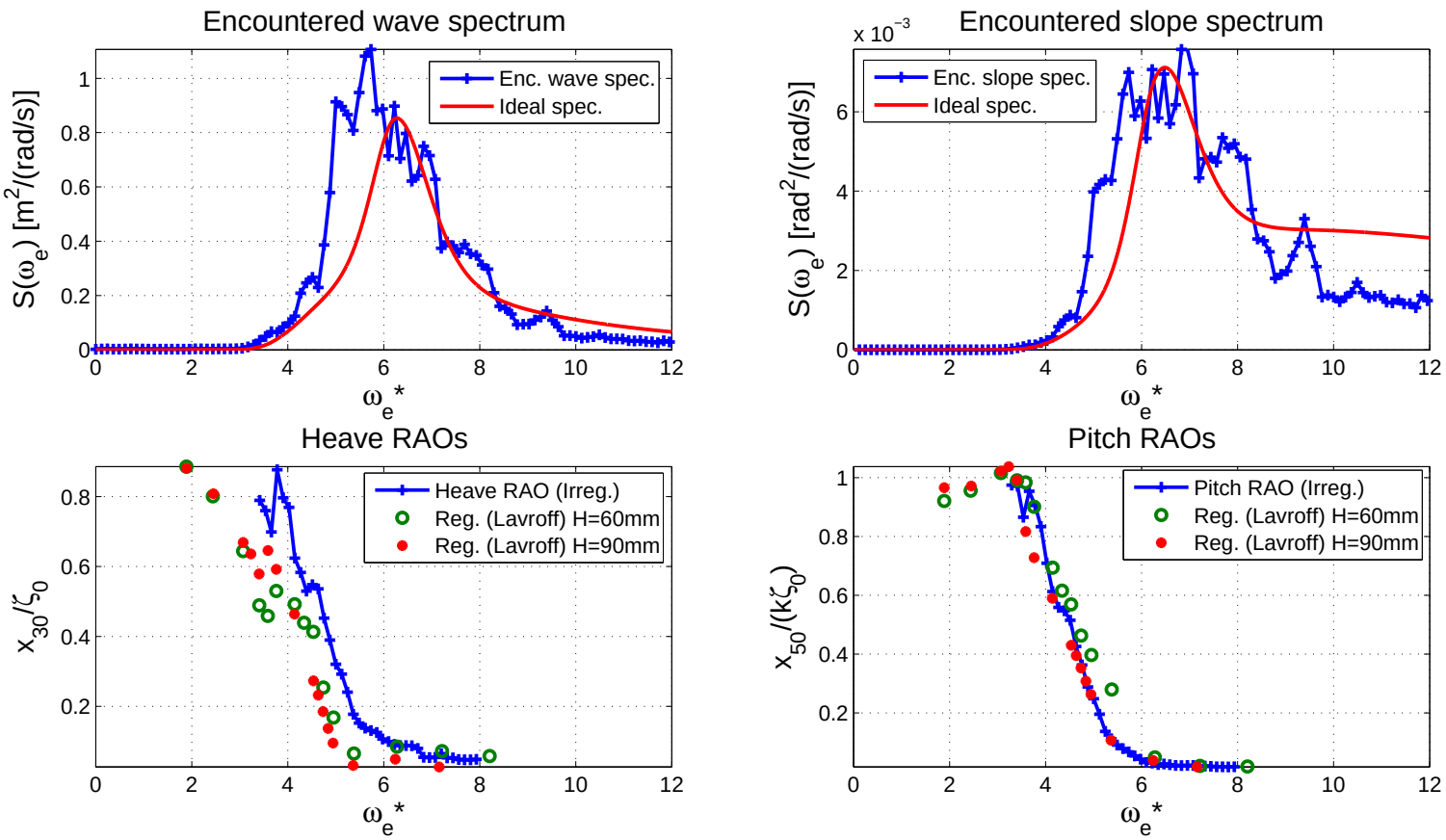

Figure A.1: Top: encountered wave height and slope spectra compared with the theoretical spectra. Bottom: measured heave and pitch RAOs compared with regular wave measurements from Lavroff [45]. Irregular Condition 90 $H_{1/3} = 78.1$mm, $T_0 = 1.0$s $U = 1.54$m/s.

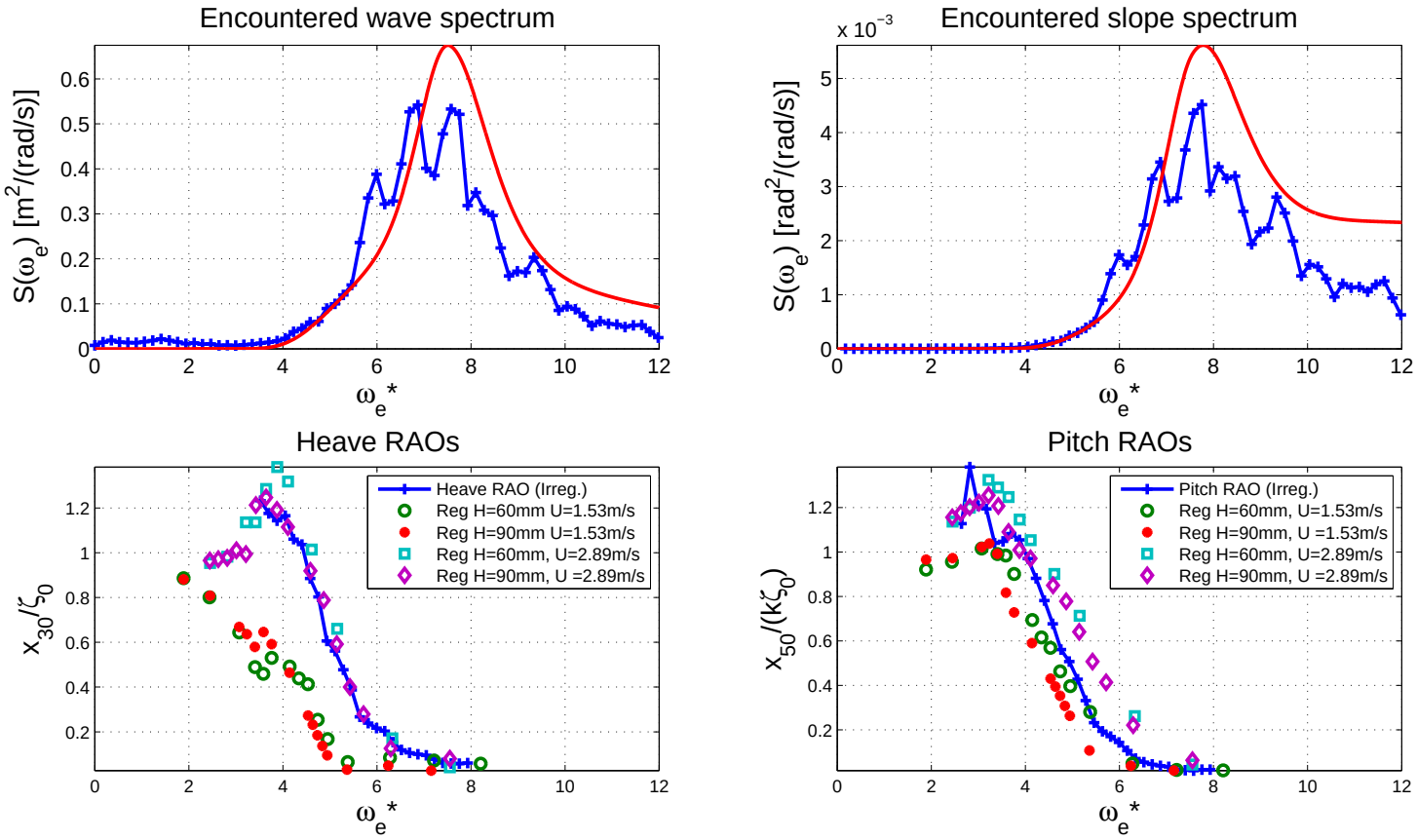

Figure A.2: Top: encountered wave height and slope spectra compared with the theoretical spectra. Bottom: measured heave and pitch RAOs compared with regular wave measurements from Lavroff [45]. Irregular Condition 91 $H_{1/3} = 78.1$mm, $T_0 = 1.0$s $U = 2.15$m/s.

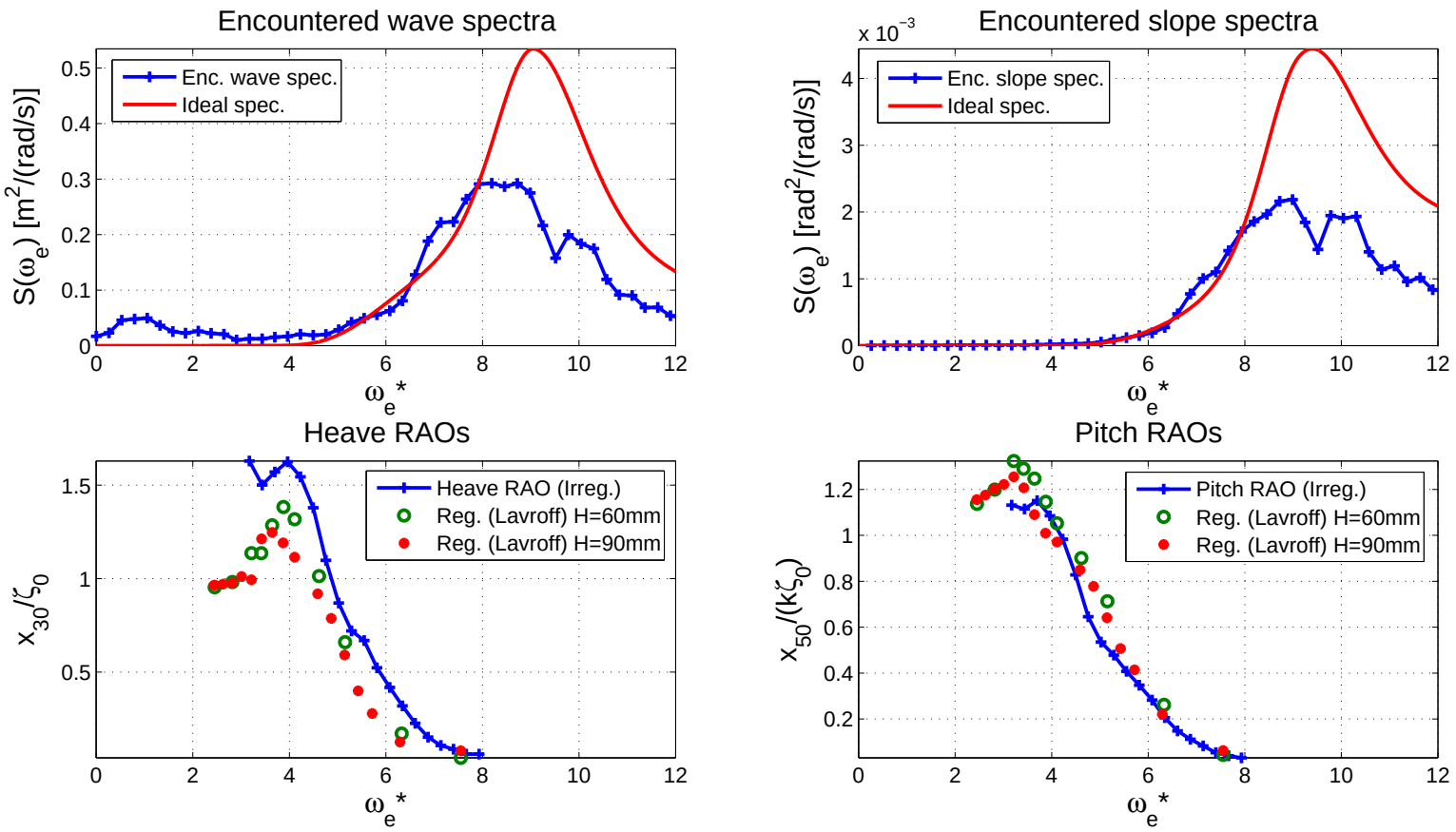

Figure A.3: Top: encountered wave height and slope spectra compared with the theoretical spectra. Bottom: measured heave and pitch RAOs compared with regular wave measurements from Lavroff [45]. Irregular Condition 92 $H_{1/3} = 78.1$mm, $T_0 = 1.0$s $U = 2.92$m/s.

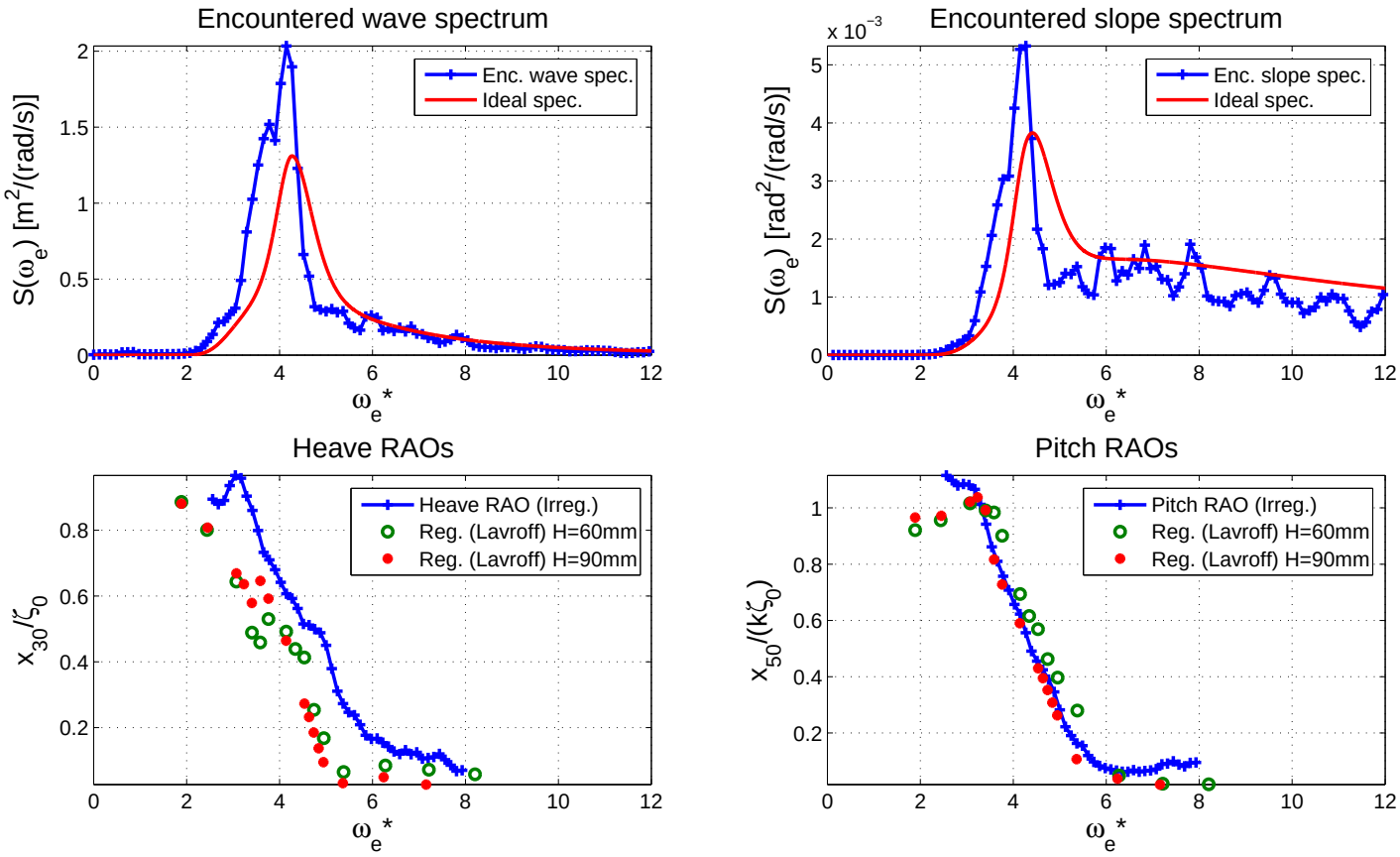

Figure A.4: Top: encountered wave height and slope spectra compared with the theoretical spectra. Bottom: measured heave and pitch RAOs compared with regular wave measurements from Lavroff [45]. Irregular Condition 93 $H_{1/3} = 78.1$mm, $T_0 = 1.3$s $U = 1.54$m/s.

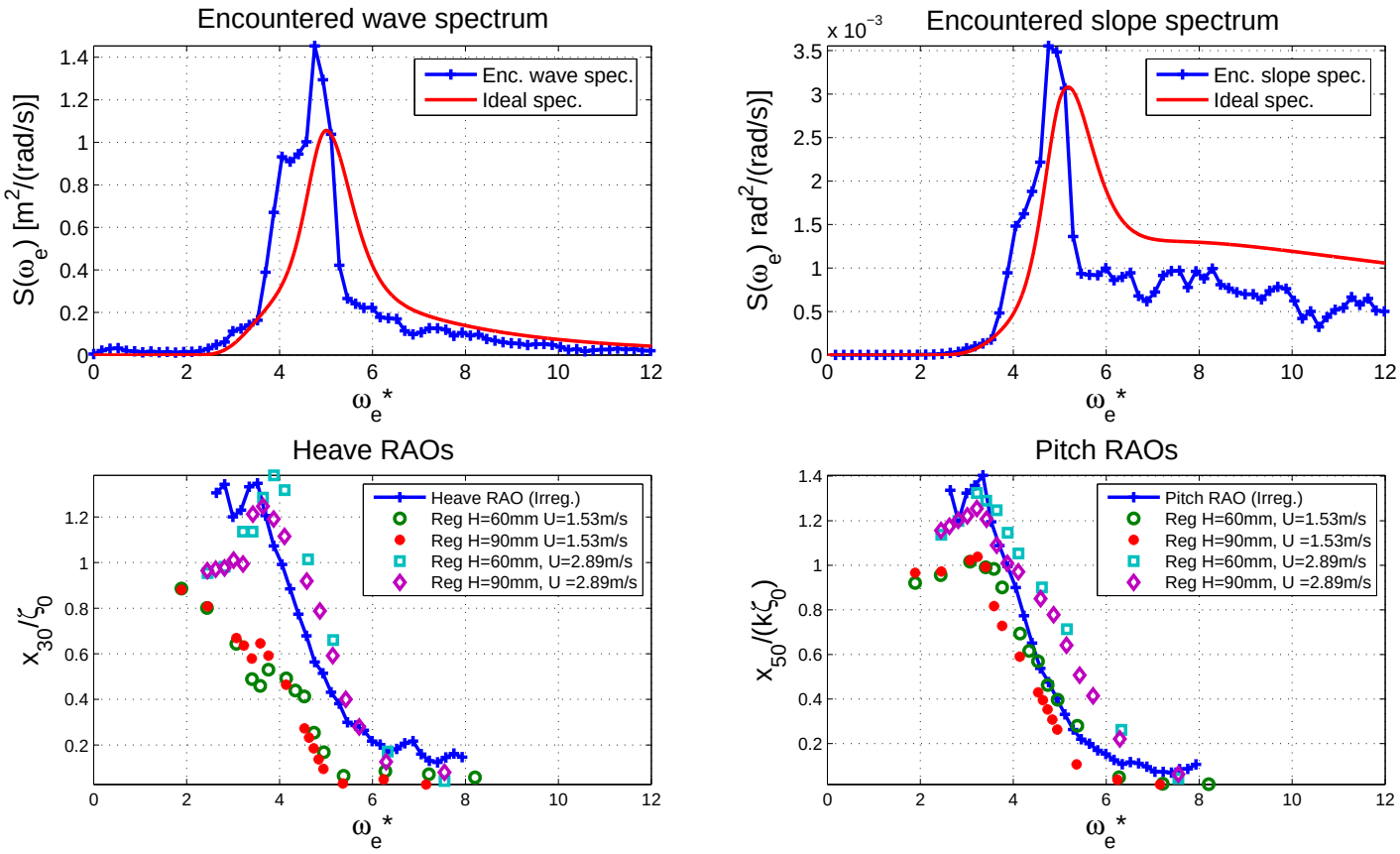

Figure A.5: Top: encountered wave height and slope spectra compared with the theoretical spectra. Bottom: measured heave and pitch RAOs compared with regular wave measurements from Lavroff [45]. Irregular Condition 94 $H_{1/3} = 78.1$mm, $T_0 = 1.3$s $U = 2.15$m/s.

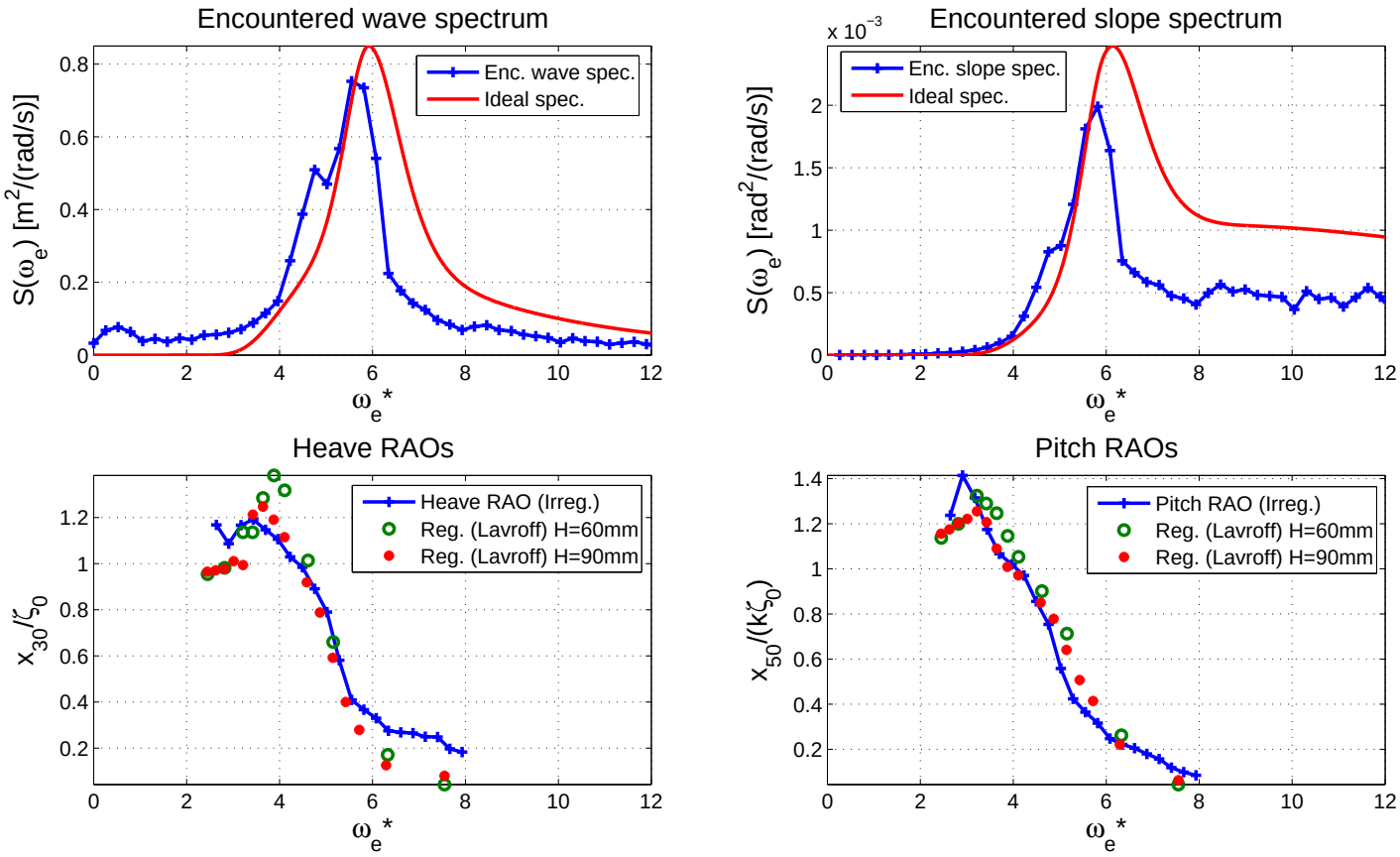

Figure A.6: Top: encountered wave height and slope spectra compared with the theoretical spectra. Bottom: measured heave and pitch RAOs compared with regular wave measurements from Lavroff [45]. Irregular Condition 95 $H_{1/3} = 78.1$mm, $T_0 = 1.3$s $U = 2.92$m/s.

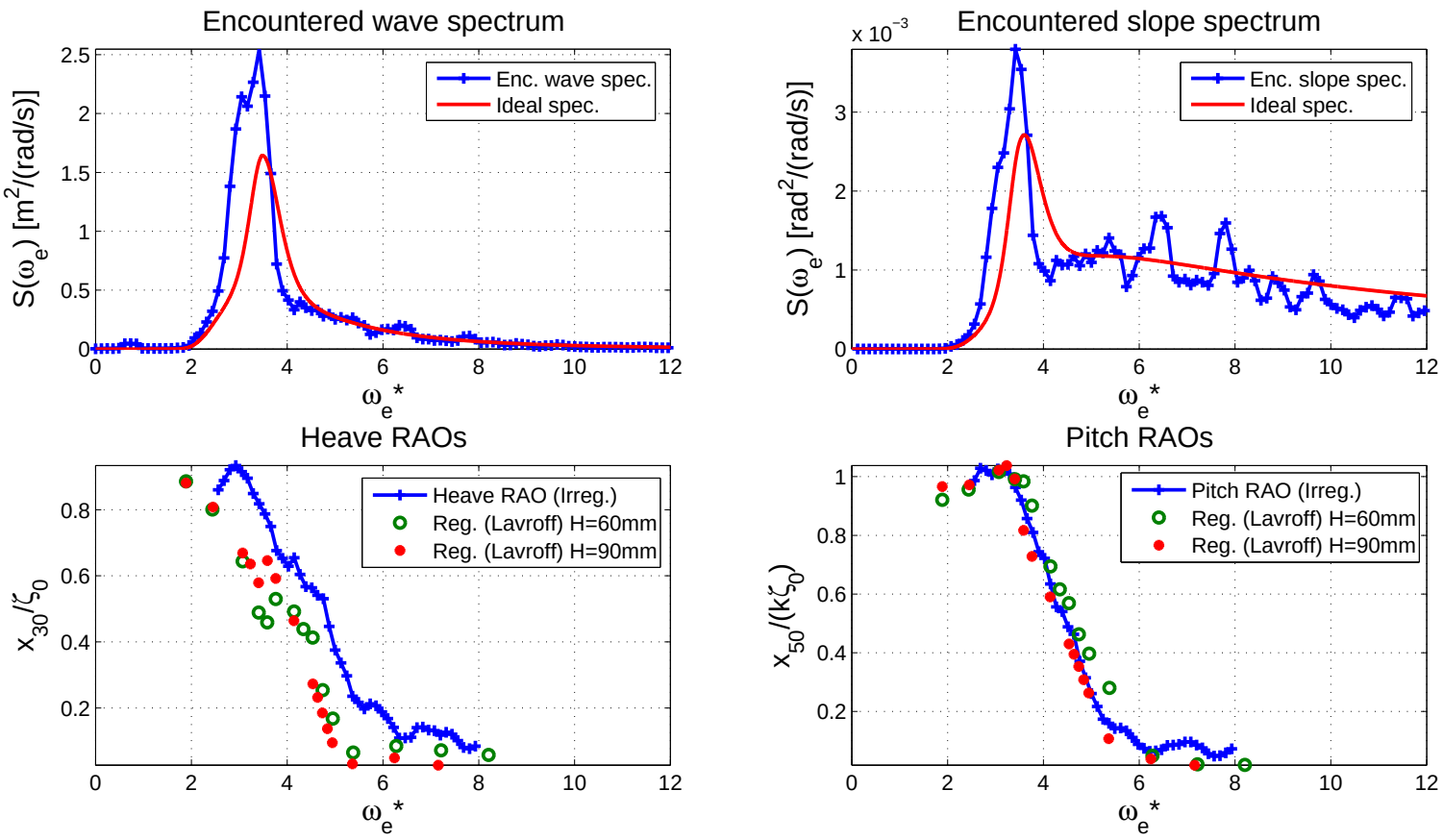

Figure A.7: Top: encountered wave height and slope spectra compared with the theoretical spectra. Bottom: measured heave and pitch RAOs compared with regular wave measurements from Lavroff [45]. Irregular Condition 96 $H_{1/3} = 78.1$mm, $T_0 = 1.5$s $U = 1.54$m/s.

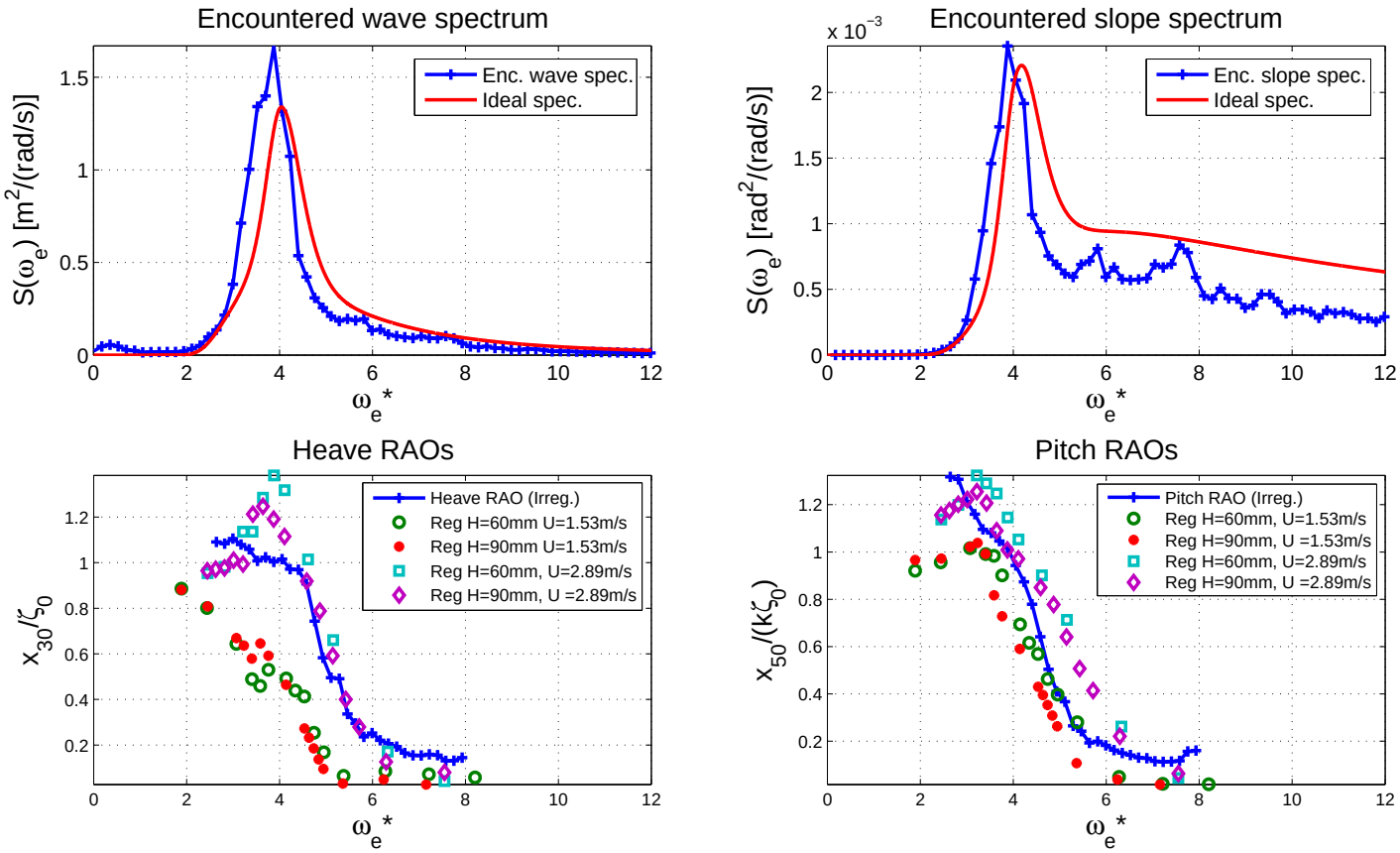

Figure A.8: Top: encountered wave height and slope spectra compared with the theoretical spectra. Bottom: measured heave and pitch RAOs compared with regular wave measurements from Lavroff [45]. Irregular Condition 97 $H_{1/3} = 78.1$mm, $T_0 = 1.5$s $U = 2.15$m/s.

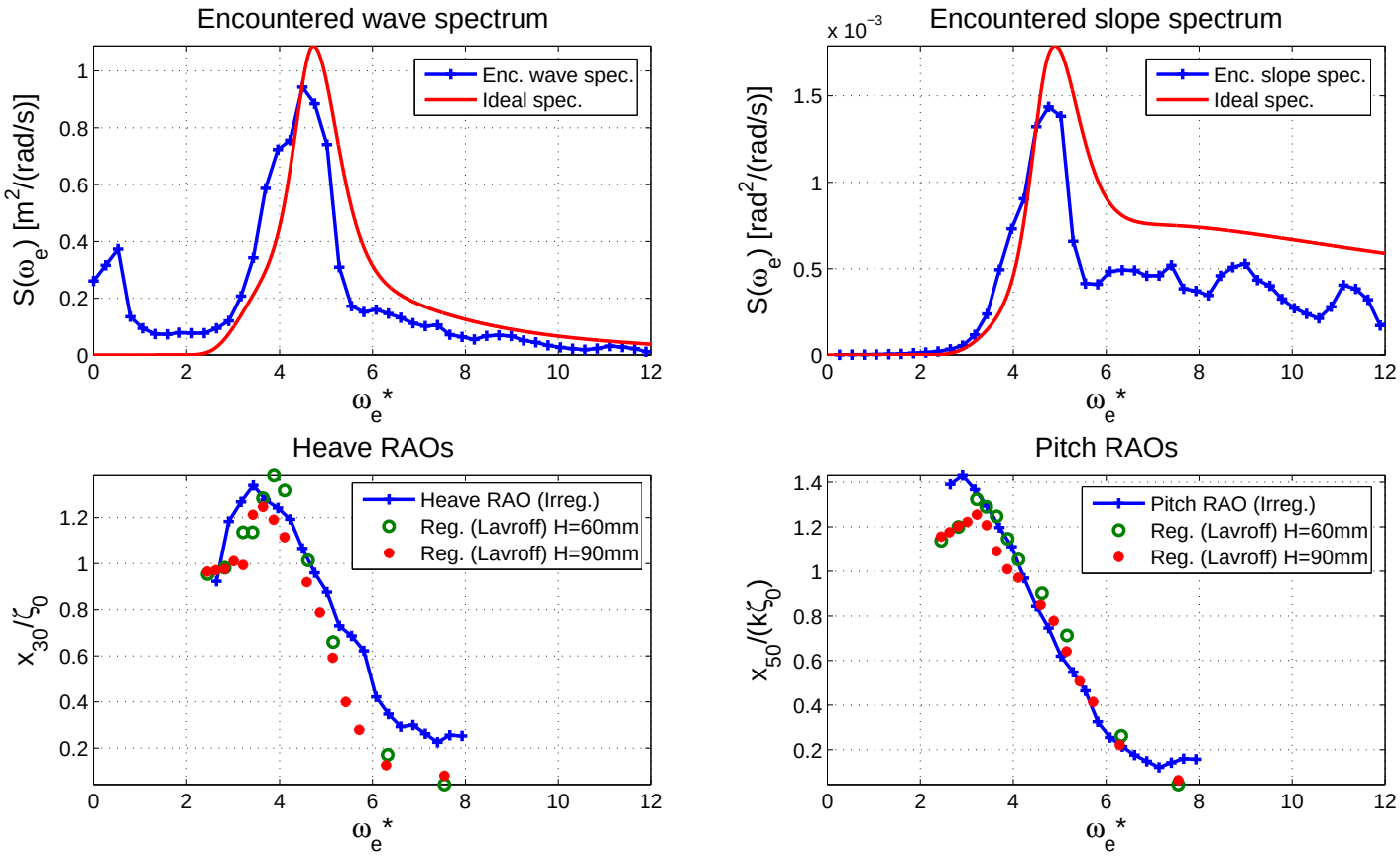

Figure A.9: Top: encountered wave height and slope spectra compared with the theoretical spectra. Bottom: measured heave and pitch RAOs compared with regular wave measurements from Lavroff [45]. Irregular Condition 98 $H_{1/3} = 78.1$mm, $T_0 = 1.5$s $U = 2.92$m/s.

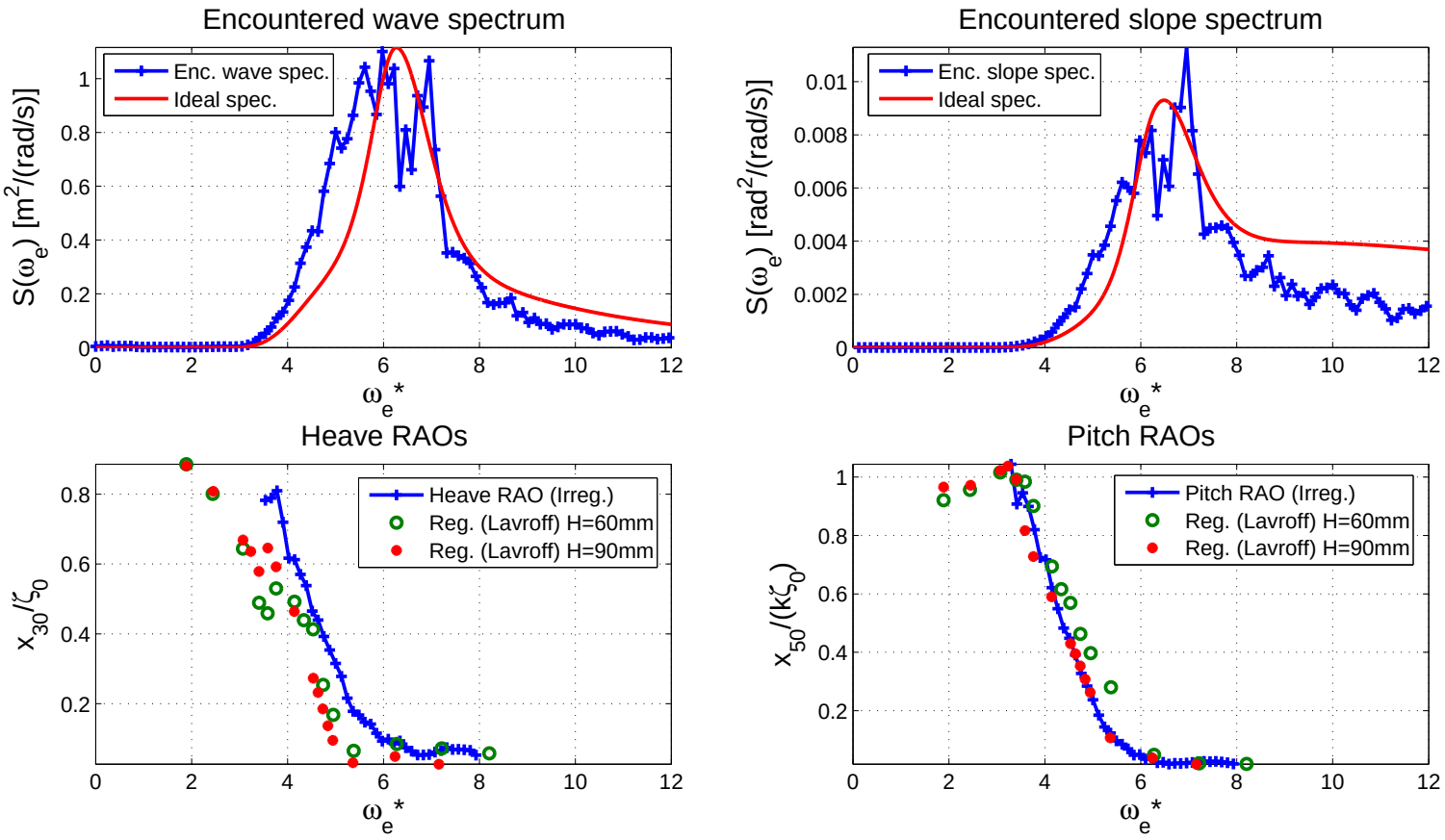

Figure A.10: Top: encountered wave height and slope spectra compared with the theoretical spectra. Bottom: measured heave and pitch RAOs compared with regular wave measurements from Lavroff [45]. Irregular Condition 99 $H_{1/3} = 89.3$mm, $T_0 = 1.0$s $U = 1.54$m/s.

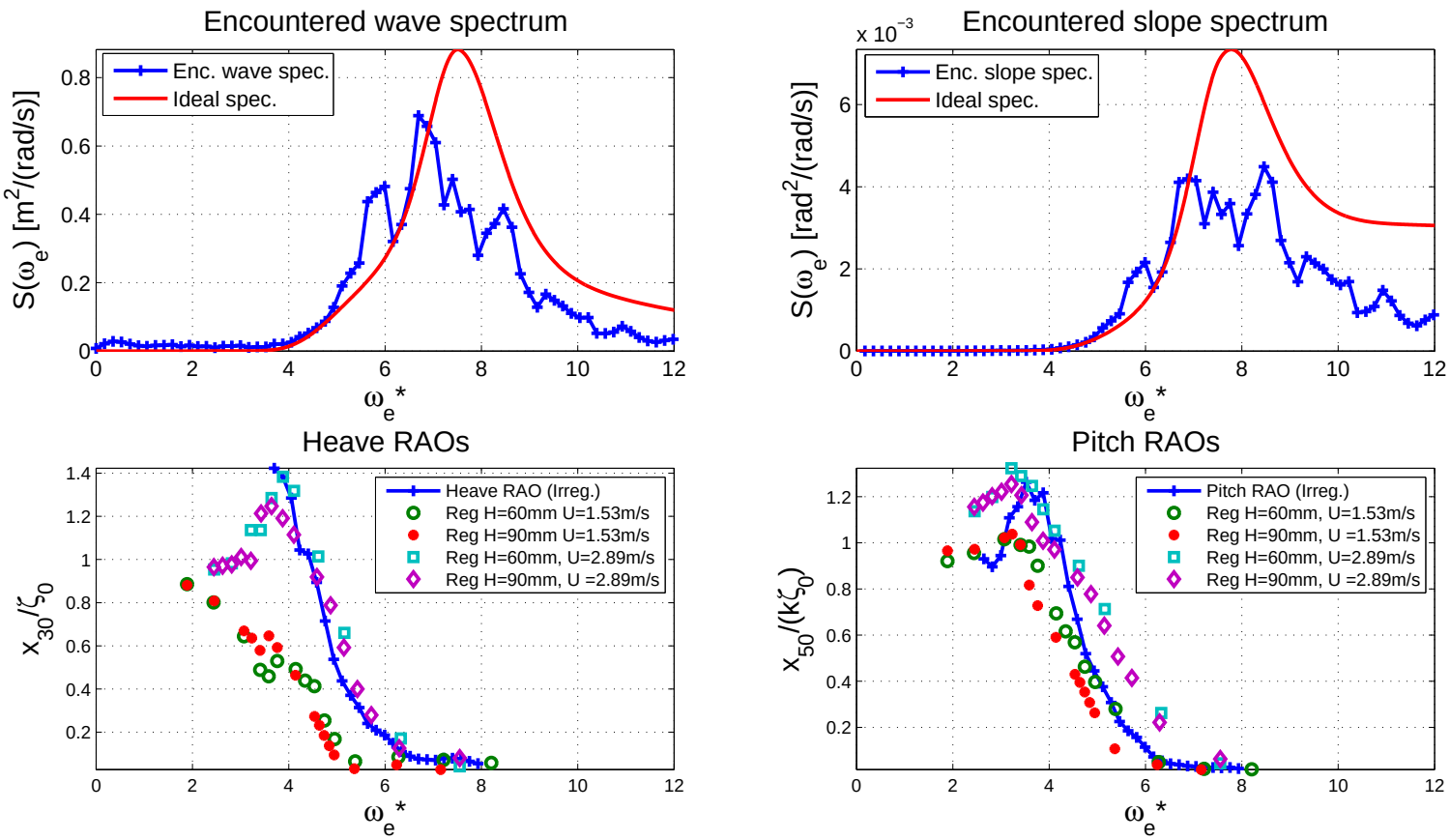

Figure A.11: Top: encountered wave height and slope spectra compared with the theoretical spectra. Bottom: measured heave and pitch RAOs compared with regular wave measurements from Lavroff [45]. Irregular Condition 100 $H_{1/3} = 89.3$mm, $T_0 = 1.0$s $U = 2.15$m/s.

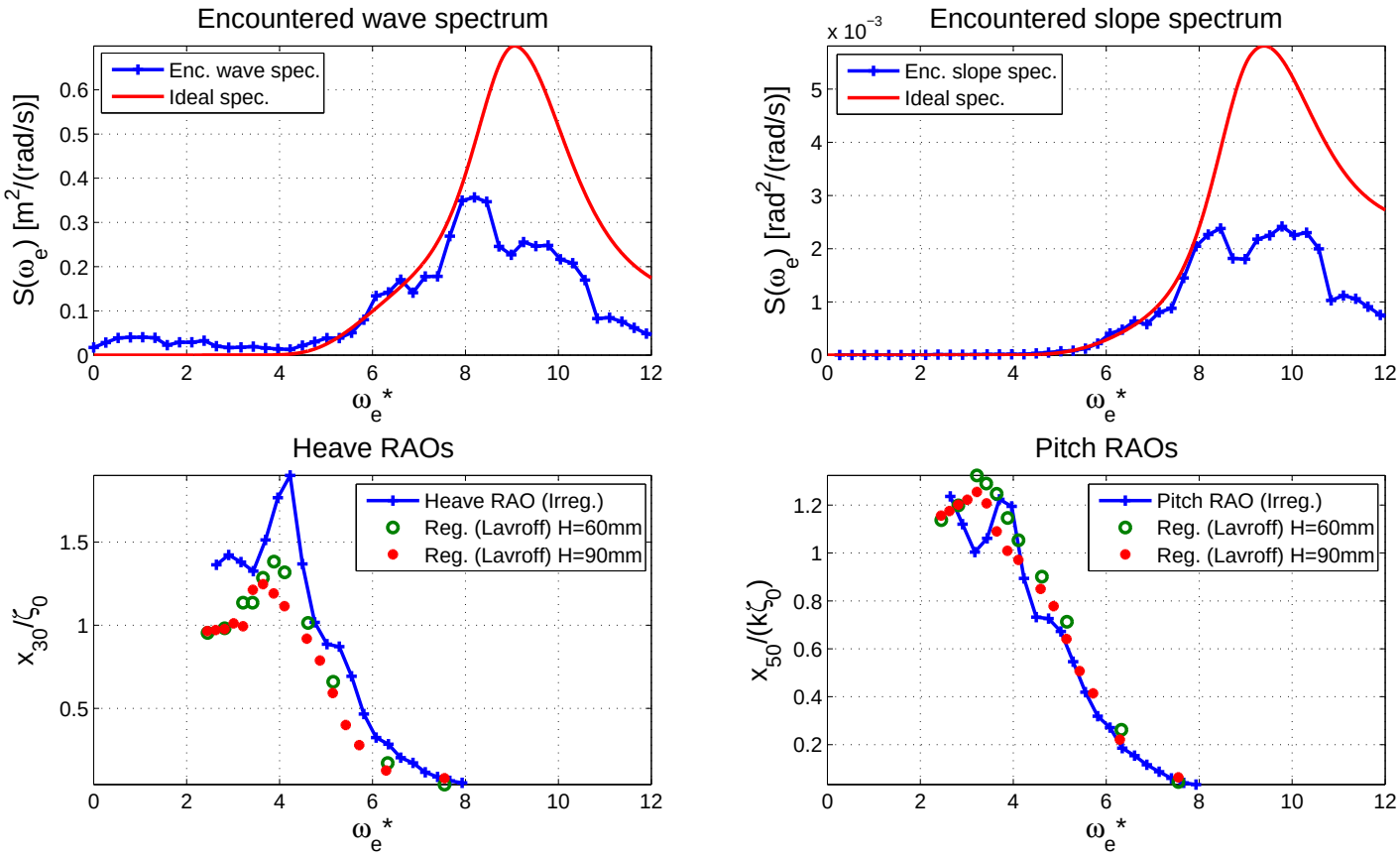

Figure A.12: Top: encountered wave height and slope spectra compared with the theoretical spectra. Bottom: measured heave and pitch RAOs compared with regular wave measurements from Lavroff [45]. Irregular Condition 101 $H_{1/3} = 89.3$mm, $T_0 = 1.0$s $U = 2.92$m/s.

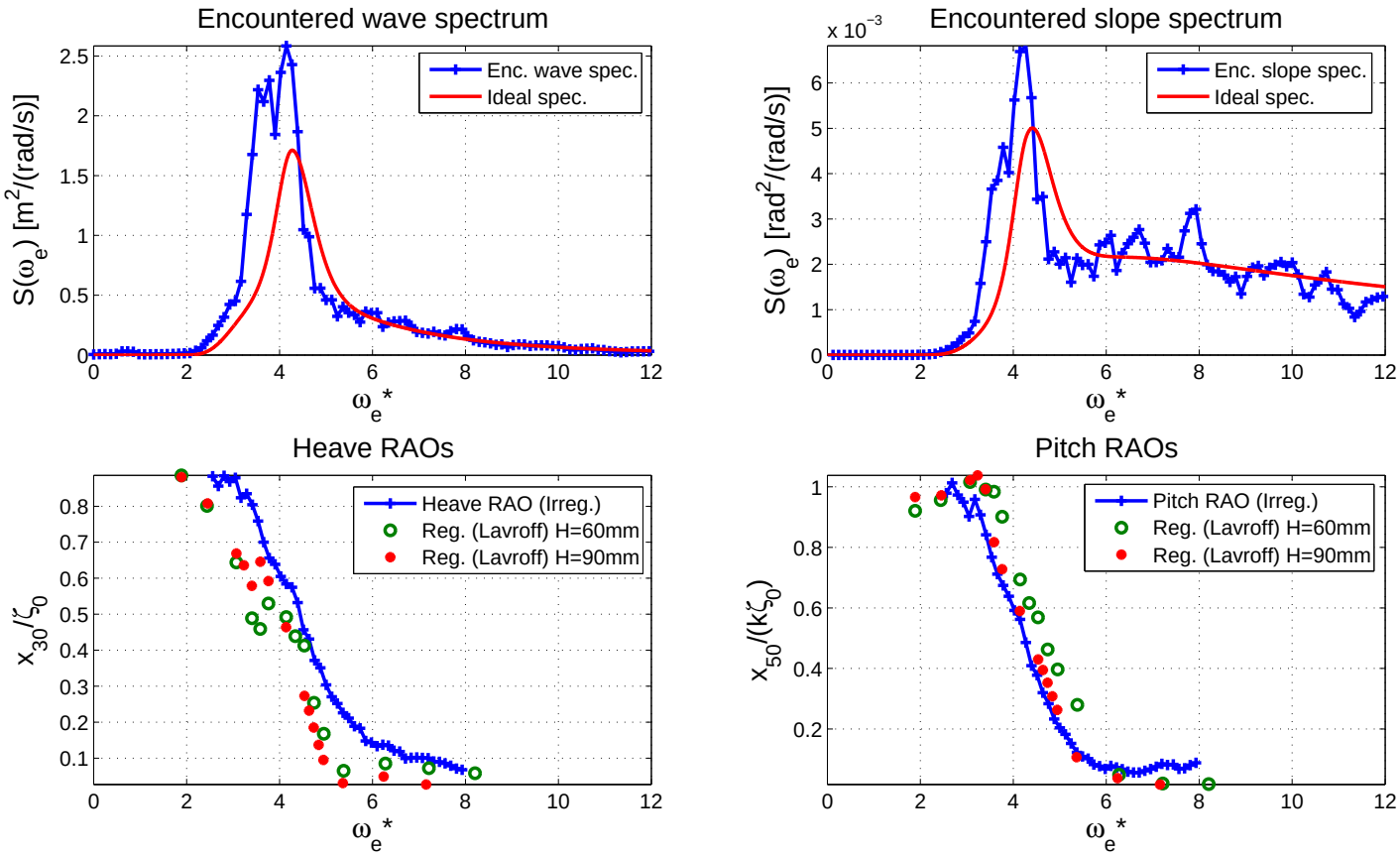

Figure A.13: Top: encountered wave height and slope spectra compared with the theoretical spectra. Bottom: measured heave and pitch RAOs compared with regular wave measurements from Lavroff [45]. Irregular Condition 102 $H_{1/3} = 89.3$mm, $T_0 = 1.3$s $U = 1.54$m/s.

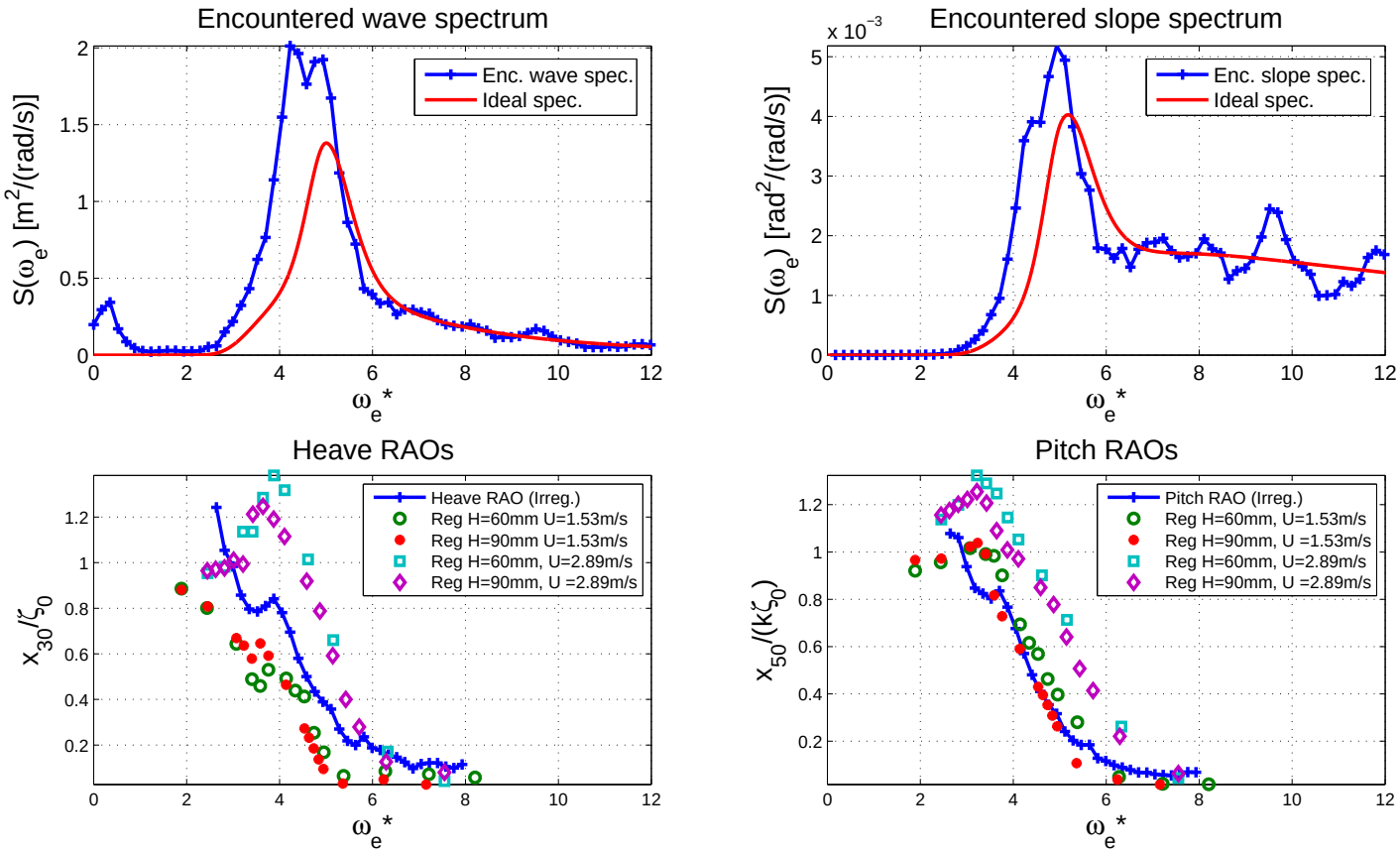

Figure A.14: Top: encountered wave height and slope spectra compared with the theoretical spectra. Bottom: measured heave and pitch RAOs compared with regular wave measurements from Lavroff [45]. Irregular Condition 103 $H_{1/3} = 89.3$mm, $T_0 = 1.3$s $U = 2.15$m/s.

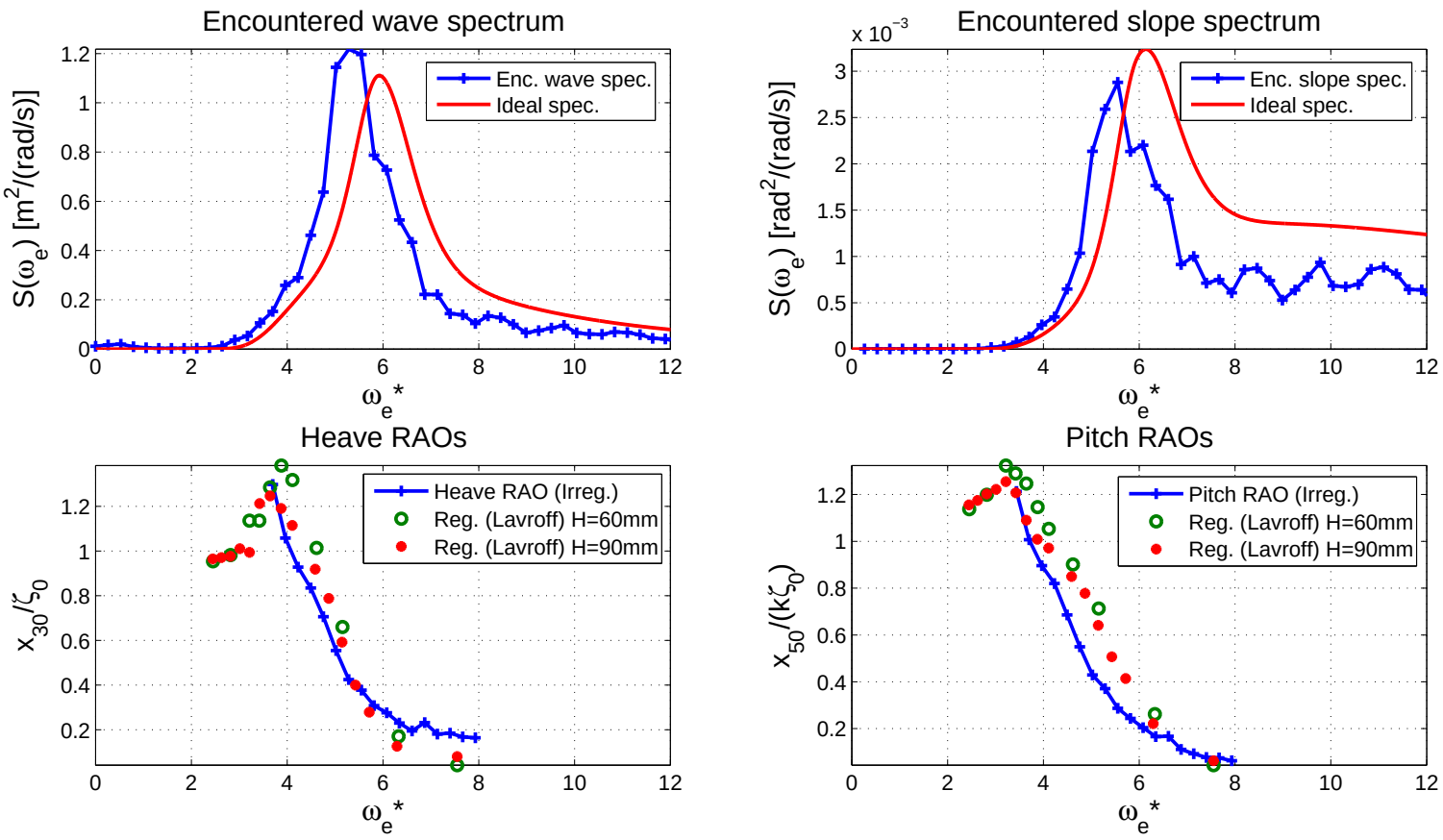

Figure A.15: Top: encountered wave height and slope spectra compared with the theoretical spectra. Bottom: measured heave and pitch RAOs compared with regular wave measurements from Lavroff [45]. Irregular Condition 104 $H_{1/3} = 89.3$mm, $T_0 = 1.3$s $U = 2.92$m/s.

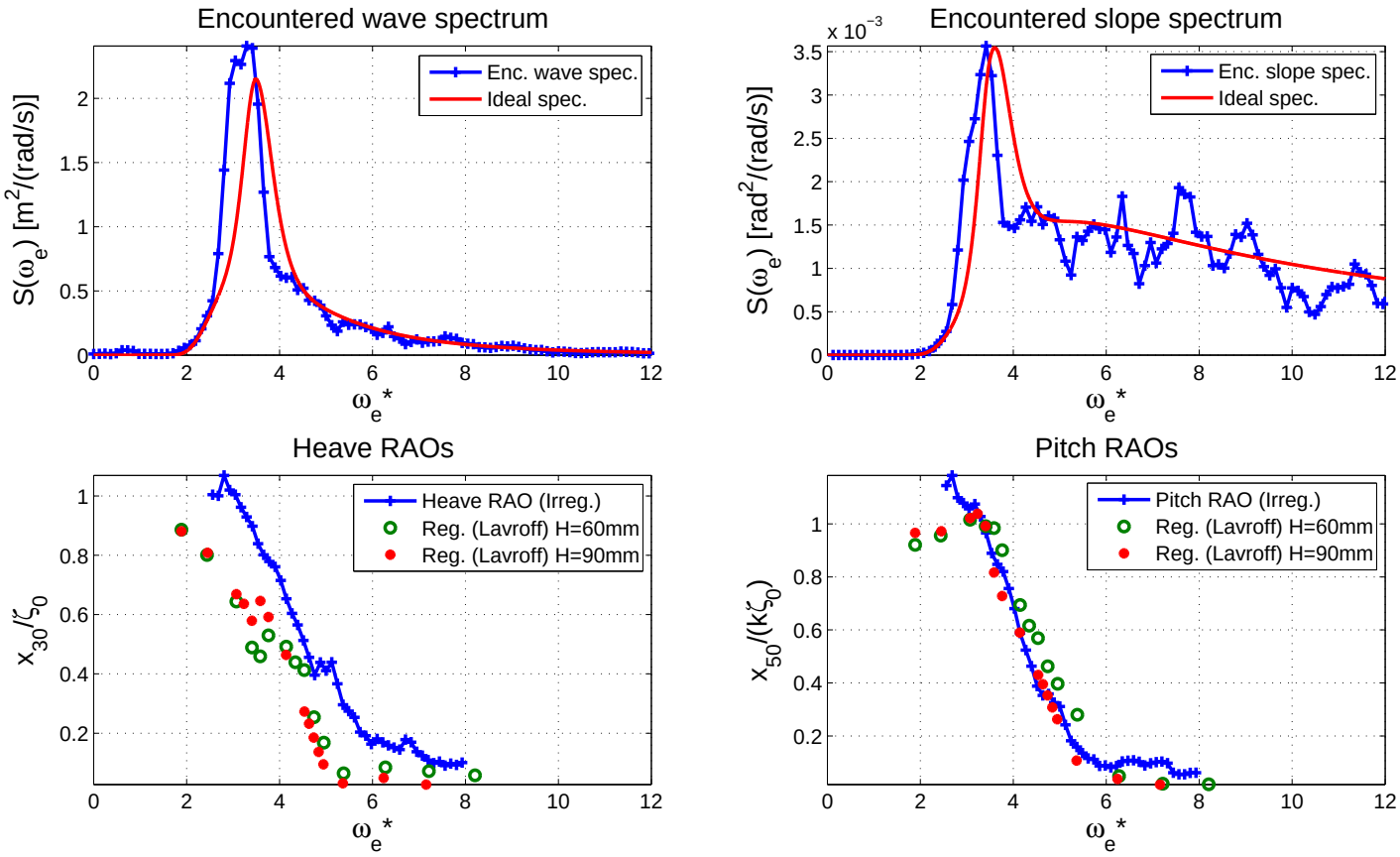

Figure A.16: Top: encountered wave height and slope spectra compared with the theoretical spectra. Bottom: measured heave and pitch RAOs compared with regular wave measurements from Lavroff [45]. Irregular Condition 105 $H_{1/3} = 89.3$mm, $T_0 = 1.5$s $U = 1.54$m/s.

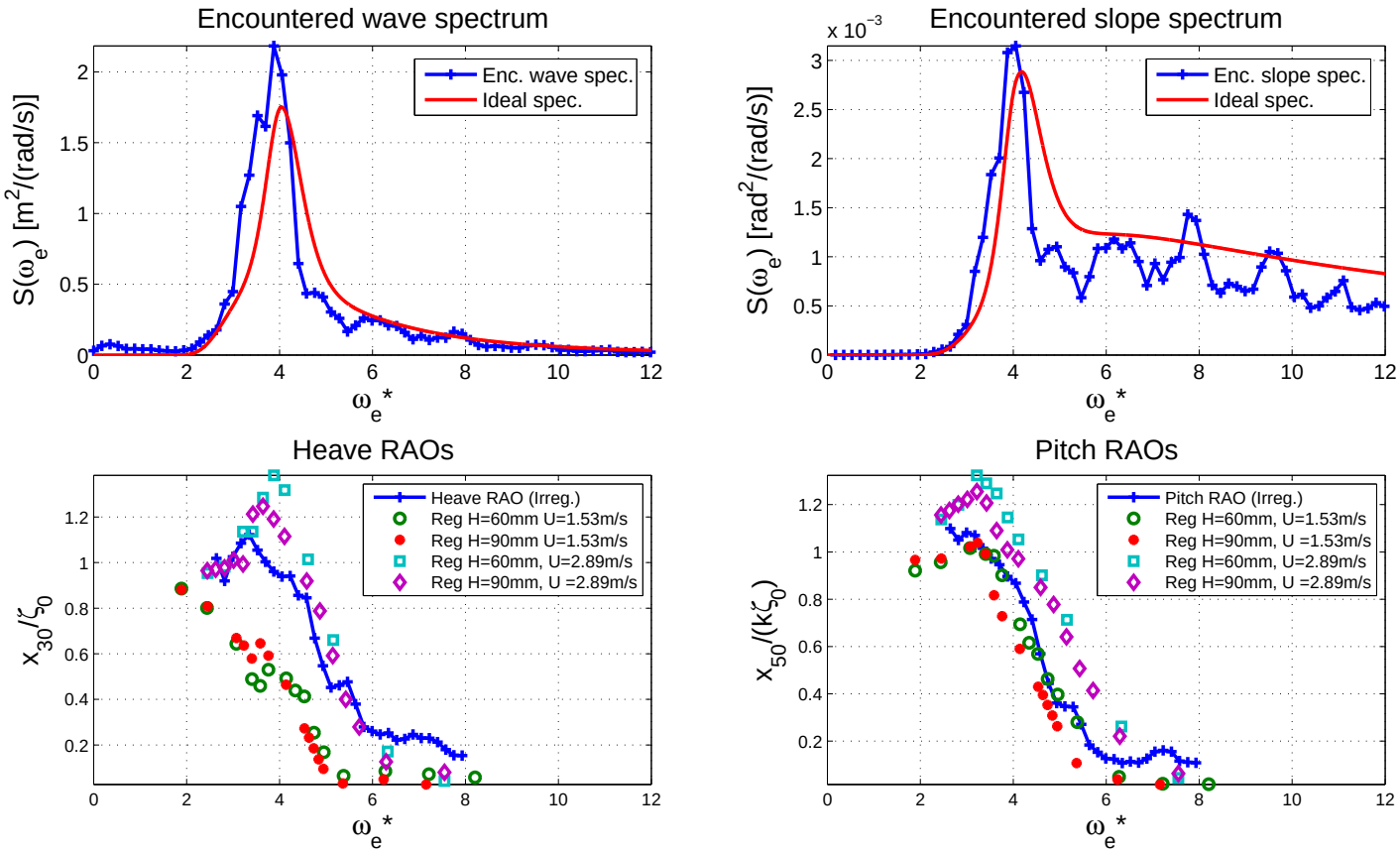

Figure A.17: Top: encountered wave height and slope spectra compared with the theoretical spectra. Bottom: measured heave and pitch RAOs compared with regular wave measurements from Lavroff [45]. Irregular Condition 106 $H_{1/3} = 89.3$mm, $T_0 = 1.5$s $U = 2.15$m/s.

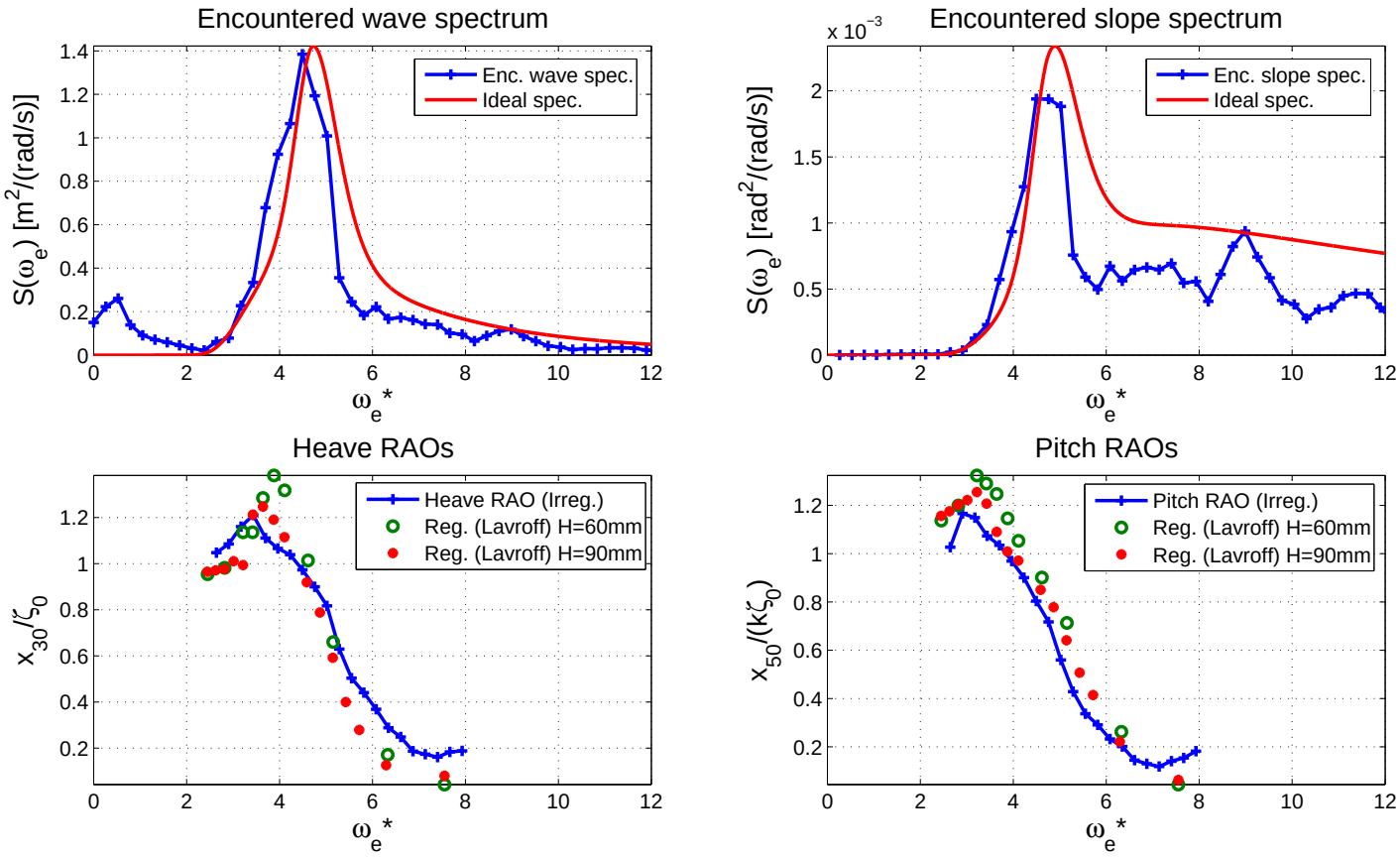

Figure A.18: Top: encountered wave height and slope spectra compared with the theoretical spectra. Bottom: measured heave and pitch RAOs compared with regular wave measurements from Lavroff [45]. Irregular Condition 107 $H_{1/3} = 89.3$mm, $T_0 = 1.5$s $U = 2.92$m/s.

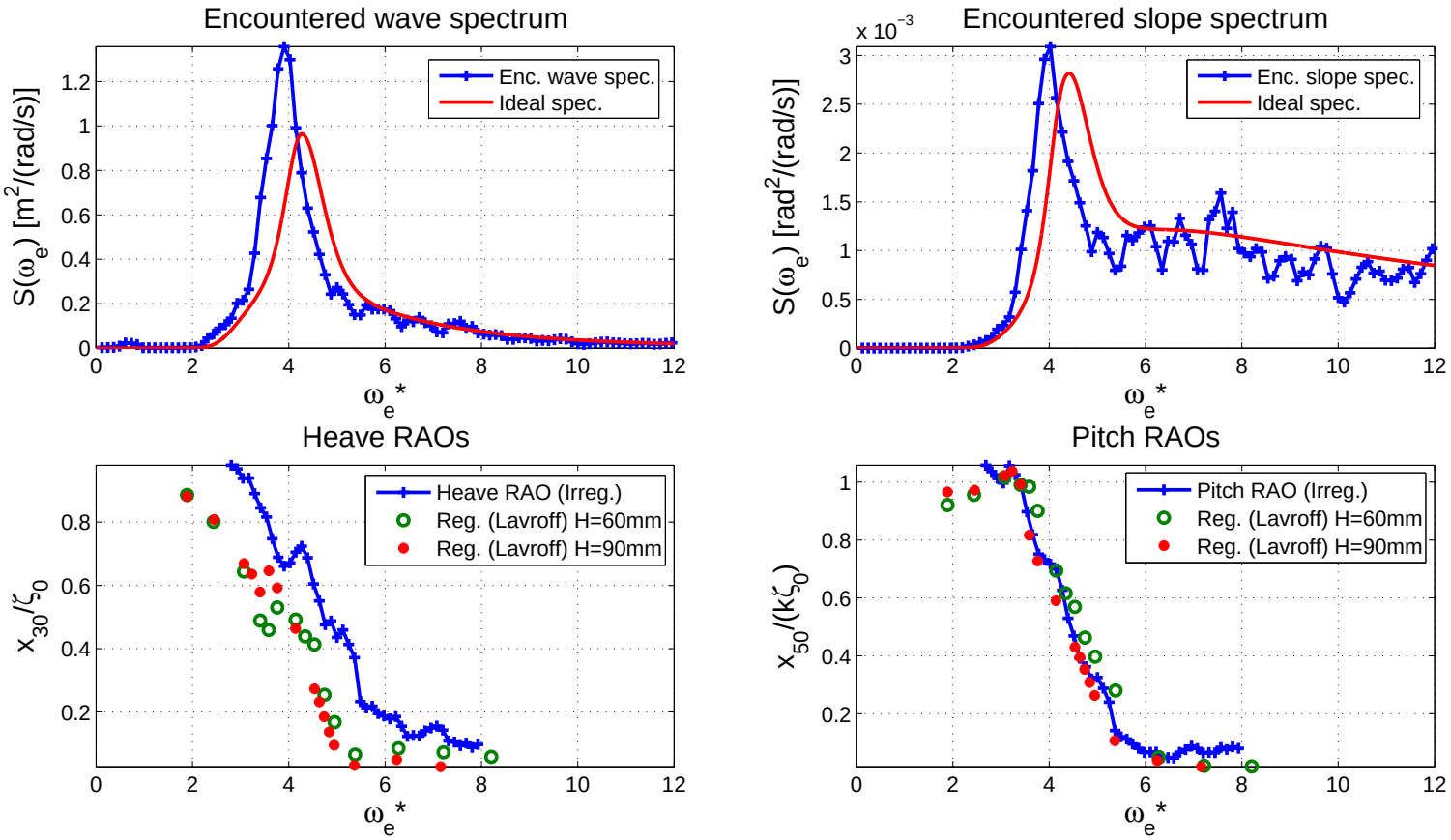

Figure A.19: Top: encountered wave height and slope spectra compared with the theoretical spectra. Bottom: measured heave and pitch RAOs compared with regular wave measurements from Lavroff [45]. Irregular Condition 108 $H_{1/3} = 67.0$mm, $T_0 = 1.3$s $U = 1.54$m/s.

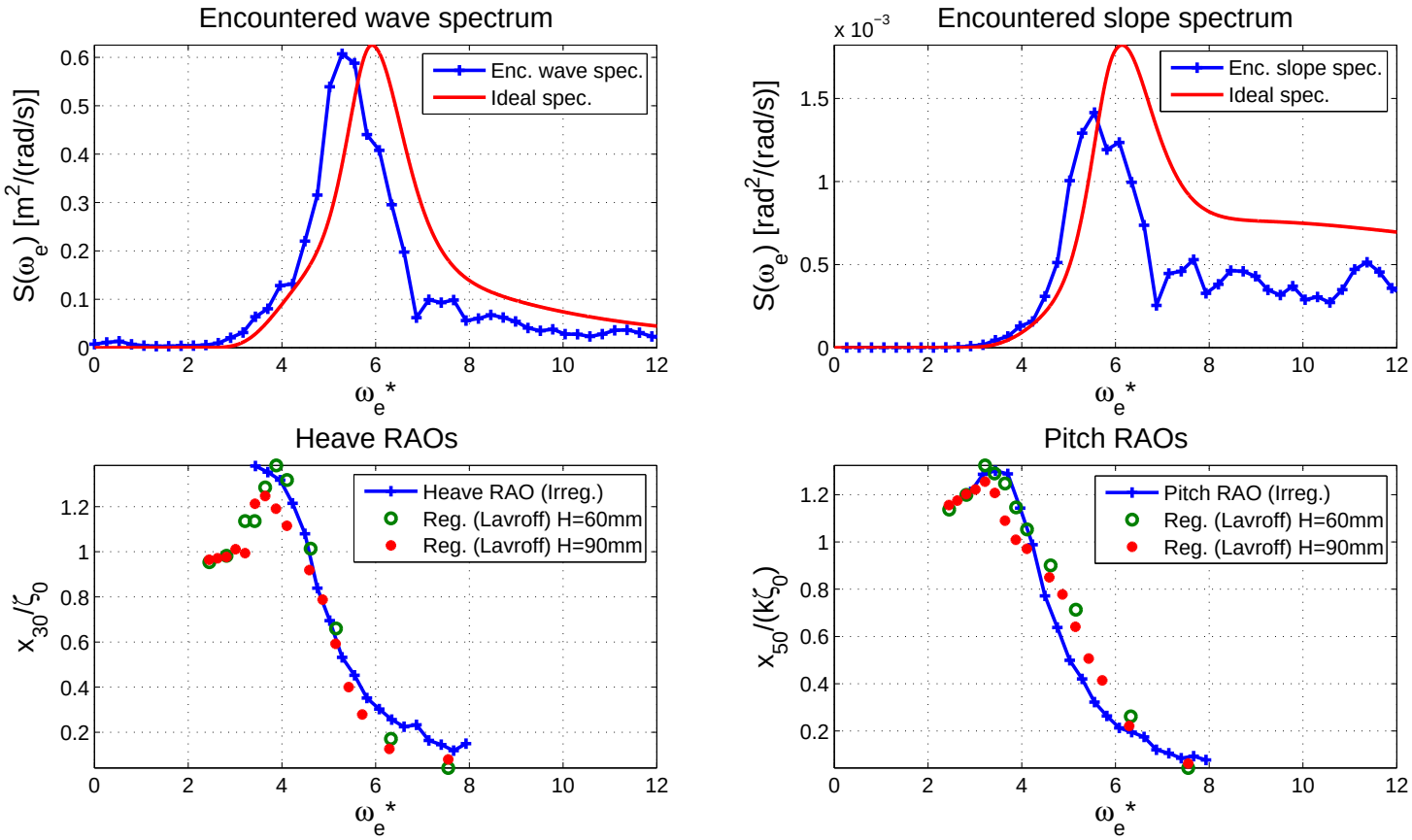

Figure A.20: Top: encountered wave height and slope spectra compared with the theoretical spectra. Bottom: measured heave and pitch RAOs compared with regular wave measurements from Lavroff [45]. Irregular Condition 109 $H_{1/3} = 67.0$mm, $T_0 = 1.3$s $U = 2.92$m/s.

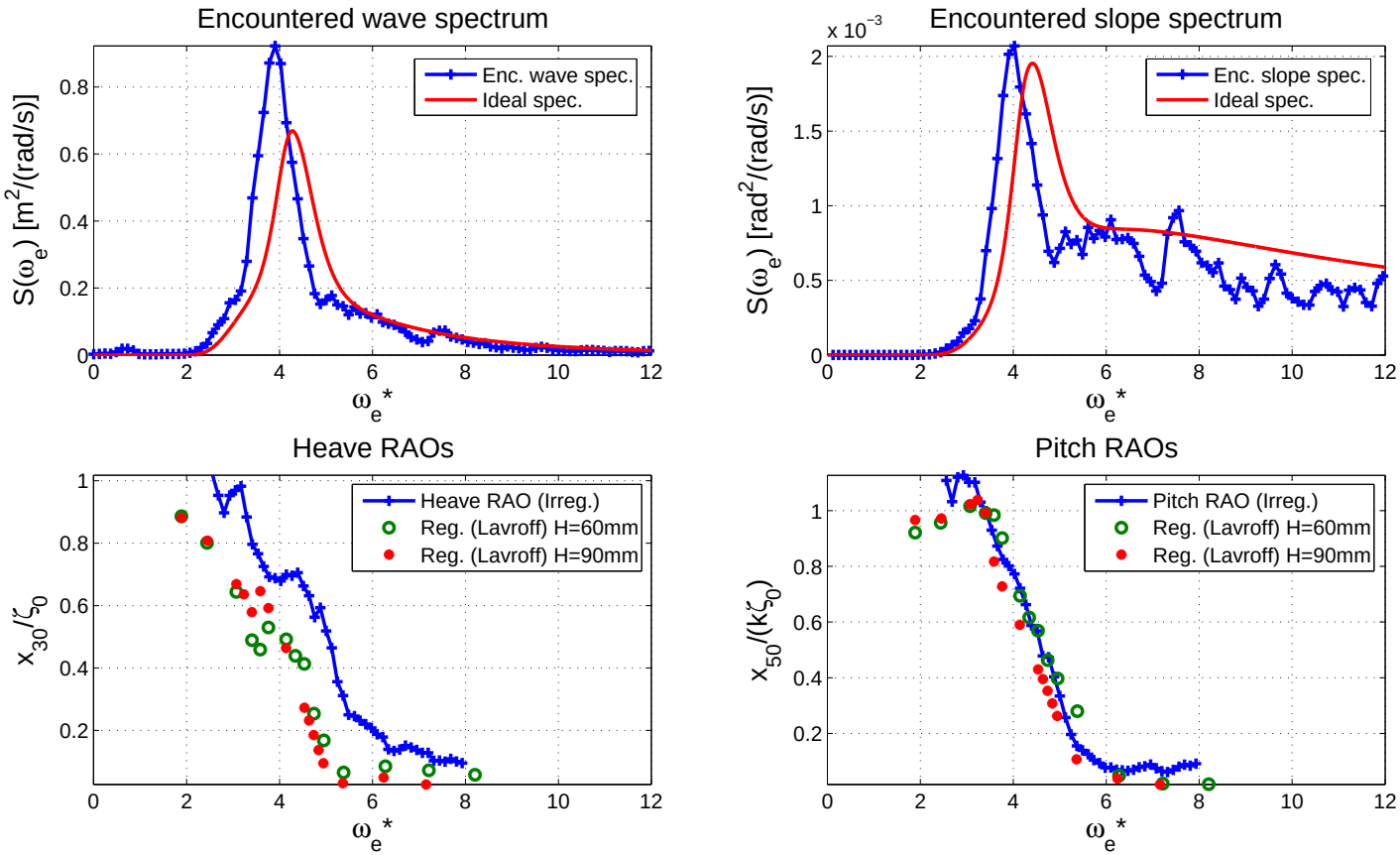

Figure A.21: Top: encountered wave height and slope spectra compared with the theoretical spectra. Bottom: measured heave and pitch RAOs compared with regular wave measurements from Lavroff [45]. Irregular Condition 110 $H_{1/3} = 55.8$mm, $T_0 = 1.3$s $U = 1.54$m/s.

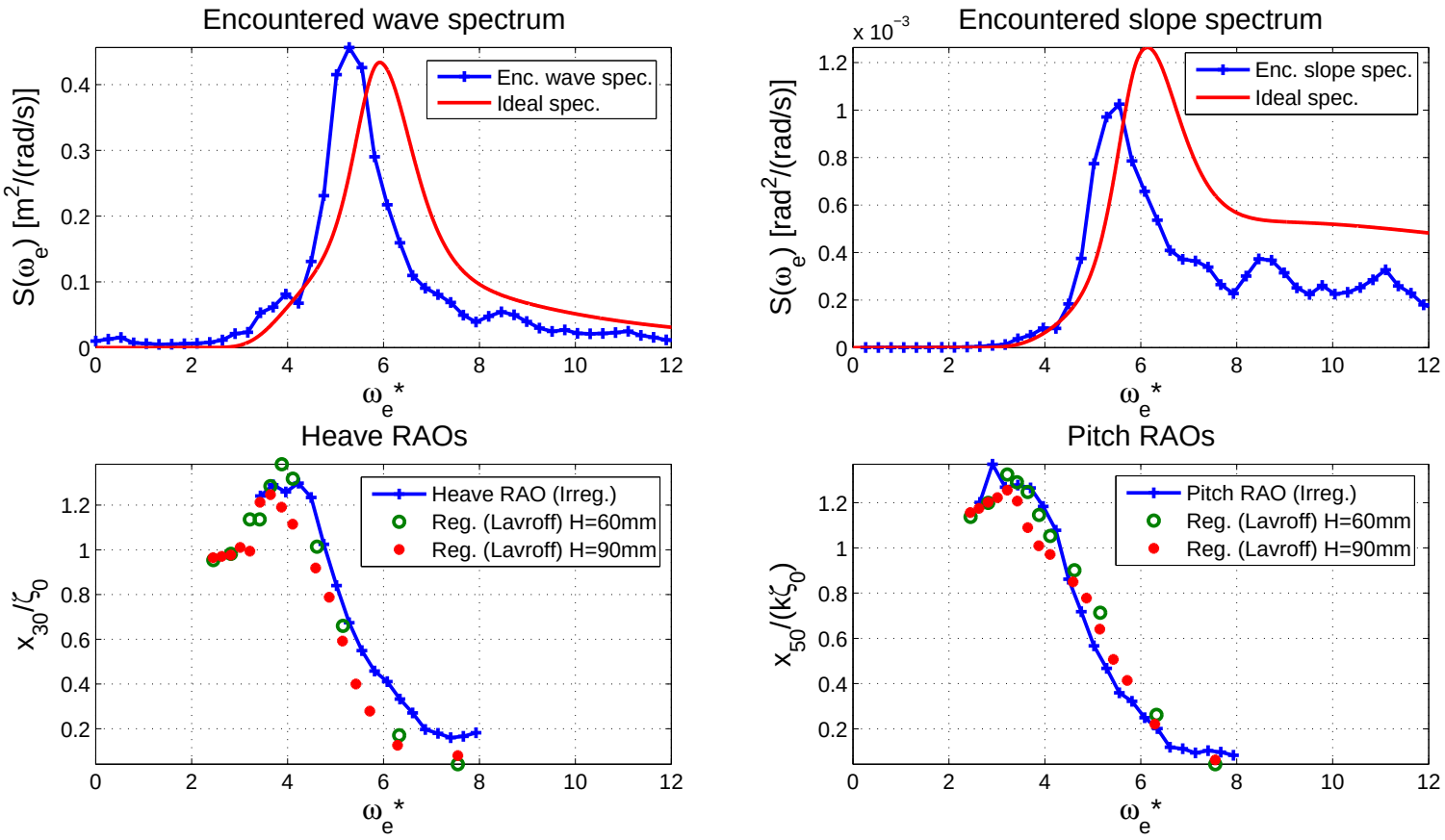

Figure A.22: Top: encountered wave height and slope spectra compared with the theoretical spectra. Bottom: measured heave and pitch RAOs compared with regular wave measurements from Lavroff [45]. Irregular Condition 110 $H_{1/3} = 55.8$mm, $T_0 = 1.3$s $U = 2.92$m/s.

Appendix B

Motions Prediction Investigation

The response magnitude offset observed in Chapter 4 is not only present in the 112m class vessels (Incat Hull 064 to 067) but also in earlier Incat designs. The United States Navy conducted extensive full scale seakeeping measurements on Incat Hull 061 (also known as HSV-2 Swift, a 98m class vessel), and raw data from these trials were released to Incat Tasmania, the University of Tasmania and the Australian Maritime College in 2011 for further analysis. A selection of this data was analysed by Jacobi [39]. Motion comparisons (with and without ride control operating) between Hull 061 and the time-domain seakeeping predictions revealed the same resonance offset as seen in Chapter 4[1]. This shows that the problem is not unique for the 112m hull, but is an issue for all Incat hull forms.

A number of factors have been identified that could attribute to this discrepancy in resonant frequency, these are discussed briefly in the following sections.

Vertical Damping Force Coefficient

Davis and Holloway [15] compiled a comprehensive study validating this code for 14 different hull forms against towing tank data for conventional slender hulls suitable for high speed catamarans, monohulls, SWATH (small water area twin hull) and semi-SWATH hull forms. Motions of an NPL 5b catamaran model were also satisfactorily predicted in oblique seas in a separate investigation [64]. Peak magnitudes of the RAOs were found to be particularly sensitive to damping effects, therefore the empirical vertical damping force per section equation was introduced. The drag force is (per unit length) defined as:

$$\vec{D} = C_s \frac{1}{2} \rho \left| \vec{V} \right|^2 B \tag{B.1}$$

In the direction of $-\vec{V}$, where $\vec{V} = U\hat{\imath} + V_{\text{rel}}\hat{\jmath}$, B is the beam and U is the forward speed of the ship. Assume that $V_{\text{rel}} \ll U$. Therefore the vertical component of the drag force is:

[1] Work by Jacobi et al. [40] comparing full scale motions with the time-domain simulation is currently in press at the time of writing.

$$\vec{D} \cdot \hat{\jmath} = -C_s \frac{1}{2} \rho \left| \vec{V} \right| \vec{V} \cdot \hat{\jmath} B \tag{B.2}$$

$$\simeq -C_s \frac{1}{2} \rho U \vec{V} \cdot \hat{\jmath} B \tag{B.3}$$

$$= -C_s \frac{1}{2} \rho U V_{\text{rel}} B \tag{B.4}$$

Alteration of this damping coefficient can significantly change peak responses of the heave RAO, with smaller reductions in pitch, however it does little to shift the resonance in the frequency dimension. The values for C_s vary, but are less than 0.15 and commonly of the order of 10^{-2} for simple geometries [15]. Figure B.1 shows the influence of the sectional friction coefficient C_s on the resonant motions of the 112m class Incat vessel compared with scale model results in regular seas (scale model data from Lavroff [45]). When a sectional friction coefficient of 0.1 is selected, the magnitude of the peak compares well with scale model results however the obvious shift in frequency remains. A coefficient of 0.08 was used for the motions plots presented in Chapter 4 (Figures 4.8 to 4.11).

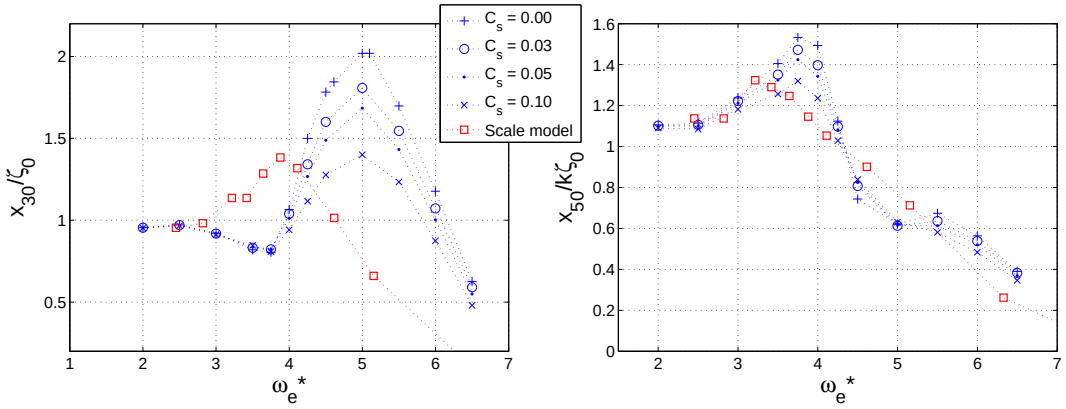

Figure B.1: Influence of sectional vertical damping force coefficient C_s on the resulting heave and pitch RAO. Head seas in regular waves, $H = 60$mm, $U = 2.98$m/s model scale (2.7m, 38kts full scale).

Number of Panels

As mentioned in Section 4.5.2, 14 panels per section were found to adequately model vessel motions. The Incat catamarans are much more complex in shape (wave-piercing semi-SWATHs with a centre bow, a flat hull bottom and an almost rectangular section near the stern), therefore the influence of the number of panels on the solution was re-examined.

A number of RAOs were calculated for the 112m class vessel by subjecting the vessel to a regular wave and then determining the dimensionless heave and pitch by calculating the average peak heave and pitch with a root-mean-square method, and then dividing by the wave height or slope. This process was repeated for 13 regular wave frequencies to construct the RAO,

and three different numbers of panels per section. Figure B.2 shows the results of this test. The vessel speed was 19.55m/s (38 knots) and a wave height of 2m (headseas), 80 sections per demihull (with centre bow). Little improvement can be seen by doubling the number of panels from 14 to 28 per section. Therefore it can be concluded that the sectional panelling resolution is not a major contributor to the frequency response error.

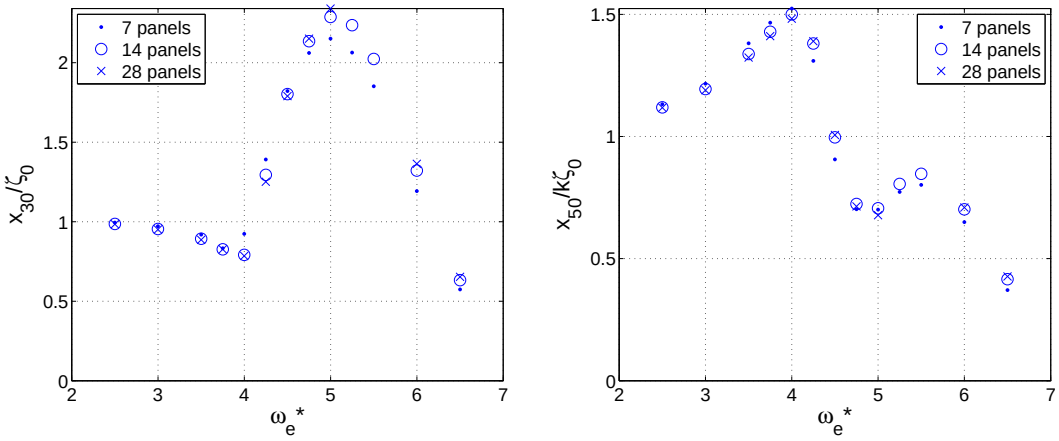

Figure B.2: Heave (left) and pitch (right) RAOs from the time-domain seakeeping code for different number of panels per section.

Wave Height and Centre Bow Action

The presence of virtually a third hull, the centre bow, makes the Incat design unique from many catamarans. Since the centre bow is designed to be out of, or just touching the water in calm seas, it only comes into action by providing reserve buoyancy in moderate to large wave conditions, therefore the motions of the vessel is said to be nonlinear with respect to wave height. This has been observed in scale model testing where the heave and pitch RAOs are seen to be functions of wave height [45, 53]. Generally as the wave height increases the peak of the RAO decreases and moves to lower frequencies.

The seakeeping code is also a nonlinear formulation and should be able to detect a change in non-dimensional heave and pitch for different wave heights. Figures B.3 and B.4 show the predicted heave and pitch RAOs for differing wave heights. Computational stability problems were encountered when predicting motions at 3.0m and 3.5m around the resonance response frequency for both solution sets. The failed points have been left off the plots and the RAOs for these wave heights are incomplete. The centre bow is included in Figure B.3 and was removed from the geometry file prior to computing the results shown in Figure B.4. As wave height is increased, the magnitude of the peak response decreases and shifts to left, as expected from previous model tests. Interestingly the same trend is apparent in Figure B.4 where the centre bow was neglected. A comparison between RAOs with and without the centre bow modelled is shown in Figure B.5, the peak magnitude of the heave RAO is larger when the centre bow was not modelled, suggesting that the action of the centre bow entering and leaving the water

reduces motions by providing extra damping. The addition of the centre bow seems to shift the natural frequency of the vessel to the right, implying that the increase in stiffness provided by the reserve buoyancy of the centre bow overshadows any increase in added mass produced by the motion of the bow in the water.

Added Mass

Forward Speed Correction The strip theory presented by Salvensen, Tuck and Faltinsen [60] included extra terms in their added mass and damping coefficient formulations not usually included in strip theories. These terms have not been included in the time domain seakeeping code employed here. Equations B.5 and B.6 (known as the 'end term effect') show the added mass and damping coefficients for heave motions in a form convenient for a frequency domain solution. Similar added mass and damping coefficient equations exist for the other motions and couplings.

$$A_{33} = \int a_{33} d\xi - \frac{U}{\omega^2} b_{33}^A \tag{B.5}$$

$$B_{33} = \int b_{33} d\xi + U a_{33}^A. \tag{B.6}$$

Here a_{33} and b_{33} are the two-dimensional sectional added mass and damping coefficients for heave and the integrals are over the length of the ship. U is the forward speed and ω is the encountered wave frequency. The terms with superscript A represent the two-dimensional sectional coefficients at the very last section (transom) that were not included in earlier strip theory methods.

Salvesen et al. [60] argue that these end terms have considerable effect on the motions of vessels with wide transom sterns. The application of strip theories to vessels with transom sterns has also been questioned, since the transom violates the strip theory assumption of small longitudinal changes along the hull. They also point out that at speed the sudden change in geometry at the transom does not cause a jump in the flow field and thus the strip theory assumption is restored, however they do admit that the main justification for including these terms for transom stern ships is that results seem to agree better with model tests.

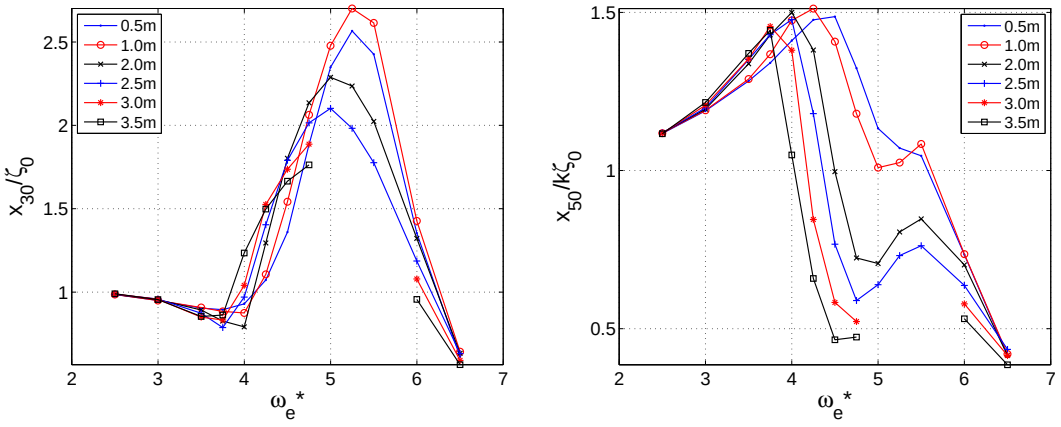

Figure B.3: Heave and pitch RAOs from the time-domain seakeeping code for different wave heights (head seas, regular waves $U = 38$kts centre bow modelled). Note the 3.0m and 3.5m wave height solutions failed around the resonant peak.

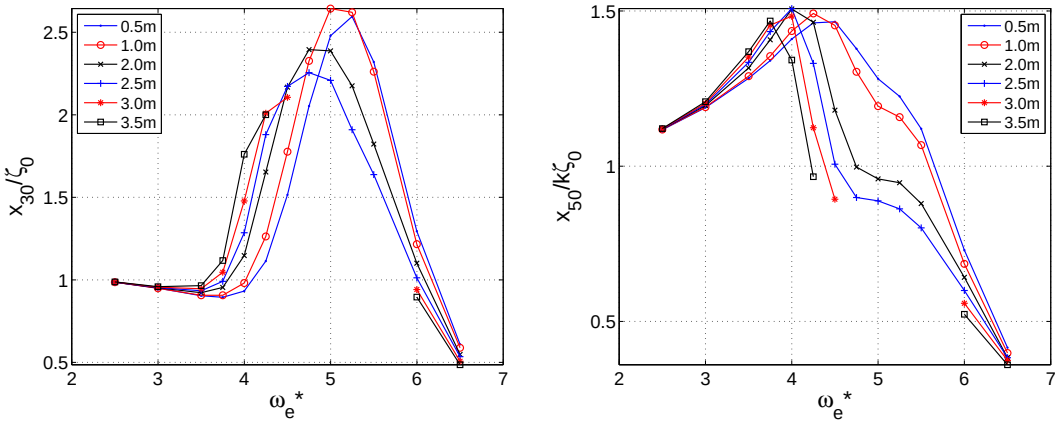

Figure B.4: Heave and pitch RAOs from the time-domain seakeeping code for different wave heights (head seas, regular waves $U = 38$kts, centre bow *not* modelled). Note the 3.0m and 3.5m wave height solutions failed around the resonant peak.

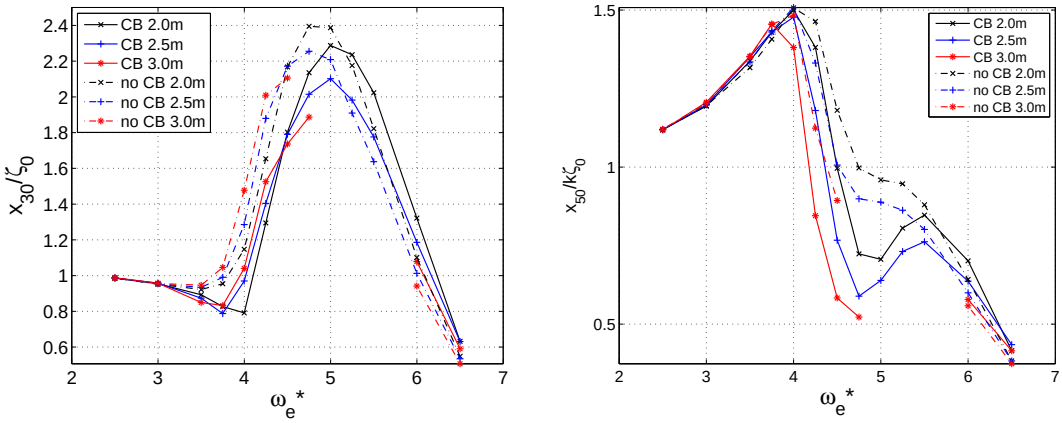

Figure B.5: RAO comparison between selected wave heights with and without the centre bow included in the solution.

Chines Separation and eddies induced by the vertical motion of the sections, particularly towards the aft of the vessel where the sections become near rectangular may be a source of extra added mass present in the physical models but not accounted for in the strip theory.

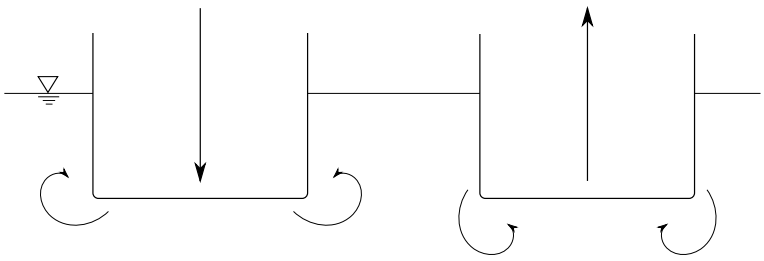

Figure B.6: Flow separation - potential source of added mass not considered in the current formulation.

Appendix C

Slam Distributions

The following figures have been placed in this appendix in an attempt to streamline the already figure intensive Chapter 5.

Figures C.1 to C.3 are probability density function representations of the box plots shown in Figures 5.9 to Figures 5.11 from Section 5.4.1. Slam load distributions are shown when the data is grouped by Froude number, significant wave height and model period respectively.

Figures C.4 to C.18 compares distributions of different slam characteristics (namely the maximum relative vertical velocity prior to the slam event, the relative vertical velocity at the time the slam was identified, the immersion of the centre bow truncation and the slam locations) when they are grouped by the three condition parameters (Froude number, modal period and significant wave height). The left hand plot in each figure show box plots effectively representing the probability density function (pdf) of the different parameters and the right hand figures show the respective cumulative distribution functions (cdf).

Figures C.19 and C.20 are scatter plots of slam location against maximum immersion. They are to complement Figures 5.29 and 5.30 on pages 89 and 90.

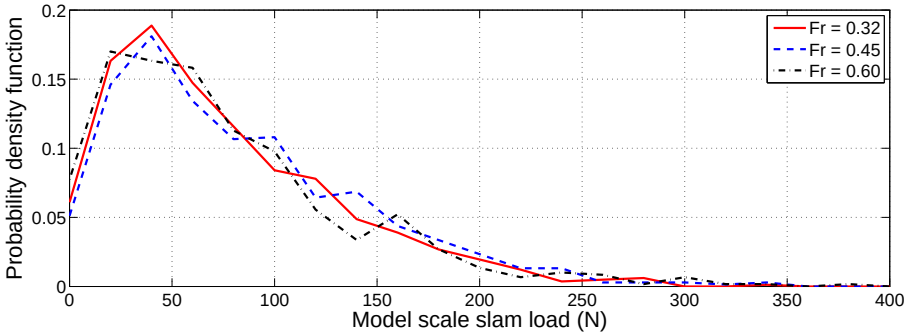

Figure C.1: Slam magnitude probability density function. Data is grouped by Froude number.

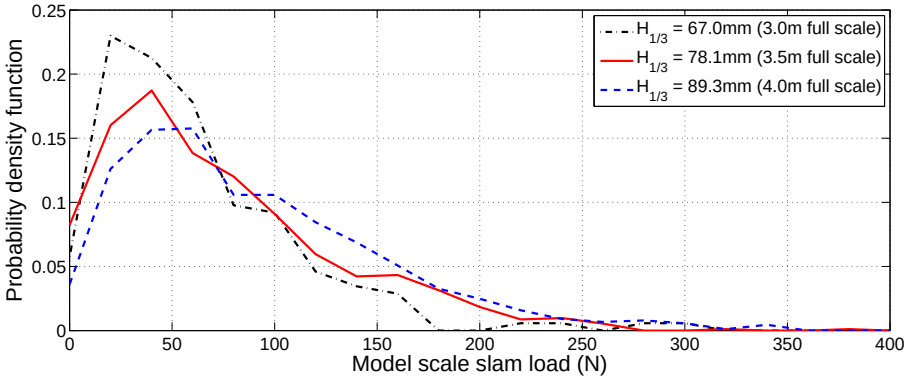

Figure C.2: Slam magnitude probability density function. Data is grouped by significant wave height.

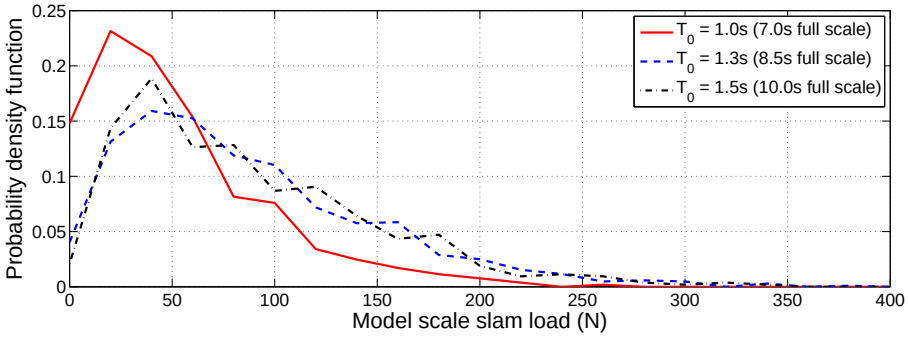

Figure C.3: probability density function. Data is grouped by modal period.

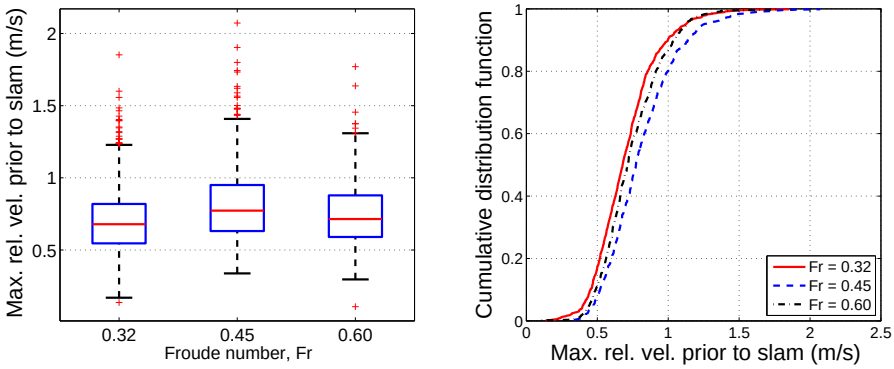

Figure C.4: Distributions of maximum velocity prior to slam for differing Froude numbers.

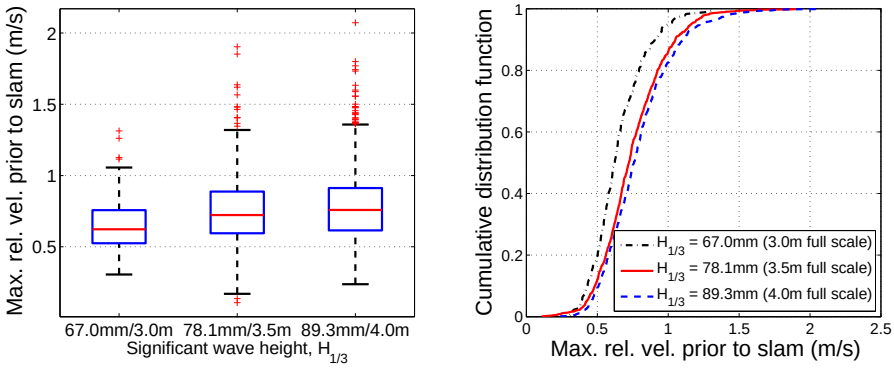

Figure C.5: Distributions of maximum velocity prior to slam for differing significant wave heights.

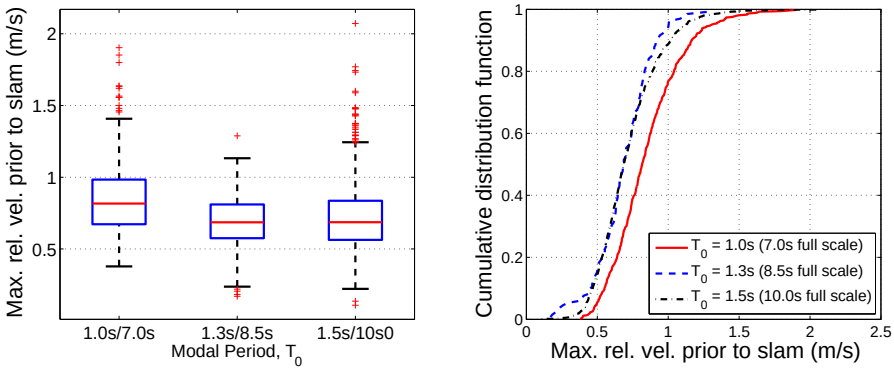

Figure C.6: Distributions of maximum velocity prior to slam for differing modal periods.

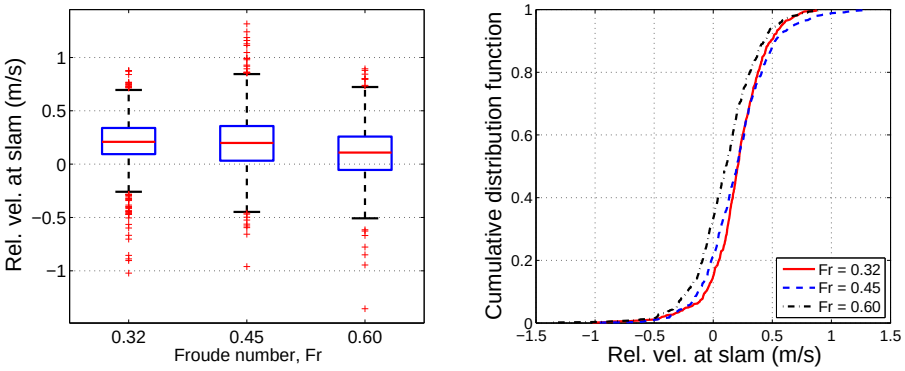

Figure C.7: Distributions of velocity at slam for differing Froude numbers.

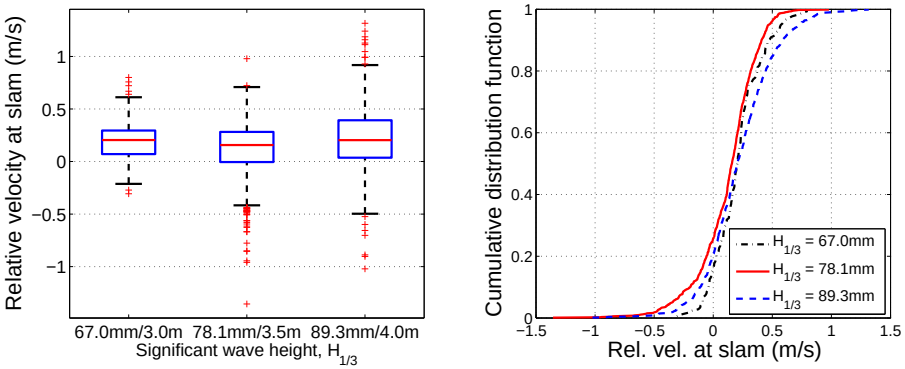

Figure C.8: Distributions of velocity at slam for differing significant wave heights.

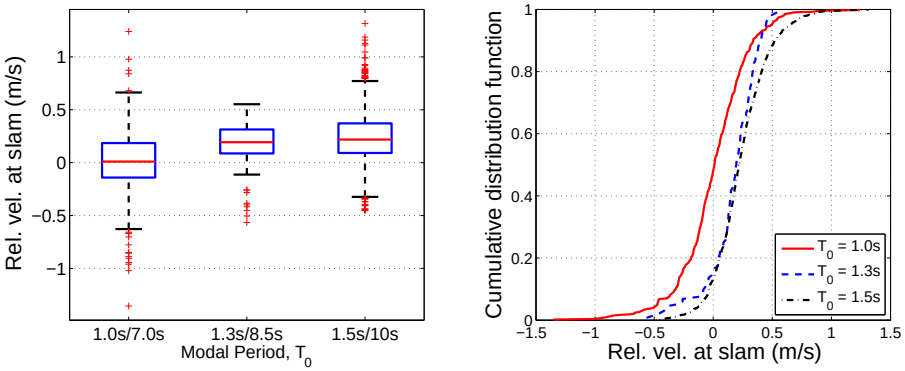

Figure C.9: Distributions of velocity at slam for differing modal periods.

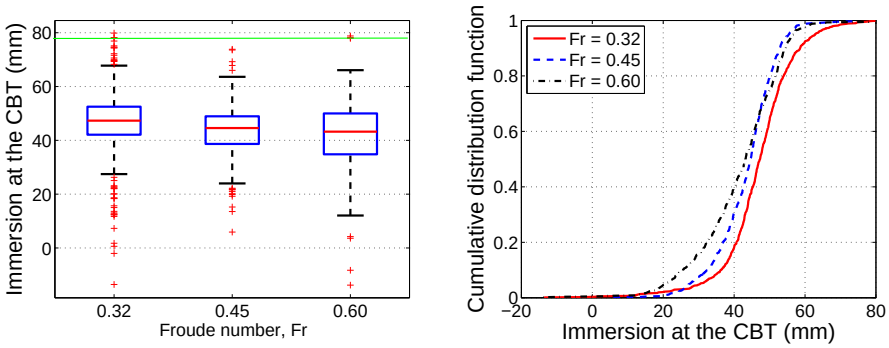

Figure C.10: Distributions of immersion at the centre bow truncation for differing Froude number. The maximum arch height at this location is also shown on the box plot.

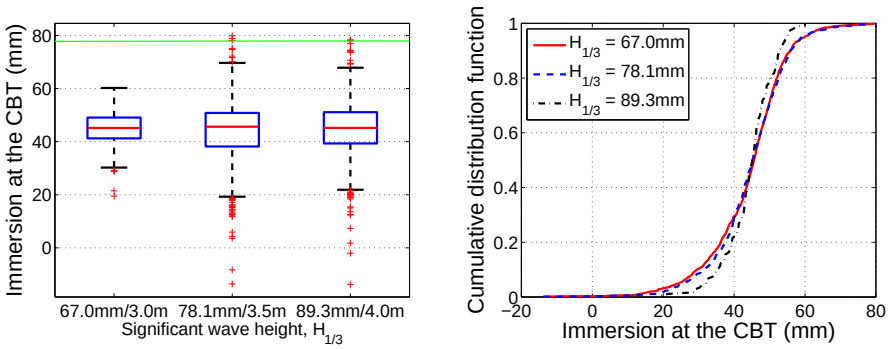

Figure C.11: Distributions of immersion at the centre bow truncation for differing significant wave height. The maximum arch height at this location is shown on the box plot.

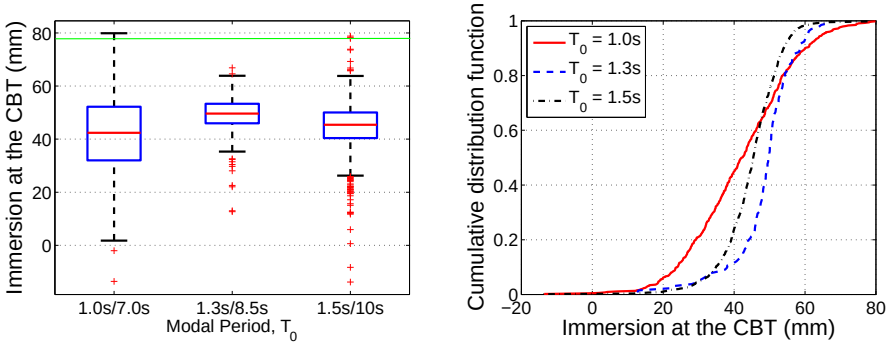

Figure C.12: Distributions of immersion at the centre bow truncation for differing modal period. The maximum arch height at this location is shown on the box plot.

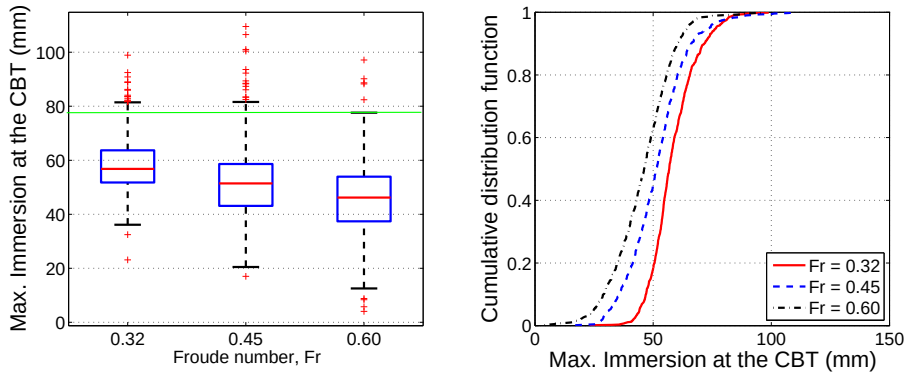

Figure C.13: Distributions of maximum immersion at the centre bow truncation for differing Froude number. The maximum arch height at this location is also shown on the box plot.

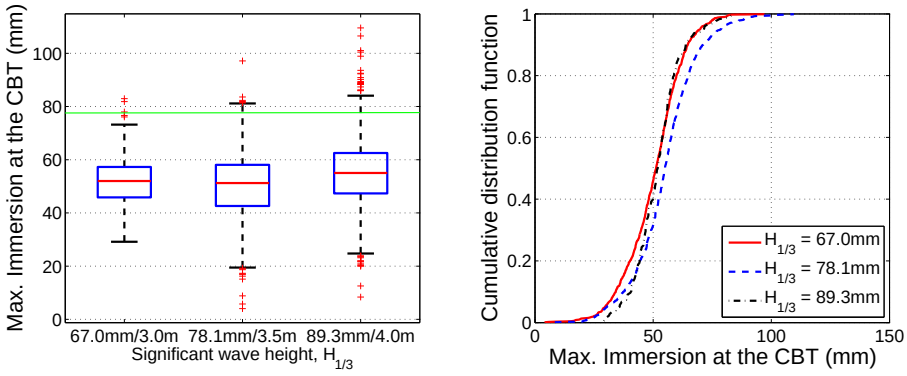

Figure C.14: Distributions of maximum immersion at the centre bow truncation for differing significant wave height. The maximum arch height at this location is shown on the box plot.

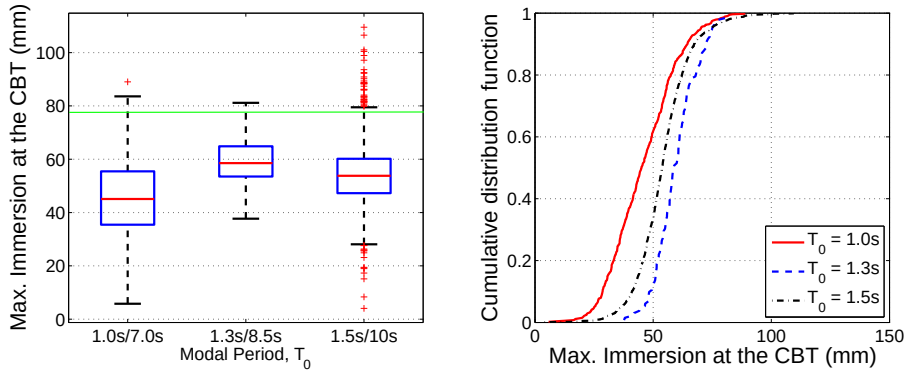

Figure C.15: Distributions of maximum immersion at the centre bow truncation for differing modal period. The maximum arch height at this location is shown on the box plot.

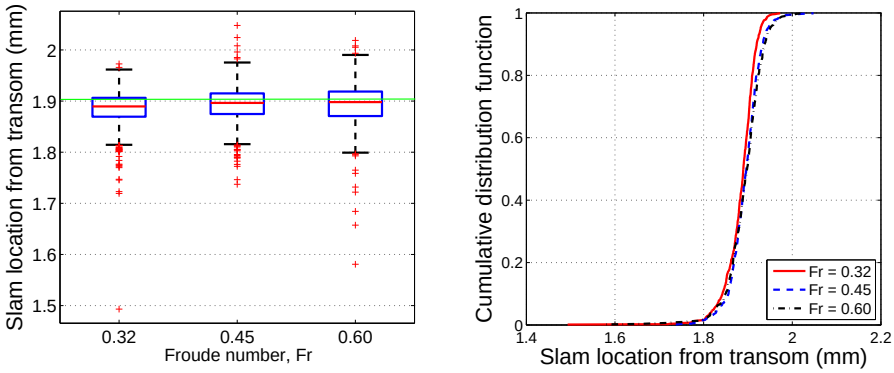

Figure C.16: Distributions of slam location for differing Froude number. The centre bow truncation is shown on the box plot.

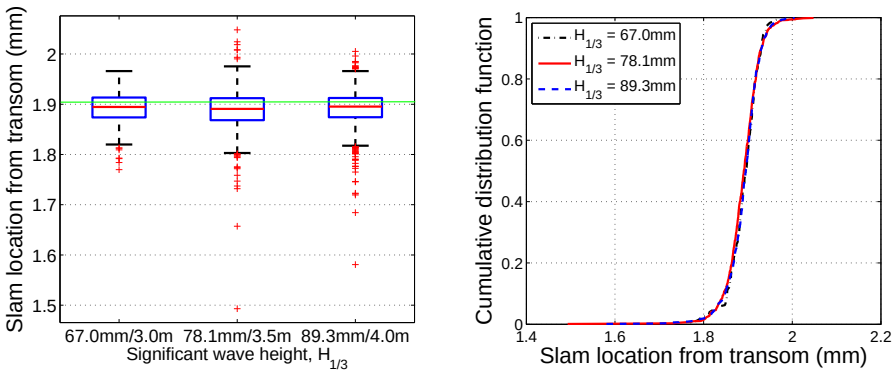

Figure C.17: Distributions of slam location for differing significant wave height. The centre bow truncation is shown on the box plot.

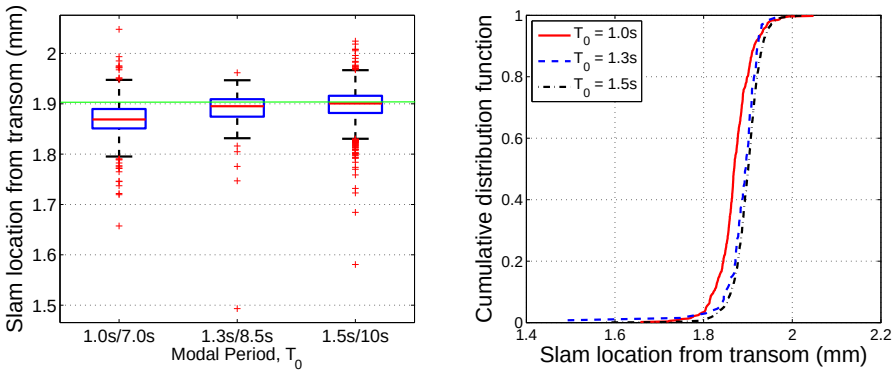

Figure C.18: Distributions of slam location for differing modal period. The centre bow truncation is also shown on the box plot.

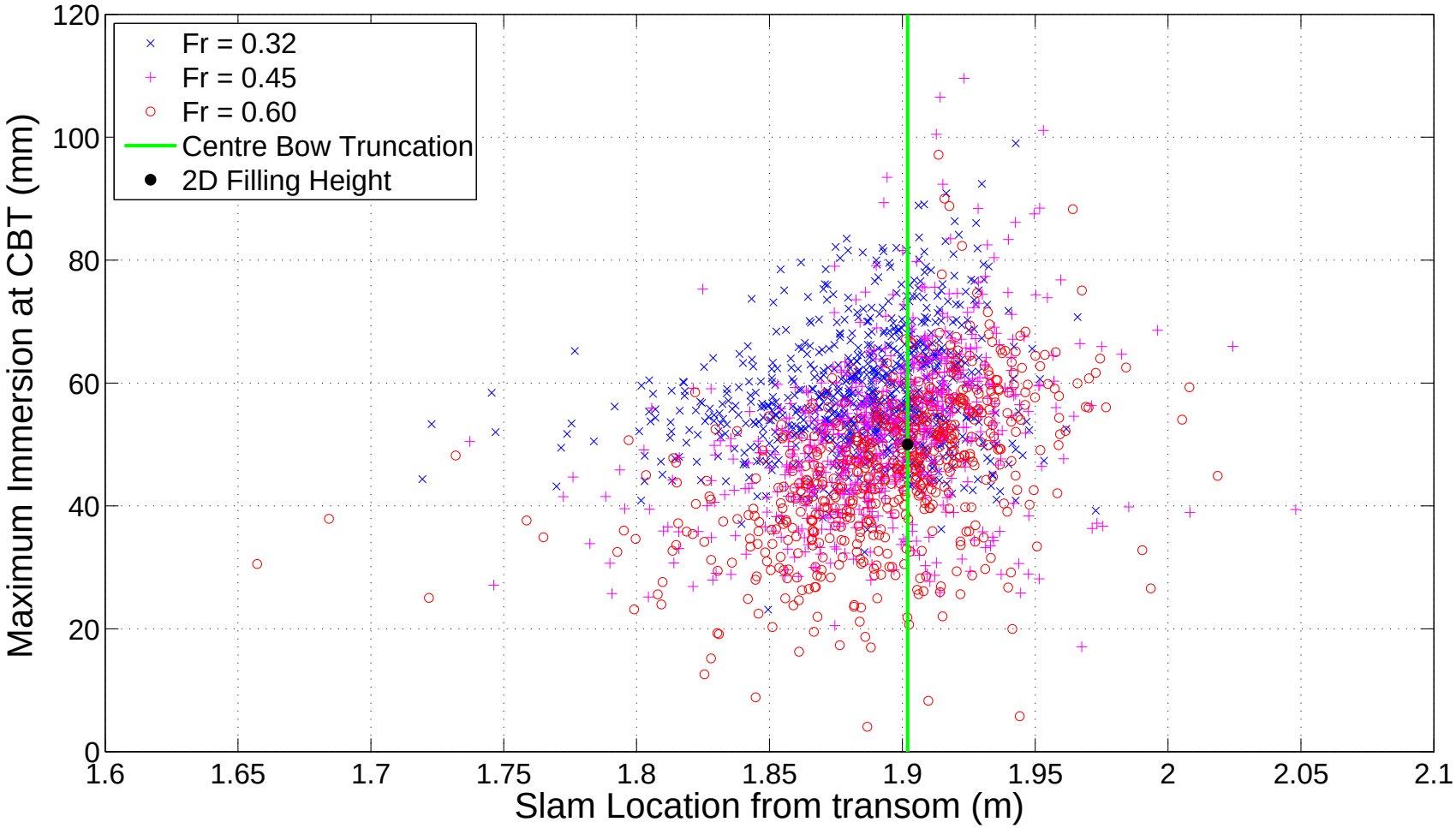

Figure C.19: Slam location against *maximum* immersion at the centre bow truncation, location of the CBT and the 2D filling height is included. Data grouped by Froude number.

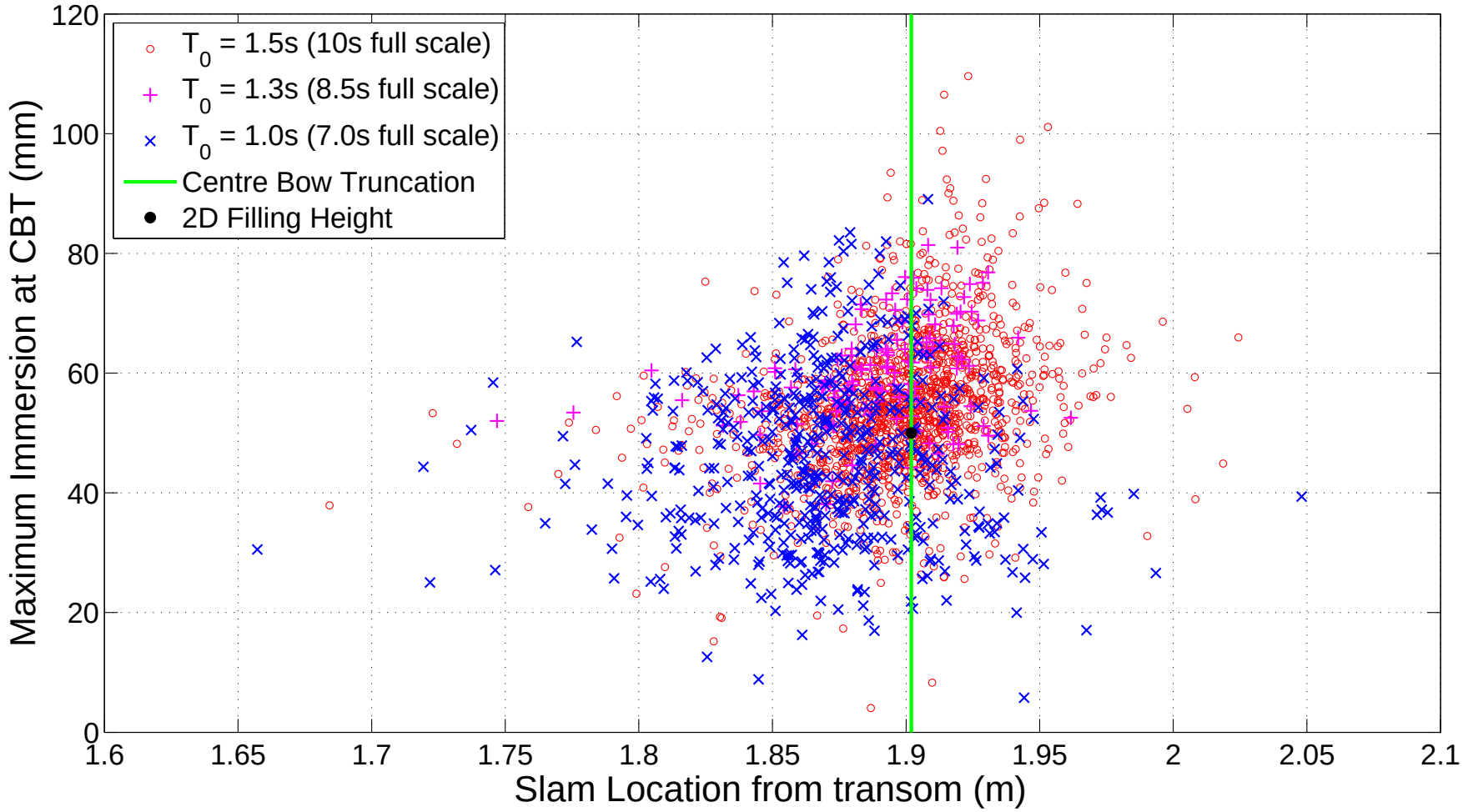

Figure C.20: Slam location against *maximum* immersion at the centre bow truncation, location of the CBT and the 2D filling height is included. Data grouped by modal period.